Connectomic Analyses of Songbird Area X

Alexandra Elke Rother

Dissertation zur Erlangung des Doktorgrades der Naturwissenschaften

Fakultät für Biologie
der Ludwig-Maximilians-Universität München

München, 19. September 2025

Erstgutachter: Prof. Dr. Benedikt Grothe
Zweitgutachter: Prof. Dr. Winfried Denk
Tag der Abgabe: 19. September 2025
Tag der mündlichen Prüfung: 13. Januar 2026

Abstract

Connectomics is a field dedicated to the high-resolution analysis of neural circuits. Making use of nanometer scale resolution provided by volume electron microscopy (EM), analysis allows information on the level of individual synapses and other subcellular structures.

This thesis presents a comprehensive analysis of a connectomic dataset from the songbird brain, specifically Area X—a nucleus involved in song learning and part of the avian basal ganglia. The work includes improvements to the processing pipeline, morphological characterization of neurons and glia, and detailed analyses of synaptic connectivity and subcellular organelles.

To facilitate this analysis, the existing EM data processing pipeline was extended to include classification of glial cells, migratory neurons, and three newly described GABAergic interneurons. Additionally, to enable analysis of further subcellular structures, the endoplasmic reticulum (ER), the Golgi apparatus (GA), and individual synaptic vesicles were predicted. This culminated in the first dataset that, alongside dense reconstructions of over 8,500 neurons, includes densely segmented synapses, mitochondria, ER, GA, and individual vesicles.

Mitochondria, vesicles and axonal ER densities were found to correlate with known firing rates and help to bridge information between EM and functional methods.

The dataset provides the first connectomic overview of basal ganglia circuitry in any species. Analyses revealed analogues of the direct, indirect, and hyperdirect pathways. In terms of synaptic connectivity, the direct pathway is the strongest pathway through Area X, while the hyperdirect pathway appears to be its strongest antagonist. The indirect pathway is poorly segregated from the direct pathway and also weak in terms of synaptic connectivity. Since one cell type of the indirect pathway, the GPe, is more involved in a feedback loop with novel GABAergic interneurons, the results challenge the idea of basal ganglia connectivity being mainly in the form of feedforward pathways.

As not all cell types transmit information via synaptic transmission, individual vesicles were used to further analyze the possibility of volume transmission. The presence of vesicles outside synaptic loci was common in cholinergic and dopaminergic axons, consistent with their reported use of volume transmission and their surroundings were in line with a global signal.

Finally, dense reconstructions of glial cells and migratory neurons allowed for organelle-level comparisons, providing insight into their metabolic demands. To highlight their role in neuronal plasticity, contact sites with neurons were analyzed as a first proxy for neuron-glia interactions.

In summary, this thesis presents the first dense connectomic analysis of an avian basal ganglia nucleus, integrating synaptic, morphological, and subcellular data. These findings not only provide new insights into the structure and function of Area X and into connectivity within the vertebrate basal ganglia, but also demonstrate how extending connectomic pipelines to include organelles and non-neuronal cells can unlock richer biological interpretations from EM datasets.

Zusammenfassung

Das Forschungsfeld der Konnektomik beschäftigt sich mit der Analyse neuronaler Schaltkreise basierend auf Daten aus der volumetrischen Elektronenmikroskopie (EM). Diese ermöglicht eine Auflösung im Nanometerbereich und damit die Untersuchung auf der Ebene einzelner Synapsen und subzellulärer Strukturen.

Diese Arbeit präsentiert eine umfassende Analyse eines konnektomischen Datensatzes aus dem Gehirn des Zebrafinken, speziell aus Area X – einem Hirnareal, das für das Erlernen von Gesang notwendig und Teil der avianen Basalganglien ist. Die Arbeit umfasst Verbesserungen der Datenverarbeitungspipeline, die morphologische Charakterisierung von Neuronen und Gliazellen sowie detaillierte Analysen der synaptischen Konnektivität und subzellulärer Organellen.

Zur Durchführung dieser Analyse wurde die bestehende EM-Verarbeitungspipeline erweitert, um die Klassifikation von Gliazellen, migrierenden Neuronen und drei neu identifizierten GABAergen Interneurontypen zu ermöglichen. Um Informationen von weiteren subzellulären Strukturen analysieren zu können, wurden auch das endoplasmatische Retikulum (ER), der Golgi-Apparat (GA) und einzelne synaptische Vesikel vorhergesagt. Das Ergebnis ist der erste Datensatz, der neben der dichten Rekonstruktion von über 8.500 Neuronen auch die vollständige Segmentierung von Synapsen, Mitochondrien, ER, GA und Vesikeln umfasst.

Die Dichten von Mitochondrien, Vesikeln und axonalem ER korrelierten mit bekannten Feuerraten und können damit die Lücke zwischen EM-Daten und funktionellen Methoden weiter schließen.

Der Datensatz bietet erstmals einen umfassenden konnektomischen Überblick über die Verschaltung der Basalganglien. Analysen identifizierten Analoga der direkten, indirekten und hyperdirekten Signalwege. Der direkte Weg stellt den stärksten Verschaltungsweg durch Area X dar, während der hyperdirekte Weg als ihr stärkster Antagonist fungiert. Der indirekte Weg war nur schwach ausgeprägt und nicht klar von dem direkten getrennt. Da ein Zelltyp des indirekten Signalwegs, GPe, vor allem in Rückkopplungsschleifen mit den neu beschriebenen Interneuronen eingebunden ist, stellen diese Ergebnisse die klassische Vorstellung von vornehmlich vorwärts-organisierten Signalwegen in den Basalganglien in Frage.

Da nicht alle Zelltypen Informationen ausschließlich über synaptische Übertragung weitergeben, wurden einzelne Vesikel genutzt, um mögliche volumenbasierte Übertragungsmechanismen zu untersuchen. Vesikel außerhalb von Synapsen waren insbesondere in cholinergen und dopaminergen Axonen häufig, was zu ihrer vermuteten Rolle in der Volumenübertragung passen würde. Zelltypen und Synapsen in der Umgebung der Vesikel außerhalb der Synapsen waren entsprechend ihrer Häufigkeit im Datensatz vertreten, was auf ein global wirkendes Signal hindeutet.

Abschließend ermöglichten die dichten Rekonstruktionen von Gliazellen und migrierenden Neuronen erstmals organellbasierte Vergleiche, die Rückschlüsse auf den Energiebedarf dieser Zelltypen zulassen. Um ihre Rolle in der neuronalen Plastizität zu beleuchten, wurden Kontaktflächen mit Neuronen als

erster Proxy für neuron-gliale Interaktionen analysiert.

Zusammenfassend präsentiert diese Arbeit die erste konnektomische Analyse eines avianen Basalganglien-Kerns, in der synaptische, morphologische und subzelluläre Daten integriert wurden. Die Ergebnisse liefern neue Einblicke in die Struktur und Funktion von Area X sowie in die Konnektivität der Basalganglien bei Wirbeltieren und zeigen, wie die Einbindung von Organellen und nicht-neuronalen Zelltypen die Aussagekraft von EM-Datensätzen erweitern kann.

Abbreviations

ACh acetylcholine

ACSF artificial cerebrospinal fluid

AFP anterior forebrain pathway

AIS axon initial segment

ATLUM Automatic Tape-collecting Lathe Ultramicrotome

ATP adenosine triphosphate

BBB blood-brain barrier

CB cacodylate buffer

CNN convolutional neural networks

CR+ calretinin-positive interneurons

DA dopamine

DLM medial portion of dorsolateral thalamus

dMSN direct pathway medium spiny neuron

dph days post-hatch

DTI diffusion tensor imaging

ECS extracellular space

EM electron microscopy

ER endoplasmic reticulum

FFN flood-filling networks

FIB focused ion beam

FS fast-spiking neurons

GA Golgi apparatus

GABA γ-aminobutyric acid

GCIB gas cluster ion beam

GPe globus pallidus externus

GPi globus pallidus internus

iMSN indirect pathway medium spiny neuron

LMAN lateral magnocellular nucleus of the anterior nidopallium

LTD long-term depression

LTP long-term potentiation

LTS low-threshold spiking neurons

mSEM multibeam scanning electron microscopy

MSN medium spiny neuron

NGF neurogliaform neurons

NSCs neural stem cells

NXIIts tracheosyringeal branch of the hypoglossal nerve

OPC oligodendrocyte precursor cell

PFA paraformaldehyde

RA robust nucleus of the arcopallium

RFC random forest classifier

RFECV recursive feature elimination with cross-validation

RPE reward prediction error

SA spine apparatus

SBEM serial block-face electron microscopy

SEM scanning electron microscopy

SNc substantia nigra pars compacta

SNr substantia nigra pars reticulata

STN subthalamic nucleus

TAN tonically active neurons

TCH thiocarbohydrazide

TEM transmission electron microscopy

VP ventral pallidum

VTA ventral tegmental area

Contents

Introduction

To navigate our world and all of its different stimuli, we first need to learn. Learn what all things we hear, see, smell and feel mean, how we move through this world and how we communicate with others. This makes learning the main task during development of most animals and continues into adulthood to maintain and expand our behavioral repertoire.

Learning all these different behaviors is no simple task and understanding how learning is facilitated in the brain is one of the biggest challenges in neuroscience. There are several ways to study learning; one well-known method is conditioning tasks. In these tasks, animals—often mice—learn to perform a specific action, such as pressing a lever. When they perform the action correctly, they receive a reward, such as water, sugar water, or fruit juice. Monitoring different brain regions via electrophysiology or imaging techniques during or after learning this task provides insight into their role in learning. For example, monitoring dopamine neurons during one of these tasks showed that they signal the prediction of rewards and errors in this prediction (Schultz et al. 1997), key concept introduced further in section 1.3.2.

While these studies are essential for understanding learning, they only provide insight into controlled environments. They do not necessarily explain all aspects of innate behaviors, such as learning how to move or communicate with peers.

A common model organism to study learning of an innate behavior, song learning, is the zebra finch. Zebra finches use their songs for courtship. Listening to the song as it improves makes it easy to track the learning process.

The goal of this thesis is to contribute to our understanding of the learning of innate behaviors by studying them in songbirds. The focus is on Area X, a part of the basal ganglia commonly associated with learning in vertebrates. Unlike the examples above, I am not studying this in behavioral assays. Instead, I am examining it on a much smaller scale to study the connection motifs that underlie the function of this critical brain region. The field dedicated to studying neuronal connections in detail is called connectomics. In the following paragraphs, I will introduce all of the aforementioned aspects of this thesis.

1.1 Cellular and subcellular neurobiology

Analyzing a specific brain region in detail requires paying special attention to its cells. Santiago Ramón y Cajal presented the idea that the brain consists of individual cells in 1888 as the "neuron doctrine" (López-Muñoz et al. 2006). Through his detailed drawings of neurons, Cajal demonstrated the significant

morphological differences between different types of neurons.

In addition to adult neurons, which process and distribute information via electrical and chemical signals, the brain consists of migratory neurons and developing neurons that migrate through the brain, as well as different types of glial cells. Glial cells maintain the environment, nourish neurons, influence neuronal plasticity, act as immune cells, and comprise the blood-brain barrier. Originally, all of these cell types were called "glia" (Old Greek for "glue") due to ignorance of their diverse tasks and importance for brain function. Further studies revealed their different morphologies and allowed for further classification.

1.1.1 Neurons

Neurons are necessary for processing information by communicating via electrical and chemical signals. They usually consist of three compartments: 1) the dendrite, 2) the soma (cell body), and 3) the axon (see figure 1.1). Neuronal cell types differ in their morphology and their neurotransmitters.

Neuron structure

Neurons receive incoming signals from other cells on either the dendrites or the soma. The dendritic tree consists of several primary dendrites that branch further after emerging from the soma. The extent of branching varies by cell type (see figure 1.1).

A dendrite consists of a dendritic shaft and spines. Dendritic spines develop from filopodia, which are long, thin protrusions that vary in shape and size (Hering et al. 2001). A classical mushroom-shaped spine consists of a thin neck and a larger head. While synapses also connect to the dendritic shaft, spines can provide separate microcompartments for Ca^{2+} responses and allow for easier adaptions in synapse size. Spines can harbor one or several incoming synapses. When a spine has a single synapse, its head volume is proportional to the synaptic area (Harris et al. 1989, Holler et al. 2021).

The soma, the cell body, contains the nucleus as well as several other organelles, similar to other cell types. It is the main site of protein synthesis and maintains other cellular functions, while also processing incoming signals. If these signals lead to spiking in the neuron, an action potential is generated in the axon initial segment (AIS).

The AIS is the first region of the axon. Action potentials generated here are transmitted across the axon via either a myelinated or unmyelinated part (see figure 1.1, Debanne et al. 2011). Myelination, which acts as insulation around the axon to speed up signal transmission, is provided by a glial cell type called oligodendrocytes. To transmit signals to other cells, the axon splits into branches that synapse onto cells via axon boutons or varicosities, which are larger swellings along the axon (en passant boutons) or at its end (terminal boutons).

Neuron types

The morphology of neurons differs in all three compartments. They vary in general size, dendrite and axon branch patterns, and spine density.

The brain consists of multiple regions that can be divided into functional units called nuclei. These nuclei contain several different types of cells. Neurons that project out of their regions to transmit signals to others are called projection neurons. Those that only connect within a nucleus are called interneurons.

Neurons also differ in their effects on each other depending on the neurotransmitters used for communication. The most common inhibitory neurotransmitter is γ-aminobutyric acid (GABA), which hyperpo-

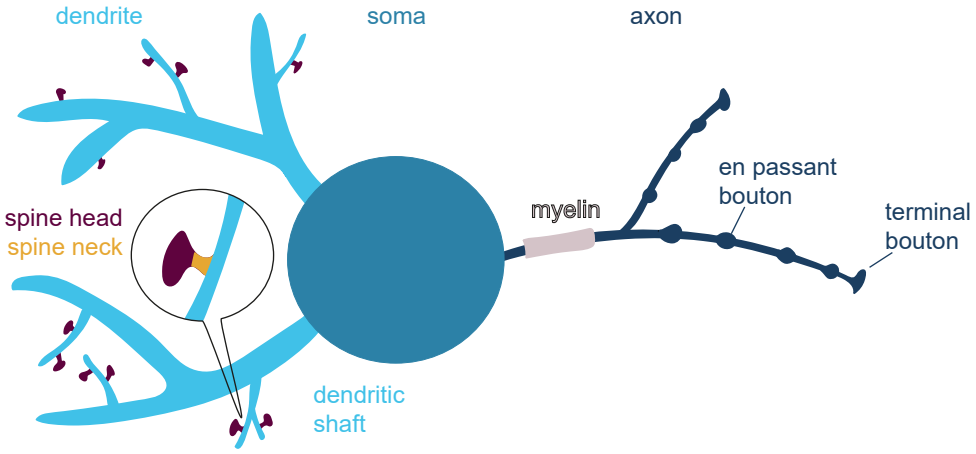

Figure 1.1: Schematic of neuron compartments: dendrite, soma and axon. Dendrites consist of a dendritic shaft and spines. The zoomed-in view shows that spines are commonly composed of a spine head and spine neck. The axon shows a myelinated part, en passant and terminal boutons.

larizes the cell membrane. The most common excitatory neurotransmitter is glutamate, which depolarizes the cell membrane (Hyman 2005). Other common neurotransmitters include acetylcholine (ACh) and dopamine (DA), the effects of which depend on the type of receptor they bind to (Abudukeyoumu et al. 2019, Beaulieu et al. 2011).

While most neurons are expected to release only one type of neurotransmitter, the co-release of several neurotransmitters has been reported in several types of neurons (Hnasko et al. 2012). One example are DA neurons, which co-release GABA or glutamate (Morales et al. 2017), and even release DA and glutamate on the same axons in different locations (Zhang et al. 2015).

In addition to their morphology and neurotransmitter types, neurons also vary in their electrophysiological properties and transcriptomic profiles. Therefore, grouping neurons into cell types based on similarity can vary depending on the characterization technique used.

1.1.2 Immature neurons

New neurons are generated throughout development and adulthood. These neurons originate from neural stem cells (NSCs) in neurogenic niches and must then migrate to their designated brain region. In adult mammals, NSCs primarily differentiate into glial cells, though new neurons are found in certain regions of the brain, such as the hippocampus and striatum (Götz et al. 2016, Inta et al. 2015).

In other vertebrates, such as birds, new neurons are common in other regions of the brain such as the forebrain. Until they reach their destination, these new neurons travel as migratory neurons. Migratory neurons are bipolar, with an elongated soma and a few trailing processes (Scott et al. 2012, see result figure 3.10).

1.1.3 Glial cells

Glia cells perform a variety of tasks that support brain function. Types of glia cells found in the brain include astrocytes, microglia, oligodendrocytes, and oligodendrocyte precursor cells (OPCs).

Astrocyte

Astrocytes are the most abundant glial cell type, making up an estimated 20 - 40 % of the cells in the brain (Baldwin et al. 2024). In the context of this thesis, the relevant astrocytes are located in the gray matter, which are called protoplasmic astrocytes. They have an elongated soma and several branches that form a complex tree. These branches end in constrictions and expansions that result in several thin processes. Astrocytes also have a high density of mitochondria and at least one endfoot that contacts a blood vessel (Baldwin et al. 2024, Salmon et al. 2023, see result figure 3.10).

They have several functions. One is controlling access to the brain as part of the blood-brain barrier (BBB).

The second is controlling the environment in which they are organized into an astrocytic network that is coupled via gap junctions (Gutnick et al. 1981, Peng et al. 2023).

The third is a role in synaptic plasticity. There, astrocytes respond to various neurotransmitters and influence synaptic communication by releasing different gliotransmitters, including glutamate, GABA, D-serine, and adenosine triphosphate (ATP, Durkee et al. 2019). Thereby, individual astrocytes are not restricted to using only one gliotransmitter. When excited, astrocytes display changes in cytosolic Ca^{2+} concentrations.

Astrocytes are also part of the tripartite synapse. In this structure, an astrocytic process ensheats the synapse and can release its gliotransmitters in close proximity to the synapse, thereby regulating synaptic homeostasis (Lalo et al. 2021).

Microglia

Microglia are the immune cells of the brain. In their "resting" state, they are not actually resting, but rather surveilling the environment. In this state, they have a ramified morphology consisting of a small soma from which several processes emerge and split into thin branches (Kettenmann et al. 2011, see result figure 3.10).

When brain homeostasis is altered by trauma or disease, for example, microglia transform into their "activated" state, in which their morphology resembles that of macrophages in the rest of the body. Their somata swell, their processes become less complex, and their appearance becomes more amoeboid. In this state, they can migrate toward an infection site and phagocytose damaged cells or microbes (Kettenmann et al. 2011).

In addition to their immune function, they participate in synaptogenesis and the regulation of neuronal activity. In states of hypoactivity, e.g., under anesthesia, they increase neuronal firing; conversely, they reduce it in states of neuronal hyperactivity (Umpierre et al. 2021). They also remove inhibitory synapses via phagocytosis (Hashimoto et al. 2023) or induce synapse formation through dendritic contact (Miyamoto et al. 2016). This dendritic contact is followed by a Ca^{2+} response that leads to filopodia formation, thereby increasing synapse formation.

Oligodendrocyte

The main function of oligodendrocytes is to myelinate axons during development and adulthood. Myelin, an extension of the cell's plasma membrane, enhances signal transmission across the axon (Elbaz et al. 2019). This process, known as saltatory conduction, allows action potentials to propagate via "gaps" in the myelin layers (nodes of Ranvier), where sodium channels are located.

To create a myelin layer, oligodendrocytes have several processes that originate from the soma and wrap around the axons multiple times (see result figure 3.10). Unlike Schwann cells, which are their counterparts in the peripheral nervous system, oligodendrocytes can myelinate several axons (Elbaz et al. 2019). Myelination depends on axon diameter and is only initiated when a certain threshold diameter is reached. For cultured oligodendrocytes, this threshold is 0.4 µm (Lee et al. 2012, Matthews 1968). Through the accumulation of neurofilaments and phosphorylation, myelination can also increase axon diameter further (Elbaz et al. 2019). Myelination is also a dynamic process regulated by Ca^{2+} activity in oligodendrocytes and neuronal plasticity (Elbaz et al. 2019). Myelinated axons are not usually continuously myelinated (Tomassy et al. 2014).

In addition to their function as insulators, myelin sheets provide metabolic support to neurons and transfer generated lactate to axons (Elbaz et al. 2019).

Oligodendrocytes develop from oligodendrocyte precursor cells (OPCs).

Oligodendrocyte precursor cell

Oligodendrocyte precursor cells (OPCs), which are also sometimes referred to as oligodendrocyte progenitor cells, fulfill functions even before developing into oligodendrocytes.

OPCs can interact with neurons and directly receive synaptic input and respond to both, glutamate and GABA (Buchanan et al. 2022). They have a round soma with several processes that branch into finer processes (see result figure 3.10). These processes can also engulf axons (Buchanan et al. 2022).

Additionally, OPCs have immunomodulatory capabilities, can sample their environments with their dynamic filopodia and migrate to injury sites (Elbaz et al. 2019, Hughes et al. 2013).

To ensure OPCs are available to replace oligodendrocytes when needed, OPCs are distributed throughout the tissue at a constant density (Hughes et al. 2013).

1.1.4 Signaling in the brain

There are different modes of signaling in the brain: direct contact, such as chemical and electrical synapses, and volume transmission, which involves the release of neurotransmitters or neuropeptides into the extracellular space (ECS).

Chemical synapses

In chemical synapses (hereafter only referred to as synapses), signals are transmitted via different neurotransmitters. These neurotransmitters are released by the presynaptic cell into the synaptic cleft, where they are taken up by receptors on the membrane of the postsynaptic cell. Prior to release, neurotransmitters are stored in synaptic vesicles that fuse with the cell membrane, a process promoted by the second messenger Ca^{2+} (Brini et al. 2014, see figure 1.2).

The presynaptic terminal is usually an axon, and the postsynaptic terminal is usually a dendrite or soma. However, exceptions include axo-axonic synapses and autapses, which are synapses onto the same

cell.

To facilitate learning and memory storage, synapses can strengthen or weaken, which is accompanied by changes in synaptic size. The synaptic area, as measured by electron microscopy (EM), is thereby correlated with the synaptic strength, as measured by electrophysiological recordings (Holler et al. 2021).

The strengthening or weakening of synapses is called synaptic plasticity. In its simplest form, Hebbian plasticity refers to an increase in synaptic strength when neurons on the presynaptic and postsynaptic sites fire nearly simultaneously. This process is also referred to as spike-timing dependent plasticity (Magee et al. 2020) and is summarized by the phrase "neurons that fire together wire together". This mechanism relies on the overlap of increased postsynaptic Ca^{2+} levels with synaptic input and action potentials, operating on a timescale of tens of milliseconds.

If this strengthens a synapse over time, it is referred to as long-term potentiation (LTP). The process that weakens a synapse over time is called long-term depression (LTD).

Simple Hebbian plasticity does not account for all learning rules in the brain. In order to strengthen synapses that lead to suitable behavior, synaptic plasticity must be able to react to behavioral output that occurs a second later. To facilitate this process, Hebbian plasticity is expanded into a three-factor plasticity rule. In addition to the firing of presynaptic and postsynaptic neurons, a modulatory neurotransmitter (e.g., DA), which spreads over a large area via volume transmission, must reach the synapse to strengthen it (Magee et al. 2020). In this concept, the firing of pre- and postsynaptic neurons together only marks the synapse with an eligibility trace that degrades over the course of one to two seconds. This plasticity concept is especially important in reinforcement learning, which will be introduced later (section 1.3.2).

Electrical synapses

Electrical synapses, also known as gap junctions, are connections between cell types that convey electrical charges and small metabolites bidirectionally. In vertebrates, they are composed of connexins, which are transmembrane proteins (Nielsen et al. 2012). They are regulated by voltage, pH or Ca^{2+}.

Transmission via electrical synapses occurs on a fast timescale, with coincidence detection happening in less than a millisecond. This process is continuous and maintained through a high turnover of connexins (Alcamí et al. 2019).

Electrical synapses, which mainly form axo-axonic or dendro-dendritic connections, coexist with chemical synapses in neurons (Gutiérrez 2023). In glial cells, gap junctions exist in connections between astrocytes and oligodendrocytes (Peng et al. 2023).

Volume transmission

Another form of signaling in the brain occurs without direct contact between cells and is called volume transmission. In this process, neurotransmitters or neuropeptides are released directly into the ECS. This form of transmission is mainly limited by the diffusion of neurotransmitters and can reach receptors several micrometers away, and up to millimeters away for neuropeptides, in a time frame of several milliseconds to potentially minutes (Özçete et al. 2024). Thus, volume transmission is less specific than synaptic transmission and acts as a global signal over a larger area.

Neurotransmitters are released from small, clear, core vesicles with diameters of 40-50 nm, while neuropeptides are released from larger, dense core vesicles named for their appearance in EM with diameters of 80-120 nm (Takamori et al. 2006, Özçete et al. 2024).

Several neurotransmitters, such as DA, ACh, glutamate, GABA, and serotonin, are released outside of clear synaptic loci in the axon (Trueta et al. 2012). While it has been shown that DA vesicle release depends on machinery similar to that in synapses, this machinery is only present in around 30 % of axonal varicosities (Liu et al. 2018). It is unclear if this is true for other neurotransmitters.

Neuropeptides, such as substance P and oxytocin, are exocytosed from the axons, dendrites, and somata of neurons (Trueta et al. 2012, Özçete et al. 2024). Although neuropeptide signaling has been less studied in vertebrates, it has been shown to connect neurons in a denser and more decentralized fashion than the synaptic network in C. elegans (Ripoll-Sánchez et al. 2023).

1.1.5 Organelles

Neurons and glia cells contain a variety of organelles that ensure their basic functionality. Some of these organelles, such as mitochondria, the endoplasmic reticulum (ER), the Golgi apparatus (GA), and vesicles, are surrounded by lipid bilayer membranes similar to cell membranes. Due to the specific staining of these membranes in EM (section 1.4.1), these organelles and their outlines can be clearly identified. This is why they will be the focus of this thesis.

Nucleus

The nucleus is part of the cell's soma. It is surrounded by a lipid bilayer membrane connected to the ER and contains the cell's DNA. For protein biosynthesis, RNA is transported through nuclear pores into the cytoplasm (see figure 1.2).

In the opposite direction, Ca^{2+} signals can travel from synapses to the nucleus, where they can activate genetic programs (Brini et al. 2014).

Mitochondria

Mitochondria are the main source of ATP production through aerobic glycolysis in cells. The inner membrane structure consists of several cristae, and the enclosed matrix includes the mitochondrial genome, RNAs, and ribosomes that translate several mitochondrial proteins (Frey et al. 2000, see figure 1.2, inset 1). Depending on the type of neuron, the shape of the cristae can change. For example, fast-spiking cells in the hippocampus have more elongated cristae (Cserép et al. 2018).

In addition to their role in energy production, mitochondria act as Ca^{2+} buffers and transfer of Ca^{2+} from the ER is facilitated via mitochondria-ER contact sites (Devine et al. 2018, Tsuboi et al. 2021). Mitochondria can also react to changes in intracellular Ca^{2+} by stopping in areas with high Ca^{2+} to provide support in local energy production and Ca^{2+} buffering (López-Doménech et al. 2023).

Mitochondria are present in all neuronal and glial compartments. Their shapes and sizes vary depending on the compartment (Salmon et al. 2023, Turner et al. 2022, Thomas et al. 2023), as well as on energy demands. Longer mitochondria are more efficient and protected against mitophagy and are usually found in the soma and dendrites (López-Doménech et al. 2023, Turner et al. 2022). In the axon, mitochondria are typically smaller and rounder, likely to adapt to larger transport distances and local requirements for Ca^{2+} buffering.

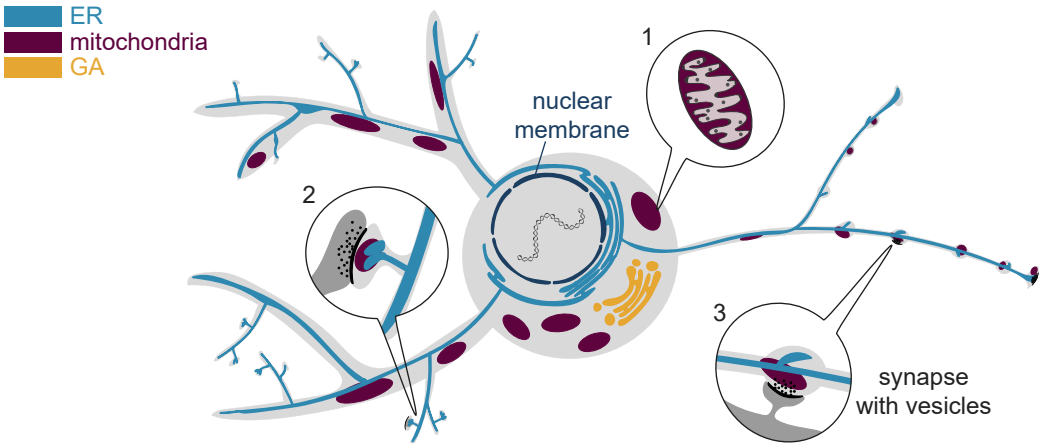

Figure 1.2: Schematic of organelles in the different neuronal compartments. One mitochondrion is shown with its internal composition. Inset 1 shows that the internal structure of the mitochondria consists of ribosomes (round) and cristae. Inset 2 shows a synapse on the spine of the depicted neuron. The ER extends into the spine as the spine apparatus. Inset 3 shows an outgoing synapse from an en-passant terminal of the depicted neuron.

Endoplasmic reticulum

The ER is well-known for its role in protein synthesis and trafficking. Important for neuronal plasticity and signaling in the brain, ER also has Ca^{2+} buffering and storage properties (Tsuboi et al. 2021).

The ER is present in all neuronal and glial compartments as an interconnected network of thin tubules, especially in axons and spines, where they can be as thin as 15–30 nm in diameter (see figure 1.2, Tsuboi et al. 2021, Terasaki 2018, Wu et al. 2017). In the soma, the ER exists as rough and smooth ER, distinguished by the rough ER's attached ribosomes. In the axon and dendrite, the ER is mostly smooth.

As mentioned above, the ER contacts and interacts with mitochondria in all compartments to regulate Ca^{2+} (Wu et al. 2017). Due to the high concentration of Ca^{2+} near the ER, contact with the ER is necessary for mitochondrial Ca^{2+} uptake (Tsuboi et al. 2021).

The ER can expand its surface area in spines by organizing into several cisterns, forming the spine apparatus (SA, see figure 1.2 inset 2). The SA is present in larger spines, especially large mushroom spines (Cooney et al. 2002, Dorkenwald et al. 2022, Spacek et al. 1997, Wu et al. 2017). The role of the SA in learning is still unclear. One study of the mouse hippocampus reported that spine enlargement is accompanied by a loss of SA (Uytiepo et al. 2025), while another study of the rat hippocampus found that the presence of SA is required for long-term potentiation (Chirillo et al. 2019).

Golgi apparatus

The Golgi apparatus (GA) consists of several stacks of cisternae and vesicles that move between them (see figure 1.2). The GA's main functions are intracellular membrane trafficking, protein sorting, and modification. This is why the GA interacts closely with the ER (Chen et al. 2023).

GA is primarily found in the soma, though it can extend to the initial segment of dendrites (Chen et al. 2023). Golgi outposts are typically found in longer dendrites, with one per neuron, especially in pyramidal cells of the hippocampus (Horton et al. 2005) and, rarely, in astrocyte endfeet (Boulay et al. 2017).

Vesicles

Vesicles are transport containers for different substances, such as neurotransmitters and neuropeptides.

As mentioned previously (section 1.1.4), the size and appearance in EM differ depending on the contents. Neurotransmitters are transported in small, clear core vesicles with a diameter of 40-50 nm, while neuropeptides are transported in large, dense core vesicles with a diameter of 80-120 nm (Takamori et al. 2006, Özçete et al. 2024).

The shape of the vesicles can differ depending on their contents. For example, in chemically fixed tissue for EM, GABA-containing vesicles are more oval-shaped than glutamatergic vesicles (Korogod et al. 2015).

Vesicles are also used in the soma for the general transport of proteins into and out of the cell via endo- and exocytosis. In this thesis, however, the term "vesicles" refers to small, clear core vesicles that transport neurotransmitters.

1.2 Basal ganglia

The basal ganglia are a subcortical brain region that includes several nuclei in the diencephalon and mesencephalon (see figure 1.3, Tisch et al. 2004, Shipp 2017). They receive input from cortical and midbrain structures and project to the thalamus in several basal ganglia pathways.

They are involved in motor control, motor learning, and action selection. Dysfunction is associated with neurodegenerative diseases, such as Parkinson's or Huntington's, as well as psychiatric disorders, such as addiction and obsessive-compulsive disorder (Fazl et al. 2018).

The basal ganglia are an evolutionarily conserved structure across vertebrates, with striking similarities between lampreys and mammals that are separated by over 500 million years of evolution (Grillner et al. 2016). Since the basal ganglia of mammals, especially rodents, are the most well-studied, they will be used as a reference for common basal ganglia mechanisms.

1.2.1 Mammalian basal ganglia

The mammalian basal ganglia consists of several nuclei that receive cortical input and project between different regions, as well as outside the basal ganglia to the thalamus (Fazl et al. 2018).

These nuclei include the putamen, which can be separated into the striatum (named after its striped appearance), the globus pallidus externus (GPe), the globus pallidus internus (GPi, in mouse also endopeduncular nucleus, hereafter referred to as GPi), subthalamic nucleus (STN), substantia nigra pars reticulata (SNr), and the substantia nigra pars compacta (SNc, see figure 1.3 a).

Of these, the striatum and the STN are typically considered input nuclei because their primary input comes from cortical projections (Shipp, 2017). The GPe and SNc only project to other basal ganglia nuclei. The GPi and SNr are output structures that project to the thalamus. All nuclei also receive dopaminergic input from either the SNc or the ventral tegmental area (VTA) of the midbrain (Cragg

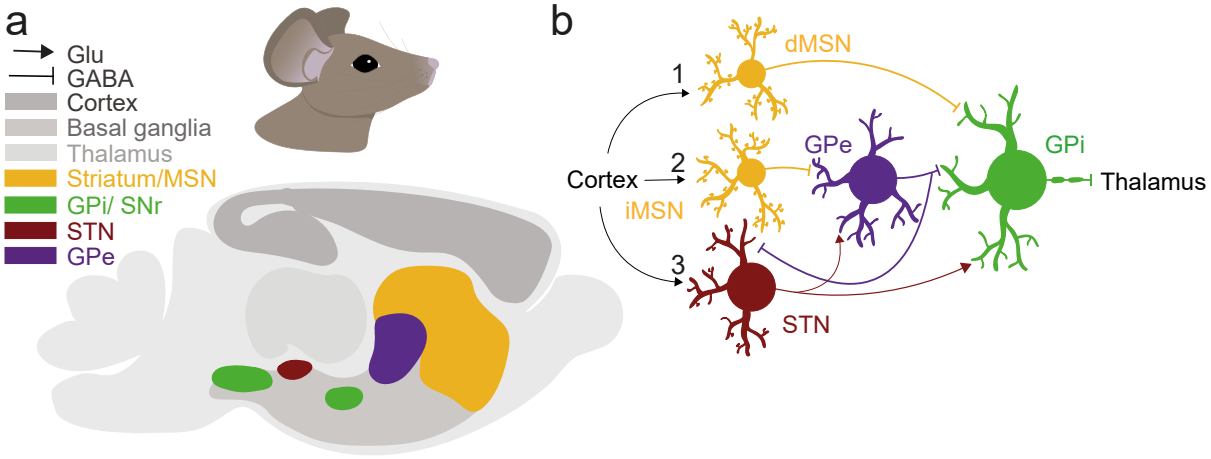

Figure 1.3: Schematic of mammalian basal ganglia. a Schematic of the mouse brain with different basal ganglia nuclei. b Basal ganglia pathways: 1) the direct pathway, 2) the indirect pathway, and 3) the hyperdirect pathway.

et al. 2004, Fazl et al. 2018, Tisch et al. 2004).

All projection neurons of the basal ganglia nuclei are GABAergic, except for those of the STN, which are glutamatergic.

The basal ganglia output through these nuclei is mainly controlled by three pathways to facilitate learning and movement initiation: 1) the direct pathway, 2) the indirect pathway, and 3) the hyperdirect pathway (see figure 1.3 b)

Basal ganglia pathways

All three pathways begin with cortical input and lead over different nuclei to GPi/SNr which projects to the thalamus. Since projection neurons of GPi and SNr are large, GABAergic, have a high firing rate and are tonically active, the thalamus is inhibited in the default state. In the context of motor learning and control, this results in a state in which no movement is executed (see figure 1.3, Shipp 2017).

The direct pathway begins with cortical input to the striatum. The striatum's projection neurons are medium spiny neurons (MSN, sometimes also referred to as striatal projection neurons). MSNs make up 90 - 95 % of the striatum, have a small soma of 12 - 15 µm diameter and densely spiny dendrites (Fazl et al. 2018, Gagnon et al. 2017, Tisch et al. 2004). In the direct pathway, the MSN project to the GPi/SNr. The GABAergic projection leads to disinhibition of the thalamus and thereby movement initiation (see figure 1.3 b1).

The indirect pathway also begins with cortical input to the MSNs of the striatum. The MSNs then project to the GPe. In the "short" version of the indirect pathway, the GPe projects to the GPi/SNr. This leads to inhibition of the thalamus and, consequently, inhibition of movement (see figure 1.3 b2, Shipp 2017). In the "long" version of the indirect pathway, the GPe first projects to the STN. The STN then excites the GPi/SNr, leading to the same effect: inhibition of the thalamus and, consequently, inhibition of movement (Shipp 2017).

To separate the direct and indirect pathway in the striatum, a different MSN subpopulation is associated with each pathway. These subpopulations can be distinguished based on their DA receptors, connectivity, and morphological differences. MSNs of the direct pathway (dMSNs) express D1-like DA receptors, leading to an excitatory effect when DA binds. In contrast, MSNs of the indirect pathway (iMSNs) express D2-like DA receptors, resulting in an inhibitory effect when DA binds (Gerfen et al. 1990). Thus, the different MSN subpopulations are regulated differently by DA. Additionally, dMSNs have longer, more branched dendrites than iMSNs (Gagnon et al. 2017, Gertler et al. 2008). iMSNs project exclusively to the GPe, while dMSNs project to the GPi with collaterals to the GPe, making the separation of these pathways less strict (Wu et al. 2000).

A third population of MSNs expresses both types of DA receptors and constitutes between 2 and 17 % of MSNs in the striatum, depending on the region and measurement technique (Bonnavion et al. 2024, Gagnon et al. 2017). These cells have a lower spine density and smaller dendritic tree, making them morphologically distinct from dMSNs and iMSNs (Gagnon et al. 2017). This population exclusively connects to the GPe, yet it contributes to the functionality of both pathways by influencing the dMSNs and iMSNs (Bonnavion et al. 2024).

The third pathway is the hyperdirect pathway, which starts with cortical projections to the STN. The STN then projects to the GPi/SNr. This projection excites the GPi/SNr, thereby strengthening the inhibition of the thalamus and leading to movement inhibition (see figure 1.3 b3). Because it involves fewer cell types than the two versions of the indirect pathway, it is thought to be a faster route to movement inhibition. Thus, it has been associated with stopping unwanted movements (Fazl et al. 2018, Shipp 2017).

In addition to their roles in the indirect and hyperdirect pathways, STN neurons send collaterals to the GPe. This creates a recurrent connection between these two nuclei (Fazl et al. 2018, Shipp 2017).

According to the classical model of basal ganglia function, the direct pathway initiates movement, while the indirect and hyperdirect pathways inhibit or stop it. However, more recent research suggests that both pathways are active simultaneously, leading to two newer models of their interaction (Bariselli et al. 2019). One model proposes that the direct pathway initiates movement, while the indirect pathway suppresses unwanted movement. The second model is based on research indicating that the two pathways are similar in terms of selectivity. It proposes that the two pathways compete for the resulting action (Bariselli et al. 2019).

Neurons in addition to basal ganglia pathways

The basal ganglia contain several other types of neurons that are important for basal ganglia function, but which are not described in classical basal ganglia pathways. These include interneurons in the different nuclei, as well as additional projection neurons.

The striatum includes several types of interneurons that contribute to the function of the basal ganglia. The following types are most commonly discussed and will be the focus of this thesis: fast-spiking neurons (FS), low-threshold spiking neurons (LTS), neurogliaform neurons (NGF), calretinin-positive interneurons (CR+), and tonically active neurons (TAN).

FS are GABAergic, parvalbumin-positive interneurons. They have medium-sized somata, varicose dendrites, and dense axonal arborizations. They also have a high firing rate of up to 199 Hz, and half of the population forms autapses (Wang et al. 2023). Receiving cortical and thalamic input, they project mainly to the MSNs, providing the largest source of feedforward inhibition from the cortex to MSNs in the striatum (Gittis et al. 2010, Johansson et al. 2020, Owen et al. 2018).

The LTS are GABAergic and co-express neuropeptide Y, somatostatin, and nitric oxide synthase. Their morphology is characterized by long, sparsely branched axons and spiny dendrites (Ibáñez-Sandoval et al. 2011, Tepper et al. 2018). They receive cortical and thalamic input and project to MSNs (Gittis et al. 2010, Ibáñez-Sandoval et al. 2011, Tepper et al. 2018). However, due to their low synaptic density, their synaptic input onto MSNs or other striatal neurons is limited, and they are thought to play a modulatory role through volume transmission (Gittis et al. 2010, Ibáñez-Sandoval et al. 2011).

The NGF are GABAergic, express neuropeptide Y and have round somata, highly branched and sparsely spiny dendrites and dense axonal arborizations (Ibáñez-Sandoval et al. 2011). They primarily receive cortical input and target MSNs.

The CR+ interneurons are GABAergic, medium-sized with aspiny dendrites and can be further divided into three morphologically and topographically distinct populations (Tepper et al. 2010, Tepper et al. 2018). They exhibit tonic activity in response to cortical activation, yet their connectivity patterns remain unknown (Tepper et al. 2018).

TANs are cholinergic interneurons with large somata, spiny dendrites, and long, branched axons (Abudukeyoumu et al. 2019). They receive input from MSNs, as well as from cortical and thalamic regions, and they project to MSNs and other striatal interneurons (Abudukeyoumu et al. 2019, Johansson et al. 2020). With limited number of outgoing synapses, TANs primarily signal via volume transmission (Abudukeyoumu et al. 2019).

Other basal ganglia nuclei contain different classes of interneurons. The STN contains GABAergic interneurons. The GPe and GPi, on the other hand, include a small population of cholinergic interneurons (Courtney et al. 2023, Miyamoto et al. 2022, Prasad et al. 2024).

In addition to interneurons, there are projection neurons in the basal ganglia nuclei that are not part of basal ganglia pathways.

One type is the arkypallidal neuron, which resides in the GPe, expresses preproenkephalin, and projects to the striatum (Mallet et al. 2012). There, they mainly target MSNs, as well as striatal GABAergic interneurons and TANs. The inhibition they receive from the prototypical projection neurons of the GPe makes them part of a feedback loop sufficient to inhibit movement in mice (Aristieta et al. 2021).

The GPe also has another class of GABAergic projection neurons that project to the midbrain, cortex and reticular thalamus (Courtney et al. 2023).

In addition to GPi projection neurons, which comprise 90 % of the neurons in the core region, the GPi has projection neurons that express somatostatin or nitric oxide synthase and project to the lateral habenula (Miyamoto et al. 2022).

The SNc provides dopaminergic projections to all the other basal ganglia nuclei and to brainstem motor centers (Grillner et al. 2016, Courtney et al. 2023). Their extensive axonal arborizations span a broad area within target nuclei, facilitating signal transmission via volume transmission (Arbuthnott et al. 2007, Liu et al. 2022). These neurons are important for movement initiation and motor learning, although they are not directly part of the basal ganglia pathways. The depletion or death of these neurons, as occurs in Parkinson's disease, leads to problems with motor control and movement initiation. In the context of motor learning, DA neurons of SNc and VTA provide the reward prediction error (RPE) that is important for reinforcement learning, which will be introduced later (section 1.3.2, Grillner et al. 2016).

Striosome-matrix organization of the striatum

In addition to being divided into different nuclei, the basal ganglia have other functional specializations. One example is the striosome-matrix organization of the striatum.

Striosomes, also known as patches, are scattered across the striatum in compartments separated by the matrix (Brimblecombe et al. 2017).

While the MSNs of both pathways are present in both the striosome and the matrix, other types of interneurons are more specific to either compartment. Some, e.g., the TANs and LTS, are commonly found in the border region between the striosome and the matrix (Brimblecombe et al. 2017).

Another difference is DA innervation and release. Although DA axons innervate both compartments, individual axons may prefer one over the other. While striosomes show a higher innervation density, for yet unknown reasons the DA concentrations in the matrix are higher (Brimblecombe et al. 2017).

The striosome and the matrix also differ in function. Striosomes are associated with the regulation of dopaminergic influences, while the matrix compartment is associated with the initiation of movement and motor control via the direct and indirect pathways (Grillner et al. 2016, Shipp 2017).

1.2.2 Avian basal ganglia

Avian basal ganglia nuclei

Although the basal ganglia is evolutionarily conserved in vertebrates (Grillner et al. 2016), there are still differences among different vertebrate classes.

The avian basal ganglia, particularly those of songbirds, consist of several nuclei: Area X, commonly referred to as striatal analogue, ventral pallidum (VP) and STN (Das et al. 2022, Chen et al. 2019, Farries et al. 2002). These nuclei all play a role in song learning and receive cortical and dopaminergic input from the VTA.

Of these areas, Area X is the largest. It contains an estimated 500,000 neurons within a 1.6 mm^3 volume in adult zebra finches (Burek et al. 1991). While the STN and VP contribute to song learning by contributing to calculations of the RPE, Area X is where this information is used to learn time-muscle associations during song (see section 1.3.2, Chen et al. 2020, Das et al. 2022).

Because this thesis focuses on analyzing a dataset of Area X, the differences between Area X and the mammalian striatum are further discussed in more detail.

The basal ganglia nucleus for song learning: Area X

Area X contains several types of neurons that are functionally and morphologically similar to those in the mammalian striatum. The most common neuron types in Area X are MSNs. Other interneuron types are similar to TAN, LTS and FS cells (Farries et al. 2002).

Whether two distinct MSN populations exist in Area X, similar to dMSNs and iMSNs in the mammalian striatum, remains unclear. While pharmacological studies and receptor expression in one study indicated that most MSNs express both D1 and D2 receptors (Ding et al. 2002, Kubikova et al. 2010), a single-nucleus RNA sequencing study identified separate MSN populations, with only 18% of coexpressing MSNs (Xiao et al. 2021).

Area X receives input from the lateral magnocellular nucleus of the anterior nidopallium (LMAN) and HVC (former higher vocal center, now used as common name), two song nuclei located in the pallium. Due to its organization into separate nuclei rather than a layered structure, the pallium differs from the

mammalian cortex. However, it is otherwise considered a cortex analog and will therefore be referred to as such throughout the thesis (Jarvis 2004). Additionally, Area X receives DA input from the VTA and projects to the medial portion of dorsolateral thalamus (DLM, see figure 1.4, Fee et al. 2011).

Based on similar cell types and input and output structures, Area X is commonly considered an avian analog of the striatum. However, Area X also contains cell types found in other basal ganglia nuclei.

These include two types of pallidal cells, the GPe and the GPi, which are named after their mammalian counterparts. The GPi was distinguished from the GPe based on its ability to project outside of Area X and its higher tonic firing rate (Farries et al. 2005, Goldberg et al. 2010).

Additionally, recordings of pallidal cells in Area X slices indicate the existence of a glutamatergic cell type that could be an STN analog in Area X (Budzillo et al. 2017).

With MSNs receiving HVC and LMAN input and connecting to analogous cells in the GPi, a direct pathway analogue has been found in Area X (Farries et al. 2005, Fee et al. 2011). The presence of another pallidal type and its close contacts with the soma and dendrites of the GPi could indicate a "short" indirect pathway analog (Farries et al. 2005), but functional or connectivity evidence is still limited. Additionally, it is unclear whether the presence of glutamatergic cells in Area X allows for connectivity similar to that of a "long" indirect or hyperdirect pathway within Area X.

1.3 The songbird brain

Zebra finches are small songbirds native to Australia and Indonesia. The males have the characteristic black stripe pattern for which they are named and which reaches from below their beaks to their breast (see figure 1.4).

Male zebra finches grow up learning one song from a tutor that they sing as part of their courtship behavior. Their songs last about one second and consist of one or several "motifs," each of which consists of two to seven syllables, each lasting around 100 ms (Fee et al. 2011). Zebra finches learn only one song, but they can sing it in a highly stereotyped fashion.

Since a good song performance is crucial for successful mating, male zebra finches are innately driven to learn their songs. It takes around 50-60 days for them to first start singing, and around 90 days post-hatch (dph) for their song to reach its "crystalized" stage (Fee et al. 2011).

Song learning occurs in several phases. In the first phase, the sensory phase, zebra finches listen to and memorize their tutor's song (Rundstrom et al. 2021). During the sensorimotor phase, the birds first "babble" and produce an unstereotyped, highly variable subsong. Over the course of learning, this subsong turns into a highly stereotyped, crystallized song with a clear structure (Fee et al. 2011, Rundstrom et al. 2021).

This learning process and its phases are similar to how humans learn speech (Mooney 2018, Rundstrom et al. 2021). To maintain the ability to sing, adults must continue to sing and practice daily to maintain the muscle physiology needed for precise performance of the song (Adam et al. 2023).

The innate drive to learn, the high precision of its song, its similarity to human speech learning, and the relatively short time frame make the zebra finch an ideal model organism for song and thus motor learning.

The songbird has distinct brain circuits for producing and learning songs, which will be discussed in the following sections.

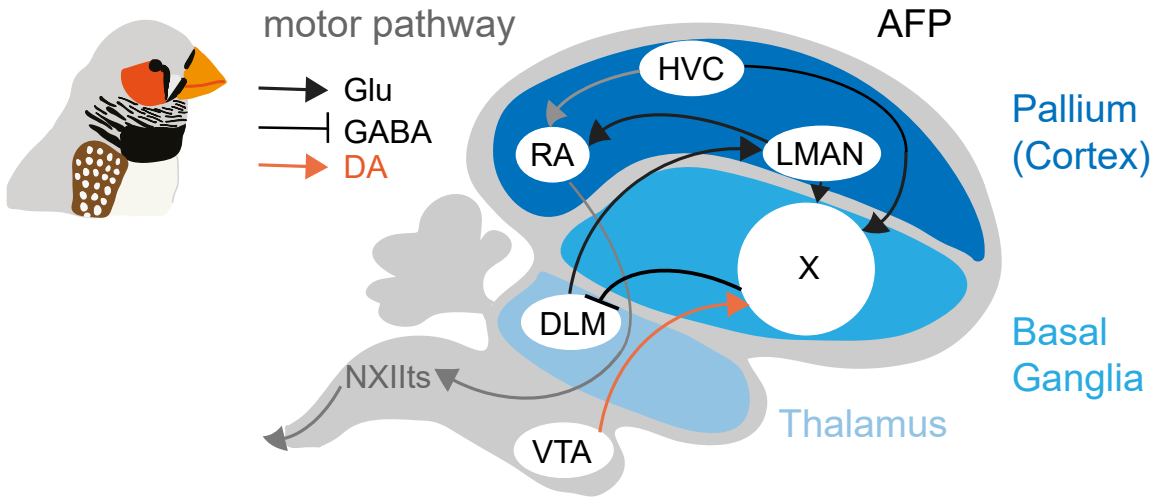

Figure 1.4: Schematic of a male zebra finch and its brain, showing the motor pathway for song production and the anterior forebrain pathway (AFP), which is used for song learning. In addition to the HVC and LMAN projections to Area X that are part of the AFP, VTA DA neurons also project to Area X.

1.3.1 Song production: the motor pathway

Songbirds use the song motor pathway for song production (see figure 1.4).

In this pathway, the pallial (cortical) nucleus HVC transmits timing information to the robust nucleus of the arcopallium (RA). The RA then projects to the tracheosyringeal branch of the hypoglossal nerve (NXIIts), which projects to eight muscle pairs in the bird's vocal organ, the syrinx (Fee et al. 2011, Adam et al. 2021).

HVC neurons signal timing by activating a population of RA neurons for a few milliseconds during a song motif, thus activating them at a specific time in the song (Kozhevnikov et al. 2007). To control the high temporal precision of the song, the syrinx is made of superfast muscles capable of acoustic modulations up to 250 Hz (Elemans et al. 2008). Additionally, muscle fibers in the syrinx are tightly controlled by the NXIIts, with 50 % of its neurons innervating ≤ 3 muscle fibers and 13 - 17 % innervating only one muscle fiber (Adam et al. 2021).

1.3.2 Song learning: the anterior forebrain pathway

To learn their song, or more specifically, to learn which muscles to activate and when during a song, songbirds have a different brain circuit called the anterior forebrain pathway (AFP, see figure 1.4).

Information about which muscle to activate and when is stored in HVC-RA connections. During learning, outputs from LMAN to RA, the output of the AFP, bias HVC-RA connections (Andalman et al. 2009).

In the AFP, both HVC and LMAN project to Area X, which projects back to LMAN via the thalamic nuclei DLM (see figure 1.4, Fee et al. 2011). HVC conveys timing information, while LMAN provides a

copy of the information sent back to Area X while adding variability.

Together with the dopaminergic input from VTA, inputs from HVC and LMAN allow for song learning in a reinforcement learning paradigm.

Reinforcement learning

In general, reinforcement learning describes a form of goal-directed learning driven by a reward. Although reinforcement learning is common in animals, many of the ideas and terms used originate from computer science. It is also used in machine learning, with AlphaGo being a prominent example (Silver et al. 2016).

Central to the idea of reinforcement learning is the maximization of reward through trial-and-error search (Sutton et al. 2017).

To illustrate this, imagine a computer game about volleyball. The player is the "reinforcement agent", and their goal is to win the match. The agent tries out different moves to learn which ones increase the chance of winning.

However, since a volleyball match is only won once a team reaches 25 points, giving a reward only at the end of the match would be too sparse. Too many actions happen before the outcome, making it hard to know which one was helpful. This is known as the 'credit assignment problem' (Sutton et al. 2017).

To make learning easier, rewards could be given after every point scored. The agent would then try to maximize points. But without clear guidance, it might learn that prolonging the game leads to the most points. After all, in theory, the longer a match lasts, the more points can be scored. This shows that the reward signal must be designed carefully so it encourages the right behavior and doesn't stretch across too many steps.

In addition to rewards, reinforcement learning uses a value function, which helps define the ultimate goal (Sutton et al. 2017). In the volleyball example, this would be winning the match. It ensures that the agent not only scores points, but also finishes the game with a win. While some actions, like a strong serve, might lead directly to a reward (a point), other actions, like good team positioning or communication, don't immediately score but still contribute to winning. These are learned as valuable over time.

Reinforcement learning can be model-free, relying solely on trial-and-error, or model-based, where the agent builds a more general understanding of how the game works (Sutton et al. 2017).

While a reward signal can indicate whether an action was good, reinforcement learning can also work with a RPE (Fee et al. 2011). In this case, there is a baseline signal that increases if a suitable action is better than expected and decreases if it is worse than expected. This means that once a useful action is learned, it no longer triggers a strong signal, thereby allowing the agent to focus on learning in less familiar situations. The signal is computed from the difference between expected and actual reward.

In the brain, reinforcement learning uses an RPE in the form of DA signals (Schultz et al. 1997).

Song learning as a model of reinforcement learning

Motor learning, as well as song learning as a special form of it, follows a reinforcement learning framework.

In a proposed model, learning occurs in Area X through inputs from the HVC, LMAN, and VTA to the MSNs (see figure 1.4, Chen et al. 2020, Fee et al. 2011). In an "actor-critic" model of reinforcement learning, Area X would be the "actor." Input from the HVC provides a "context" or "state" signal that indicates the current time point in song learning. To encourage exploration during learning, the LMAN signal introduces variability in addition to providing a copy of the previous output, also known as an

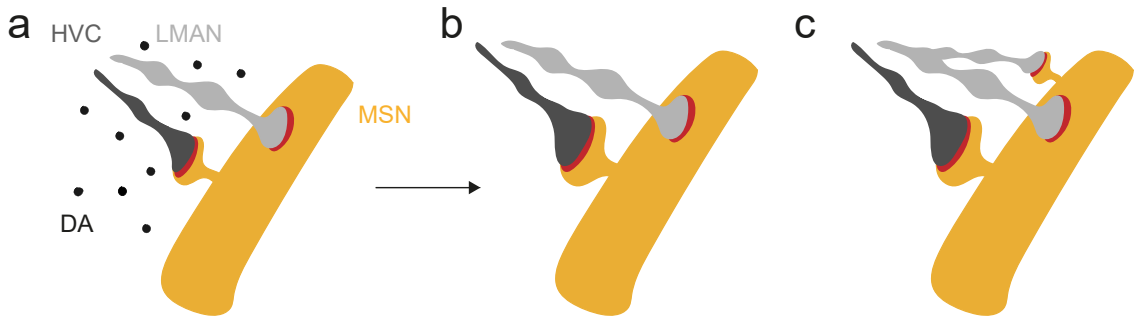

Figure 1.5: Song learning at the synaptic level in Area X, adapted from Kornfeld et al. 2020. a, b If HVC and LMAN signal to an MSN in Area X at the same time, which excites the MSN and is followed by a DA signal later, the HVC - MSN synapse is strengthened. In this model, HVC mainly targets the spines, while the LMAN mainly targets the dendritic shafts. c In a connectomics study, 86.7 % of HVC inputs target the spines of MSN neurons, while only 52.3 % of LMAN inputs do so (Kornfeld et al. 2020).

"efference copy" (Fee 2014).

The song's performance is evaluated using DA projections from the VTA in the form of an RPE. This is also referred to as a performance error because there is no external reward, but the song's performance is evaluated (Gadagkar et al. 2016, Chen et al. 2020).

Since performance can only be evaluated after the time point has passed, this learning relies on a three-factor plasticity rule similar to the one introduced earlier (section 1.1.4). There, the timing of input from HVC must coincide with the firing of the postsynaptic MSN neuron. Together with a signal from LMAN at the same time this results in an "eligibility" trace that marks the HVC-MSN synapse until a DA signal indicates whether the performance was better or worse than expected (Fee et al. 2011). Depending on the outcome, the HVC-MSN synapse strengthens or weakens. The output of the loop from LMAN mirrors this to RA. Excitation of a given RA neuron by LMAN at the same time that HVC fires strengthens the HVC-RA connection, which activates a specific muscle at a given time.

To enable muscle-specific updates, the LMAN-RA and LMAN-Area X-DLM connections are organized into topographical loops that are microscopically closed (Luo et al. 2001). This means that a subregion in the LMAN projects to a subregion in Area X, which then projects to a subregion in DLM, and so on. Whether these correspond to specific muscles or muscle parts still needs to be determined.

In this model, only the HVC-MSN synapses change size during learning, while the LMAN signal acts as a gatekeeper, allowing learning by exciting a specific MSN dendrite or not (Fee 2014). These different functions are thought to correspond to the different targets of specific axons: HVC mainly targets the spines of MSN neurons, while LMAN targets the dendritic shaft (see figure 1.5 a, b).

A connectomics study showed that, while 86.7 % of HVC inputs target the dendritic spines of MSN neurons, only 52.3 % of LMAN inputs do so (see figure 1.5 c, Kornfeld et al. 2020). Since nearly half of the LMAN inputs are also made on spines, potential spine alterations due to LMAN firing during learning cannot currently be excluded, and the role of LMAN in learning is still under discussion.

With Area X as the "actor" of learning, the VP would be the "critic" (Chen et al. 2020). The critic's role is to compute the expected reward. The VP receives input from VTA neurons that transmit

reward/performance prediction errors to Area X, along with a time representation from the thalamic nucleus Uva, which also projects to HVC. In this model, if performance is better than expected at a given time, these two inputs can strengthen the synapse at that time in the VP, leading to the expectation of better performance in the next round.

In addition to input from VP, the VTA receives input from the auditory cortex that transmits the actual error in the just-produced song (Chen et al. 2020). Based on the predicted quality at a given time point from VP and the actual error from the auditory cortex, the reward/performance prediction error can be computed in the VTA and sent to Area X in the form of a DA signal

1.4 Connectomics

The brain can be studied using a variety of techniques, such as behavioral assays, electrophysiology, functional imaging, and RNA sequencing. Another focus is on connections between brain regions, cell types, and individual cells. The latter is summarized in the field of connectomics.

Connectomics can be done on macroscale, examining the entire brain and focusing on the connections between brain areas, often using noninvasive methods such as diffusion tensor imaging (DTI; Zeng 2018). In DTI, diffusion of water is used to determine averaged axonal directions, but it does not provide sufficient resolution to visualize individual axons (Vorona et al. 2015).

At the mesoscale, different tracing techniques such as viral tracers which are then visualized with light microscopy can be used to visualize connections between neuron types of different regions (Zeng 2018).

At the microscale, connectomics is the study of connections between individual neurons, achieved by visualizing (chemical) synapses (Zeng 2018, Abbott et al. 2020). This thesis focuses on microscale connectomics, so the term "connectomics" will refer only to microscale connectomics.

To study the connections between neurons, the synapses must be explicitly visualized because membrane contact alone does not indicate a synapse (Holler et al. 2021, Kasthuri et al. 2015). As synapses strengthen or weaken during the course of learning, it is noteworthy that the synaptic transmission strength correlates with the synaptic area as visualized in EM, and connectomics can thereby measure connection strength (Holler et al. 2021).

To visualize synapses, a high-resolution 3D volume is acquired, with a resolution of around 30 nm per pixel needed in the x-y direction. This was first achieved with EM, which was used to completely reconstruct the brain of the worm C. elegans, which has roughly 5×10^4 µm^3 (Abbott et al. 2020, White et al. 1986) and the fruit fly Drosophila melanogaster with approximately 5×10^7 µm^3 (Abbott et al. 2020, Zheng et al. 2018). For comparison, the brain volume of a mouse is around 5×10^{11} µm^3 (Abbott et al. 2020), and a zebra finch brain is roughly at the same size.

Recent advances in expansion microscopy have enabled a light microscopy-based connectomics approach in which synapses can be identified using molecular markers (Tavakoli et al. 2025). Improvements in X-ray tomography have demonstrated the ability to resolve individual synapses, suggesting its potential application in connectomics analysis in the future (Bosch et al. 2023). Currently, no in vivo imaging technique can achieve the required resolution for connectomics; thus, all of the aforementioned approaches image tissue postmortem.

This thesis focuses on EM-based connectomics, so it will introduce this technique and its workflow in more detail. The process of EM-based connectomics can generally be divided into four steps: 1) sample preparation, 2) cutting and imaging, 3) data processing, and 4) data analysis (see figure 1.6).

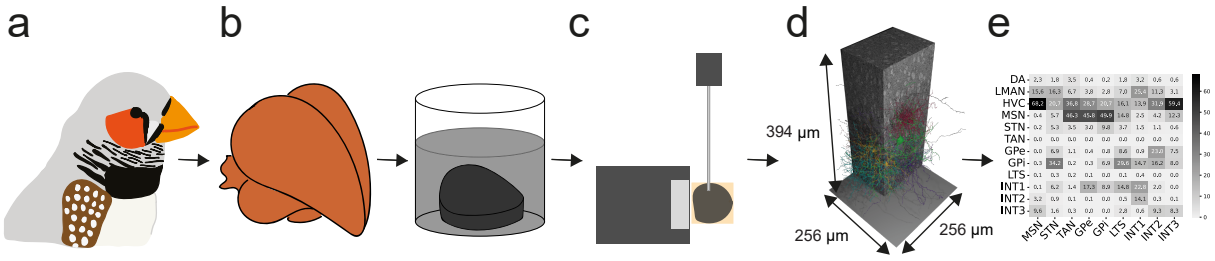

Figure 1.6: Schematic of connectomics pipeline. a Zebra finch b Sample preparation: Brain extraction and heavy metal staining. c Cutting and imaging. The image shows a knife boat that cuts a sample, which is imaged by an electron beam. d Data processing (image shows dataset j0251). e Data analysis (image shows connectivity matrix, from section 3.4.2, figure 3.31).

1.4.1 Sample preparation for electron microscopy

In EM, electrons are shot at the sample. Depending on the atomic mass of the molecule, the electrons are transmitted or scattered back at different angles. Biological samples consist mostly of carbon, hydrogen, oxygen, and nitrogen, all of which have similarly low masses. Therefore, imaging of native tissue yields little contrast, so molecules of interest must be stained with heavy metals to produce contrast.

In connectomics, the target structures for staining to visualize cells and their connections are lipid-double membranes. This process also visualizes organelles with lipid bilayer membranes, such as the nucleus, mitochondria, ER, and GA.

To achieve high contrast between the membranes and cytoplasm or ECS, the staining must be uniform across the tissue, and the tissue's ultrastructure must be preserved as much as possible. To facilitate this, the sample is extracted and fixed before staining. After staining, the sample is embedded in epoxy resin for cutting and imaging.

Tissue extraction and fixation

There are three different methods for extracting and fixing the tissue.

The first method involves extracting the brain via decapitation and then cryo-fixing the tissue, which is also referred to as "high-pressure freezing". Although cryo-fixation effectively preserves the ultrastructure and approximately 15 % ECS of the brain, it is only sufficient for samples up to 200 µm (Korogod et al. 2015, Studer et al. 1995).

The second method is immersion fixation with aldehydes. In this method, the brain is extracted after decapitation and immersed in a mixture of glutaraldehyde and paraformaldehyde (PFA). During aldehyde fixation, ions from the ECS enter cellular compartments, causing them to swell and reducing the ECS (Harreveld et al. 1967, Harreveld et al. 1968). Increasing the osmolality of the fixative buffer during immersion fixation can counteract aldehyde-induced swelling in small samples with less than 1 mm thickness (Cragg 1980, Fulton et al. 2020, Pallotto et al. 2015).

In addition to ultrastructural preservation, preserving ECS aids in the penetration of heavy metals and antibodies. Preserving 6 % of the ECS also aids in the segmentation of cells for data processing (Pallotto et al. 2015).

Compared to cryo-fixation, aldehyde fixation changes the appearance of synapses, vesicles, and astrocytic processes (Korogod et al. 2015). In vertebrates, synapses, especially glutamate and GABAergic synapses, can be distinguished based on whether they have an asymmetric or symmetric postsynaptic density (Colonnier 1968, Gray 1959). Aldehyde-fixed tissue reveals distinct shapes of vesicles containing GABA or glutamate at high resolution, while astrocytic coverage of synapses increases (Korogod et al. 2015).

The third method involves perfusing the brain with an aldehyde fixative. This method uses the brain's vasculature to distribute the fixative solution and is used for larger samples, such as whole mouse brains (Mikula et al. 2015, Song et al. 2023, Lu et al. 2023). As with the aforementioned effects of aldehyde fixation, without additional measures, this method's ECS preservation is low. To improve ECS preservation, pressure can be applied during perfusion (Cragg 1980) or a mannitol gradient can be used to achieve a more uniform result (Lu et al. 2023).

Heavy-metal staining

To stain lipid-membranes, the most commonly used heavy metal is osmium tetroxide (OsO_4). OsO_4 binds to several active groups, including C-C double bonds, diols, and thiols, in various structures, such as proteins, polysaccharides, and, most prominently, lipids.

To increase the contrast and bind more OsO_4 to the membranes, thiocarbohydrazide (TCH) was used between two OsO_4 staining steps in the "OTO" protocol (Seligman et al. 1966). TCH binds to OsO_4, allowing new OsO_4 to attach to it in a subsequent staining round.

Next, reducing the OsO_4 with ferrocyanide before the first step reduced protein staining but maintained membrane contrast in a protocol termed "ROTO" (Willingham et al. 1984). This protocol can be combined with others using heavy metals, such as uranyl acetate and lead aspartate (Deerinck et al. 2010, Walton 1979). It has also been adapted for en bloc staining of small samples up to 0.5 mm (Briggman et al. 2011, Pallotto et al. 2015). Further modifications included separating the reduced osmium step into an incubation with OsO_4 alone, followed by an incubation with ferrocyanide in the tissue. This modification worked with samples up to 1 mm (Hua et al. 2015).

For larger samples, TCH was found to induce ruptures through the formation of nitrogen bubbles. Therefore, it was replaced with pyrogallol for staining whole mouse brains (Mikula et al. 2015). Further modifications to the protocol, such as changing buffers, adjusting incubation times, adding washing steps, and altering temperatures, have led to more reliable protocols for staining samples ranging from a few millimeters thick to whole mouse brains (Lu et al. 2023, Song et al. 2023).

Embedding into epoxy resin

To further prepare the sample for imaging, the stained tissue is embedded in epoxy resin. First, the sample is dehydrated using a gradient of ethanol. Then, it is washed several times with an organic solvent, such as acetone, and incubated with increasing concentrations of resin in the organic solvent.

Epoxy resins are polymers that for proper infiltration are initially viscous at room temperature before they are hardened at temperatures of 60 - 80 °C. To increase homogeneity, the resin is degassed before infiltration. For optimal cutting, the resin requires a specific hardness (Tegethoff et al. 2024).

Depending on the cutting and imaging method (see section 1.4.2), sample is cut with a knife, milled with ions, or both. This determines which epoxy resin is the best choice.

Spurr's resin (Spurr 1969) is known for its low viscosity at room temperature, which improves infil-

tration. Its hardness values are ideal for ultrathin sectioning (20-50 nm), and it can be milled with ion beams (Hayworth et al. 2020, Tegethoff et al. 2024).

Hard-Plus Resin 812 is an alternative used for thicker sections (500 nm) to ensure less compression during cutting (Kormacheva 2023). For other methods, such as X-ray tomography, qualities such as high radiation resilience are important. Thus, other resins, such as "tough resin," are recommended for these methods (Bosch et al. 2023).

1.4.2 Cutting and imaging in connectomics

Connectomics works with volume EM data. To create a volume, several EM images are stacked together after imaging. Thus, the z-resolution of the volume depends on the thickness of the sections that can be imaged. Several methods are used for cutting and imaging. In one method, the sample is first cut, and then the sections are imaged. In another method, called en bloc imaging, cutting and imaging are done repetitively. A third method is a mixture of the first two.

If samples are cut before imaging, they are cut into ultra-thin sections of 20 - 50 nm with a diamond knife. These sections are then collected on grids or copper tape. Tape collection can be automated as part of the Automatic Tape-collecting Lathe Ultramicrotome (ATLUM) pipeline and used for transmission EM (TEM) or scanning EM (SEM, Hayworth et al. 2006).

In TEM, transmitted electrons are used to generate the image, which is therefore restricted to ultrathin sections. In contrast, SEM uses electrons emitted from the surface as either backscattered or secondary electrons, allowing it to image larger blocks (Kubota et al. 2025). Because it scans the image pixel by pixel, SEM is slower than TEM. To increase SEM speed, microscopes with up to 91 beams have been used for multibeam SEM (mSEM, Eberle et al. 2015, Kubota et al. 2025).

Instead of first cutting the sample into sections that are then imaged, serial block-face EM (SBEM) repetitively cuts and images (Denk et al. 2004). In this method, a microtome is incorporated into the microscope to cut a section after imaging (see figure 1.6 c). Thus, the z-resolution is limited to the capacity of the diamond knife, as it also is for ATLUM. This technique was also used to acquire the dataset analyzed in this thesis (j0251, Kornfeld 2017, Schubert et al. 2022).

To increase the z-resolution beyond the capacities of diamond knives, an alternative approach is to use a focused ion beam (FIB) to remove tissue after imaging, a process also referred to as milling (Knott et al. 2008). The FIB-SEM approach has achieved z-resolution as low as 4 nm (Xu et al. 2017).

Instead of using FIB for milling, the sample surface can be milled with argon clusters, which allows for milling in larger areas. This process is called gas cluster ion beam (GCIB) milling (Hayworth et al. 2020, Kubota et al. 2025). To image larger tissue stacks without compromising the high z-resolution, this approach can be combined with diamond knife sectioning. In this method, the sample is cut into semi-thin sections ranging from 100 to 500 nm. These sections are collected on silicon wafers and imaged using GCIB-SEM (Hayworth et al. 2020). For higher throughput, this approach can be combined with mSEM (Kormacheva 2023).

1.4.3 Data processing for connectomics

After EM images are aligned and stacked into an EM volume, the data must be processed before it can be analyzed to answer biological questions.

In the C. elegans connectome, manual identification of every synapse and cell was required (White et al. 1986). However, with computer programs like KNOSSOS, which trace cells via a skeleton representation,

the necessary time for manual annotation could decrease (Helmstaedter et al. 2011, Kornfeld 2017).

To enable the analysis of larger data sets and further reduce manual annotation time, convolutional neural networks (CNN) are used to segment cells and identify subcellular structures, such as synapses, mitochondria, and other organelles. Manual annotations are still needed to provide labeled data for training, but this is limited to a fraction of the data.

Flood-filling networks (FFNs), which use a recurrent approach, are commonly used for cell segmentation (Januszewski et al. 2018). To identify synapses, vesicle clouds, and mitochondria, frameworks such as SyConn have been developed (Dorkenwald et al. 2017). In this pipeline, organelles are first identified with a CNN, and synapses are additionally overlaid with the contact areas of cells to ensure that each synapse connects two different cells. This is followed by a random forest classifier (RFC) to estimate the probability that each identified structure is a synapse. An RFC includes multiple decision trees and, in this case, is trained on sets of correctly and incorrectly identified synapses. The resulting probability directly translates to the fraction of correctly identified synapses; for example, a synapse probability of 0.8 means that 80 % of synapses with this label are true synapses. This can then be used as a filtering criterion for analysis.

In addition to identifying synapses and cells, neural networks can be used to classify cellular compartments and cell types using either 2D images or point clouds (Schubert et al. 2019, Schubert et al. 2022). Various neural network architectures have been employed to classify synapses with different neurotransmitters (Eckstein et al. 2024) and identify up to 35 organelle classes (Heinrich et al. 2021), as well as extract synapse features for unsupervised classification (Wilson et al. 2023).

Errors that can result from neural network predictions include false predictions of structures, missing structures, splitting cell fragments that belong together, and merging parts that do not belong to the same cellular structure. The latter are also referred to as split-and-merge errors. Manual reviewing and/or proofreading of neuronal structures is required to address these errors.

To minimize the need for additional manual labor, different approaches can be implemented. One approach is the aforementioned use of additional classifiers, such as RFCs, to assign probabilities for additional filtering and estimate expected error rates (Dorkenwald et al. 2017). Another strategy is to develop proofreading frameworks that distribute the workflow to multiple users, such as FlyWire (Dorkenwald et al. 2022) and the Connectome Annotation Versioning Engine (CAVE, Dorkenwald et al. 2025). Lastly, the PATHFINDER framework (Precise Analysis, Tracing, and High-Fidelity Interpretation of Neuronal Data for Exhaustive Reconstruction) uses multiple neural networks to identify potential errors based on the shape of neurons (Januszewski et al. 2025).

1.4.4 Connectomic data analysis

The analysis of connectomic datasets depends on the size of the dataset, the data processing pipeline, and the focus of the biological question. As neural networks for segmentation and identification of synapses and other organelles become more widely available, the amount of data increases, requiring more sophisticated analysis tools.

Since the synaptic area correlates with synaptic transmission strength (Holler et al. 2021), it is important that analyses focus not only on the presence of a synapse, but also on its area and the cumulative area between two neurons.

The first step in connectomic analysis is commonly the generation of a connectivity matrix, which shows the summed synaptic area of individual neurons or neuron classes (see figure 1.5 e with results from section 3.4.2, Dorkenwald et al. 2017, Helmstaedter et al. 2013, Dorkenwald et al. 2024). While

this provides a comprehensive overview of the data, a matrix alone is insufficient for answering specific biological questions. This is the case when focusing on compartment-specific connectivity, which is lost in overviews of neuronal connections alone, and also because pathways that cover multiple steps are indirectly visible only in this visualization.

Depending on the size of the dataset, connectomic analysis can answer different biological questions. For example, it can compare the target structure, such as the spine versus the shaft of different inputs to the same neuron, in smaller datasets (Kornfeld et al. 2020). Alternatively, it can identify prominent signal pathways in larger datasets, such as a complete Drosophila brain (Dorkenwald et al. 2024). These signaling pathways were identified by tracing the presumed flow of information through several neuronal connections.

With several connectivity datasets available, analysis can either focus on specific developmental differences such as the number and summed area of synapses to a specific target structure over time (Gour et al. 2021) or on comparisons between species which can yield results such as an increased interneuron network in humans and macaques compared to mice (Loomba et al. 2022).

When additional information about the neurons is available from different techniques, such as molecular markers or two-photon imaging, the first step of the analysis is to match the data across the different imaging modalities. Then, the analysis can focus on differences between labeled synapses throughout learning and their ultrastructure (Uytiepo et al. 2025) or on relating functional information with differences in the connectivity of different neurons. The latter approach was used with a mouse cortical column dataset to demonstrate that neurons with similar functional properties, as determined by 2-photon imaging, also tend to connect with each other (Ding et al. 2025).

1.5 Aims and Hypothesis

This thesis aims to provide a comprehensive understanding of a previously acquired dataset, j0251, from Area X of the songbird brain (Kornfeld 2017), focusing on the morphology, organelles, and connectivity of neuronal and glial cell types. This is not only to improve the understanding of Area X's role in song learning but also to analyze basal ganglia pathways in connectomics for the first time.

In order to achieve this, first, the data processing pipeline was improved. Second, the morphology and subcellular structures of neuronal and glial cell types were characterized. Third, the connectivity between adult neuronal cell types was analyzed, with a specific focus on basal ganglia pathways, and then the implications of volume transmission by modulatory neurons were examined.

1.5.1 Data processing

Over the past decade, neuronal networks and computational pipelines have enabled the analysis of thousands of cells and millions of synapses in connectomics datasets (see section 1.4.3). However, in-depth biological analysis of specific connections, morphologies, and subcellular structures still requires manual proofreading. This is due to "merge errors," in which several neurons are segmented as one; misclassifications; and biases in the ground truth. These biases can include predicting short fragments as a specific cell type that has shorter fragments in the ground truth or overestimating the certainty of a specific type of synapse or cell due to its greater prevalence in the dataset, which is then transferred to the ground truth.

To improve connectomics analysis and reduce the aforementioned biases in the ground truth, this thesis

focuses on creating a new ground truth in order to improve synapse classification and the separation of mitochondria, as well as the classification of different projecting axon types. The thesis also aims to add new cell type classes, such as novel interneuron types, various glial cell types, and migratory neurons.

EM allows visualization of organelles surrounded by lipid double layers, such as mitochondria, ER, GA and vesicles. So far, only mitochondria and vesicle clouds have been processed, even though the number of vesicles has been linked to synapse size in the mammalian hippocampus and neocortex (Harris et al. 1989, Murthy et al. 2001, Kasthuri et al. 2015), and the ER is related to synaptic function via its role as a Ca^{2+} source and buffer (Tsuboi et al. 2021). One goal of this thesis is to segment and process these organelles in order to analyze them in relation to neuron morphology and firing properties.

While previous connectomics datasets have used information from different organelles (Kasthuri et al. 2015, Simon et al. 2021, Uytiepo et al. 2025) and a detailed organelle atlas of different cell types was recently released (Xu et al. 2021), this dataset j0251 is the first to densely reconstruct synapses, mitochondria, ER, GA, and individual vesicles spanning thousands of cells.

1.5.2 Morphology of neurons and glia and their subcellular structures

With over 8,500 neurons, this dataset of Area X, j0251, is the largest connectomics dataset not only of zebra finch but also generally of a basal ganglia nucleus so far. One goal of this thesis is to provide a detailed understanding of the different neuronal cell types and identify potential mammalian analogues. This includes identifying differences in subcellular structures and describing previously undescribed neuron types, including three types of GABAergic interneurons.

Since information about mitochondria, vesicle clouds, and synapse density has been found useful for classifying cell types (Dorkenwald et al. 2017), the second goal is to identify which morphological and subcellular structures are useful for classifying cells into different types in the context of connectomic analysis.

Additionally, higher firing rates during singing have been linked to higher densities of mitochondria and vesicle clouds in a smaller dataset with only coarse cell type classification (Dorkenwald et al. 2017). The third goal of the analysis is to determine whether this correlation extends to the ER, which stores Ca^{2+}, and to the densities of the GA and individual vesicles. If so, densities of organelles in novel interneuron types could predict their firing rates in vivo and facilitate identification in singing birds.

1.5.3 Connectomic analyses of Area X

Area X includes cell types analogous to those in several anatomically distinct basal ganglia nuclei in mammals. These cell types are connected via known basal ganglia pathways. Thus, j0251 provides the first opportunity to study these pathways together in a single connectomic dataset, which is the main goal of this thesis.

The presence of GPi neurons and the connection of MSNs to them has identified a direct pathway through Area X. Although an indirect pathway in Area X has been hypothesized, no synaptic contacts have been identified to confirm its existence (Farries et al. 2005). Additionally, a glutamatergic cell type that may fulfill functions similar to those of the STN has been identified in Area X slices (Budzillo et al. 2017), but its morphology and connectivity have not yet been studied to determine whether it gives rise to an analog of the hyperdirect pathway. Thus, the first goal is to determine whether analogues of the direct, indirect, and hyperdirect pathways exist in Area X.

Electrophysiological measurements have shown that the synaptic area of a synapse is related to its

strength (Holler et al. 2021). Thus, it is hypothesized that the summed synaptic area of a pathway can indicate its functional importance. The second goal is to compare the basal ganglia pathways based on their overall synaptic area and input fraction to Area X's output neurons, the GPi. Since estimating the synaptic area of several thousand neurons requires densely reconstructed EM data, this is the first time that basal ganglia pathways can be compared in this manner.

The third goal is to analyze the connectivity and relationship of three novel GABAergic interneuron types to the basal ganglia pathways. While the connectivity of different interneurons in the mammalian basal ganglia is known, their relative influence on basal ganglia pathway neurons in terms of synaptic area has never been studied.

LMAN, Area X, and DLM are connected via a microscopically closed topographical loop (Luo et al. 2001). Within Area X, this topography contains LMAN-MSN and MSN-GPi synapses. It is unclear how this closed loop extends to synaptic connectivity. Individual LMAN neurons could "focus" their information on a small number of GPi cells via indirect connectivity with MSN cells. This creates a closed topographical loop and allows for feedback loops at the level of individual cells. Alternatively, LMAN neurons could indirectly spread information to all GPi neurons in their vicinity. The fourth goal is to address this question using the current Area X dataset.

In summary, achieving these goals would lead to a comprehensive analysis of the connectivity between different types of neurons in Area X. This analysis would shed light on song learning and basal ganglia pathways in general.

1.5.4 Synaptic and non-synaptic vesicles

Because the locations of individual vesicles are available throughout the dataset, their relationship with synaptic transmission can be determined, and they can be used as a proxy for non-synaptic transmission.

First, the relationship between the number of vesicles, either in total or in close proximity to the synapse, and synaptic area will be examined. This relationship has been demonstrated in the mammalian hippocampus and neocortex (Harris et al. 1989, Murthy et al. 2001, Kasthuri et al. 2015).

Second, it will be tested whether vesicles can be found at greater distances from synapses and in proximity to the cell membrane, and whether there are differences between cell types. Although proximity does not indicate vesicle release at a particular site, the presence of non-synaptic vesicles close to the membrane is necessary for release. In the absence of molecular markers for docked vesicles, the presence of these vesicles serves as a proxy for volume transmission in this dataset. With projections from the VTA and the presence of TANs, Area X contains two cell types that signal via volume transmission in mammals (Abudukeyoumu et al. 2019, Arbuthnott et al. 2007).

If evidence of volume transmission is found in DA and TAN axons, the environment of non-synaptic vesicles in these cell types can be analyzed further. The third goal is to analyze this environment to determine whether the presence of non-synaptic vesicles correlates with specific cell or synapse types, and whether cells with high receptor densities are in closer proximity.

Additionally, volume transmission plays a central role in learning and affects synapse size in the striatum (Abudukeyoumu et al. 2019, Yagishita et al. 2014). Therefore, the fourth goal is to test whether the synaptic area differs in proximity to non-synaptic modulatory vesicles.

1.5.5 Glia cell types and migratory neurons in Area X

Glia cell types are as prevalent as neurons in the brain and perform essential cellular functions. However, their presence in connectomic datasets was not acknowledged until recently, when they became the focus of several studies (Buchanan et al. 2022, Yener et al. 2025, Salmon et al. 2023, Uytiepo et al. 2025). Previous songbird connectomic datasets (Dorkenwald et al. 2017, Kornfeld et al. 2017) or in previous analyses of this dataset (Schubert et al. 2022) did not identify them as cell types.

Thus, the first goal is to determine if the morphology of songbirds' basal ganglia is similar to that described in mammals and to identify the glial cell types present in the current dataset.

Immature neurons have previously been identified in the HVC of songbirds (Shvedov et al. 2024). To allow for a better understanding of structural plasticity in the adult songbird brain, the second goal was to identify and classify migratory neurons.

For the first time, dense reconstructions of not only cells, but also mitochondria, the ER, and the GA are available together in several completely segmented glial and migratory neurons. Therefore, the third goal was to analyze the densities of these organelles to characterize these cell types further. Since higher mitochondrial density has been associated with higher reported firing rates in neurons (Dorkenwald et al. 2017), the organelle densities of glial and migratory cells compared to neurons may also provide insight into their metabolic demand.

The interaction between glial cells and neurons, as well as between glial cells themselves, is the subject of ongoing studies. The fourth goal is to analyze the contact areas of glial cell types with different neuron types and with each other to get an initial estimate of these interactions in EM.

Materials and Methods

2.1 Sample preparation

The sample preparation in this thesis focuses primarily on preparing the analyzed dataset, j0251 (section 2.1.1, but also involves additional experiments with larger samples (section 2.1.2).

2.1.1 j0251 dataset

j0251 sample preparation

The j0251 dataset was prepared by Joergen Kornfeld via serial block-face electron microscopy (SBEM), as previously described (Kornfeld 2017, Schubert et al. 2022). The dataset was collected from an adult male zebra finch (> 120 days post-hatch (dph)). The sample preparation procedure included high-pressure perfusion to open the blood-brain barrier, as previously suggested (Cragg 1980), heavy-metal staining according to the ROTO protocol (Briggman et al. 2011), and cutting with 25 nm thickness with a custom-built in-chamber microtome (Denk et al. 2004). The volume of the dataset is $256 \times 256 \times 384$ µm^3, and the resulting voxel size is $10 \times 10 \times 25$ nm^3 in the x, y, and z directions (Kornfeld 2017, Schubert et al. 2022).

ECS estimation

To understand how much extracellular space (ECS) could be preserved with the aforementioned preparation, first the fraction of voxels in a cube which were not included in the cell segmentation were estimated. Google Research provided the cell segmentation using flood-filling neural networks (FFNs, Januszewski et al. 2018, see section 2.2.1 for more details). To achieve this, 1,000 random offsets were generated within 15 µm of the dataset boundaries to ensure that all offsets lay completely within the data. At each offset, a cube measuring $864 \times 864 \times 864$ voxels ($8.64 \times 8.64 \times 21.6$ µm^3) was loaded. Then, the fraction of voxels not included in the segmentation — i.e., the ones not predicted to belong to a cell — was computed.

Not only ECS but also blood vessels, small neurites, and myelin are not included in the cell segmentation. To obtain an exact estimate of the ECS, 501 coordinates were manually reviewed by Riccardo Morbio. These coordinates were randomly selected from the offset coordinates of the aforementioned estimate for non-segmented voxels.

substance	amount in 1 L	concentration [mM]
NaCl	5.084 g	87
NaH_2PO_4	0.15 g	1.25
KCl	0.186 g	2.5
sucrose	25.675 g	75
glucose	4.504 g	25
$NaHCO_3$	2.1 g	25
$MgCl_2$	7 mL	7
$CaCl_2$	1 mL	1

Table 2.1: Ingredients in 1L of ACSF. $MgCl_2$ and $CaCl_2$ were added after stirring and bubbling with CO_2.

2.1.2 Preparation of 2.5 mm zebra finch samples for ECS experiments

To study the preservation of ECS in larger samples, 2.5-mm-thick samples were fixed via immersion fixation and then stained.

Animal statement

All of the zebra finches used in this section and the following one were wild-type males (> 120 dph) from the animal facility at the Max Planck Institute for Biological Intelligence in Seewiesen. All animal procedures were performed according to the Government of Upper Bavaria's guidelines.

Immersion fixation

Immersion fixation is a fixation procedure in which the extracted brain is placed in a fixative that enters the sample via diffusion. This procedure was performed as previously described (Fernholz 2022, Pallotto et al. 2015, Weiler 2018). The immersion fixations described in the following sections were prepared and planned together with Jonas Hemesath.

First, artificial cerebrospinal fluid (ACSF) was prepared according to table 2.1, adapted from Fernholz 2022 and Peters et al. 2023. All ingredients except for $MgCl_2$ and $CaCl_2$ are added. Then, the ACSF is kept on ice and bubbled with 95 % O_2/ 5%$CO_2$for 15-20 minutes. Then, $MgCl_2$ and $CaCl_2$ are added, and the pH should be 7.5. The osmolality was 344 mOsm. The ACSF is then stored on ice or at 4 °C until needed.

Brain extraction was then performed as previously described (Fernholz 2022, Weiler 2018), with adaptations for zebra finches. Zebra finches were decapitated with surgical scissors, then the brain extracted. The steps from decapitation to fixation are time sensitive because the brain should have minimal contact with air. To accomplish this, the brain was extracted on a closed Petri dish filled with ice and wetted with ACSF. First, the skull was opened by carefully grating scissors on the top side to create an unclosed circle, and then it was opened with tweezers. The dura was carefully removed with fine, sharp tweezers. Finally, the brain was removed and placed briefly in a small beaker filled with ACSF and kept on ice.

Next, the brain is cut into 2.5 mm thick slabs. A custom-made form designed by Jonas Hemesath according to measurements from the zebra finch MRI brain atlas (Poirier et al. 2008) was used for this.

sucrose concentration	5 %	7%	9 %
osmolality [mOsm]	120	205	273

Table 2.2: Osmolality of rinse solutions for different fixatives

The form was designed so that a 2.5-mm slab could be cut to include most of the song system nuclei and be separated from the rest with two razor blades. Before use, the form was rinsed with ice-cold ACSF. The brain was then cut into two hemispheres, each of which was cut into one 2.5-mm slab and the rest of the hemisphere, which was around the same thickness.

The cut slices were incubated overnight in the fixative at 4 °C in a rotating wheel to gently move the samples during fixation. Increasing the osmolality of the fixation buffer aids in ECS preservation (Pallotto et al. 2015). Previously, a mixture of sucrose and CB (Cragg 1980), or for retina samples, high concentrations of sucrose only (Pallotto et al. 2015) were used for this purpose.

All samples were fixed with 2 % glutaraldehyde and 2 % PFA in varying sucrose concentrations. For samples prepared for EM, sucrose concentrations of 5, 7 and 9 % were used (see table 2.2 for measured osmolalities). The rinse solution was measured to determine the osmolality of the different solutions because it does not contain glutaraldehyde and PFA (Pallotto et al. 2015).

After fixation, the samples were rinsed in a sucrose solution with the same concentration as the fixative. Then, they were kept at 4 °C for 48 hours until the staining process began.

Heavy metal staining for EM

Heavy metal staining was performed using a protocol adapted from Hua et al. 2015 and Lu et al. 2023, together with embedding from Kormacheva 2023 according to table 2.3. The first osmium step was performed using the same sucrose concentrations in which the samples were fixed.

To monitor the diffusion of heavy metals in the sample, a MicroCT was used (Ströh et al. 2022, Lu et al. 2023). The MicroCT (CT portable, PXR) had a voxel size of 24.41 µm, was operated at 48.5 kV and 500 µA, and had a magnification factor of 2.03. Before the experiment, the detector was corrected using 500 images, resulting in an offset of -30.85 pixels, a skew of -0.024°, and a horizontal misalignment of 1.527 µm. During the first and second osmium steps, the 7 % sucrose sample was imaged every hour. All samples were imaged after the ferrocyanide and second osmium steps, as well as after the lead step, to ensure complete diffusion. Additionally, all samples were imaged during the lead step. All scans were performed with 200 ms imaging time, no averaging, and 400 images per rotation. Example images illustrate diffusion over time for the 7 % sucrose sample during the first osmium step (see figure 2.1). Although diffusion was not complete after 5.5 hours, the sample appeared uniform during the full six hours and the subsequent ferrocyanide step.

During embedding, 100 % solutions of Hard-Plus Resin 812 (Electron Microscopy Sciences) were degassed with a vacuum pump to remove air bubbles. The samples were then dried in custom-made silicone forms made with the Sylgard 184 elastomer kit (Dow), with a 10:1 mixture of silicone and hardener. After hardening, the samples were removed from the oven, trimmed into a hexagonal shape in the workshop, and smoothed with an ultramicrotome (Leica). Then, a 100-nm section was collected on a plasma-cleaned silicon 2-inch wafer and imaged with a Zeiss Ultra electron microscope at an accelerating voltage of 1.5 kV, a dwell time of 12.8 µs, an aperture of 60 µm, and a pixel size of 5 nm.

Day	staining step
1	2 % OsO_4 (fix buffer), 6 hrs, RT
1	0.15 M CB, 1, 10, 20, 30 min, RT
1	0.15 M CB, ON, 4 °C
2	0.15 M CB, 30 min, RT
2	2.5 % $KFe(CN)_6$, 0.15 M CB, 6 hrs, RT
2	0.15 M CB, 1, 10, 20, 30 min, RT
2	0.15 M CB, ON, 4 °C
3	0.15 M CB, 30 min, RT
3	0.32 M pyrogallol, 6 hrs, RT
3	0.15 M CB, 1, 10, 20, 30 min, RT
3	0.15 M CB, ON, 4 °C
4	0.15 M CB, 30 min, RT
4	2 % OsO_4, 0.15 M CB, 6 hrs, RT
4	0.15 M CB, 1, 10, 20, 30, 30 min, RT
4	lead aspartate, 23 hrs, 50 °C
5	ddH_2O, 1, 10, 20, 30 min, RT
6	ddH_2O, 1 hrs, RT
6	50, 75 % EtOH, 30 min, 4°C
6	100 % x 3, EtOH, 30, 45, 60 min, 4°C (freshly opened bottle)
6	100 % x 3, Acetone, 30 min, RT (freshly opened bottle)
6	80 % Acetone, 20 % Hard-Plus Resin 812, 48hrs, RT
9	60 % Acetone, 40 % Hard-Plus Resin 812, 48hrs, RT
11	40 % Acetone, 60 % Hard-Plus Resin 812, 48hrs, RT
13	20 % Acetone, 80 % Hard-Plus Resin 812, 48hrs, RT (fresh)
15	100 % Hard-Plus Resin 812, 24hrs, RT (fresh, degassed)
16	100 % Hard-Plus Resin 812, 24hrs, RT (fresh, degassed)
17	100 % Hard-Plus Resin 812, 24hrs, RT form (fresh, degassed)
18	70 °C (oven), at least 48 hrs

Table 2.3: Staining and embedding of 2.5 mm samples. Lead aspartate is prepared according to Walton 1979 and the pH adjusted to 5.5 with NaOH.

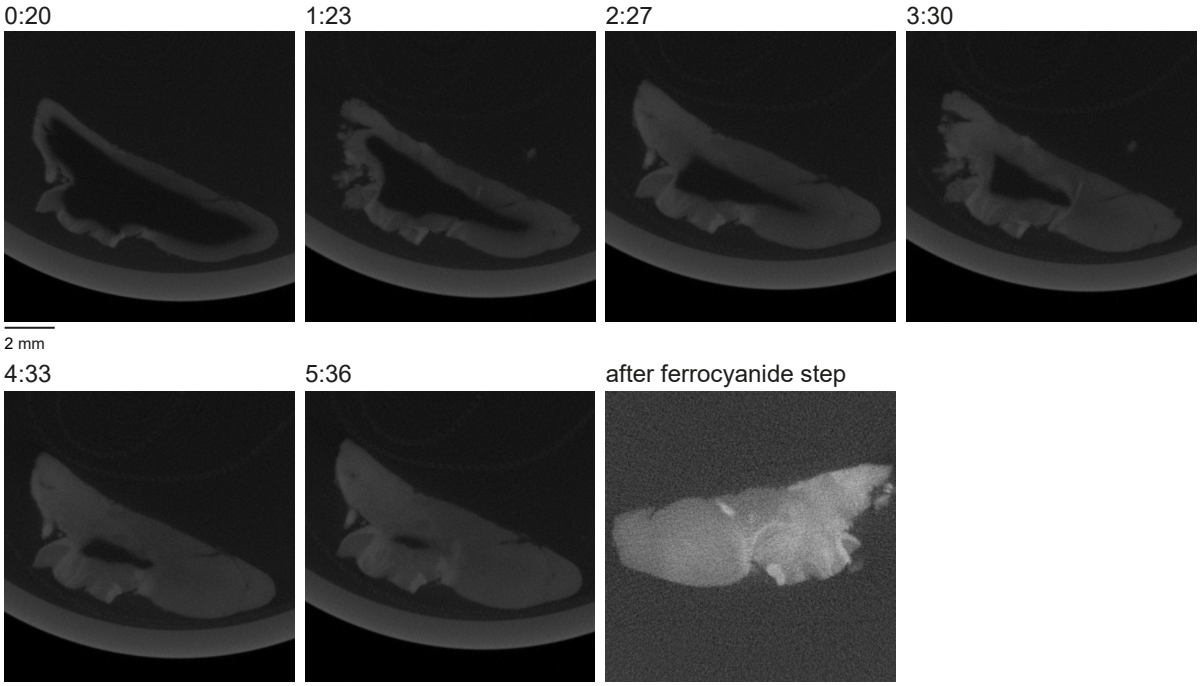

Figure 2.1: MicroCT images of a 7 % sucrose sample during the first osmium step. The exact times after the solution change are given in hours:minutes. The last image was taken after the ferrocyanide step.

	weight [g]
NSA	5.9
ERL	4.1
DER	0.95
DMAE	0.1

Table 2.4: Spurr's resin (Spurr 1969) for 10 mL (weighed).

Day	dehydration and embedding step
1	50, 75, 96 % EtOH, 30 min, 4°C
1	100 % x 2, EtOH, 30 min, 4°C (freshly openend bottle)
1	100 % x 3, Acetone, 30 min (or 30, 45, 60), 4°C (freshly openend bottle)
1	25 % Spurr's, 75% Acetone, ON, RT (fresh)
2	50 % Spurr's, 50% Acetone, 6hrs, RT (fresh)
2	75 % Spurr's, 25% Acetone, ON, RT (same day)
3	100 % Spurr's, 6hrs, RT (fresh, degassed)
3	100 % Spurr's, ON, RT form (same day)
4	70 °C (oven), at least 48 hrs

Table 2.5: Sample embedding for ETS staining.

2.1.3 Light microscopy of 2-3 mm zebra finch samples

To determine whether artifacts around the blood vessels appear during fixation or staining, a light microscopy image was taken immediately after fixation. For this purpose, a sample was fixed using immersion fixation with 2 % glutaraldehyde, 2 % PFA and 7 % sucrose as described above. The fixed tissue was dehydrated and embedded in Spurr's resin (see table 2.4, Spurr 1969) as described in table 2.5, adapted from Kormacheva 2023.

The sample was placed in a silicone mold and trimmed as described above. Then, a 100-nm section was cut with an ultramicrotome, as described above. This time, the section was collected on a glass slide that had been cleaned with ethanol and heated to 65 °C for a few seconds to remove wrinkles.

For contrast, a stain of toluidine blue and basic fuchsin was used, which is commonly used as an electron microscopy overview stain (Epoxy Tissue Stain, Electron Microscopy Services). The stain was applied for 20 seconds before the excess stain was removed with ddH_2O. Then, the sample was covered with a glass cover slip and a drop of Spurr's solution. Imaging was performed using a Leica SP8 confocal microscope.

2.2 Data processing

Computing resources

Data processing and analysis were performed on the Cajal cluster, which is hosted by the Max Planck Computing and Data Facility in Garching.

This cluster has 51 nodes for parallel computing, each with 64 cores (Intel(R) Xeon(R) Platinum

8358 CPU @ 2.60GHz), for a total of 3,264 CPU cores. Each node includes two GPUs (2 x NVIDIA A40 GPUs) and 1 TB of RAM (`https://docs.mpcdf.mpg.de/doc/computing/clusters/systems/Biological_Intelligence.html`). Job allocation and parallel processing across nodes were performed using SLURM (Yoo et al. 2003).

For data processing, which included several steps in the SyConn pipeline (section 2.2.1, Schubert et al. 2022) and vesicle extraction (section 2.2.3), code was executed on up to 46 nodes. With these resources, the SyConn steps took around one month to run and the vesicle extraction took one day.

The data analysis was configured to use one node with multiprocessing, which allows for parallel computing on multiple cores.

Visualization with SyConn Neuroglancer

EM images, cell segmentations, and 3D renderings of cells, mitochondria, synapses, vesicle clouds, endoplasmic reticulum (ER), and the Golgi apparatus (GA) are available via SyConnWeb (`https://syconn.esc.mpcdf.mpg.de`, Schubert et al. 2022), which uses Neuroglancer (`https://github.com/google/neuroglancer`) to display the data. After processing the data to its current state, as described in the following sections, Hashir Ahmad updated the data in SyConnWeb.

To access the data described in this thesis, select the dataset "j0251" and version "j0251_72_seg_20211027_agglo2_syn_20220811_celltypes_20230822". Coordinates can be inserted in the top left ("x", "y", "z") and a cell ID in the top right under "Select". Figures in this thesis will reference either the location of the raw data, the ID of the displayed cell, or both. Tutorials on further functions are available on the website.

2.2.1 Improvements to the SyConn pipeline

SyConn is an API that provides a pipeline for processing volumetric EM data (Dorkenwald et al. 2017, Schubert et al. 2019, Schubert et al. 2022). It uses convolutional neural networks (CNNs) for several steps and works in an object-oriented fashion. Cells are objects ("SuperSegmentationObject") with subcellular structures ("SegmentationObject") assigned to them, such as mitochondria, vesicle clouds, and synapses, along with attributes like their volume. To allow for easier processing, attributes such as the compartment of the synapse and the synapse IDs, are stored in several numpy arrays that are sorted similarly. To visualize cells and their organelles in 3D, a mesh is generated for each cell, which can be seen in SyConnWeb (section 2.2).

In this thesis, the SyConn pipeline was used as previously described (Dorkenwald et al. 2017, Schubert et al. 2022) but with adjustments that will be described in the following sections.

Neurite reconstructions and compartment predictions were used from Schubert et al. 2022. Segmentations were provided by Google Research using FFNs (Januszewski et al. 2018).

The CNNs used for compartment predictions and cell classifications were trained using the elektronn3 framework (`https://github.com/ELEKTRONN/elektronn3`). For compartment predictions, the cell compartments were classified as coarse or fine with three CNNs in total (Schubert et al. 2022, Schubert 2022). The coarse prediction divided the cell into soma, dendrite, or axon compartments. The first fine prediction was used to distinguish terminal and en passant boutons. In this thesis, these axon compartments were not distinguished. The second fine prediction differentiated dendritic compartments into dendritic shaft, spine head, and spine neck.

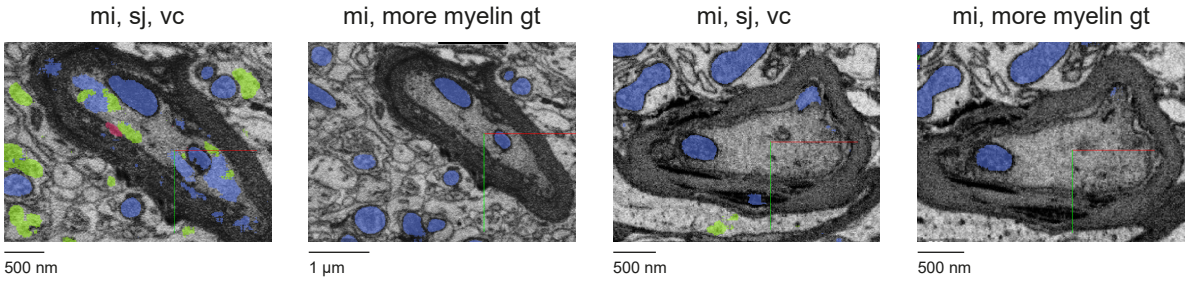

Figure 2.2: Mitochondria detection in the first prediction and addition of ground truth for mitochondria in myelinated axons. Left coordinates: 15265, 14275, 12997, right: 12051, 14156, 310. c.f. For raw data see section 2.2.

Improvements to synapses, mitochondria, and vesicle clouds

Synapses, mitochondria and vesicle clouds are already part of the SyConn pipeline (Dorkenwald et al. 2017). For this thesis, the segmentation of synapses and mitochondria was based on new ground truth, while the segmentation of vesicle clouds was reprocessed using the same ground truth as previously used (Schubert et al. 2022).

The ground truth consisted of 51 cubes, each sized 300 × 300 × 150 voxels, where mitochondria and synaptic junctions were annotated. Additionally, six cubes of the same size that included myelin, were annotated for mitochondria, as the original predictions performed poorly around myelin (see figure 2.2). To ensure that individual mitochondria would not be predicted together, binary erosion was performed for two iterations with a border value of 1 (`https://docs.scipy.org/doc/scipy/reference/generated/scipy.ndimage.binary_erosion.html`). Annotations were done in KNOSSOS (`https://knossos.app/`) by thirteen trained student annotators under my supervision. The annotations were then reviewed by two of the annotators, Delta Schick and Julian Hendricks, and final revisions were done by Joergen Kornfeld and me.

The new segmentations were trained and predicted by collaborators at Google Research under the supervision of Michał Januszewski.

Synapse, mitochondria, and vesicle cloud processing was done with Hashir Ahmad according to the steps described in the SyConn2 pipeline (Schubert et al. 2022). To extract subcellular structures, mitochondria and vesicle clouds were first predicted and split into different connected components. Then, they were overlaid with the cell segmentation to map them to the cells (see figure 2.3). The extraction process for synapses involved more steps.

To ensure that each synapse is a connection between two different cells, the synapse prediction was first overlaid with the contact sites (cs) where the cell membranes of different cells touched. While this removes false positives within a cell, it also removes autapses.

Second, the synaptic objects between two cells were split into individual objects ('syn ssv') by connected component analysis. These objects are represented as 3D meshes with a pancake-like shape, from which their volume and surface area are computed (see figure 2.3, Dorkenwald et al. 2017). Next, they were overlaid with the cell segmentation to map them to the cells.

To estimate the area of the synapse, the surface mesh area was divided by two to determine the contact area between the two cells. Because of its pancake shape, the surface mesh area is mostly determined

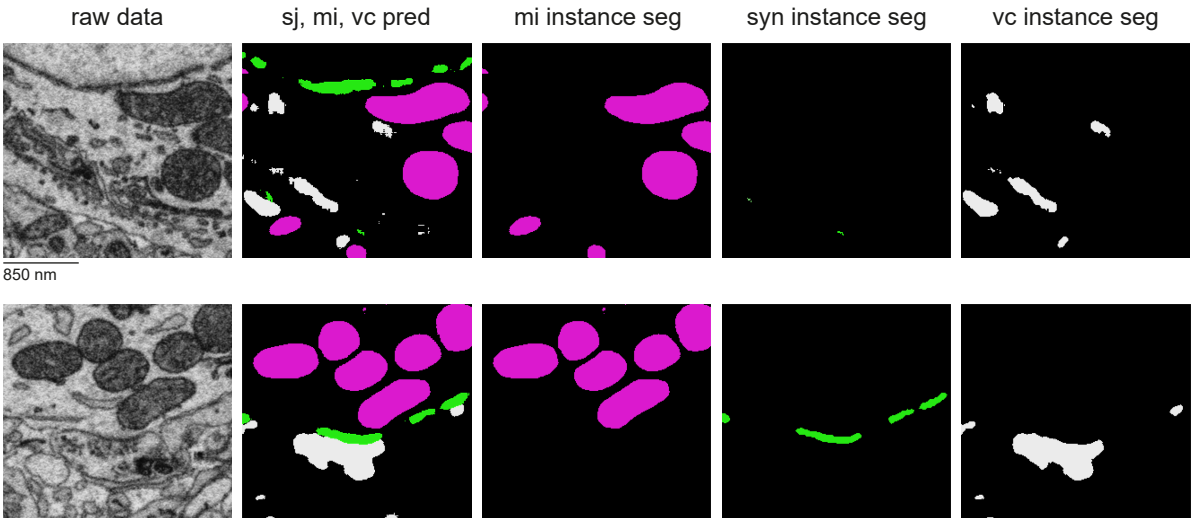

Figure 2.3: Processing of synapses, mitochondria, and vesicle clouds. All scale bars show 850 nm. The prediction from Google Research includes synaptic junctions (sj), mitochondria (mi) and vesicle clouds (vc). These are separated and individual objects found to generate the different instance segmentations. For synapses, the sj predictions are overlaid with contact site (cs) predictions. Top coordinates: 14750, 18722, 7747. Bottom: 14140, 14081, 7748.

by the contact area on each side of the mesh. Therefore, dividing by two yields a good estimate of the contact area between the presynaptic and postsynaptic cells.

In the final step, a random forest classifier (RFC) was used to estimate the accuracy of the synapse prediction (Dorkenwald et al. 2017, Schubert et al. 2022). This probability represents the proportion of synapses with a given label that were correctly predicted. For instance, a synapse probability of 0.8 indicates that 80 % of synapses with that label were correctly predicted. Manual verification of the RFC results is described later (section 2.2.1).

The ground truth for the RFC was updated to include synapses from the current prediction and, unlike previous approaches, contained samples of all cell types to avoid the underrepresentation of less frequent cell types. Specifically, the updated ground truth included 330 synapses, with 30 randomly selected from each cell type. INT1-3 were divided into FS and NGF only. For neuronal cell types in Area X, there were 15 incoming and 15 outgoing synapses. Only axo-dendritic and axo-somatic synapses were selected. Three biological annotators (Riccardo Morbio, Delta Schick, and Laura Werner) and I manually labeled the selected synapses as true or false. The annotators were given information only about the synaptic coordinates to verify with SyConnWeb, where information about cell type, but not mesh area, was available. The final label was assigned by majority vote. In case of a tie, I determined the final label. This resulted in 234 true and 96 false synapses. After cross-validation, the resulting F1 score was 0.88, the non-synaptic score was 0.68, and the accuracy was 0.82 (see result section 3.1.2, table 3.1).

Evaluation of synapse quality

To assess the quality of the synapses and verify the accuracy of the RFC synapse probability scores, a random subset of synapses was manually reviewed by biological annotator Riccardo Morbio.

Specifically, 330 synapses were randomly selected from various probability categories (0-0.2, 0.2-0.4, 0.4-0.6, 0.6-0.8, and 0.8-1) and cell types. Three synapses were selected for each presynaptic cell type within each category. 180 of these synapses were filtered so that only one synaptic partner was an axon (axo-axonic synapses were permitted). The remaining 152 synapses were filtered with a minimum synaptic area of 0.1 µm. Only axo-dendritic and axo-somatic synapses were permitted, as well as synapses between neuronal cell types that met the criteria used for data analysis later on (see section 2.3.1, minimum path length of 50 µm for projecting axons, 200 µm for other neuronal cell types). In the lowest probability bin (0-0.2), there were eight synapses total and all were included.

To avoid potential bias, the annotator was given only the synaptic coordinates and the two cell IDs of the presynaptic and postsynaptic partners that could be evaluated in SyConnWeb, where information about cell type is available (section 2.2), but no information about the assigned synaptic probability or synaptic area. After the initial evaluation by the annotator, I reviewed the few synapses (fewer than five) classified as "unclear" for final classification.

2.2.2 Cell type classification

A supervised machine learning approach operating on point clouds of cell meshes was used for cell classification (Schubert et al. 2022). The cell types were based on literature descriptions (Kornfeld et al. 2020, see table 2.6) and were extended from Schubert et al. 2022 (253 cells, referenced as 'v4/'SyConnv2', see table 2.7).

The ground truth was expanded in two steps: first, an intermediate version, "v5" (324 cells total),

and then the final version, "v6" (393 cells total), which was used for data analysis in this thesis (see table 2.7). The new additions to the ground truth included the projection of axon fragments of different lengths and the inclusion of new interneuron types, glial cell types, and migratory neurons, as described in the following sections.

The prediction model was trained using the entire ground truth, excluding myelin information, with 50,000 points, a 20-µm context, and a redundancy of 20. This means that 20 predictions were made per cell (small fragments were sampled with replacement). The model was subjected to a 10-fold cross-validation separately on three different splits of the data into training and validation sets, as previously described (Schubert et al. 2022).

The cross-validation results were summarized to report the mean and standard deviation of the F1 scores across three runs, as well as the mean of the confusion matrices for different redundancy values (1, 10, 20, and 50).

Projecting axon classification

To avoid potential bias related to fragment length, the ground truth for projecting axon types (HVC, LMAN, and DA) was expanded to include different lengths within each class.

First, Joergen Kornfeld added additional HVC and LMAN axons to v5, especially longer fragments (see table 2.8).

The prediction method works with randomly selected contexts, extracting parts of the point cloud. If a certain axon class only has very short fragments, then the randomly selected context may often contain a cutoff axon end. To prevent the classifier from associating a cutoff axon end with a specific cell class, the number of axons in the ground truth within a specific length category was analyzed.

Since in v4 and v5 LMAN did not have short fragments, while DA only included them, the ground truth needed to be extended (see result section 3.1.2). To accomplish this, ten random samples were selected from all LMAN, HVC, and DA fragments for each cell type and length category and reviewed by Joergen Kornfeld and me. Ultimately, 28 axon fragments were added to fill in missing categories (see table 2.8).

The randomly selected cells did not contain an HVC fragment longer than 1 mm, but, since 11 fragments were larger than 500 µm, no additional HVC axons were selected. Since some morphological differences result in differences in fragment length (e.g. LMAN axons branch frequently, whereas HVC axons do not), omitting longer LMAN axons was not in the best interest. This is why the different cell types did not have the exact same number of axons in each length category for training.

Identification of novel GABAergic interneurons

While the ground truth for most neuronal cell types remained consistent across versions, an examination of the NGF class revealed morphological differences that allow it to be clustered into two distinct cell types (see result section 3.1.2). Manual inspection and previous results showing two UMAP clusters (Schubert et al. 2022), led to further analysis of NGF morphology.

The cells used for this analysis met the following criteria: the presence of an axon, a dendrite, and a soma compartment was verified by the existence of at least one skeleton node that was predicted to be such; the skeleton length of the axon and the dendrite was 200 µm each. Additionally, three FS class cells and five NGF cells were excluded due to mergers (7) or uncharacteristic morphology (1). In a later version, exclusions due to mergers and merger error rates were defined differently (section 2.3.1).

Cell type	Soma	Dendrites	Axon	Synapses	Incoming	Outgoing	References
DA	-	-	few synaptic junctions in boutons	inhibitory/ modulatory	-	MSN	Henselmans et al. 1994 (in reptile)
HVC	-	-	unbranched, regular en-passant boutons	excitatory	-	MSNs, interneurons, GP	Fortune et al. 1995
LMAN	-	-	branched, cohesive terminal domains	excitatory	-	MSNs, interneurons, pallidal	Vates et al. 1995
MSN	small diameter < 10 µm	spiny	-	inhibitory/ modulatory	HVC, LMAN, FS and LTS	GP, MSNs, interneurons	Farries et al. 2002
GPe	large diameter > 10 µm	aspiny	large boutons	inhibitory	HVC, MSN	GP	Farries et al. 2002 Luo et al. 1999
GPi	larger than GPe > 10 µm	aspiny	large boutons, projecting to DLM	inhibitory	HVC, MSN	GP	Farries et al. 2002 Luo et al. 1999
STN	-	-	-	excitatory	pallidal	pallidal neurons	Budzillo et al. 2017
TAN	large diameter > 10 µm	aspiny, sparse	-	inhibitory/ modulatory	-	MSN	Farries et al. 2002 Henselmans et al. 1994
LTS	large diameter > 10 µm	aspiny, sparse	sparse	inhibitory	-	MSNs, interneurons, GP	Farries et al. 2002
INT1	median diameter 12 µm	aspiny	densely branched	inhibitory	-	-	broadly resembling FS Farries et al. 2002
INT2	small diameter 9 µm	spiny	densely branched	inhibitory	-	MSN	broadly resembling FS Farries et al. 2002
INT3	larger diameter 14 µm	aspiny	densely branched, thick with boutons	inhibitory	-	MSN	broadly resembling FS Farries et al. 2002
ASTRO	elongated core regions	branchy processes, touch blood vessels with one process, densely packed cytoplasmic protrusions		-	-	-	Buchanan et al. 2022
MICRO	elongated soma, lipofuscin granules	several long, thin and branchy processes		-	-	-	Buchanan et al. 2022 Xu et al. 2008
OLIGO	smooth, ovoid soma	thin processes (often cut off), connected to myelin, partially wrapping around neuron		-	-	-	Buchanan et al. 2022
MIGR	elongated soma	elongated shape, few thin processes, bipolar morphology		-	-	-	Scott et al. 2012
FRAG	small fragments, often located around blood vessels			-	-	-	
OPC	oblong nucleus, round soma	ramified form with 15–17 highly branched processes, up to 50 µm from soma, filopodia on tips		-	-	-	Buchanan et al. 2022

Table 2.6: Characteristics of different neuronal and glial cell types in Area X, adapted from Kornfeld et al. 2020. See section 2.2.2 for details on INT1–3 classification.

	number of ground truth cells		
cell type	v4/SyConnv2	v5	v6
DA	19	17	26
LMAN	31	48	58
HVC	33	39	53
MSN	32	31	31
STN	35	34	34
TAN	12	12	12
GPe	14	13	13
GPi	17	15	15
LTS	10	9	9
FS/INT1	27	24	24
INT2	-	-	16
INT3	-	-	16
ASTRO	-	12	17
OLIGO	-	12	14
MICRO	-	17	17
MIGR	-	-	14
FRAG	-	24	24
NGF	23	17	-

Table 2.7: Cell types and the number of cells in different versions of the ground truth. The version labeled "v4/SyConnV2" refers to the data used in Schubert et al. 2022. Version "v5" is an intermediate version, and "v6" is the version used for data analysis

axon type	0 - 50 µm	50 - 100 µm	100 - 500 µm	500 - 1000 µm	$>$ 1000 µm pathlength
DA v4	2	5	10	1	1
DA v5	1	5	10	1	0
DA v6	2	5	10	4	5
LMAN v4	0	0	1	3	27
LMAN v5	0	0	0	5	43
LMAN v6	1	3	4	7	43
HVC v4	2	5	16	10	0
HVC v5	0	0	28	11	0
HVC v6	4	4	34	11	0

Table 2.8: Projecting axon fragment length in different versions of the ground truth. The version labeled "v4/SyConnV2" refers to the data used in Schubert et al. 2022. Version "v5" is an intermediate version, and "v6" is the version used for data analysis.

morphological parameter	manually set threshold
axon median radius	0.11 µm
axon mitochondria volume density	0.025 $\mu m^3/\mu m$
soma diameter	11.5 µm
spine density	0.025 1/µm

Table 2.9: Manually set thresholds to separate the NGF class into two interneuron populations based on morphology.

Morphological analysis revealed differences in NGF soma diameter, axonal mitochondrial volume density, axon median radius, and spine density. These parameters could be separated in a principal component analysis (PCA) with one principal component based on these parameters (see result section 3.1.2).

The soma diameter was calculated based on the median label of vertices (mesh surfaces) predicted to be soma. Spines were identified by skeleton nodes labeled "spine neck" or "spine head" by the compartment classifier. One spine was identified as the connected component using the NetworkX connected component function (`https://networkx.org/documentation/stable/reference/algorithms/generated/networkx.algorithms.components.connected_components.html`) after removing the graph nodes labeled as dendrites. To calculate spine density, the number of spines was divided by the skeleton length of the dendrite after removing the spines so that the number of spines would not influence the overall dendritic length. The median radius was calculated from the "diameter" attribute of the skeleton of all skeleton nodes predicted as axons by the compartment classifier. This attribute represents the thickness of the neurite at the node's location. Mitochondria volume density in the axon was calculated by dividing the volume of all mitochondria in the axon compartment by the total skeleton length of the axon compartment.

Two subtypes of NGF were identified using manually set thresholds based on all four parameters (see table 2.9). Cells with a lower soma diameter, axonal mitochondrial volume density, and axon median radius than the threshold, but a higher spine density, were labeled "NGF type 1/INT2". Cells with a higher soma diameter, axonal mitochondrial volume density, and axon median radius, but a lower spine density, were labeled "NGF type 2/INT3". All other cells were classified as "NGF undefined".

When FS cells were analyzed using the same morphological parameters, the results showed that their cluster was morphologically intermediate between the two NGF subtypes (see result section 3.1.2). Since the FS and the two NGF subtypes resemble the FS cell type described in the literature (Farries et al. 2002), they were relabeled as INT1, INT2, and INT3 for a new classification. For the ground truth, all previous FS cells were relabeled as INT1.

For NGF, I manually classified all existing ground truth cells into the two subtypes and checked if this classification overlapped with the thresholds from the analysis. Six of the 17 NGF cells in the v5 ground truth could be placed into each subtype this way; the other five cells were removed. Additionally, ten cells from each NGF type were added to the ground truth according to the thresholds. NGF type 1 cells were labeled INT2 and NGF type 2 cells were labeled INT3.

Glial cell types and migratory neurons

In addition to neuronal cell types, the brain includes various glial cell types. In order to analyze them, they first had to be recognized as distinct cell types.

In an initial version, Joergen Kornfeld and I added examples of astrocytes (ASTRO), microglia (MICRO), and oligodendrocytes (OLIGO) to the ground truth, based on literature descriptions (see table 2.6). For microglia, only resting microglia were identified.

To further characterize these glial cell types, Delta Schick manually inspected several of them as part of his master's thesis, which I supervised. Cells were reviewed when they had a cell-type certainty of at least 0.8 (a parameter provided by the cell-type classifier) and a skeleton length that varied depending on the glial cell type (Schick 2023). Oligodendrocytes, which are often cutoff due to their thin processes, had to have minimum skeleton pathlengths of 100 µm, microglia of 200 µm, and astrocytes of 500-1000 µm. Astrocytes with pathlengths over 1000 µm often included mergers and were therefore discarded.

During this analysis, 14 cells that were initially classified as microglia were found to have more morphological similarities with migratory neurons. These cells were verified to be migratory neurons by Ben Scott, Naomi Shvedov and Simon Castonguay (Scott et al. 2012, Shvedov et al. 2024). In the next ground truth version (v6), these cells were added as "MIGR".

Additionally, JoAnn Buchanan manually inspected and verified several cells classified as microglia to fulfill the criteria of oligodendrocyte progenitor cells (OPCs), such as a round soma and filopodia on the tips of their processes. In contrast to microglia cells, there was an absence of lipofuscin granules (see table 2.6, Buchanan et al. 2022, Xu et al. 2008). For analysis, Delta Schick manually inspected all microglia and labeled them as either "microglia" or "OPC". These labels were then used in the following analysis. An earlier version of the analysis with OPCs was presented as a conference poster with Delta Schick (co-first authorship) and is available online (Schick et al. 2024). Additionally to supervising the analysis, I made all 3D renderings in the poster that are also used in this thesis. Unless otherwise specified in the figure caption, I also created the raw data images.

2.2.3 Organelle segmentation

Not all of the subcellular structures visible in EM were processed with SyConn. To further investigate the relationship between subcellular structures and cell type characteristics, ER, golgi apparatus (GA), and individual vesicles were predicted as additional subcellular structures.

A neural network (U-Net) was used for prediction, and then the organelles were processed to extract individual objects that could be analyzed and mapped to the cells.

Ground truth for organelle segmentation

In order to segment synaptic vesicles individually and include the GA and ER, a new ground truth based on manual segmentation of these organelles had to be generated. Mitochondria, ER, GA, synapses, and individual vesicles were annotated in 14 ground truth cubes measuring 4 µm × 4 µm ×5 µm (400 × 400 × 200 voxels, x, y, z) using KNOSSOS. Twelve biological annotators performed the annotations under my supervision. Delta Schick also oversaw the annotations and provided feedback on the initial reviews while I oversaw the final reviews.

A total of 4,286 hours were spent on the annotation and review process, with a median of 305.5 hours per cube. The time spent varied depending on the content of each cube and the number of reviews, ranging from 39 to 522 hours. Ground truth cubes included various features of the dataset, such as

Number	Start coordinates	GA	Soma	Myelin	Darker cytosol	Cutting artefacts	Blood vessel	Used for validation
1	886, 1728, 15040	no	no	no	no	no	no	no
2	1439, 16976, 15061	yes	yes	yes	no	no	no	no
3	1777, 3033, 5791	yes	yes	no	no	yes	no	no
4	1904, 11933, 5806	no	no	no	no	no	yes	no
5	2265, 18393, 14730	no	no	yes	no	no	no	no
6	3234, 2032, 8941	yes	partial	no	yes	no	no	no
7	4465, 2131, 9	yes	yes	no	no	no	no	no
8	7293, 13339, 2716	no	no	yes	yes	no	no	no
9	13306, 13460, 7748	yes	yes	yes	no	no	no	yes
10	13523, 13667, 774	no	no	yes	no	no	no	no
11	13677, 16740, 1489	yes	yes	yes	no	yes	no	no
12	15984, 1104, 824	no	no	yes	no	yes	no	no
13	16012, 14119, 7831	no	no	no	no	no	yes	yes
14	22468, 18096, 1413	yes	yes	yes	no	no	no	no

Table 2.10: Coordinates and contents of the ground truth cubes used for organelle prediction. All cubes contained mitochondria, ER, synapses and synaptic vesicles. Two cubes were selected for validation: one contained a soma, GA, and myelin, and the other contained a blood vessel. A previous version of the vesicle segmentation was initially used to identify individual vesicles in cubes 7, 10, 11, and 12. Cube 10 served as the validation cube for this segmentation.

myelin, soma, blood vessels, and cells with slightly darker-stained cytosols, as well as cutting artifacts, such as debris in the image (see table 2.10, figure 2.4, appendix figures A2, A3).

All ground truth cubes included mitochondria, ER, synapses, and synaptic vesicles. However, GA was only present in some of them because not all contained soma. Unfortunately, the raw images of vesicle clouds often showed overlap of individual vesicles, making distinction difficult.

The resources used as references for the different organelles in the EM data were SynapseWeb (`https://synapseweb.clm.utexas.edu/`) and OpenOrganelle (Heinrich et al. 2021, Xu et al. 2021, `https://openorganelle.janelia.org/`).

The ground truth annotators were able to separate the GA and ER stacks. Due to the thin, tubular structure of the ER, it was often fragmented, especially in thin axons or dendritic spines. Larger ER stacks were visible in the soma, especially if they were close to the nuclear membrane (see figure 2.4 b).

Single vesicle segmentation

First, only individual vesicles were segmented. A preliminary version of the vesicle annotation of four ground truth cubes (7, 10, 11, 12, see table 2.10) was used to accomplish this. One cube (10, see table 2.10) was excluded from training and only used for validation, while the model was trained on the other three cubes. The final prediction was performed using a model trained on all cubes.

Training and prediction of a 3D U-Net (modified from Ronneberger et al. 2015, `https://github.com/ELEKTRONN/elektronn3/blob/8111e5df4/elektronn3/models/unet.py`) was done by Martin Bucella

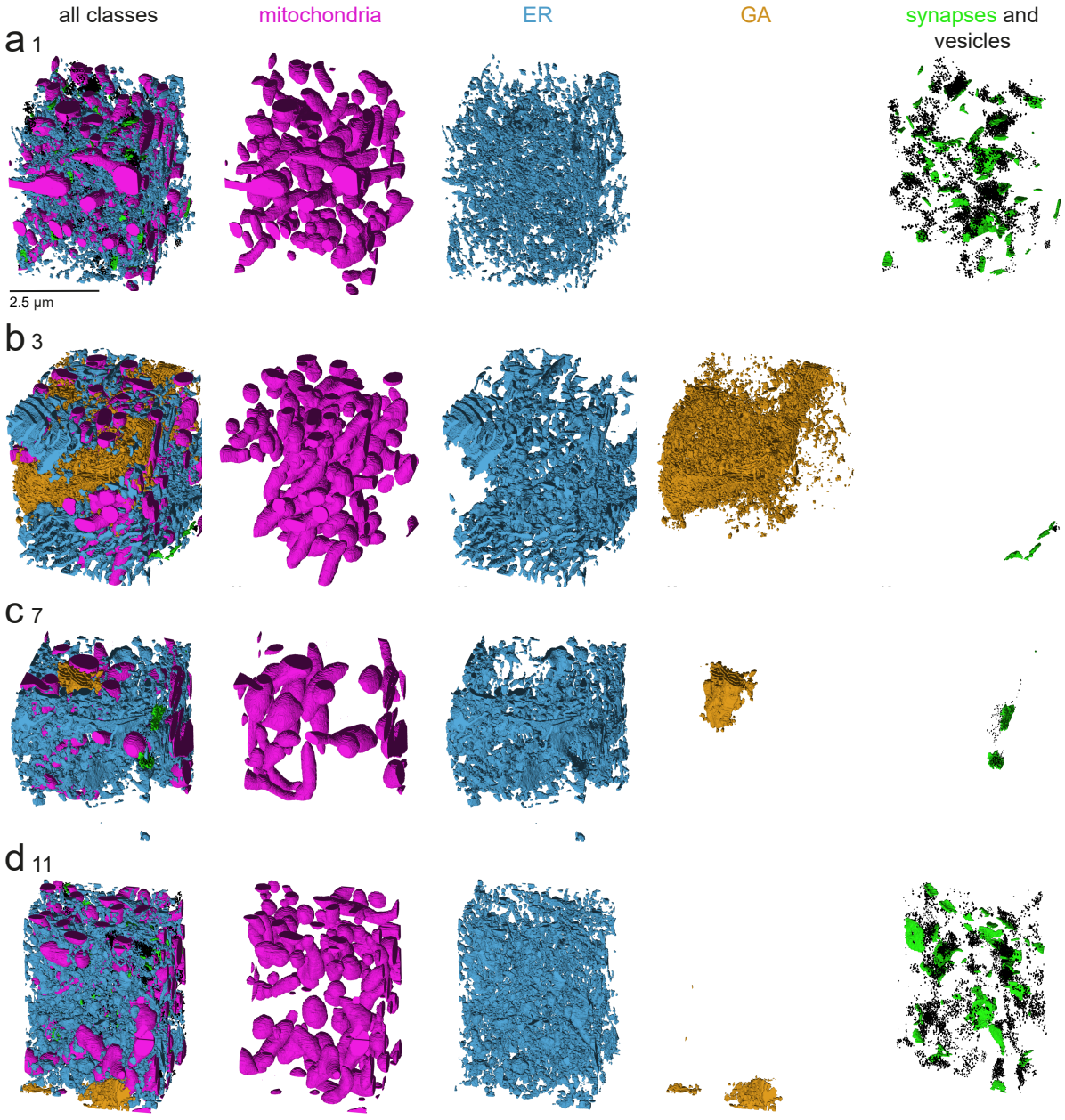

Figure 2.4: Examples of annotated cubes used for ground truth generation. They are all on the same scale. The numbers indicate the cube numbers in table 2.10. For the rest of the cubes see appendix figures A2, A3.

using the electronn3 machine learning toolkit (`https://github.com/ELEKTRONN/elektronn3`). Training was performed using randomly augmented 3D crops of size 88 × 88 × 88 voxels and took 22 hours. The SyConn predict_dense_to_kd function was used for prediction.

Martin Bucella, Joergen Kornfeld, and I wrote extraction code to convert the prediction into individual vesicles and find the central coordinate of each vesicle for analysis. To map the vesicles to cells, we overlaid the center coordinates with the cell segmentation. Using the distance_transform_edt function (`https://docs.scipy.org/doc/scipy/reference/generated/scipy.ndimage.distance_transform_edt.html`, we also calculated the distance to the closest cell membrane.

Multi-class segmentation with ER, GA and single vesicles

In a second step, all new classes—ER, GA, and individual vesicles—were predicted together. This was done using the entire ground truth set of 14 cubes, two of which were used for validation (see table 2.10).

Training and prediction were performed by Martin Bucella using a 3D U-Net, as described above. Different organelle classes were assigned different weights in the training loss function based on their frequency in the data: background = 0.1, ER = 1, GA = 2, vesicles = 2, synapses = 2 and mitochondria = 0.5; organelles that appeared more frequently in the data received a lower class weight. The model was trained twice: once with all five classes and once with only the ER, GA, and vesicles. The run times were between 11.4 and 11.7 hours. The training and validation losses were similar (tr = 0.269, val = 0.642 for three classes, tr = 0.239, val = 0.637 for five classes, 2 ground truth cubes for validation). Therefore, the final model was trained on all five classes. Training for the final model was done on all ground truth cubes.

The processing of individual vesicles was performed as described above. ER and GA were processed by Hashir Ahmad using the SyConn pipeline for subcellular objects such as mitochondria (section 2.2.1), with modifications.

GA was processed with a minimum voxel size of 10 to allow identification of small vesicles when split into individual objects. During the prediction process, the GA stacks were connected rather than kept separate. This resulted in one large GA object containing several stacks after the connected component step was run (see figure 2.5 a, b). To avoid mapping falsely labeled vesicles or close ER fragments to the corresponding cells, only GA objects containing multiple stacks were mapped to cells, requiring a minimum voxel count of 10,000. In the two examples, only the pink object with the GA stacks was mapped to the cells. Since the cell segmentation does not fully cover the GA because dense membrane stacks were misinterpreted as cell membranes in the prediction (see figure 2.5 a, b, cell segmentation), the mapping ratio was set low to 0.1. The mapping ratio describes how much overlap an object needs to have to be mapped to one cell.

The ER stretches across the cell and forms an interconnected network in all compartments (Tsuboi et al. 2021). In the axon, especially, narrow ER tubules of 15-30 nm are common and are almost exclusively connected to each other when examined manually. The same applies to spines, where the ER is thin and connected to the dendrite (Terasaki 2018, Wu et al. 2017). Due to the small diameter of only a few voxels in our dataset, the automatic processing of the ER could not produce an interconnected network. Instead, it identified a large number of small fragments (figure 2.5 a-c). Processing the ER with the SyConn default would mean splitting it up into a large number of connected components that are not biologically relevant, and it would require a lot of computing power to process each of these fragments as individual objects. Thus, to process the ER as one network, the prediction was overlaid with the cell segmentation and the cell ID was assigned to all objects with a minimum voxel size of 100. This resulted

in one ER object per cell, which was then processed with SyConn, as with the other organelles described above.

ER, GA, and single vesicle evaluation

The performance of the prediction was manually evaluated by Riccardo Morbio in three different evaluations.

First, the prediction of single vesicles, which was trained using only single vesicles (four ground truth cubes, see section 2.2.3) was compared to the prediction of vesicles trained with all classes (14 ground truth cubes, see section 2.2.3). The goal was to evaluate the accuracy of the prediction and determine which parameters could be used to identify vesicles touching the membrane. The annotator was given coordinates to evaluate in SyConnWeb, unaware whether it was the single-class or multi-class prediction and which distances were calculated for the vesicles.

To evaluate the overall accuracy of the individual vesicles, 286 single-vesicle coordinates were randomly selected, with 26 coordinates per cell type (11 neuronal cell types, v5 cell type classification, section 2.2.2). All of the cells used were part of the ground truth.

To determine the best filter criteria for identifying vesicles that touch the membrane, different calculated distances to the next membrane were tested: 5, 10, 15, and >15 nm. Vesicles are reported to have a diameter of around 40 nm (Südhof 2004, Takamori et al. 2006). Several values lower than the radius were selected to account for deviations from the vesicle's exact center in the prediction. For each cell type and potential distance threshold from the membrane (5, 10, 15, and >15 nm), five random coordinates were selected. A vesicle was manually classified as membrane-close if it visibly touched the cell membrane in two out of three viewports.

To include a mixture of vesicles close to the synapse and potential non-synaptic vesicles, three coordinates per cell type were selected within 500 nm of the next synapse. Additionally, three coordinates were selected more than 5 µm from the closest synapse. All of these coordinates were within 15 nm of the membrane. The threshold of 5 µm distance to the closest synapse was selected because large axonal boutons can span several millimeters in diameter (see figure 3.37).

Second, the accuracy of the ER, GA, and single-vesicle multi-class prediction was evaluated. All of the cells used were part of the ground truth. Fifteen coordinates were randomly selected per organelle and cell type. ER and single vesicle prediction were evaluated in 16 cell types (the fragment class was excluded), while GA prediction was evaluated in only 13 cell types because projecting axon types were excluded due to their lack of soma in the data. This resulted in a total of 675 coordinates to evaluate.

For single vesicles, only the center coordinates were predicted, so those were selected. For the ER and GA, random coordinates were selected from the mesh vertices. During evaluation in SyConnWeb, the annotator could see the cell ID and cell type, but not which of the three organelles the coordinate was predicted as. Additionally, during the manual review of the coordinates, the compartment in which the predicted coordinate was located was noted ('axon', 'soma', 'dendrite', or 'glial process').

The aforementioned evaluation aims to identify the number of true and false positives, i.e., the number of correctly predicted organelles and the number of organelles incorrectly predicted as such. Another type of error in the prediction is a false negative, meaning an organelle was not predicted. To identify false negatives, a subset of the raw data must be manually screened and compared to the prediction. Since the number of ER and vesicles was very high, this evaluation was only performed on GA stacks.

Thus, the third evaluation aims to understand the false positive and false negative rates in GA by examining connected GA stacks in a random subset of somata. To achieve this, three random cell IDs

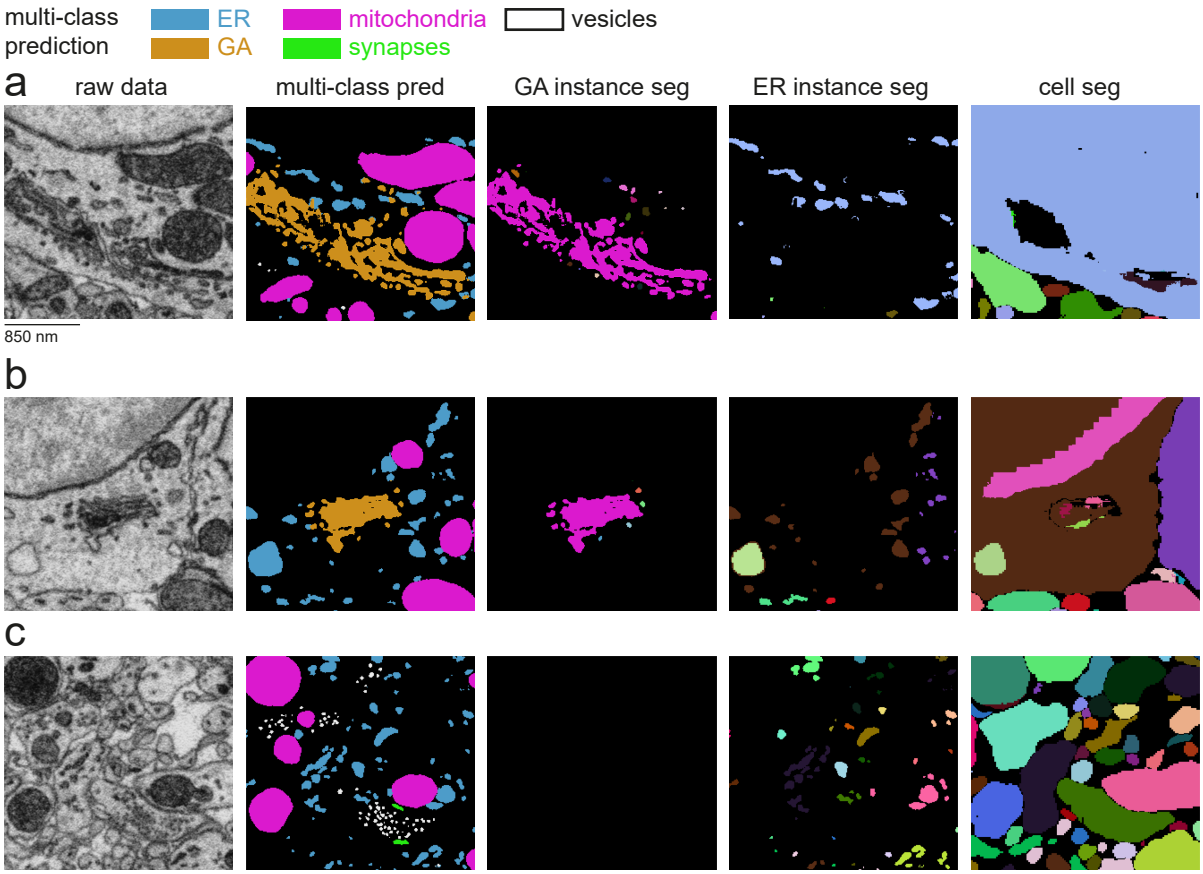

Figure 2.5: Generation of ER and GA objects. The GA was processed analogously to the syn, mi, and vc, and was split into an instance segmentation by connected components. ER segmentation was performed by overlaying the ER prediction with the cell segmentation, rather than splitting it into individual objects. Processing was done by Hashir Ahmad. All scale bars show 850 nm. a Coordinates: 14750, 18722, 7477. b Coordinates: 13441, 13529, 7747. c Coordinates: 14454, 18944, 7750.

from 13 cell types were selected. Neuronal cells were filtered based on the presence of a soma and a 200 µm axon and dendritic path length, while glial cells were manually reviewed for completeness by Delta Schick (see section 2.2.2). The number of unconnected GA stacks was counted in the raw data and the prediction. The number of correctly predicted GAs, true positives, false positives, and missed GAs ("false negatives") was then calculated.

2.3 Data analysis

After processing, dataset j0251 was analyzed with respect to cell morphology, subcellular structures, and synaptic connectivity. The analysis was performed using the updated subcellular structures (sections 2.2.1, 2.2.3) and the new cell classification ('v6', section 2.2.2). In addition to processing, cells, axon fragments, and synapses were filtered for analysis.

The code used for data analysis was written to work with connectomics data processed using SyConn. It is available on GitHub (`https://github.com/StructuralNeurobiologyLab/areaX-connectomic-analysis.git`).

2.3.1 General preparations for analysis

Filtering of cells and axon fragments

To obtain connectivity and morphological data from the same subset of cells and reduce misclassifications, the cells and axon fragments were filtered for completeness.

For neuronal cell types residing in Area X (MSN, STN, GPe, GPi, TAN, LTS, INT1, INT2, and INT3), only cells with at least one skeleton node in each compartment (soma, axon, and dendrite) were used for prediction. The compartment predictions were the same as those used previously (Schubert et al. 2022). Additionally, cells needed a minimum of 200 µm of axon and dendrite path length each. These cells are referred to as "full" or "complete" throughout the thesis.

Additionally, manual reviews were conducted to estimate the number of mergers within the cells. To do so, all "complete" cells of the GPe, GPi, LTS, STN, and TAN cell types were manually reviewed by either Riccardo Morbio or myself. Cells that did not contain all three compartments, or cells fused with a fragment of at least a 50-µm path length or one synapse, were excluded (24 cells in total, see appendix table A14). Due to the high number of MSNs and dense axonal branching in INT1-3, not all cells of these types were reviewed manually, but rather, a subset of randomly selected cell IDs (500 MSNs and 10 INT1-3s) was used to estimate the merger rate. For comparison, the connectivity matrices in the connectivity analysis (section 3.4.2) were computed without excluding any cells from the GPe, GPi, LTS, STN, and TAN (see appendix figure A28). This resulted in 8,576 cells being used for the analyses.

One analysis examined the morphological differences of MSNs in relation to their connectivity to GPe and GPi cells (section 3.4.1). To ensure that the reported results were not due to cutoff dendrites, the analysis was performed again with only MSNs that had their dendrites completely within the dataset. Since dendrites are thicker than axons, the risk of them being cut off in the middle of the dataset due to segmentation errors is very low. To identify cutoff dendrites, we checked if the skeleton of a dendrite was within 7 µm of the dataset boundaries. If so, the MSN cell was excluded from the analysis. The 7 µm threshold was chosen from the dataset boundary, not the segmentation boundary. Due to the shift in alignment, the effective size of the dataset ($256 \times 256 \times 384$ µm^3) is not perfectly cubed and therefore

smaller than the bounding box of the dataset displayed on SyConnWeb or used in the data processing (271 × 271 × 387 µm^3). To bridge the distance between the bounding box and the start of the segmentation, 7 µm was manually selected as the threshold (e.g. visible at this coordinate: 27125, 10327, 5365).

Because the axons projecting into Area X (LMAN, HVC, and DA) were fragmented, different filtering criteria were applied depending on the type of analysis. For morphological and subcellular analyses, fragments with a skeleton path length of at least 200 µm were selected for comparison with complete cells within Area X. For connectivity analyses, a path length of 50 µm was selected.

This threshold for connectivity analysis was chosen as a compromise. Since most axon fragments are less than 100 µm in length, applying a connectivity analysis filter of 200 µm would underestimate the synaptic area of projecting axons compared to full cells (section 3.1.2). However, including all fragments would overestimate their influence on connectivity compared to full cells. This is because, in those cell types, fragments from cells outside the dataset boundaries are also excluded, and the fraction of path length attributed to incomplete cells varies by cell type (see appendix table A1). Additionally, it could include misclassified axon types because classifying cells based on short fragments is more uncertain than classifying them based on longer ones. To demonstrate the impact of these filtering criteria, the connectivity matrix was calculated using two thresholds: 0 µm for projecting axons (with only one skeleton node) and 50 µm for full cells (see appendix figure A28).

As previously described in section 2.2.2, glia cells and migratory neurons were first filtered and then manually reviewed.

Filtering synapses

To ensure an accurate connectivity analysis, synapses were filtered for all analyses. Only larger synapses with a synaptic size of at least 0.1 µm^2 (section 2.2.1) and a synapse probability of at least 0.6 were included (section 2.2.1).

Synapses had to be axo-dendritic or axo-somatic to be included in the analysis. The compartment prediction, mapped to the mesh vertices of the cell and averaged over 10,000 vertices (key = 'axoness_avg10000', Schubert et al. 2022) , was mapped to the synapses using scipy.cKDTree. Synapses that were not between an axon and a dendrite or soma were excluded.

To determine compartment-specific connectivity, the 'axoness_avg10000' key was used to identify whether a synapse was connected to a dendrite or soma. To distinguish between the dendritic shaft, the spine neck, and the spine head, the dendrite-specific compartment prediction was used and mapped from the mesh vertices to the nearest synapse (key = 'spiness', Schubert et al. 2022).

Only synapses between filtered neurons and filtered axon fragments were included in the connectivity analyses.

Mapping of organelles to cellular compartments

In the SyConn pipeline, all subcellular structures are mapped to cells. However, synapses are also mapped to different compartments. For the other subcellular structures, this compartment-specific mapping was performed on all complete cells used in the analysis beforehand using SciPy's ckdtree to map the compartment prediction stored in the skeleton nodes to the objects. The results were saved in NumPy arrays in a cell-type-specific manner, similar to SyConn, for more efficient computing.

The general attributes of the complete cells, such as the skeleton path length and mesh surface area of each compartment, were stored in dictionaries for faster access.

2.3.2 Data visualization

The data were visualized in Python using the Seaborn (`https://seaborn.pydata.org/index.html`) and Matplotlib (`https://matplotlib.org/`) packages. Cell meshes were visualized with Blender versions 3.0.1 and 4.2 (`https://www.blender.org/`).

To visualize cell meshes and subcellular structures, the cells were exported using syconn.proc.meshes.write_mesh2kzip which uses the PlyData library (`https://pypi.org/project/plydata/`) to export the meshes as .ply files. The meshes of the subcellular structures were filtered according to the aforementioned criteria, mapped to the cells — sometimes compartment-specific — and then exported in a similar fashion. Individual vesicles visualized in Blender were rendered as spheres with a 20 nm radius from their center coordinates.

All schematics were created with Adobe Illustrator 2021 by me.

2.3.3 Statistics

Statistical analyses were performed in Python using the scipy.stats library (`https://docs.scipy.org/doc/scipy/reference/stats.html`). Since most of the analyzed parameters were categorical or log-normally distributed, non-parametric tests were generally used.

This means that the correlations were tested using the Spearman rank correlation coefficient. The differences among groups with more than two cell types were tested using the Kruskal-Wallis test, and a Wilcoxon rank sum test was used as a post hoc test. P-values less than 0.005 were considered significant.

The analyses of individual vesicles in relation to synaptic size had an extremely large sample size (partially $> 10^7$ vesicles), which is not suitable for the aforementioned statistical tests without additional analysis. Therefore, bootstrapping was also used here, as explained in more detail later (section 2.3.6).

2.3.4 Neuronal morphological analyses

To quantify the morphology of different cell types and their subcellular structures, several analyses were performed using cell skeletons, meshes, and mapped organelles.

Neuronal morphology parameters

Cell type classification is based on morphological parameters (section 2.2.2, Schubert et al. 2022) and previous analyses have shown that cell types can be separated based on morphology using custom-made parameters (Kornfeld et al. 2020) or latent-space embeddings (Schubert et al. 2022). To quantify the differences between the cell types in our dataset and provide a detailed description of previously undescribed cell types in Area X, INT1-3, the morphology was analyzed with respect to parameters that are commonly used to describe neurons also with other microscopy techniques.

Specifically, the parameters used for this analysis were the following: skeleton path length of the axon and dendrite; mesh surface area of each compartment; median radius of the axon and dendrite; soma diameter; axon myelin fraction; spine density; and cell volume. Analysis of axonal or dendritic length refers to the skeleton length of each compartment based on compartment predictions mapped to cells (Schubert et al. 2022). The mesh surface area is the sum of all triangles that can be mapped to different cell compartments via cell skeleton nodes.

The soma radius was calculated using the median distance to the soma center. The center was the median coordinate of all vertices of the cell that were predicted to be the soma. The median axon radius

was calculated from the diameter of skeleton nodes predicted by the compartment classifier to be axons.

For the axon myelin fraction, the myelin was mapped to the cell skeleton nodes (Dorkenwald et al. 2017). Then, the path length of the myelinated axon was divided by the total axon path length.

Spine density was computed by dividing the number of connected components after removing all nodes from the dendritic skeleton that were not "spine head" or "spine neck" by the dendritic length after removing the spines.

The cell volume is equal to the number of voxels in the cell segmentation (cell.size in SyConn) multiplied by the voxel size (10 nm in x, 10 nm in y, and 25 nm in z).

These parameters were used to create an 11-dimensional feature space to which UMAP (a non-linear dimensionality reduction method) was applied using the umap-learn library (`https://umap-learn.readthedocs.io/en/latest/`). Since the scales of the parameters differ, the values were standardized to z-scores using sklearn.preprocessing.StandardScaler (`https://scikit-learn.org/stable/modules/generated/sklearn.preprocessing.StandardScaler.html`). UMAP was performed once on all cell types and once without the MSNs because the high number of MSNs would otherwise overshadow differences between the other cell types. MSNs that were not part of the MSN cloud (UMAP $1 > 7.5$; 46 cells) were manually reviewed for mergers by Riccardo Morbio.

To differentiate between specific cell types is GPe or GPi (section 3.4.1) or INT1-3 (section 2.2.2, 3.1.2) a PCA was used based on a smaller set of features. PCA was performed using sklearn.decomposition (`https://scikit-learn.org/stable/modules/generated/sklearn.decomposition.PCA.html`) on standardized parameters, as described above. For GPe and GPi differentiation, the parameters were axon mitochondria volume density, axon median radius, axon myelin fraction, and soma diameter. For INT1-3, the parameters were soma diameter, axon mitochondria density, axon median radius, and dendritic spine density.

Analyses of neuronal organelle densities

To analyze organelles, organelle densities in different neuronal compartments were examined. The analyses had three aims: 1) to quantify potential differences in organelle density, 2) to test a correlation with reported firing rates, and 3) to determine if organelle density aids in cell classification.

The organelle density was generally calculated as the volume density, meaning the summed volume of an organelle in a compartment divided by the compartment's path length (e.g., axon or dendrite) or the estimated soma volume. The cell mesh cannot be divided into different compartments because the generated meshes are not watertight. For the axon and dendrite, the path length was used to calculate the density. For the soma, the skeleton follows a random pattern. Thus, the soma diameter is estimated from the mesh vertices, as described above. Then, the soma volume is calculated assuming a spherical shape. Organelles were mapped to specific compartments using their representative coordinates, which could be on either side of the organelle. This means that larger organelles, such as long mitochondria that begin in one compartment, may be entirely mapped to that compartment, even if most of their volume is in another compartment.

Vesicle clouds and vesicles were only processed for neuronal axons in all analyses to focus on neurotransmitter-containing vesicles. For the vesicle density, the number of vesicles was divided by the axon path lengths, as vesicles were not processed as volumes.

GA and ER are organelles that optimize their shape to maximize surface area. For GA, which was only analyzed in the soma, the area density was calculated by dividing the summed GA surface area by the surface area of the soma mesh. Unfortunately, the processed GAs do not have separate stacks. For

cell type	firing rate singing [Hz]	reference
MSN	1.58 ± 1.46	Goldberg et al. 2010
FS	19.1 ± 0.6	Goldberg et al. 2010
LTS	35.8 ± 7.5	Goldberg et al. 2010
TAN	65.1 ± 19.8	Goldberg et al. 2010
GPe	135 ± 42	Goldberg et al. 2010
GPi	258 ± 66	Goldberg et al. 2010
HVC	< 1	Kozhevnikov et al. 2007
LMAN	34.9 ± 8.5	Kao et al. 2008
DA	15 ± 8	Gadagkar et al. 2016
STN	(20)	Budzillo et al. 2017

Table 2.11: The mean firing rates of different cell types during singing, as reported in the literature and adapted from Schick 2021. STN neurons were not recorded during singing in zebra finches, but rather in isolated Area X slices (Budzillo et al. 2017).

the ER, only the summed area per compartment could be calculated because the individual fragments were not processed as separate objects. To separate the ER into different objects, the mesh would need to be divided into several fragments, some of which might not be fully closed. This would make them "not watertight," a requirement for computing volumes with the mesh library, similar to cell meshes. To compare ER density to the densities of other organelles, density was computed twice: once in relation to axon and dendritic path length, and once in relation to the surface area of all compartments.

For synapse densities, the summed synaptic area per compartment was divided by the axon and dendritic pathlength, as well as by the mesh surface area of each compartment (synaptic area density).

To test whether different organelle densities correlate with reported firing rates, the firing rates reported in the literature during singing (see table 2.11, adapted from Schick 2021, a Bachelor's thesis co-supervised by me), were correlated with the median and mean organelle densities.

A firing rate of 1 Hz was used for HVC in the correlation. Since it was unclear which INT1-3 corresponds to the measured FS cell type, it was not included in the analyses. For STN, the firing rate was recorded from synapses with pallidal cells in isolated Area X slices and not during singing in zebra finches (Budzillo et al. 2017). For this reason, the STN value was used as a reference only. Linear regression using StatsModels (`https://www.statsmodels.org/stable/regression.html`) was used to estimate the firing rates for INT1-3 and STN.

For cell type classification, point clouds of mitochondria, vesicles, and synapses are presented to the CNN (Schubert et al. 2022). To determine whether information about cell organelles aids in cell type classification, a UMAP was run on morphological features and organelle densities. Synapse area densities of the axon, dendrite, and soma, vesicle density, and mitochondria volume density of all compartments were added, as well as soma GA area density and ER area density of all three compartments, resulting in a 22-dimensional feature space. The density used for synapses, GA, and ER was calculated in relation to the surface area of the compartments. To have only one parameter for specific information, vesicle cloud volume density and vesicle density were not selected both. The UMAP was run with both options, but there was not much difference, so vesicle density was selected due to its better resolution of vesicles (see appendix figure A20). The UMAP was run once on all neuronal cell types and once without MSNs. In the UMAP without MSNs, one cluster contained LTS together with some cells from STN, INT1, INT2, and

GPe. This cluster (UMAP 1 $<$ 3.9) consisted of 117 cells and contained all 37 LTS cells. The remaining 80 cells were manually inspected for potential misclassifications or incomplete cells.

RFC for selecting parameters to differentiate cell types

To test whether organelle densities are necessary for better cell type separation, an additional RFC was trained using all 22 parameters with the scikit-learn library (`https://scikit-learn.org/stable/modules/generated/sklearn.ensemble.RandomForestClassifier.html`).

To determine which parameters are necessary, the RFC was employed alongside recursive feature elimination with cross-validation (RFECV, `https://scikit-learn.org/stable/modules/generated/sklearn.feature_selection.RFECV.html`). In this process, the RFC is trained recursively, omitting the least important feature as determined by cross-validation. Ultimately, the procedure selects the optimal number of features, which is the feature set with the fewest parameters and no decrease in the cross-validation score.

The RFECV was run once with MSNs and once without to see if the large number of MSN neurons would bias the separation of the other cell types. A UMAP was then run on the resulting features. To observe the effect on different parameters, the mean accuracy was calculated for each parameter individually (see table A32).

2.3.5 Connectivity analysis

The analyses of connectivity focused on the filtered synapses and neurons described in section 2.3.1.

Connectivity between cell types

For the analysis of connectivity between different cell types, especially for the analysis of basal ganglia pathways, connectivity was examined at various levels of detail, ranging from differences between cell types to differences at the level of individual synapses.

All synapses of cells of the same type were grouped together, and the summed area for each combination of pre- and postsynaptic cell types was divided by the total synaptic area in the dataset. The results were summarized in a matrix normalized to 100 % (see figure 3.31 c).

Second, connectivity was analyzed at the level of cell types. The connectivity of a given cell type was analyzed by summing the synaptic areas of its input and output synapses, which were grouped by cell type. Then, fractional input and output were measured as the sum of the synaptic area from a given cell type, divided by the sum of all incoming and outgoing synapses. The values shown in figure 3.31a and b represent the median percentage of the sum of synapse sizes on each compartment. Here, the input and output fractions each add up to 100 %. The results are plotted as either boxplots, where each data point represents one cell of the given cell type (see figures 3.23 b, 3.24 g,h, 3.25 d, 3.27, 3.28, 3.29c), or as a matrix, where the value of each element shows the summed value per cell type (see figure 3.31 a,b). In the matrix, normalization to inputs corresponds to columns adding up to 100 %, while for the matrix normalized to outputs, the rows add up to 100 %.

Third, connectivity is calculated between individual cells. Here, the synaptic area is summed for all entries from one cell to another. Synapses in the same direction from one cell to another are also called multi-synapses, and their number was plotted. Each data point in the plot represents a cell pair, meaning each cell is represented by the number of cells it makes synapses with. Since some cells form more than

ten synapses with the same cell, the number of multi-synapses is grouped into 1, 2–5, 5–10, and > 10 for plotting (see figures 3.23 e, f, 3.24 d,e, 3.25 f, g, appendix figure A25 b, c).

Fourth, the sizes of individual synapses between the two cell types are analyzed. In this analysis, all synapse sizes are pooled together, regardless of the cell to which they belonged. Each data point represents an individual synapse (see figures 3.23 d, 3.24 c, 3.25 e, appendix figure A25 a).

MSN to GPe/i preference

In addition to analyzing MSN-to-GPe/i connectivity in the aforementioned ways, MSN-to-GPe/i connectivity was compared to a shuffled version of the data. This comparison aimed to determine if individual MSNs showed a preference for either GPe or GPi that exceeded the expected ratio of synapses (75 % of the synaptic area from MSNs to GPe/i goes to the GPi, and 73 % of the synapses are to the GPi).

First, the GPi/GPe synaptic area ratio was calculated using the observed data. MSNs that only synapse to GPi would have a value of 1, while those that only synapse to GPe would have a value of 0. MSNs that did not connect to either the GPe or the GPi were excluded from the analysis (2.4 %, 197 cells; see figure 3.23 c).

Then, to test whether the preference exceeded the expected ratio, the data was shuffled. The synapses and their targets remained the same, but their association with MSN presynaptic cells changed. Thus, the number of synapses and the synaptic area for each target remained consistent with the observed data. This shuffling was performed for 100 iterations. After each iteration, the number of cells per bin was calculated, along with the mean and 95 % confidence interval (CI) of the shuffled data. Thirty bins were used for plotting both the shuffled and observed data. In each iteration, the number of MSN cells with a GP ratio of at least 0.9 was also calculated to estimate how many MSN cells were highly selective for GPi (see figure 3.23 g).

Cell-specific recurrent inhibition analyses

If a cell receives input and sends output to the same cell type, it is possible that the interaction is between individual cells, indicating a recurrent connection. This analysis was performed for STN-GPi, STN-GPe, and MSN-TAN connections (see figures 3.26, 3.29 e, f). Cells that did not both receive input and project to the other cell type were excluded.

To test this, the sum of the synaptic areas from the two individual cells was calculated for one cell, as described above (section 2.3.5). To evaluate recurrency, two metrics were tested: overlap in synaptic area and strongest partner reciprocity.

The overlap of synaptic areas was calculated as a ratio for both incoming and outgoing sides. This was done by dividing the sum of the synaptic areas of cells on both sides by the total sum of incoming synapses from that cell type (and likewise for outgoing synapses). To estimate the entire cell type, the median of the overlap to input and output was used.

The strongest partner reciprocity is a binary score that tests whether the cell with the largest summed incoming synaptic area was also the cell with the largest summed outgoing synaptic area. The fraction of cells that had the strongest partner reciprocity was then calculated for the whole cell type.

Compartment-specific connectivity

Functionally, there might be a difference between synapses targeting a spine head and synapses targeting the dendritic shaft or soma of a postsynaptic cell. Therefore, connectivity was also analyzed with respect

to the postsynaptic compartment.

To differentiate between the soma and the dendrite on the postsynaptic side, the "axoness_avg10000" parameter was used to categorize the synapses. If the compartment prediction was a dendrite, the "spiness" parameter was used to differentiate between the spine neck, spine head, and dendritic shaft. The results were then normalized per incoming cell type. For example, the fraction of soma synapses from GPe to MSN was normalized to the total number of synapses from GPe to MSN. In the box plots, each cell is one data point (see figure 3.34a, appendix figure A27).

To highlight the differences in specific example connections, the median percentage of the sum of synaptic sizes was shown for the spine head, spine shaft, and soma. Therefore, these percentages do not add up to 100 % (see figure 3.30 c, d).

LMAN - MSN - GPi analysis

The connectivity from LMAN to Area X to DLM is reported to be topographic and microscopically closed (Luo et al. 2001). However, it is unclear how focused this is at the level of individual cells. To analyze this, the number of different GPi cells that are indirectly innervated by LMAN via MSN was analyzed.

The filter criteria used for synapses, MSN, and GPi cells are described above (section 2.3.1). Since there is no information indicating which LMAN cell or axon fragment enters the dataset, the analysis focused on large LMAN axons, which are likely to originate from different LMAN cells. This means the axons must enter the dataset myelinated and branch within it. To fulfill these criteria, LMAN axons with a skeleton path length of at least 5 mm were manually selected and excluded if a myelinated branch entered the dataset again. These criteria were fulfilled by 46 axons. Of the 8,093 MSNs, 5,135 received input from at least one of the 46 LMAN axons and project to the GPi. These MSNs were included in the analysis.

To understand how focused the loop is, the cell IDs of the MSNs connected to each LMAN axon were saved, as well as the number of synapses and summed synaptic area per MSN cell. This process was repeated for incoming synapses from LMAN to MSN per MSN cell, outgoing synapses to GPi per MSN cell, and incoming synapses from MSN to GPi cell. The median number of cells innervated by one LMAN axon, one MSN cell, and one GPi cell could then be calculated (see figure 3.32). Additionally, the number of GPi cells that each LMAN cell indirectly innervates (and vice versa) was computed (see figure 3.33 a,b).

To determine whether most MSNs innervated by one LMAN go to the same GPi, the fraction of MSNs that go to the same GPi was calculated and the highest number plotted per LMAN cell. The same analysis was performed for each GPi cell (see figure 3.33 c, d). To test whether one GPi cell is indirectly targeted by most MSN cells, the fraction of synapses that go to the five most indirectly innervated GPi cells per LMAN axon was calculated for each LMAN axon (see figure 3.33 e).

Autapses

Autapses were not registered as synapses in the SyConn framework (section 2.2.1). Therefore, the identification of autapses was done manually by Riccardo Morbio and me. To determine the fraction of each cell type with at least one autapse within 10 µm of the soma, we examined all cells from the GPe, GPi, STN, LTS, TAN, INT1, INT2, and INT3 datasets with complete somata. Additionally, 50 randomly selected MSNs were reviewed. Riccardo Morbio also manually reviewed wrinkled nuclei and nuclear infoldings in those cells.

GPi cells with and without autapses were then compared to each other using different morphological parameters, including axon and dendrite synaptic area density, axon myelin fraction, soma and dendrite surface area, axon and dendrite mitochondria volume density, and vesicle density. Additionally, the incoming and outgoing synaptic areas per cell type were analyzed independently (see figure 3.35, appendix figure A29).

2.3.6 Vesicle analysis

To analyze individual vesicles, all vesicles in the axons of complete cells or cell types from projecting axons were analyzed (filtered as described in section 2.3.1, minimum axon path length 200 µm). Synapses included in the analysis followed the aforementioned filtering criteria (section 2.3.1).

To analyze potential release candidates, vesicles within 10 nm of the closest membrane were called "membrane-close" vesicles. However, as only 50 - 60 % of synapses within this distance actually touch the membrane, as determined by manual evaluation (section 2.2.3), this is not an indicator of actual release, but rather an estimate of proximity to the membrane.

Vesicle number and synapse size

To analyze the relationship between the number of vesicles and synapse size, the number of vesicles within a given distance from the closest outgoing synapse of the same cell was counted and correlated with the synaptic area (see figure 3.36, appendix figure A31). For the coordinate of the synapse, the representative coordinate saved in SyConn was used, which is not necessarily the center. To avoid cutting off vesicles on the other side of a large synapse, the analysis was performed with different distance thresholds from the synapse: 0.5, 1, and 2 µm. The analysis was repeated using only "membrane-close" vesicles.

Membrane-close, non-synaptic vesicles

To test for hints of volume transmission in the data, the density of membrane-close synaptic and non-synaptic vesicles was analyzed across different cell types.

Vesicles within a distance of 500 nm from the synapse were counted as "synaptic" while those with a distance of 3 µm were counted as "non-synaptic". The 3 µm distance was selected because some cell types, such as GPi, GPe, and INT3, have large axonal boutons filled with vesicles that span 3 µm in diameter (see figure 3.36, 3.37). However, the median distance between synapses in INT3, the cell type with the highest synaptic density, is 2.73 µm (see appendix table A40). Therefore, a much greater distance from the synapse could result in the omission of non-synaptic vesicles in cell types with dense synapses. However, to ensure that the effects are not strictly related to this threshold, the analysis was also run with distances of 1, 2, and 4 µm (see appendix figure A32).

The vesicle density in relation to the axon path length was calculated for both synaptic and non-synaptic vesicles. Additionally, the fraction of non-synaptic, membrane-close vesicles of all membrane-close vesicles in each cell was calculated.

Membrane-close, non-synaptic vesicles in proximity to different cell types and synapses

Since the TAN and DA cell types had the highest fraction of close-membrane, non-synaptic vesicles and a much higher non-synaptic density than synaptic vesicle density, it was assumed that this was due to the volume transmission reported in these cell types (Abudukeyoumu et al. 2019, Arbuthnott et al. 2007).

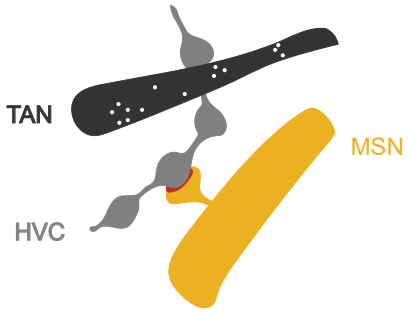

Figure 2.6: Schematic of an HVC-MSN synapse in proximity to a TAN axon filled with vesicles. The synapse is shown in red.

To analyze differences in the surroundings of membrane-close, non-synaptic TAN and DA vesicles, both cell surfaces and synapses within a given distance were analyzed. Vesicles were counted as non-synaptic if they were at least 3 µm away from the closest synapse, as in the aforementioned analysis.

To determine whether cell types occur differently in spatial proximity to close-membrane TAN and DA synapses, the mesh surface area within 2 µm of each close-membrane non-synaptic vesicle was analyzed. This threshold was selected because DA release in the mammalian striatum using nanosensors revealed hotspots with a median size of 2 µm (Beyene et al. 2019). For this analysis, the vertex coordinates of each cell with a close-membrane non-synaptic vesicle within a 2 µm radius were saved, and the surface area between these coordinates was computed for each cell. Then, the surface area was summed for all cells of one cell type. The cell type from which the vesicles originated was excluded from the analysis. For example, TAN cells were not analyzed for TAN vesicles.

Since some cells have a higher total surface area in the dataset, the summed surface area close to the vesicles was divided by the total surface area of this cell type for normalization (see figure 3.38).

To analyze whether specific synapses occur more frequently in close proximity to TAN and DA close-membrane non-synaptic vesicles, a similar analysis was performed on synapses of various cell types. In this analysis, all synapses (filtered and between filtered cells) within a 2 µm distance of a close-membrane non-synaptic vesicle were examined. The surface area was summed for synapses of the same pre- and postsynaptic cell types, and the sum was plotted as a matrix similar to the connectivity matrices. Additionally, the matrix was normalized by the total synaptic area of these synapses in the complete dataset (see figure 3.39).

Both analyses were also performed at distances of 1 and 5 µm from the vesicles (see appendix figures A33, A34).

Analysis of synapse sizes in proximity to modulatory vesicles

To determine whether TAN and DA vesicles affect synapse size, the number of vesicles from TAN and DA axons in proximity to small and large synapses was analyzed (see schematic in figure 2.6). Only non-synaptic vesicles located at least 3 µm away from the closest synapse were analyzed, regardless of their distance from the membrane.

Small and large synapses were defined as the lowest and highest quantiles of synapse size between

two cell types. This means that the number of small and large synapses analyzed is the same for each combination of presynaptic and postsynaptic cell types. Therefore, differences in vesicle numbers do not arise due to differences in synapse numbers when comparing "small" and "large" synapses. Since all of the analyzed synaptic size distributions follow a log-normal distribution (see figures 3.23, 3.24, 3.25) and not a bimodal one, there is no visible threshold that clearly separates small and large synapses. Consequently, the size thresholds for small and large synapses vary between connections (see appendix table A44).

The distance of the vesicles from the "small" and "large" synapses was calculated separately. For all the vesicles that had a synapse within a 5 µm distance, the distance to the closest synapse was calculated. To test for differences in vesicle number surrounding small and large synapses, the distribution from 0 to 5 µm was plotted as a histogram.

First, the Wilcoxon-ranksum test was used for a statistical analysis to determine a p-value. Then, the two-sample Kolmogorov-Smirnov (KS) test was used to determine the effect size and p-values. The Wilcoxon rank-sum test focuses on differences in medians, e.g. shifts in entire distributions, while the KS test is more sensitive to differences in shape.

The number of vesicles surrounding the synapse within 5 µm varies depending on the number of synapses between two cell types in the dataset (see appendix table A44), between 2444 (TAN, GPi - STN) and over 40 Million (DA, HVC - MSN). The shape of the distribution is mainly determined by the number of synapses. Therefore, the distributions for "small" and "large" synapses of the same pre- and postsynaptic cell types have a similar shape. This was verified by selecting different numbers of synapses from a connection with a high number of synapses: HVC - MSN (see appendix figure A35). Consequently, if there is a difference between small and large synapses, the distributions would shift the curve rather than modify its shape. Thus, the Wilcoxon rank-sum test is a better indicator of potential statistical significance. This is also why KS effect sizes (KS d) are generally not expected to be very large.

Since the p-values from both the Wilcoxon rank sums and the KS tests depend on sample size, the p-values were generally low when these tests were performed on full distributions, regardless of visual differences between distributions, e.g. for HVC-MSN synapses in proximity to TAN vesicles ($p < 0.001$, KS $d = 0.01$, see figure 2.7 a, appendix table A44).

To better estimate the significance of the different effects, bootstrapping was used. There, different random subsets were drawn from each distribution for 1000 iterations and then the Wilcoxon-ranksum test was performed for each iteration. This produced a distribution of p-values.

To determine an appropriate bootstrapping sample size that would represent the distribution while yielding more reliable p-values, a range of bootstrapping sample sizes were tested in three different example connections with differences in synapse number and effect size with TAN vesicles. The HVC-MSN connection has a high sample size and low effect size (>400,000 vesicles for each synapse type; KS $d = 0.01$, see figure 2.7 a). The MSN-GPi connection has a slightly lower sample size (> 100,000 vesicles; KS $d = 0.02$, see appendix figure A4 a, b). Both connections have highly overlapping distributions. The GPi-STN connection has a smaller sample size, a slightly larger effect size, and distributions that are not fully overlapping (> 20,000 vesicles, KS $d = 0.0$, see figure 2.7 c, d). There are visible differences in the distribution of p-values between these different connections with 100, 1000, or 10,000 samples for each draw. While HVC-MSN and MSN-GPi follow a more uniform distribution with 100 samples, GPi-STN's p-values lean toward lower values. For 10,000 samples, all three distributions are left-skewed.

To quantify these differences, the fraction of significant ($p < 0.05$) p-values, the median p-value, and the p-value of the one-sample KS test were calculated for each sample size. The one-sample KS test was used to compare the p-value distribution to a uniform distribution. For the GPi-STN sample, the fraction

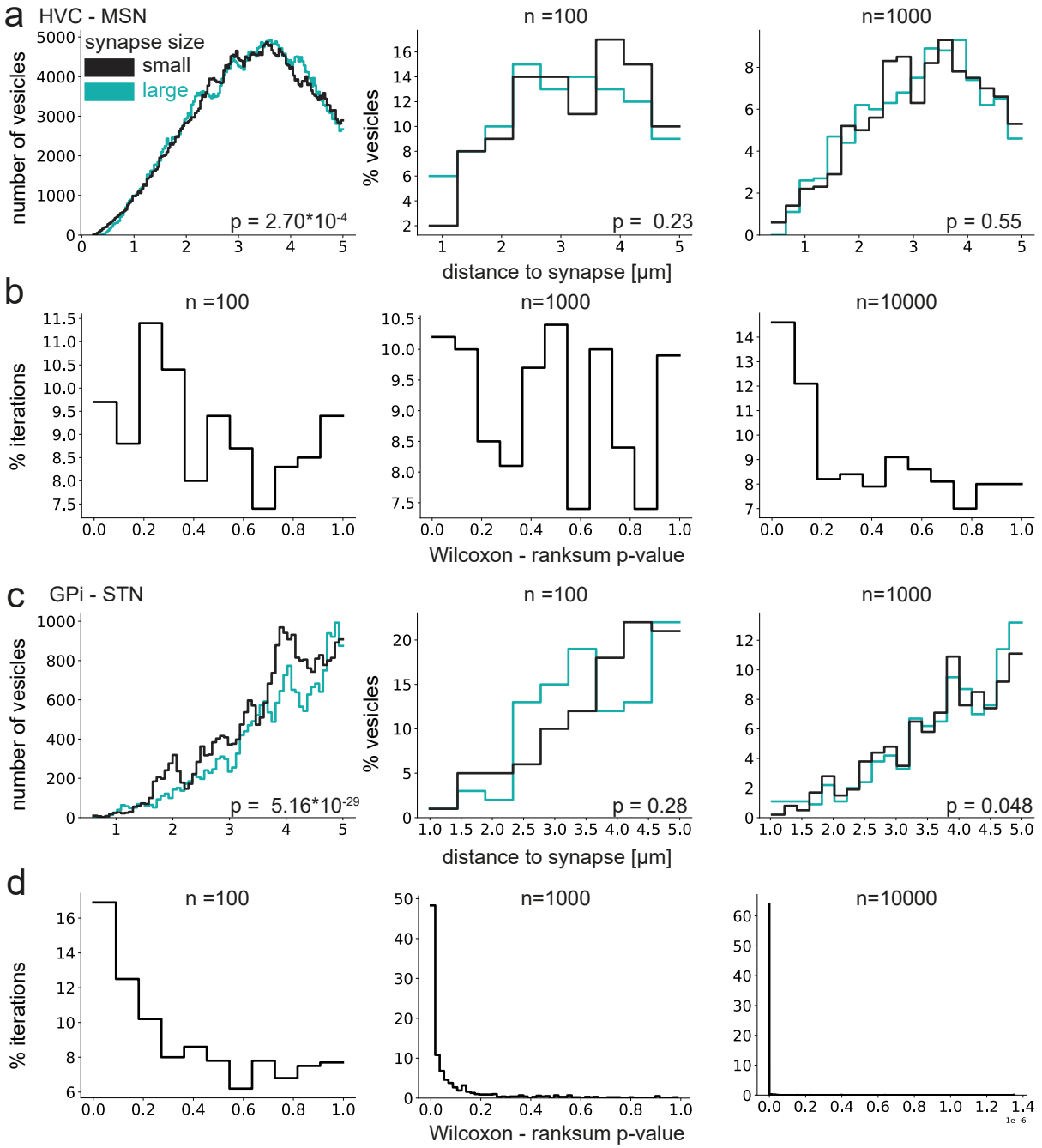

Figure 2.7: Non-synaptic TAN vesicles in proximity to HVC - MSN and GPi - STN synapses. TAN vesicles were considered non-synaptic if they were at least 3 µm away from the distance of the vesicles for the lowest and highest quantiles of synapse sizes ('small' and 'large', respectively). See appendix table A44 for more detail on vesicle numbers and synapse sizes. a Distance of vesicles for all synapses (left) of HVC-MSN, then a random sample of 100 or 1,000 vesicles was used for bootstrapping. b P-values of the Wilcoxon rank sum test across 1,000 iterations of bootstrapping with different sample sizes (n) for each iteration. c,d Same as a,b but for GPi-STN synapses.

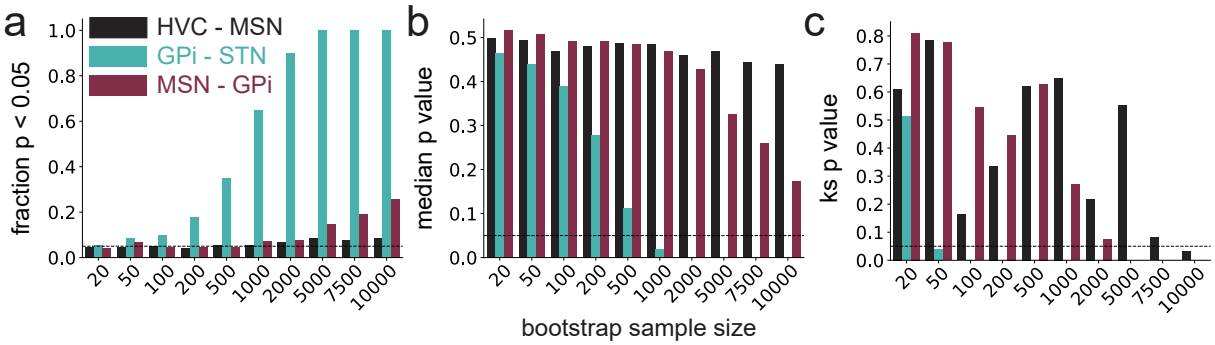

Figure 2.8: Statistical parameters depending on the sample size per bootstrapping iteration for different connections (HVC-MSN, GPi-STN, and MSN-GPi). All results were computed with 1,000 bootstrapping iterations. a Fraction of p-values from a Wilcoxon rank sum test that are smaller than 0.05 with different sample sizes. b Median p-value from the Wilcoxon rank sum test with different sample sizes. c P-values from the Kolmogorov–Smirnov test to determine whether the distribution of p-values resembles a uniform distribution depending on different sample sizes. The dotted black line indicates 0.05.

of p-values less than 0.05 increases the fastest, while the median p-value and the KS p-value decrease the fastest (see figure 2.8).With 1,000 samples, over 60 % of p-values and the median are below 0.05. For HVC-MSN, on the other hand, the fraction of $p < 0.05$ and the median p-value remain constant; the KS p-value varies and begins to decrease at 7,500 samples. For MSN-GPi, $p < 0.05$ increases at 5,000 samples; the median p-value decreases starting at 1,000, reaching a value close to 0.2 at 10,000 samples. The KS p-value varies, decreasing starting at 1,000 and becoming significant with 5,000 samples.

Based on these results, a sample size of 1,000 per draw was selected as a compromise: large enough to reflect the distribution, yet with little bias toward significant p-values based on sample size. Since the number of vesicles varies greatly, connections with high synapse numbers, which result in high sample sizes, were also tested with a larger sample size.

Connections with more than 10^5 vesicles were additionally tested using a bootstrapping sample size of 2,000, $> 5^5$ vesicles with 5,000 and $> 10^6$ vesicles with 10,000, given a significant p-value in the original distributions.

2.3.7 Analysis of glia and migratory neurons

After identifying different glial cell types and migratory neurons based on their morphology (section 2.2.2), their organelle densities and their contact areas with neurons were analyzed. The cells used were manually selected as previously described. Note that oligodendrocytes have fine processes that are often cut off during segmentation, and myelin was not segmented as part of the oligodendrocyte.

Organelle densities

To determine whether differences in metabolic activity are reflected in organelle density, the densities of mitochondria, ER, and GA were compared.

Organelle density was calculated by summing the volumes of all organelles within a cell and dividing

that sum by the cell's total volume. For reference, the same analysis was performed using MSNs and GPi as the cell types with the lowest and highest reported mean firing rates, respectively, during singing (see table 2.11, figure 3.42).

A previous version of the mitochondrial analysis, without manually reviewed GPis for mergers, was performed by Delta Schick in his masters thesis (OPCs, MIGR part of microglia, supervised by me, Schick 2023) and presented in a shared poster at FENS 2024 (Schick et al. 2024).

Glia contact site analysis

To better understand potential glia-glia and glia-neuron interactions, the contact sites between glial and neuronal cells, as well as between different glial cell types, were analyzed.

This analysis was performed by Delta Schick. It is the same version presented as a shared poster (Schick et al. 2024), and an update compared to his Master's thesis (supervised by me, Schick 2023). The neurons for this analysis were filtered using the aforementioned criteria (section 2.3.1) but, rather than being systematically reviewed, 77 mergers were manually identified and excluded. Projecting axon cell types were not included in the analysis.

Contact sites (cs) are areas of contact between cell membranes of different cells. They are generated as part of the SyConn pipeline (Dorkenwald et al. 2017, Schubert et al. 2022). Cs are processed as individual objects, resulting in a pancake-shaped 3D mesh similar to synapse objects. To estimate the contact area, divide the surface mesh of each object by two, as in the synapse size estimation (section 2.2.1).

For the analysis, the sum of the contact areas was calculated for all contacts with a specific cell type and one glial cell. To determine if there were preferences for a specific cell type, the contact sites were normalized by the mesh surface area of the given cell type (see appendix table A49). This is referred to as the contact site ratio, which can be described by the following formula for astrocytes and MSNs:

$$ratio = \frac{\sum A_{cs}}{\sum A_{MSN}}$$

A_{cs} is the area of contact between astrocytes and MSNs, and A_{MSN} is the surface area of the MSN mesh (see figure 3.43 b).

Results

This thesis presents advancements in processing the EM dataset j0251 (section 3.1). After processing, the analyses aim to provide a comprehensive understanding of cell types and their connectivity in Area X, including analyses of morphology and subcellular structures (section 3.3), connectivity (section 3.4) with respect to known basal ganglia pathways, analysis of non-synaptic vesicles and their surroundings in neuromodulatory cell types (section 3.5) and glial cells (section 3.6).

3.1 Data processing in connectomics

The data processing in this thesis aims to improve the steps of the SyConn pipeline (Dorkenwald et al. 2017, Schubert et al. 2022) to enable the biological analysis of the Area X dataset j0251 from the adult zebra finch. The updates to the data processing build on the work in Schubert et al. 2022 and include an updated and extended organelle and cell type classification.

3.1.1 J0251 dataset

The data set j0251 was acquired by Joergen Kornfeld (Kornfeld 2017) with serial block-face electron microscopy (SBEM). The dataset size is $256 \times 256 \times 384$ µm^3, and the voxel size is $10 \times 10 \times 25$ nm^3. The data set was taken from an adult male zebra finch that was perfused with high-pressure perfusion to preserve the extracellular space (ECS, Cragg 1980) and then stained with a heavy metal stain (see figure 3.1, methods section 2.1.1).

Before detailing the adaptations to the processing pipeline, this section focuses on the raw data itself. It shows which subcellular structures are visible at this resolution and which artifacts occurred.

ECS preservation not only counteracts swelling related to fixation (Cragg 1980, Pallotto et al. 2015), but also aids automated segmentation approaches (Pallotto et al. 2015). Thus, ECS was preserved in this dataset and can be seen between neuropil (see figure 3.2 a,b marked by black asterisks).

Heavy metals stain not only cell membranes but also organelles with lipid bilayer membranes, such as mitochondria (pink asterisks, see figure 3.2 a, c), endoplasmic reticulum (ER, blue arrows, see figure 3.2 a, c), Golgi apparatus (GA, orange arrows, see figure 3.2 c), the nuclear membrane (black arrow, see figure 3.2 c), and (synaptic) vesicles (white arrow, see figure 3.2 a). Chemical fixation also allows staining of synapses and the postsynaptic density (dark shadow, see figure 3.2 a). The synaptic cleft is indicated by a black arrow on the postsynaptic site and a white arrow on the presynaptic site (see figure 3.2 a). The myelin sheets are also visible in the data set (see figure 3.2 d, white arrows).

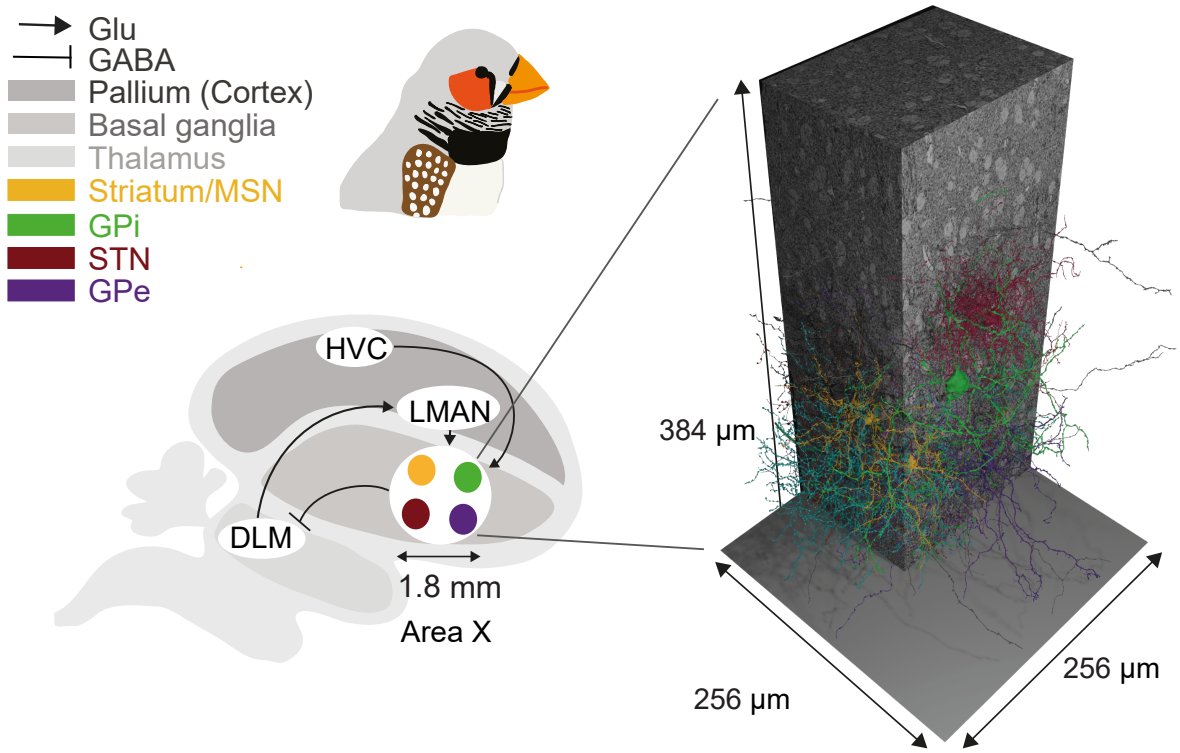

Figure 3.1: Overview of dataset j0251, which was acquired from zebra finch Area X by Joergen Kornfeld. The dataset size is 256 × 256 × 384 µm^3 (x, y, z). Cell renderings of examples from MSN, GPe, GPi, STN, INT1, INT, and INT3 cells are shown in their respective locations.

Although section loss is uncommon with SBEM acquisition, other artifacts can occur during tissue preparation and acquisition. For example, parts of the previous section (section debris) can overlap structures of the next section during imaging. While these artifacts can be found in the data (see figure 3.2 e), most structures can still be traced. Another artifact that occurs during acquisition is related to a change in angle and appears as an alignment artifact. This artifact was manually fixed by Joergen Kornfeld. It is barely visible in the XY plane but appears as a blur in the Z-axis (stitched images, see figure 3.2 f).

Another artifact visible in the data appears around blood vessels, where several white spaces indicate potentially damaged or washed-out areas (black asterisks, see figure 3.2 g, h). This artifact stems from the sample preparation process, likely due to the pressure applied during perfusion to open the blood-brain barrier (BBB) and maintain the ECS (Cragg 1980). The ECS can also be preserved via high osmolality in immersion fixation (Pallotto et al. 2015, samples $\leq$ 1 mm thickness).

When attempting this in larger samples (2.5 mm thickness) in zebra finches, the extent of the ECS in the middle of the sample could be controlled by different sucrose concentrations (see appendix figure A5 a-c). There were also artifacts around the blood vessels that looked as if cells had been washed out or broken away (see appendix figure A5 d-f). The severity correlated with the ECS content preserved. These artifacts appeared before heavy-metal staining, as confirmed by light microscopy imaging of the fixed tissue (see appendix figure A6). Since the fixation procedures were different in these cases, the similarity of the artifacts shows that they are likely due to the fixation process. The cells around the blood vessels are generally highly susceptible to pressure or osmolality differences. While the effect of these artifacts on the data is unknown, the following analysis results show that connectivity and cell morphology are not disrupted on a large scale.

ECS, myelin sheets, blood vessels, and small neurites are not included in the cell segmentation. To estimate the fraction of unsegmented data, 1000 data chunks with randomly generated offsets were computed (see methods 2.1.1). The mean fraction of unsegmented cells was 25.4 $\pm$ 5.0 % (see figure 3.3 a-c).

To obtain more accurate estimates of the ECS, myelin, and blood vessel fractions, 501 coordinates were manually reviewed (methods section 2.1.1). 9.6 % of the coordinates were ECS, 1.6 % blood vessels, 3.2 % myelin and 5.2 % unsegmented cells (see figure 3.3 d). Using this method, the unsegmented parts summed to 19.6 %, which is slightly lower than the automatic estimate.

In summary, although there are small artifacts visible in the data, the quality of j0251 allows for detailed morphological and connectivity studies. With 9.6 % ECS, ECS preservation is in a range where it is beneficial for automatic cell segmentation ($>$ 6 %, Pallotto et al. 2015), as demonstrated in subsequent sections. This enables biologically meaningful analyses.

3.1.2 Improvements to the SyConn pipeline

The SyConn pipeline involves several steps to transform raw EM data with grayscale images stacked together into a catalog of data using multiple neural networks (see methods section 2.2.1, Dorkenwald et al. 2017, Schubert et al. 2022). Ultimately, the cells are segmented into different compartments and sorted into various cell types. Additionally, multiple subcellular structures, such as contact sites, synapses, mitochondria, and vesicle clouds, are mapped onto them.

This thesis includes improvements such as the following: improved prediction of synapses and mitochondria (section 3.1.2), improved classification of projecting axons (section 3.1.2), addition of new cell types, such as novel GABAergic interneurons (section 3.1.2, glial cells and migratory neurons (section

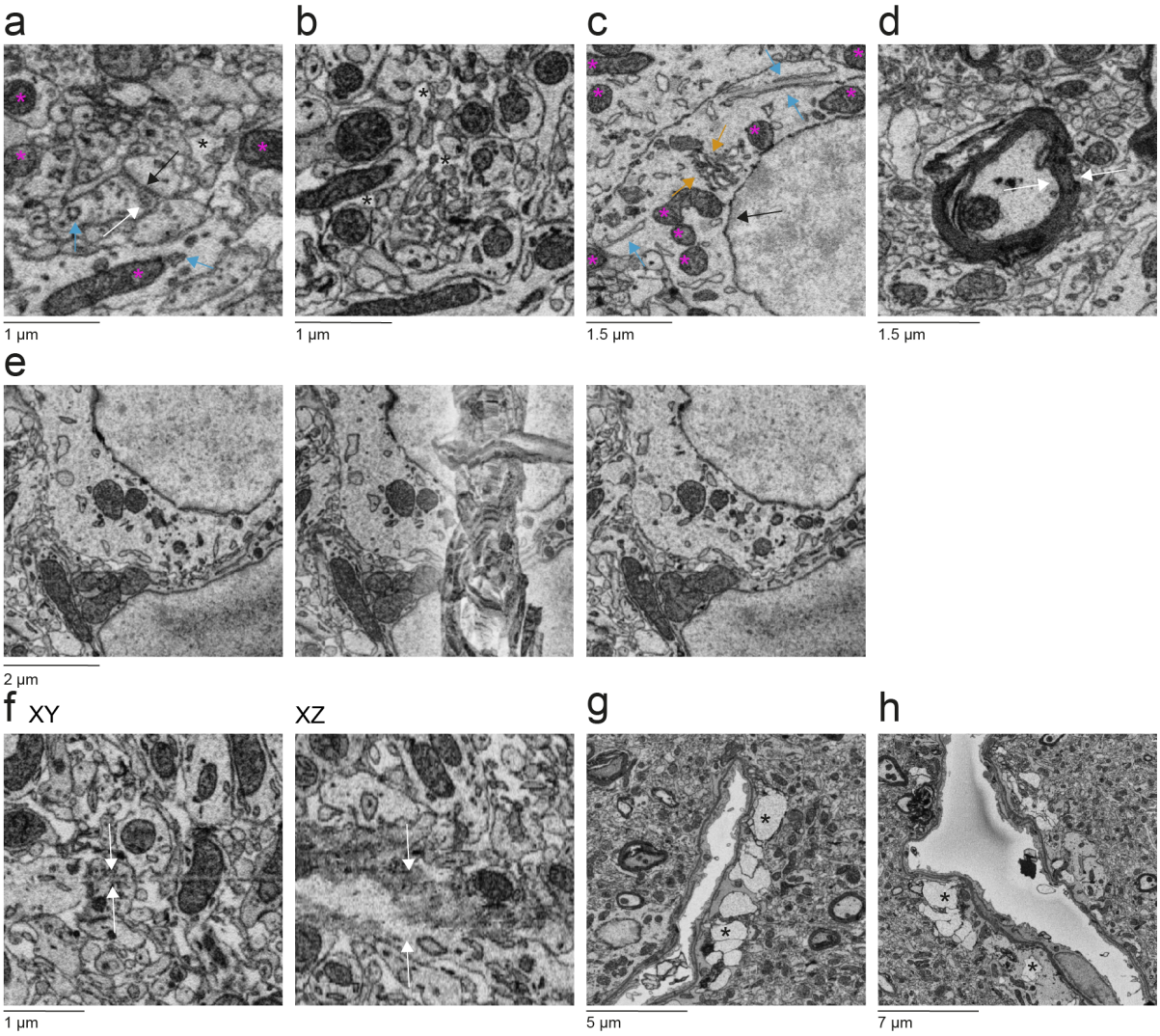

Figure 3.2: j0251 raw EM data. a Neuropil. The synaptic cleft is indicated by a black arrow on the postsynaptic site. The white arrow shows synaptic vesicles on the presynaptic site. The blue arrows point to examples of the ER, the pink asterisks show mitochondria, and the black asterisk shows an example of the ECS. Location: 14455, 13841, 7764 (see 2.2 for visualization instructions).b ECS between neuropil, indicated by black asterisks. Location: 5005, 23199, 4505. c A neuronal soma with different organelles highlighted. The black arrow points to the nuclear membrane. Blue arrows point to examples of ER sheets. Orange arrows point to sheets of the GA. Pink asterisks label mitochondria. Location: 14526, 13494, 7730. d Myelin sheet around an axon, marked with two white arrows. Location: 15617, 13627, 7503. e Section debris on top of the next section (middle), with the plane before (left) and after (right). Location: 4465, 2131, 268. f Artifact from alignment, marked with two white arrows. Shown in both the XY and XZ planes. Location: 23358, 1284, 5032. g,h Artifacts around blood vessels, marked with black asterisks, at two different locations. Location: f: 16217, 14660, 7750; g: 24929, 11960, 7691.

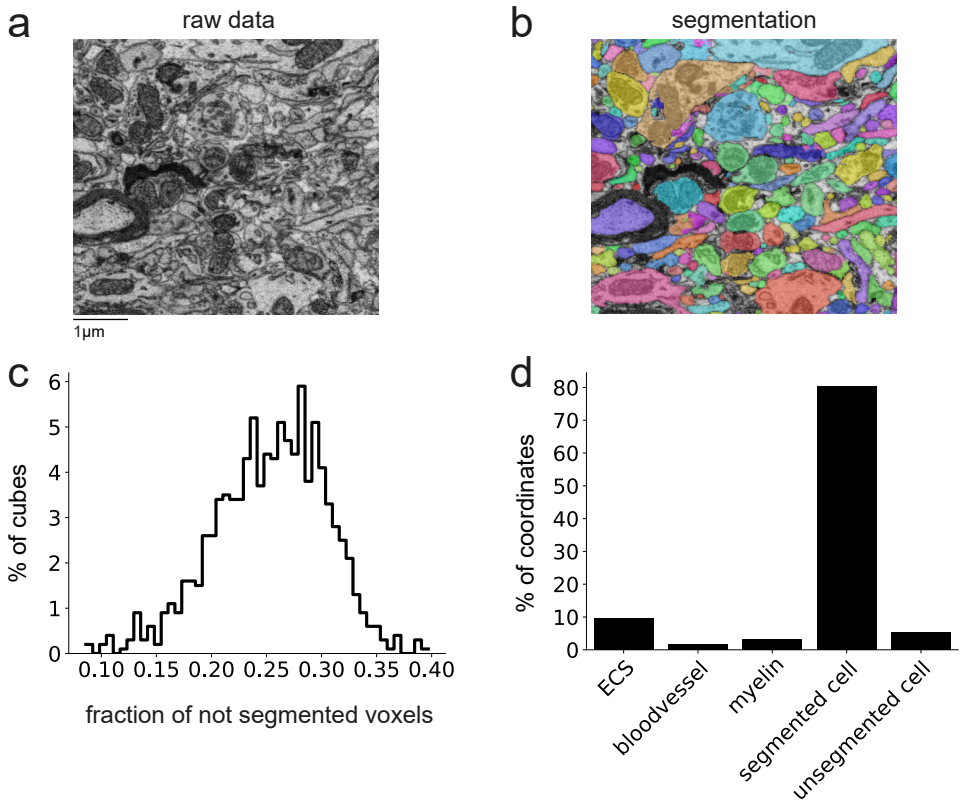

Figure 3.3: Estimate of ECS, blood vessels and myelin. a Raw data example. b Example of the cell segmentation. Both are at location 14014, 14290, 7747. c Fraction of voxels that did not belong to the cell segmentation for 1,000 randomly generated offsets. d ECS estimate alongside estimates for blood vessels, myelin, and unsegmented cells from 501 manually reviewed coordinates.

3.1.2).

New synapses, mitochondria, and vesicle clouds

To enable more precise biological analyses, synapses, and mitochondria were reprocessed based on new ground truth generated through manual annotations from thirteen biological annotators (methods section 2.2.1). Additionally, the vesicle clouds were processed using the same ground truth as previously employed (Schubert et al. 2022).

For mitochondria, an additional step of eroding the individual mitochondria was added to better separate the objects (methods section 2.2.1, see figure 3.4 a). Consequently, the number of mitochondria increased compared to Schubert et al. 2022, while the mitochondrial volume decreased (see figure 3.4 b,c, appendix figure A7). The new ground truth improved synaptic prediction by removing small, falsely labeled synapses (see figure 3.4 a), resulting in a drastic decrease in synaptic number and volume (see figure 3.4 b,c, appendix figure A7).

Since the ground truth for vesicle clouds did not change, the differences compared to the previous version resulted from differences in the prediction model only. The results show a slightly lower number of objects with slightly greater volume (see figure 3.4 b, c, appendix figure A7). These changes are the opposite of those for mitochondria, where the ground truth was updated. Therefore, changes in mitochondria can be attributed to the updated ground truth.

In summary, the new ground truth for synapses and mitochondria leads to fewer synapses and better separation of the mitochondria.

To further ensure the accuracy of synapse predictions, a random forest classifier (RFC, Dorkenwald et al. 2017) is trained to predict synapse probability and assign a number between 0 and 1, where 0 indicates uncertainty and 1 indicates certainty. This probability should correspond to the percentage of true synapses with a given value; for example, a probability of 0.8 should correspond to 80 % of true synapses with this value. This probability can then be used to filter data for analysis.

Previous versions randomly selected ground truth synapses across the dataset. This resulted in low probabilities for clear synapses from less frequent cell types, such as GPe or GPi, whose axonal boutons look different from the more frequent projecting axons (see figure 3.5, visualized is the synapse probability mapped to the cell meshes). To rate synapses from all cell types with equal precision, the ground truth was updated to include randomly selected synapses with presynaptic sites from all neuronal cell types (see method section 2.2.1).

The results of the 10-fold cross-validation of the RFC showed higher F1 scores for true synapses than the previous version (see table 3.1, previously: 300 synapses, 156 synaptic, 144 non-synaptic, true synapses: F1 score = 0.826, precision = 0.794, recall: 0.861; Schubert 2022 p. 92, 104). Scores in the non-synaptic class were lower due to the smaller number of ground truth synapses in that class (see table 3.1).

Upon inspecting the certainty of all synapses in the dataset, a much higher proportion of synapses were classified with a synapse probability greater than 0.8, particularly when filtering by minimum synapse size and axo-dendritic or axo-somatic synapses (see figure 3.6 a, b).

To confirm that this change is due to higher accuracy in predicting synapses and better RFC classification and the decrease in overall synapse number indeed due to the decreased number of false positives, synapses with different probability scores were manually evaluated.

Riccardo Morbio, who had received training in annotating different subcellular organelles, performed the manual evaluation. He was given a subset of 180 randomly selected samples, including all synapses and

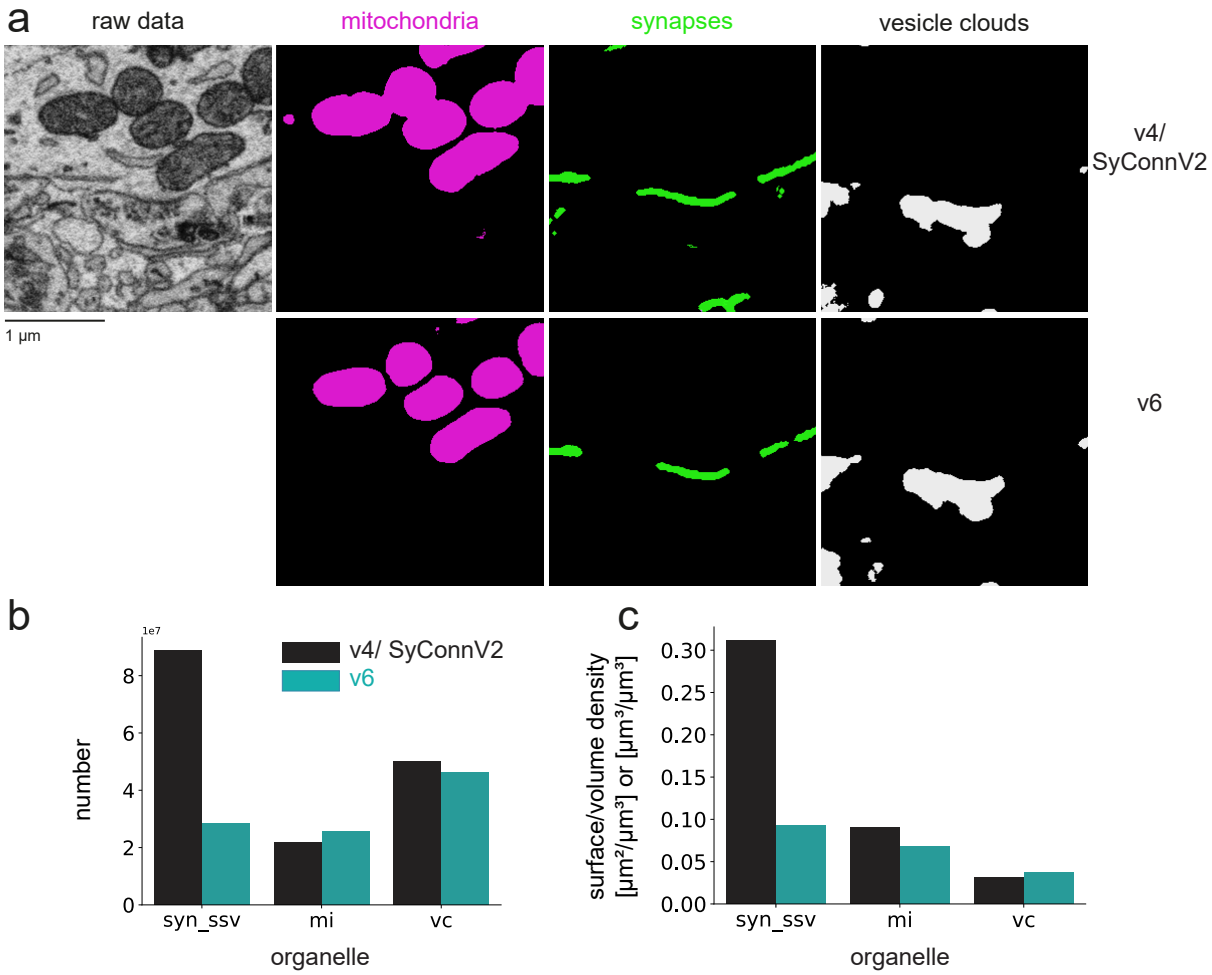

Figure 3.4: Comparison of synapses, mitochondria and vesicle cloud objects in different versions. a An example of mitochondria, synapses, and vesicle clouds at location: 14140, 14081, 7748 in the version 'v4/SyConnV2' from Schubert et al. 2022 and the current version "v6". b Number of objects in different organelle classes. c Surface and volume density for different organelle classes For synapses, the synaptic area was used for the analysis. Here, the synaptic area was divided by the dataset volume. For the other organelles, the summed volume was divided by the dataset volume.

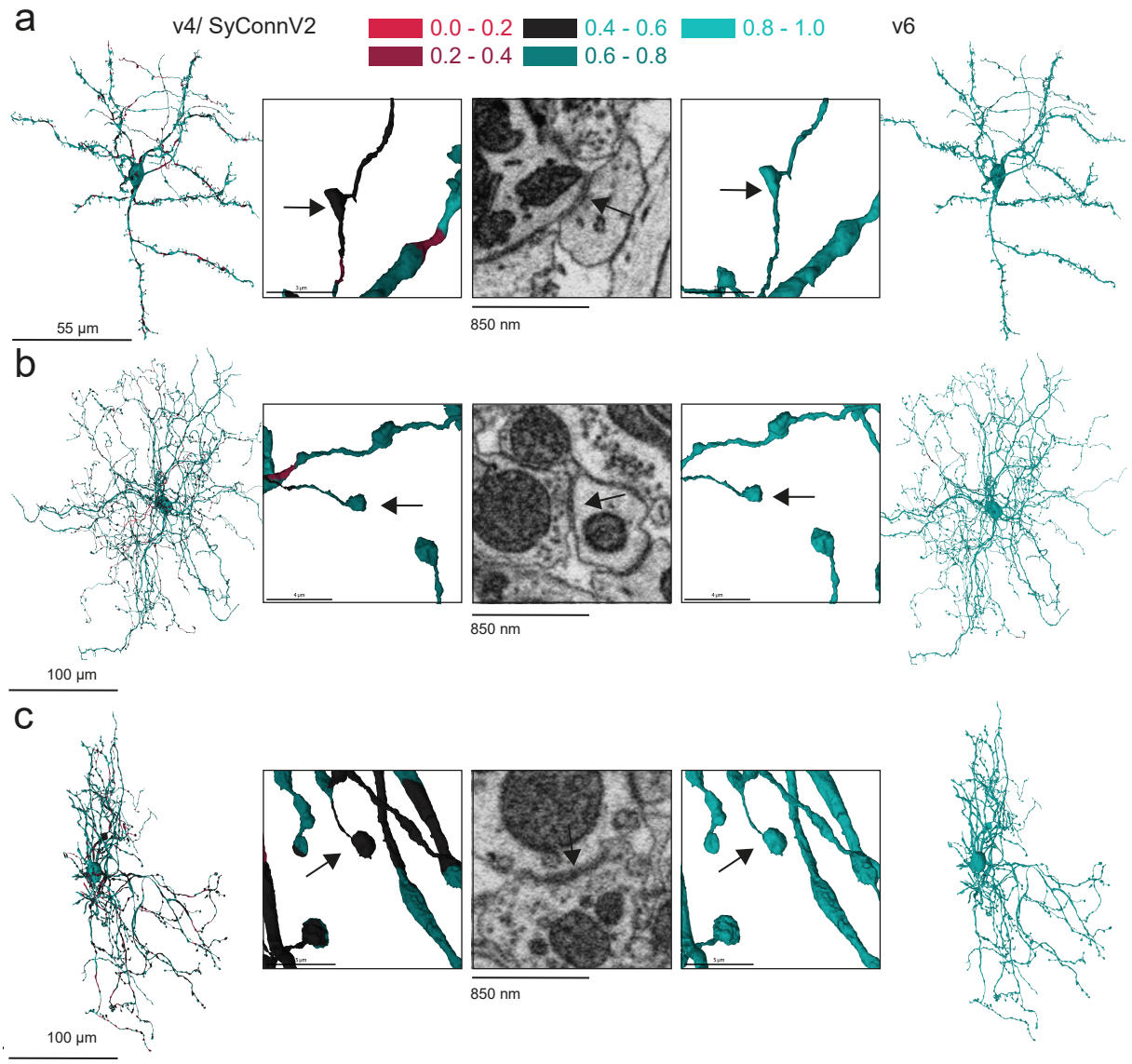

Figure 3.5: Comparison of the predicted synapse probability between v4/SyConnV2 and v6 in different examples. For visualization, the meshes were colored based on the synapse probability of the closest synapse. a MSN (id: 686847652), synapse coordinates: 6760, 22509, 4729. b GPe (id: 17748051), synapse coordinates: 11794, 18431, 4891. c GPi (id: 453097983), synapse coordinates: 5177, 7167, 11070. The scale bar of the insets of the 3D renderings shows 3, 4, and 5 µm for (a), (b), and (c), respectively. The full cell renderings are on the same scale for each example cell.

	precision	recall	F1-score	support
non-synaptic	0.70	0.67	0.68	96
synaptic	0.87	0.88	0.88	234
accuracy			0.82	330
macro avg	0.78	0.78	0.78	330
weighted avg	0.82	0.82	0.82	330

Table 3.1: Results of the RFC 10-fold cross-validation for synapse classification

filtered ones with respect to different cell types (method section 2.2.1). The results of both evaluation rounds show that the synapse probability given by the RFC correlates with the fraction of correctly predicted synapses in each probability bin (see figure 3.6 c, d).

Synapses with a probability > 0.6 (indicated in the figure in the 0.8, 1.0 bars) had a combined true positive rate of > 90 % (90,27 % for all synapses, 93,01 % for > 0.1 µm^2). To ensure a low false positive rate, a synapse probability of 0.6 was used for all subsequent analyses involving synapses.

In conclusion, changes in synaptic processing result in a large proportion of high-probability synapses, leading to a high number of accurately predicted synapses.

Improving the classification of projecting axons

Area X receives projecting axons from several areas, including the cortical areas HVC and LMAN, as well as dopaminergic projections from the ventral tegmental area (VTA, see figure 3.7 a). Their morphological differences, such as the highly branched axons of LMAN versus the straight axons of HVC (Henselmans et al. 1994, Fortune et al. 1995, see table 2.6), allow for the automatic classification of these three cell types (Schubert et al. 2022).

The ground truth for the previous classification included significantly longer LMAN than HVC and DA axons ($p < 0.005$, see appendix table A3; figure 3.7 b). This led to the prediction that DA axons would be shorter than LMAN and HVC axons on average and that LMAN axons would have a bimodal distribution with a large fraction of axons greater than 100 µm (see figure 3.7 c).

Differences in the length of the ground truth samples can result in the prediction endpoint being associated with a specific class without learning more about the morphology. An intermediate classification ("v5") based on more imbalanced ground truth data (with significant length differences in length between all three classes, see appendix table A3) leads to larger differences in length between the three classes (figure A8, appendix tables A4, A5). This points to the aforementioned bias in the ground truth data.

To improve the classification of projecting axon types, the ground truth was expanded to include a broader spectrum of lengths for all classes, especially shorter LMAN and longer DA axon fragments (method section 2.2.2, see figure 3.7 d). Due to their branched appearance, LMAN fragments were significantly longer than DA and HVC fragments (p-values in appendix table A3). The resulting predictions are in a similar length range, even though statistical differences remain (figure 3.7 e, appendix table A4). The LMAN distribution now mainly follows one distribution, with a small fraction of longer axons.

To determine whether changes in length distribution are accompanied by differences in classification between these three cell types, the identity of the new axon fragments was compared to their classification in "v4/SyConnV2" (Schubert et al. 2022).

The first difference is the lower number of classified HVC axons in the current version and the higher

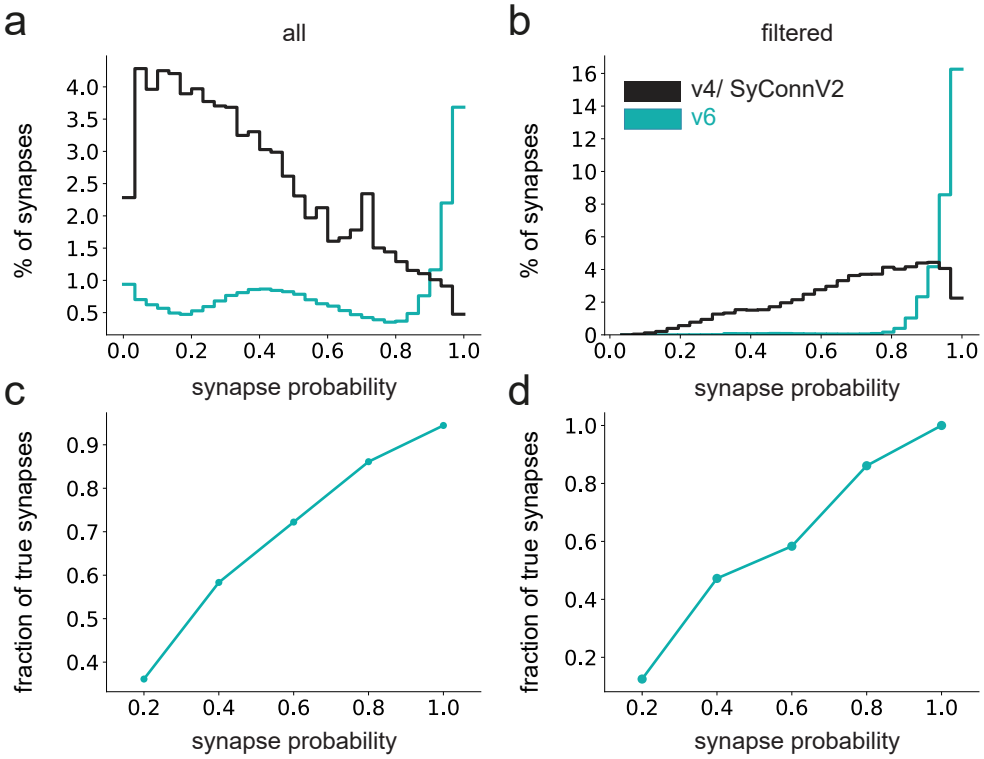

Figure 3.6: Comparison of predicted synapse probability between v4/SyConnV2 and v6. a Predicted synapse probability for all synapses. b Predicted synapse probability for synapses filtered with a minimum size of 0.1 µm^2, only axo-dendritic synapses between neurons suitable for analysis (method section 2.3.1). c Manual evaluation of 'v6' synapses in different probability bins (method section 2.2.1). d Manual evaluation of synapse probabilities filtered as in b.

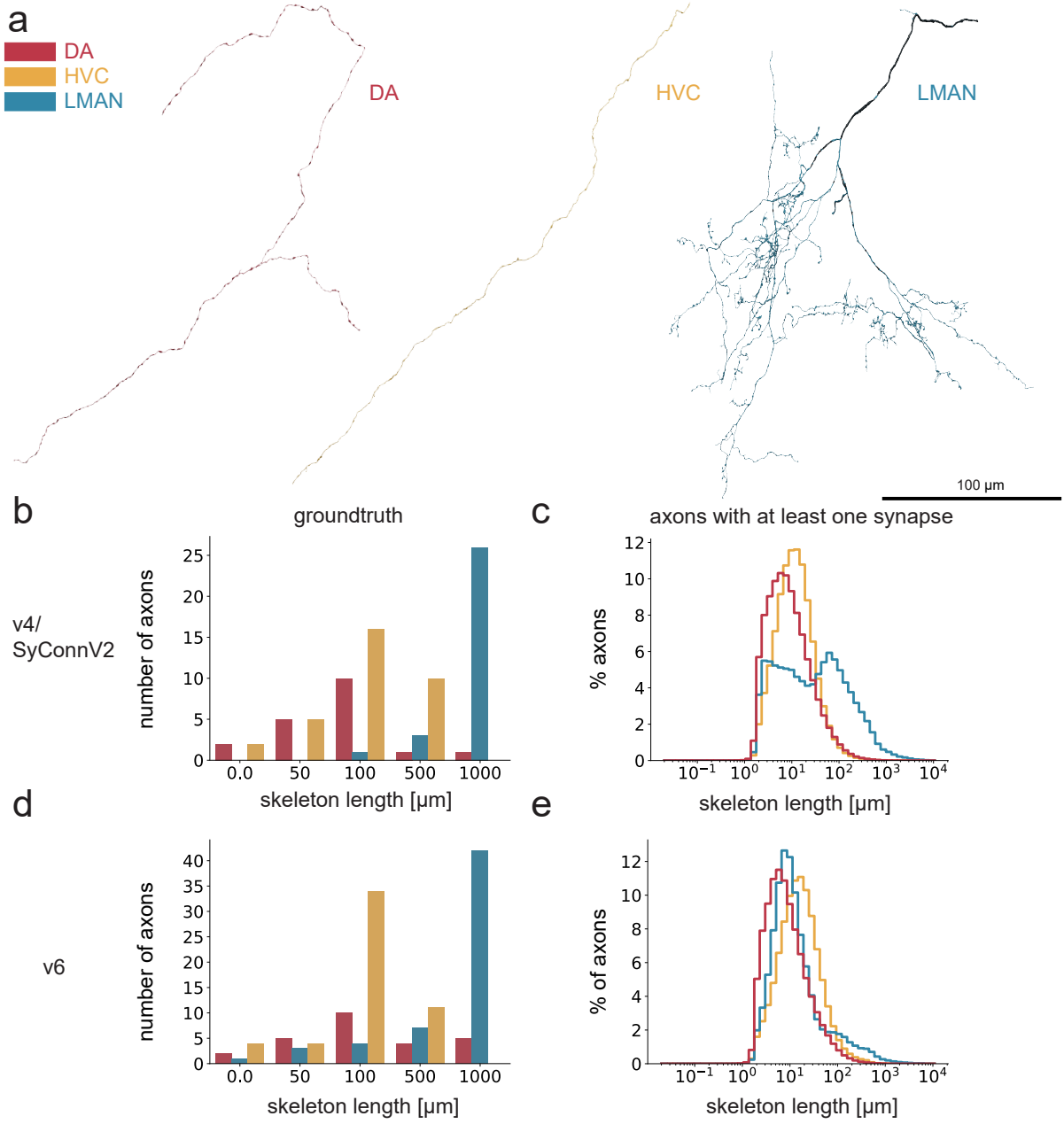

Figure 3.7: Projecting axons and their lengths. a Renderings of example ground truth projecting axons. The myelinated part of the LMAN axon is shown in black. DA ID: 139212645, HVC ID: 1126849047, LMAN ID: 436157555. b Length of fragments used for ground truth generation in Schubert et al. 2022 "SyConnV2/v4." The labels show the lower end of the corresponding bin. For example, 50 indicates axon fragments with a length between 50 and 100 µm, and 1000 indicates fragments > 1000 µm. c Length of predicted axon fragments that have at least one synapse in SyConnV2/v4. d Length of fragments used for ground truth generation in the most recent version, v6. The labels are the same as in b. c Length of predicted axon fragments that have at least one synapse in v6.

axon type	version	number of axons	number of axons with at least one synapse
DA	v4/SyConnV2	810174	673313
DA	v5	1908217	1469296
DA	v6	1889548	934246
HVC	v4/SyConnV2	2796405	2271418
HVC	v5	824085	793575
HVC	v6	2714875	2169004
LMAN	v4/SyConnV2	65908	52844
LMAN	v5	339335	255247
LMAN	v6	221924	120580

Table 3.2: Number of axon fragments for different versions.

number of classified LMAN and DA axons (table 3.2). For both the DA and LMAN classes, the newly predicted axons mainly come from axons that were previously classified as HVC (median $\sim$ 25 % DA, $>$ 30 % LMAN, figure 3.8 a). The HVC class, on the other hand, remained stable, with nearly 80 % classified as HVC beforehand. New axons in the DA class that were previously HVC also had lower certainty (median $\sim$ 0.6, figure 3.8 b). New axons that were previously HVC in the LMAN class had a high certainty (median $\sim$ 0.8), even higher than previous LMAN cellids. This is potentially due to a high HVC certainty.

In the new classification, the level of certainty did not vary much depending on the previous class, but it did increase overall with a higher cell number. Thus, HVC had the highest level of certainty (see appendix figure A9). New axon fragments in LMAN also originate from axons that were previously classified as STN, MSN, or GPi. However, in contrast to HVC, they were assigned low probabilities to the previous cell classes. This can be partially attributed to the generally lower certainties of cell types with lower cell numbers.

In summary, balancing the ground truth in terms of axon length improved their classification.

Identification of novel GABAergic interneurons

Area X contains several types of interneurons that are found in different nuclei of the mammalian brain (section 1.2.2). Examples include MSN neurons from the striatum and GP neurons from the globus pallidus. Some of these cells are projecting axons in their mammalian analogue, some of them are also interneurons there. This dataset previously identified four cell types linked to interneuron cell types from the mammalian basal ganglia: TAN, LTS, FS, and NGF (Schubert et al. 2022). While TAN, LTS, and FS cells have been reported in Area X before (Farries et al. 2002), this was the first identification of the putative NGF cell type.

Based on the separated UMAPs (Schubert et al. 2022, figure 2) and manual inspection of morphology, it was analyzed whether these cells could be further divided into two subtypes. Four morphological parameters—axon mitochondria density, axon median radius, soma diameter, and spine density— showed two distinct clusters. One cluster exhibited a high mitochondria density, thicker axons, large somata, and few spines ("NGF type 1"), while the other exhibited a low mitochondria density, smaller axons, smaller somata, and more spines ("NGF type 2"). Manual thresholds were set for each parameter (method section 2.2.2, see table 2.9). Cells that fit into one group based on all parameters were classified as "NGF

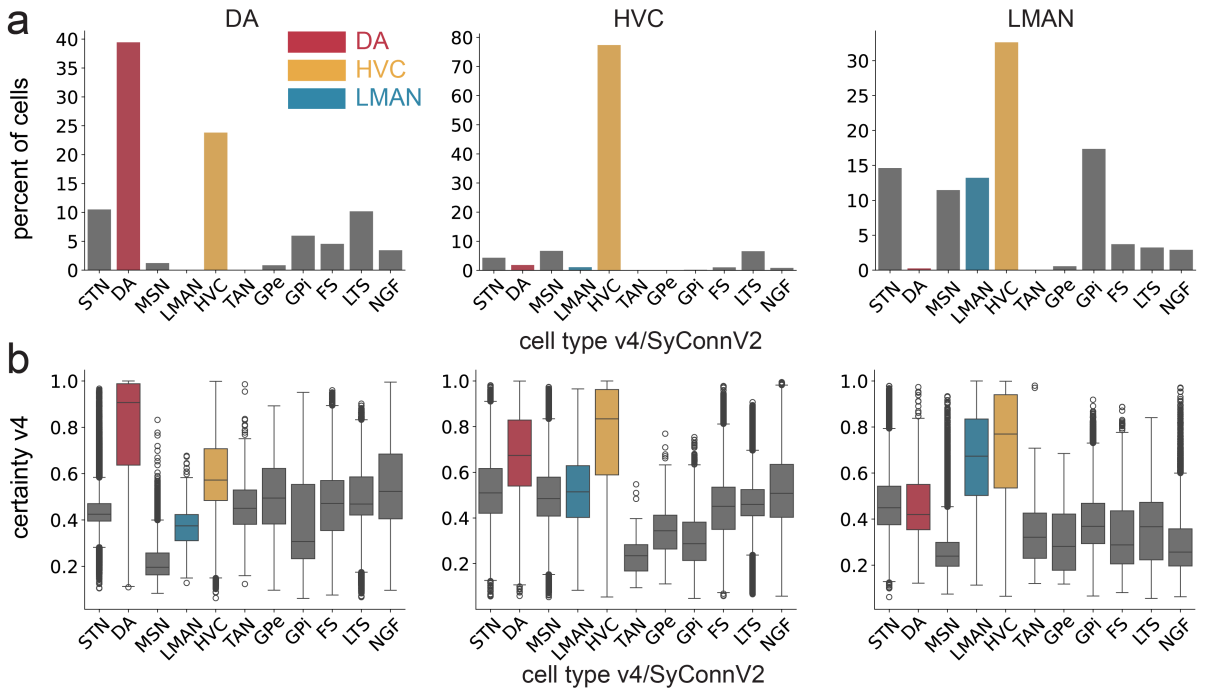

Figure 3.8: Projecting axons and their predicted certainties in different versions. a Percentage of axons of different projecting axon classes in v6 and their corresponding cell types in v4/SyConn V2 b axons in different classes and the corresponding certainties in v4. Certainties in v6 are in A9.

type 1" or "NGF type 2" (figure 3.9 a, b). Cells that did not fit into one group with the thresholds of all four parameters were labeled as "NGF undefined" (for cell numbers see appendix table A6).

The other two GABAergic interneuron groups in the dataset are LTS and FS. LTS cells have small somata and long dendrites, giving them a different morphology (methods table 2.6, Farries et al. 2002). Cells classified as "FS" have branched axons and are similar in size to "NGF" cell types (figure 3.9 c). When plotted together with the two NGF types, the FS values lie between the two NGF types in all four parameters (see appendix figure A10). They were also significantly different from both NGF types (p-values < 0.005, see appendix table A7, A8).

Based on these results, it was unclear which of the three cell types (FS, NGF type 1, and NGF type 2) corresponded to the previously previously through electrophysiology described "FS" type. Therefore, the FS and NGF types were renamed INT1 (previously "FS"), INT2 ("NGF type 1"), and INT3 ("NGF type 2"). To further analyze them, the ground truth was extended for INT2 and INT3, and they were classified as different cell types (methods section 2.2.2).

This new classification yielded three morphologically distinct cell types that can be separated using a four-dimensional principal component analysis (PCA) with the aforementioned parameters ($p < 0.005$ for all parameters, see figure 3.9 d-f, appendix tables A7, A9).

In summary, morphological analysis of "FS"-like GABAergic interneurons identified three distinct cell types in Area X. Further differences in organelle density and connectivity are analyzed in 3.3, 3.4.2).

Identification of glial cell types and migratory neurons

The brain consists not only of adult neuronal cell types, but also of several types of glial cells and migratory neurons. As these cell types had not been previously identified in the data, the first goal was to determine the extent to which they are part of the dataset and whether they could be classified alongside neuronal cell types.

Based on literature describing morphology (see table 2.6) and an iterative cell classification process aided by manual classification, four glial cell types (astrocytes, microglia, oligodendrocytes, and oligodendrocyte precursor cells (OPCs)) and migratory neurons could be identified in the data (methods section 2.2.2, see figure 3.10 a).

Using filtering for skeleton path length and classification certainty, as well as manual inspection, Delta Schick identified 390 glial cells as part of his master's thesis (see table 3.3, figure 3.10 a, Schick 2023) and subsequent work (shared conference poster at FENS 2024, Schick et al. 2024), both of which were supervised by me. All identified microglia were in their resting state (see figure 3.10 a).

Oligodendrocytes have several thin processes that produce myelin. Unfortunately, these cells are often fragmented in our data, and myelin is not segmented as part of them.

After classification, Naomi Shvedov manually selected the migratory neurons for further analysis (methods section 2.2.2, table 2.6, Shvedov et al. 2024).

At least one astrocyte process contacts a blood vessel to form the blood-brain barrier (see figure 3.10 a, b). Therefore, the blood vessels are densely surrounded by astrocytes. Due to incomplete segmentation and to improve visibility, only a few examples are shown figure 3.10 b.

Cell type classifier performance

In summary, the following changes were made to the cell type classification: First, axonal fragments of different lengths were added. Second, FS-like GABAergic interneurons were separated into three

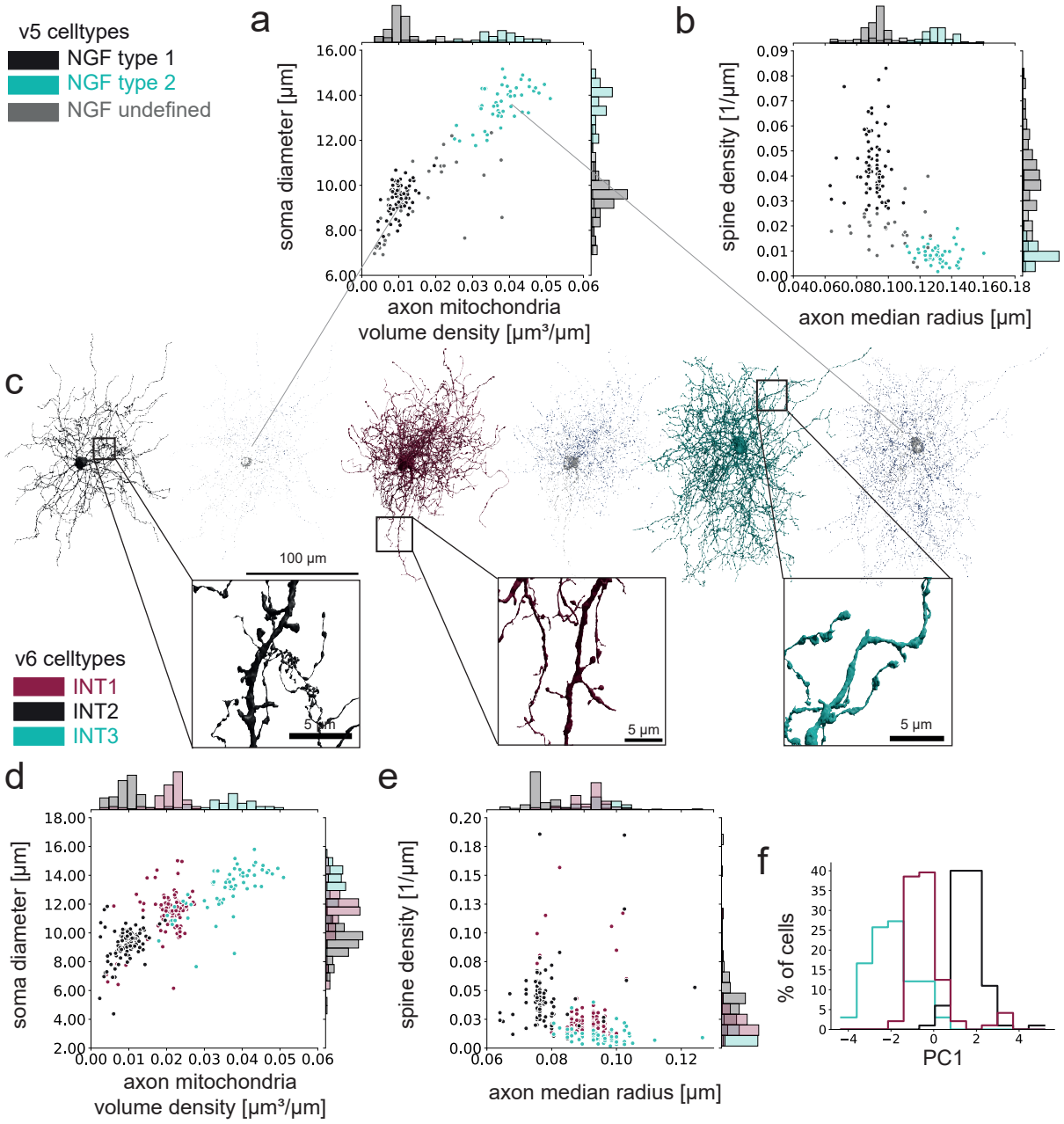

Figure 3.9: Three GABAergic interneuron types and their morphological differences. a Soma diameter and axon mitochondrial volume density of neurons classified as "NGF" in v5. b Spine density and axon median radius of the same neurons. c Renderings of three example neurons alongside their mitochondria, with insets showing dendrites with more and fewer spines. The mitochondria of the axon are labeled in blue, and the soma and dendritic mitochondria are labeled in gray. Neuron IDs: INT1: 1080627023, INT2: 126798179, INT3: 24397945. d, e Morphological parameters plotted again with the new classification of these interneurons as INT1-3. INT1 neurons were previously labeled as "FS" (see appendix figure A10).

cell type	v5 filtered	v5 manual	v6 filtered	v6 manual
astrocyte	208		105	
microglia	111	93	169	54
oligodendrocyte	71		106	33
OPC	-	1	-	126
migratory neuron	-	14		35

Table 3.3: Numbers of the different glia cell types and migratory neurons in the different versions. "Filtered" means filtered according to the criteria described in methods section 2.2.2, while "manual" means manually verified.

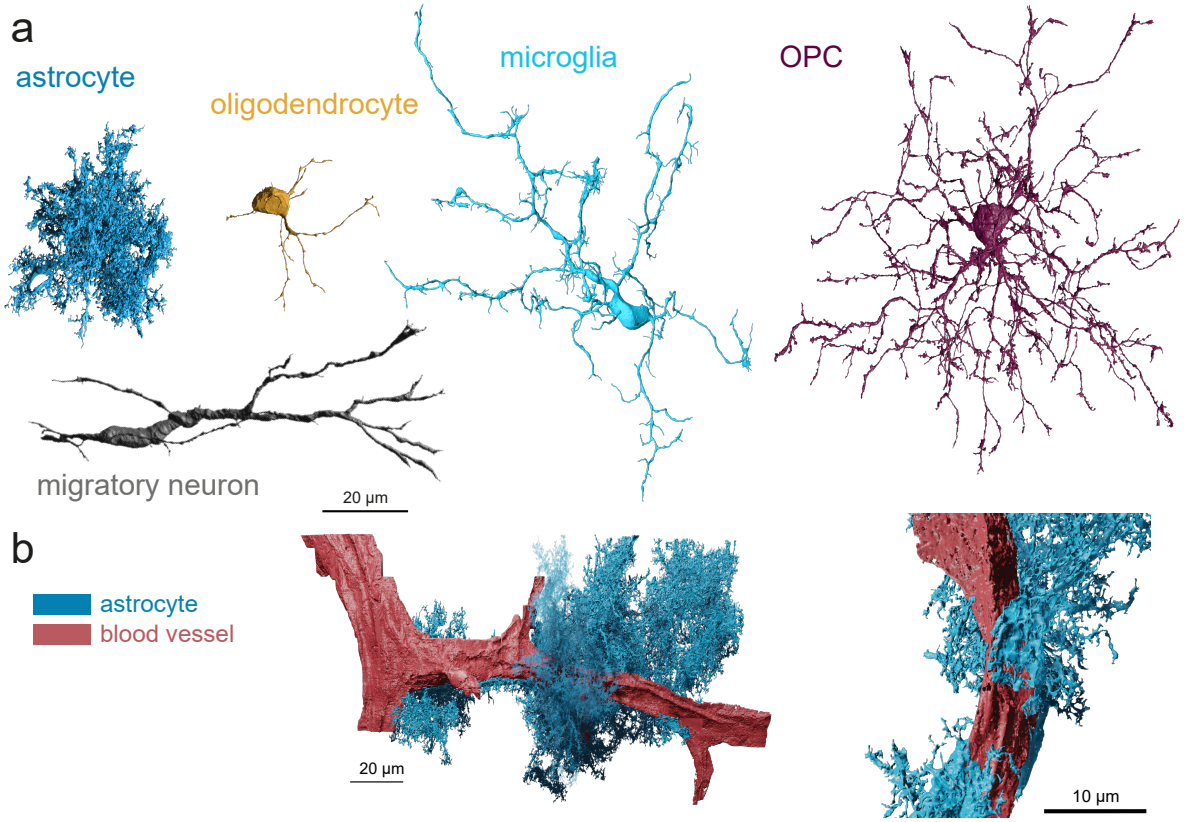

Figure 3.10: Glial cell types and migratory neurons. a Example cells of glial cell types and a migratory neuron. Cell IDs: ASTRO: 2069615083, OLIGO: 1190822162, MICRO: 1143990345, OPC: 2017622103, MIGR: 1644151292. b Example of astrocytes on a blood vessel that was incorrectly segmented as a cell. Blood vessel cell ID: 2332213096, ASTRO IDs: left: 2491837340, 2412109485,2211357026; right:2211357026, 2129941466.

	redundancy 1		redundancy 10		redundancy 20		redundancy 50	
quantity	mean	sd	mean	sd	mean	sd	mean	sd
DA	0.925	0.043	0.960	0.017	0.981	0.016	0.987	0.009
LMAN	0.862	0.020	0.953	0.013	0.942	0.000	0.953	0.007
HVC	0.886	0.004	0.959	0.012	0.949	0.004	0.956	0.004
MSN	0.884	0.006	0.995	0.007	0.995	0.007	0.995	0.007
STN	0.908	0.010	0.939	0.007	0.957	0.023	0.944	0.000
TAN	0.823	0.036	0.973	0.019	0.973	0.019	1	0.000
GPe	0.878	0.015	0.949	0.036	0.900	0.016	0.923	0.000
GPi	0.889	0.000	0.956	0.031	0.909	0.017	0.933	0.000
LTS	0.522	0.046	0.850	0.035	0.85	0.035	0.825	0.035
INT1	0.851	0.020	0.917	0.016	0.965	0.026	0.957	0.000
INT2	0.888	0.038	0.939	0.029	0.990	0.014	0.960	0.013
INT3	0.938	0.045	1	0.000	1	0.000	1	0.000
ASTRO	0.946	0.036	0.945	0.021	0.945	0.021	0.945	0.021
OLIGO	0.789	0.034	0.789	0.034	0.806	0.039	0.806	0.039
MICRO	0.857	0.010	0.872	0.018	0.872	0.018	0.872	0.018
MIGR	0.927	0.030	0.929	0.000	0.940	0.016	0.952	0.017
FRAG	0.837	0.049	0.847	0.035	0.847	0.035	0.847	0.035
f1 score macro	0.860	0.008	0.928	0.008	0.931	0.004	0.933	0.007

Table 3.4: Mean and standard deviation of f1 scores from the 10-fold cross-validation for different cell types and three different validation splits.

previously unknown types based on morphology. Third, glial cell types and migratory neurons were identified in the data. These changes resulted in a total of 16 cell classes on which a classifier was trained (plus one additional class for small fragments, Schubert et al. 2022).

To evaluate the classifier's performance, a 10-fold cross-validation was performed with different redundancy scores as previously described (see table 3.4, Schubert et al. 2022). The redundancy describes how often one cell is presented to the classifier during prediction. The confusion matrices with the corresponding redundancies are in the appendix tables A10, A11, A12 and A13. As described in Schubert et al. 2022, figure 2c, the F12-scores improve when the redundancy increases to 10, but not as much when it increases from 10 to 20 or 50. For final training to classify the cells, a redundancy of 20 was used.

Overall, the classifier successfully sorted cells into different types with an F1 score of $(0.931 \pm 0.004$. These results are comparable to the previous training with less classes and without myelin (0.932 ± 0.009, Schubert et al. 2022).

3.1.3 Organelle extraction

The raw EM images contain several different organelles with lipid bilayer membranes. While mitochondria, synapses and vesicle clouds are already processed as part of the SyConn Pipeline (Dorkenwald et al. 2017) but other organelles visible in EM, such as the ER and GA, are not yet processed, even though they are linked to neuronal function. The ER, for example, functions as a calcium storage site in close proximity to synapses (Tsuboi et al. 2021). To further enhance our understanding of neuronal morphology

and potential functional links in connectomics, ER, GA, and individual vesicles must be identified and processed in the data.

To segment ER, GA and individual vesicles, first new ground truth was generated by 12 biological annotators in a total of 4286 hours of annotation and review for 14 cubes, each measuring $4 \times 4 \times 5$ µm^3 (methods section 2.2.3). This ground truth was then used to train and predict with a U-Net by Martin Bucella, and was processed using the SyConn pipeline by Hashir Ahmad and me (methods section 2.2.3).

First, individual vesicles were predicted based on limited ground truth ("single class prediction"). Then, single vesicles were predicted alongside mitochondria, synapses, ER, and GA in a multi-class prediction (see figure 3.11 a). To evaluate the accuracy of the prediction in the context of biological data analysis, both methods were evaluated manually, and the results are shown in the following sections.

Evaluation of individual vesicles

The first evaluation focused on individual vesicles from the single-class and multi-class predictions. After processing, the coordinates of all predicted vesicles were extracted. This resulted in a dataset of approximately 3 billion single-class vesicles and 2.5 billion multi-class vesicles.

For the evaluation, 286 vesicle coordinates were randomly selected from each prediction to represent various neuronal cell types, as well as different calculated distances to the cell membrane and the next synapse (methods section 2.2.3). Manual evaluations were performed by biological annotator Riccardo Morbio.

Multi-class prediction performed slightly better than single-class prediction, with 85.3 % of vesicles being true individual vesicles overall (compared to 79.3 % in the single class; see figure 3.11 b). Apart from one in each class, all true vesicles were located in axons (see figure 3.11 c). The fraction of true vesicles differed depending on the cell type. For the multi-class prediction, all of them were over 65 %, and eight out of eleven were over 80 %. For the single-class prediction, only 46 % of MSN were true vesicles, while all other cell types had over 65 %, and seven out of eleven over 80 % of true vesicles (see appendix figure A11 a). Thus, the multi-class prediction performed better than the single-class prediction in eight cell types.

If the vesicle prediction was incorrect, it was mostly due to misclassification of the ER (see figure 3.11 d). Having the ER as a separate class slightly improved the distinction between the ER and the vesicles. In the multi-class prediction, there was less ER (54.8 % , 23 vesicles, compared to 62.7 % and 37 vesicles in the single-class prediction). Since mitochondria are sometimes stained less and appear differently in astrocytes, cistae were also sometimes labeled as single vesicles in the multi-class prediction, as well as in the current and previous vesicle cloud predictions (see figure A11 c).

Overall, both predictions can identify true vesicles, with the multi-class prediction performing slightly better.

In an additional step, it was evaluated whether the calculated distance to the membrane could predict whether a vesicle was touching the cell membrane. The fraction of different distances was similar between the multi-class and single-class predictions, with values around 0.5. The single-class prediction had the highest ratio at a calculated distance of 10-15 nm, with 59.2 % (see figure 3.11 e, A11 b). For vesicles with a large calculated distance, the fraction of membrane-close vesicles was 20 % for the multi-class prediction and 16.6 % for the single-class prediction. This shows that the distance calculation is not completely reliable in predicting vesicles that touch the membrane. For further analysis, a threshold of 10 nm was selected to identify vesicles close to the membrane, indicating proximity rather than contact.

Overall, both single-class and multi-class predictions could identify individual vesicles, with multi-class

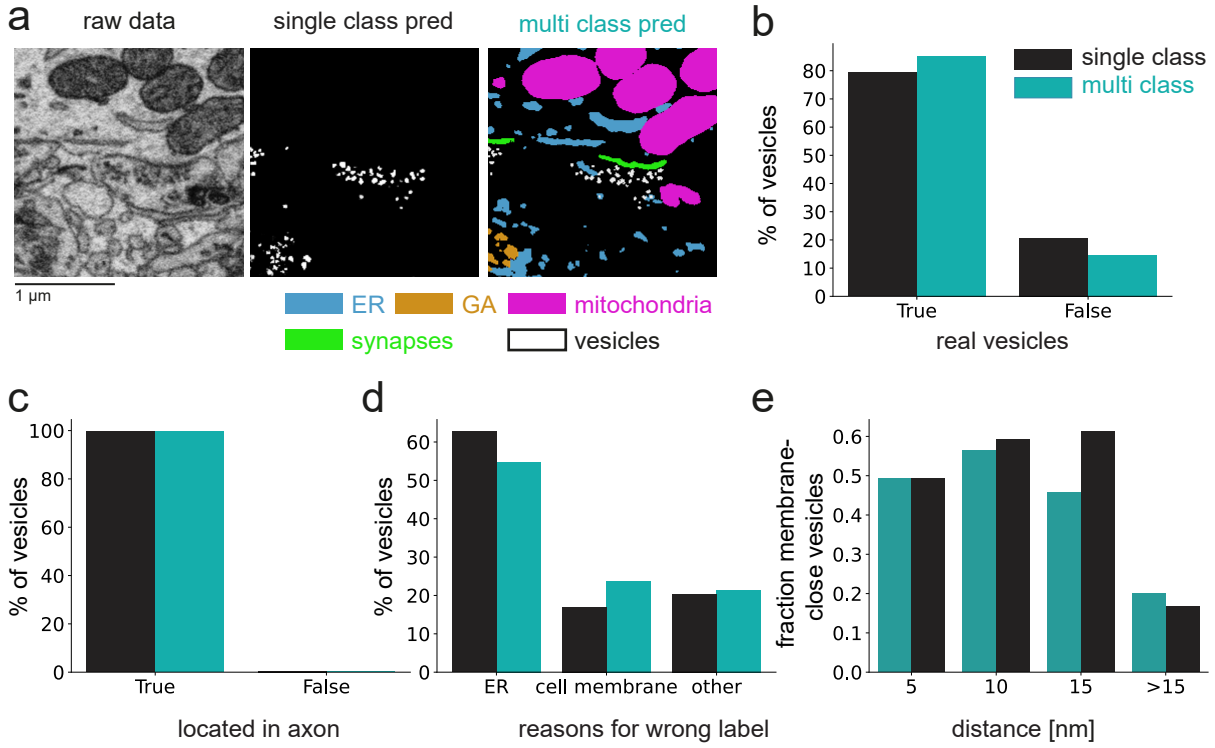

Figure 3.11: Evaluation of single vesicles in single versus multi-class prediction. a Comparison of the prediction of single vesicle segmentation in the single-class versus multi-class prediction (location: 14140, 14081, 7748). b Percentage of true and false vesicles in the evaluation set. c Percentage of true vesicles located in an axon. d Percentage of falsely labeled vesicles in different categories. e Fraction of membrane-close vesicles depending on the calculated distance to the membrane.

predictions performing slightly better. However, calculations of distance to the cell membrane do not accurately show whether the vesicle is touching the membrane; rather, they are a measure of proximity to the membrane.

Prediction of ER, GA, and individual vesicles

As described above, the multi-class prediction includes three new organelle classes: ER, GA, and individual vesicles. For GA, only large stacks were fully processed. Transport vesicles were only processed if they were in contact with one of the larger stacks (methods section 2.2.3).

To evaluate the accuracy of the three new organelle classes, Riccardo Morbio manually reviewed a total of 675 coordinates from 16 cell types (12 neuron types, three glia types, and migratory neurons, methods section 2.2.3). To estimate the error rates among these three classes, the evaluation was performed without knowing which organelle was predicted.

Overall, 84 % of all coordinates were predicted correctly. Single vesicles performed worse than the ER and GA, with 70.0 %, 90.8 %, and 92.8 % correct predictions, respectively (see figure 3.12 a). ER is common in all compartments and was therefore predicted with a similarly high degree of certainty across all compartments and cell types (see figure 3.12 c, appendix figure A12 a, d). GA and individual vesicles were annotated only in specific compartments where most of these organelles were also predicted, resulting in higher accuracy. Thus, for GA, 93.75 % of predictions in the soma were correct, as were 84 % of predictions in the axon (see figure 3.12 c, appendix figure A12 a). The elongation of soma in glial cells allows some GA to reach the glial processes, which were predicted with much less accuracy (33.3 %).

The accuracy of both GA and vesicles varied depending on the cell type. In the vesicle prediction, glial cells, migratory neurons, and MSNs performed worse than other neuronal cell types (see appendix figure A12 d). No vesicles were originally annotated for migratory neurons and glial cells, while MSNs generally have low vesicle and vesicle cloud densities, as described later (see figure 3.18). Thus, the less accurate prediction was likely due to missing or insufficient ground truth annotations for these cell types. GA predictions performed worse only in astrocytes (60 %), while predictions for all other cell types were similarly accurate ($>$ 80 %, see appendix figure A12 d).

Since only the connected components of large GA were processed, most of the predicted coordinates were part of GA stacks (76.6 %, see appendix figure A12 b, method section 2.2.3). These stacks also had a slightly higher fraction of correctly predicted coordinates (97.9 % in stacks vs 90.9 % in GA vesicles, see appendix figure A12 c).

The aforementioned manual evaluation aims to identify the number of true and false positives, i.e., the number of organelles that were correctly or incorrectly predicted in each class. To estimate the number of false negatives (i.e., organelles predicted as another class or not predicted at all), the raw data must be manually reviewed again. Due to the high density of ER and individual vesicles compared to the limited number of GA stacks in each cell, such an analysis was performed on GA only (methods section 2.2.3).

For this evaluation, three randomly selected ground truth cells were reviewed per cell type, resulting in a total of 30 reviewed cells and an average of 3.85 separate GA stacks per cell (150 stacks in total, see appendix A12 b). 88.7 % were correctly predicted GA stacks, and only two real GA stacks were false negatives (see figure 3.12 e). Both false negatives occurred in oligodendrocytes. Apart from TAN cells, the majority of the separated GA stacks were correctly predicted in all other cell types (see appendix figure A12 b). Upon manual inspection, the false positives and negatives were rather small compared to the large, correctly mapped GA stacks (see figure 3.12 a). Most of the false-positive GAs were ER (43.8 % , see figure 3.12 e), and most were in the soma (64.7 % , see figure 3.12 f).

In summary, the multi-class prediction accurately predicted ER, GA, and individual vesicles in the data when organelles were filtered by compartment (see figure 3.13). For this reason, subsequent analyses of organelles focused only on individual vesicles in axons and GA in neurons in the soma.

3.2 Cell types for data analysis

After processing the data to include new cell types and organelle classes, it was analyzed in the following sections with respect to cellular morphology, subcellular structures, and connectivity.

To ensure consistency and an accurate representation of cells within Area X, all data analysis was performed on a selected set of neuronal cells that met the criteria for completeness (methods section 2.3.1). While it cannot be guaranteed that all of these cells are truly complete, this provides a set of cells

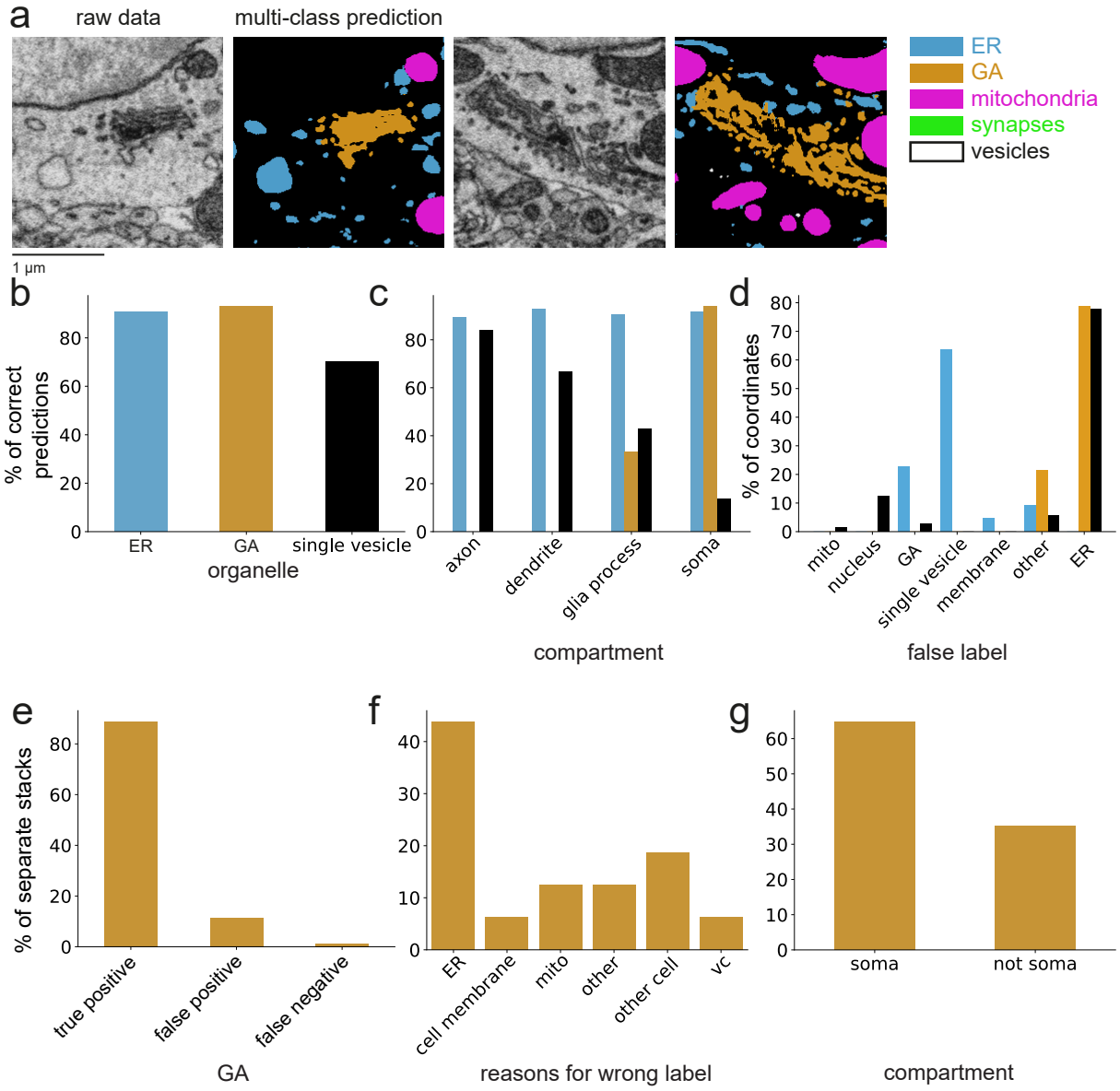

Figure 3.12: Evaluation of ER and GA. a Example coordinates of the prediction: 14750, 18722, 7747; 14750, 18722, 7477. b Percentage of true predictions of ER, GA, and individual vesicles, normalized by the coordinate count of each vesicle. c Percentage of true predictions in each compartment, normalized by compartment. d Percentage of misclassified coordinates in each category, normalized by compartment. e Percentage of separated GA stacks that were correctly predicted and mapped to cells (true positives), falsely predicted (false positives), or not predicted (false negatives). f Percentage of falsely predicted GA in different categories. VC = vesicle cloud. g Percentage of falsely predicted GA stacks inside and outside the soma.

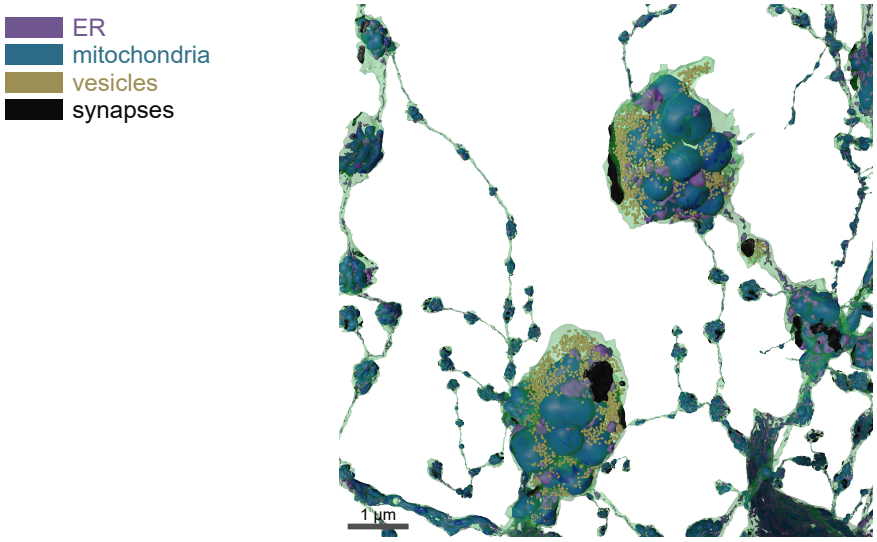

Figure 3.13: Rendering of a GPi synapse with the surrounding ER, mitochondria, and vesicles. The vesicles are rendered spheres with 20 µm radius. GPi ID = 26790127; location: 14378, 9679, 6232.

for which cellular morphology, inputs, outputs, and subcellular structures can be analyzed. For additional quality control, 775 cells were manually inspected for mergers and the presence of the three compartments. All cells of the cell types GPe, GPi, LTS, STN, and TAN were inspected, as well as a random subset of MSN and INT1-3 due to their high numbers and dense axonal arborizations, respectively (see appendix table A14; methods section 2.3.1).

As a result, 35 merged cells and six incomplete cells were identified, translating to a merger rate of 0.0096 mergers per millimeter of skeletal path length (see appendix table A14). These cells were excluded from further analysis for GPe, GPi, LTS, STN, and TAN.

In the end, 8,576 neurons were used for analysis, 94 % of which were MSNs (see table 3.5). MSNs are also the smallest neuronal cell type (se figure 3.14).

Glial cell types and migratory neurons were filtered and manually selected, resulting in a total of 390 cells (methods section 2.2.2, table 3.3).

The filter criteria for projecting axon cell types differed from those for complete cells due to the fragmentation of the former (see figure 3.7). For morphology-related analyses, a minimum path length of 200 µm was selected to accurately represent the morphology and enable comparison to neuronal cell types. Since this criterion excludes most axonal fragments, a path length of 50 µm was selected for connectivity analysis (method section 2.3.1). This results in over 34,000 axons for morphology and over 310,000 axons for connectivity analysis (see table 3.6).

3.3 Morphological and organelle differences of neuronal cell types

The first data analysis section quantifies the morphology of different neuronal cell types and their organelle densities. These are then used to test for potential correlations with neuronal firing rates during singing.

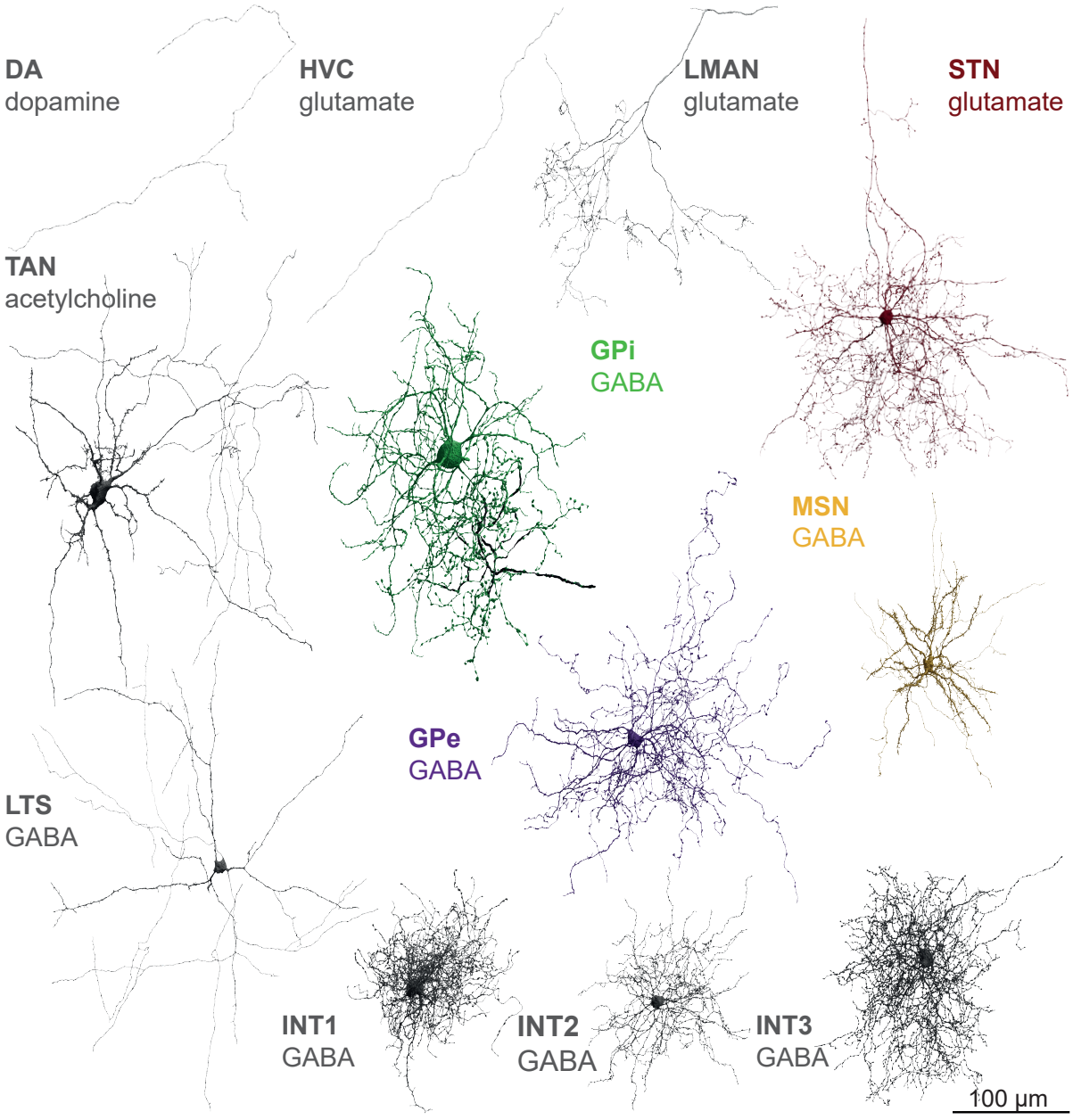

Figure 3.14: Renderings of example cells of cell types identified in Area X, along with their corresponding neurotransmitters. The cell numbers refer to the filtered axonal fragments of the projecting axon types (DA, LMAN, and HVC) and the filtered full cells. The myelinated parts of the axon are shown in white for LMAN and INT3, and in dark gray for STN and GPi. Cell IDs: DA: 139212645, HVC: 1126849047, LMAN: 436157555, STN: 7626258, TAN: 10157981, GPi: 26790127, GPe: 32356701, MSN: 27161078, LTS: 15521116, INT1: 1080627023, INT2: 126798179, INT3: 24397945.

neuronal celltype	number of neurons	putative neurotransmitter
GPe	27	GABA
GPi	47	GABA
INT1	96	GABA
INT2	100	GABA
INT3	66	GABA
LTS	37	GABA
MSN	8093	GABA
STN	102	glutamate
TAN	8	acetylcholine

Table 3.5: The number of neuronal cell types and their putative neurotransmitters, with somata, axons, and dendrite skeletons. The axons and dendrites are at least 200 µm long (methods section 2.3.1).

projecting axon cell type	number of axons [> 50 µm]	number of axons [> 200 µm]	putative neurotransmitter
DA	53522	4767	dopamine
HVC	246153	23069	glutamate
LMAN	19186	6887	glutamate

Table 3.6: Number and putative neurotransmitter of the projecting axons used for the analyses were those with a skeleton length of at least 50 or 200 µm.

3.3.1 Morphological differences of neuronal cell types

Cell type classification is based on morphological features and subcellular structures, such as synapses, mitochondria, and vesicle clouds (Schubert et al. 2022). To quantify the differences between cell types, especially previously undescribed types such as INT1, INT2, and INT3, a set of morphological parameters was analyzed.

The parameters were selected to provide an overview of the morphology and to allow comparison with other techniques, such as light microscopy. These parameters included the length and surface area of different neuronal compartments, the myelin fraction, dendritic spine density, and cell volume (see figure 3.15 a-f, see appendix figure A13 a-e, method section 2.3.4).

Some cell types have striking features. For example, TAN has a high soma surface area (see figure 3.15 c), GPi has the highest myelin fraction (see figure 3.15 d), and MSN has a high spine density (see figure 3.15 e). In general, cell types differ significantly in their morphological features (see appendix tables A17, A15, A16).

Notably, while the literature describes TANs and LTS as sparsely spiny (Farries et al. 2002; see table 2.6), the higher resolution of the dataset shows that these cell types are among the spiniest in the dataset. Additionally, some cells exhibited wrinkled nuclei or nuclear infoldings (see appendix figure A14). Upon manual inspection, wrinkled nuclei were most prevalent in the GPis, affecting 52.4 % of cells, while nuclear infoldings were most prevalent in the STNs, affecting 28.9 % of cells (see appendix table A18).

Although the cell classifier's latent space embeddings could separate neurons in an earlier version of the data (Schubert et al. 2022) and the classifier performed well with the expanded ground truth (section

3.1.2), it is unclear which specific morphological features were used.

To determine whether the aforementioned eleven parameters are useful for classifying different cell types, a UMAP analysis was performed with and without MSNs. The most abundant cell type, MSN, separated quite well from the other neurons (see figure 3.15 g, appendix figure A13 f). Of the 46 MSN cells not included in the full group, 39 (85 %) were mergers, and the MSN group not connected to the GPe or GPi was overrepresented (MSN connected to both GP: 54 %, MSN connected to neither GP: 20 %, MSN connected only to the GPe: 9 %, and MSN connected only to the GPi: 17 %, related to results in section 3.4.1). This indicates that the correct neurons are mostly separated from the other cell types. When clustering without MSNs, clusters are visible; however, apart from TAN and GPi neurons, the separation is unclear (see figure 3.15 h, appendix figure A13 g).

In summary, coarse morphological features can distinguish some cell types, such as MSN, GPi, and TAN, but they are not sufficient to clearly distinguish all 12 neuronal cell types. Additionally, clustering with these parameters can help identify mergers in large cell classes, such as MSN, without manual inspection.

3.3.2 Subcellular structures in Area X

In addition to the morphological parameters described above, subcellular structures can also differ between cell types. With the prediction of the ER, GA, and individual vesicles, as well as the improved prediction of synapses and mitochondria, five organelle classes can be analyzed in the data.

First, to quantify differences in organelles between cell types, organelle density was analyzed in different compartments. Due to differences in organelle function and attributes resulting from different processing steps, some organelles, such as mitochondria, GA, and vesicle clouds, were analyzed for volume density, while synapses and ER were primarily analyzed for surface area.

To facilitate comparison, all density analyses were performed in relation to axonal and dendritic path length. For the soma, the analyses were performed either in relation to the estimated volume or surface area (methods section 2.3.4).

Synapse density

Synapses contain information about neuronal network connectivity, but their densities and appearances can differ between cell types. For cell type classification, synapse location is used as a morphological parameter (Schubert et al. 2019, Schubert et al. 2022).

Differences in synaptic density can be seen, for example, between MSN and GPi. While the GPi appears covered in synapses, especially on the soma and dendritic shaft, the MSN mostly receives synapses on dendritic spines (see figure 3.16 a).

To quantify these differences, synapse density was analyzed in different compartments. Synaptic density differs among all cell types in all compartments, regardless of whether normalization is based on skeleton path length or surface area (see figure 3.16 b, appendix figure A15, appendix table A19).

INT3 has the highest synapse density in axons, followed by INT2, GPe, and GPi (see figure 3.16 a). With their thick dendrites and large somata (see figure 3.15), GPe and GPi have the highest synapse density in dendrites and somata (see figure 3.16 b, c). The results do not differ much between normalizations. One notable change is that the axon synapse density relative to surface area is slightly lower for INT3, resulting in a density similar to that of INT2 (appendix figure A15).

In summary, different cell types have different synaptic densities. The results were similar when

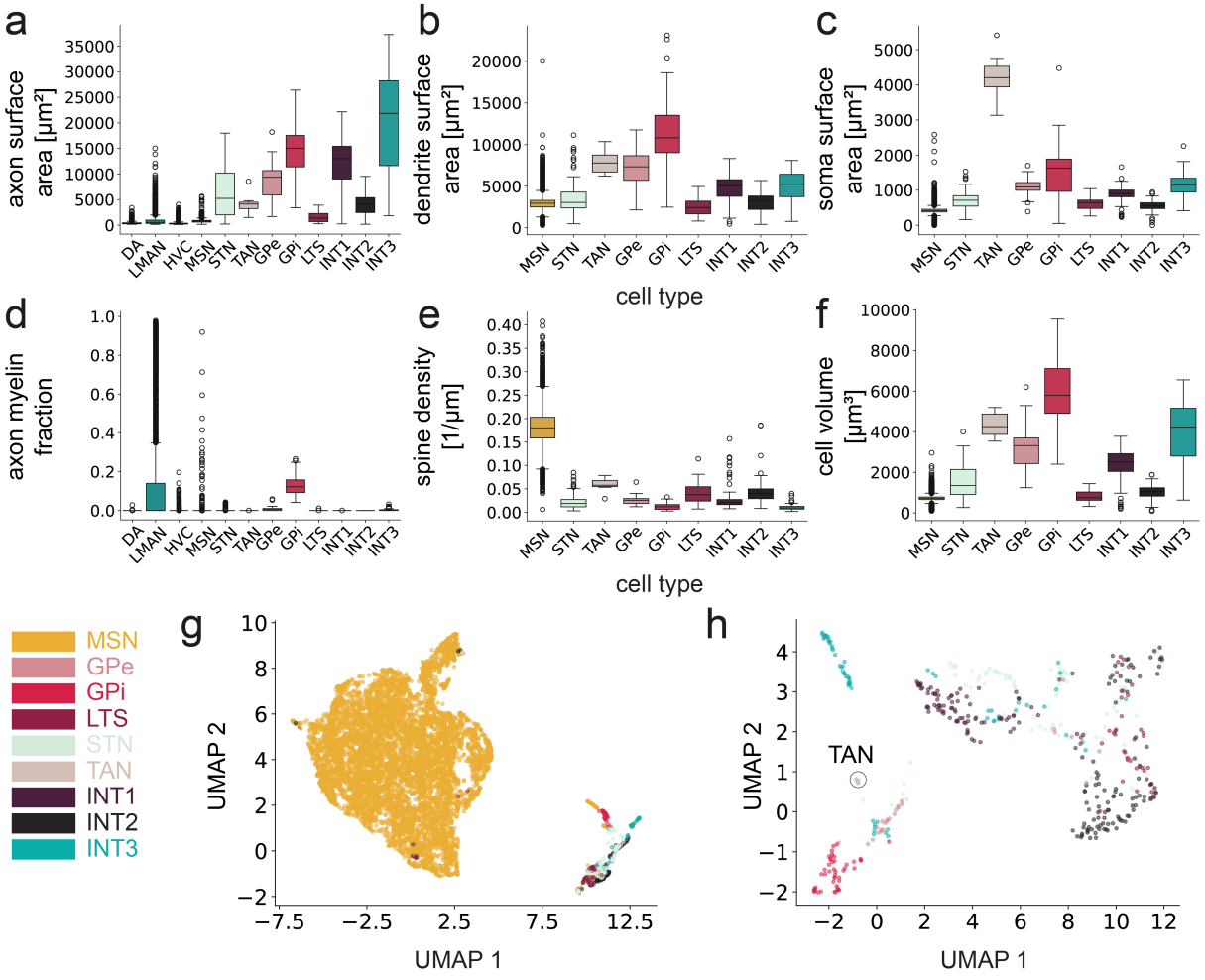

Figure 3.15: Morphological differences in neuronal cell types. a-c Surface area of the meshes of the different compartments. d Myelin fraction of the axon. e Dendritic spine density. f Volume of the cell or projecting axon. g UMAP separation of an 11-dimensional feature space, including parameters in a-f and A13 a-e. h Same as g, but without MSNs.

normalized based on path length or surface area. Further analysis of synapse density used the density of synaptic areas normalized to surface area.

Mitochondria density

Mitochondria are the main source of energy production in neurons. Therefore, higher firing rates are hypothesized to relate to higher mitochondrial densities.

Previous analyses of a smaller dataset with coarser cell typing (Dorkenwald et al. 2017) and a bachelor's thesis by Delta Schick on an earlier version of the data (Schick 2021, supervised by Philipp Schubert and me, data before Schubert et al. 2022), showed a positive correlation with firing rates reported during singing for cell types in Area X. If this correlation holds true for the current data, it could be used to predict the firing rates of the three novel GABAergic interneuron types.

First, differences in mitochondria density between neuronal cell types are analyzed. Previously, differences in axon mitochondria volume density were used to distinguish INT1, INT2, and INT3 (section 3.1.2), and manual inspection revealed striking differences in other cell types, such as MSN and GPi (see figure 3.17 a). Mitochondria density differs between cell types in all compartments (see figure. 3.17 b-d, Kruskal–Wallis test p-value = 0.0, see appendix table A21, for mean, std values per cell type: appendix table A20).

Second, the correlation between reported firing rates during singing and calculated median mitochondrial volume densities per cell type was tested. Although there is a reference value for STN, it was not measured during singing, but rather in Area X slices (Budzillo et al. 2017). Thus, this value was used as a reference for the STN only and was not included in the correlation analysis (methods section 2.3.4). There was a high correlation in all compartments with the reported firing rates, the highest being with the axon mitochondrial volume density (r-squared ≥ 0.9, $p < 0.05$, figure 3.17 e-g, appendix figure A16, appendix table A22). Using the mean or total mitochondrial density yielded a strong correlation, except for the mean somatic mitochondrial volume density (r-squared = 0.76, p = 0.055, appendix figure A16, appendix table A22). It should be noted that, although the correlation with total mitochondrial density is high, the predicted values are negative for INT2 and are therefore not physiologically plausible.

Third, the regression fits were used to predict the firing rates of STN, INT1, INT2, and INT3. The resulting firing rates were as follows: 35 Hz to 106 Hz for INT1, 14 Hz to 37 Hz for INT2, 97 Hz to 117 Hz for INT3, and 47 Hz to 62 Hz for STN (see appendix table A31).

In summary, the volume density of mitochondria in all three compartments varies greatly among cell types and correlates well with reported mean firing rates during singing. While this allows for prediction of the firing rate for INT1-3, the predictions vary greatly depending on the compartment.

Axonal synaptic and non-synaptic vesicle density

In previous analyses of a smaller dataset (Dorkenwald et al. 2017) and in a bachelor's thesis with an earlier version of the data in this dataset (Schick 2021), a high axonal synaptic and non-synaptic vesicle density was related to a higher firing rate during singing in the form of vesicle clouds (vc). However, as the volume of a vc does not provide information about the number of vesicles it contains (see figure 3.18 a, vesicles rendered with a 20-nm radius), it is unclear whether that correlation holds true for the number of individual vesicles. If so, the correlation between vc volume density or vesicle density and the reported firing rates could also be used to predict firing rates for INT1, INT2, and INT3.

First, differences in vc volume density between cell types in the axons are quantified. These two

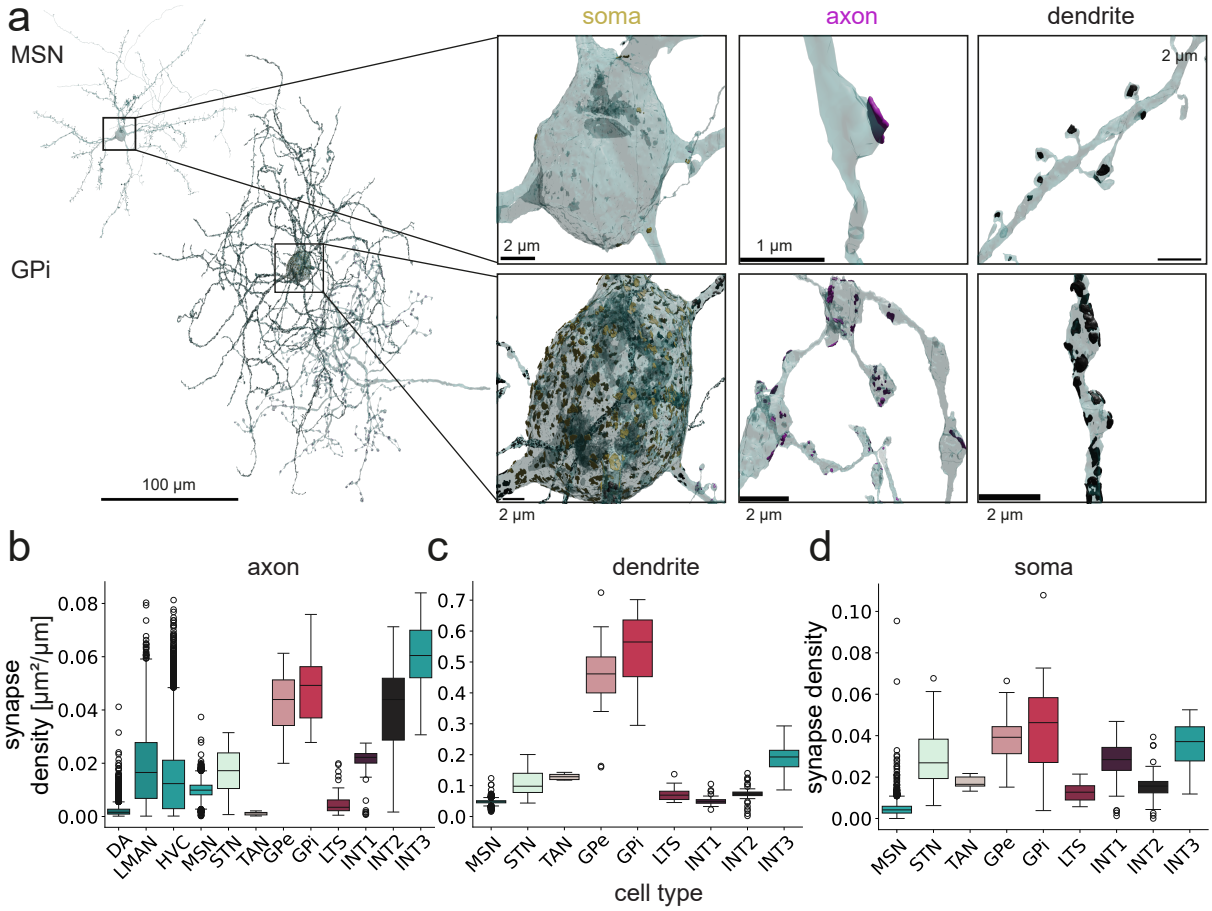

Figure 3.16: Synapse densities in different compartments.a Renderings of an MSN (ID: 832232717) and a GPi cell (ID: 26790127) with synapses in different compartments, both on the same scale. Axon synapses are pink, dendrite synapses are black, and soma synapses are yellow. The insets show the synapses in the different compartments. b,c Synapse density is shown as the summed synaptic area in relation to the skeleton path length in the axon and dendrite. d Summed synaptic area in the soma is shown in relation to the soma surface area.

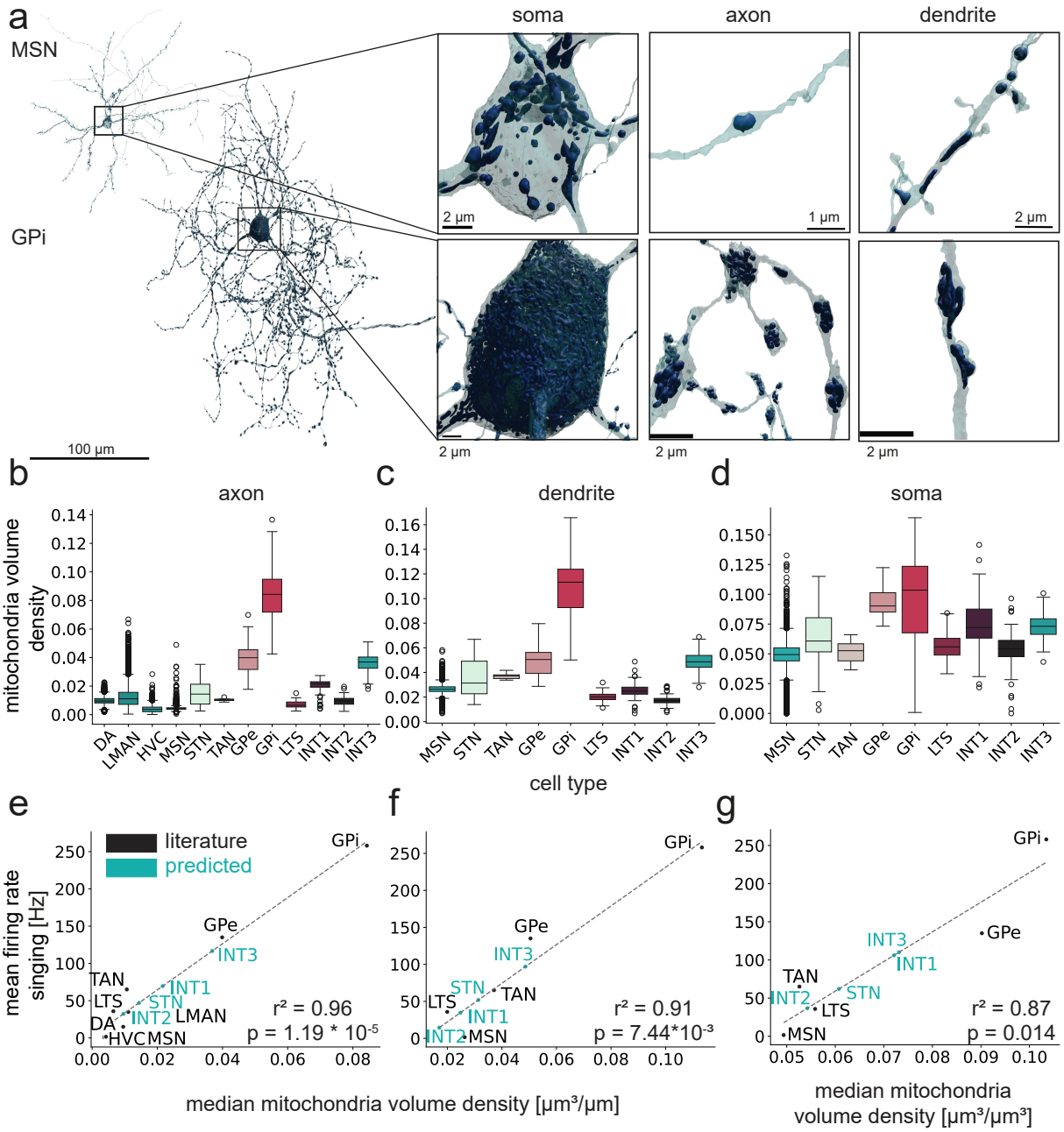

Figure 3.17: Mitochondria volume density in different cell types and compartments. a Renderings of an MSN (ID: 832232717) and a GPi cell (ID: 26790127) with mitochondria rendered on the same scale. The insets show the mitochondria in the soma, axon, and dendrite. b-d Mitochondria volume density in the axon, dendrite, and soma. For the axon and dendrite, the mitochondrial volume is divided by the skeleton path length to calculate the density; for the soma, it is divided by an estimated soma volume. e-g Mean firing rates are predicted from median mitochondrial volume densities using linear regression. Black indicates cell types for which literature values for firing rate were available. Turquoise indicates cell types predicted by the linear regression line (appendix table A22).

parameters differ significantly between cell types, and upon visual inspection, extremes such as MSN and INT3 show striking differences ($p < 0.001$, figure 3.18 b, d, appendix tables A23, A24).

Second, the correlation between the mean firing rate during singing and median vc volume density and vesicle density is analyzed. Both show a significant correlation with the reported firing rates (spearman $r = 0.83$, $p = 0.01$ for both, regression $r = 0.90$, $p < 0.005$; figure 3.18 c, e, appendix table A25). The correlation is no longer significant for mean values, but the linear regression fit remains good (spearman $r = 0.67$, $p = 0.07$ for both, $r = 0.86$ vc, 0.87 vesicles, $p < 0.005$, appendix figure A17, appendix table A25).

Third, the results of the regression analysis are used to predict the firing rates of STN, INT1, INT2, and INT3. Although the correlation with both parameters is high, the ranking order among cell types changes. For example, INT3 has the highest vesicle density, but only the second-highest vc volume density. This leads to different firing rate predictions. The predicted firing rates for the vesicle cloud volume densities are: STN = 35 Hz, INT1 = 107, INT2 = 124 Hz, INT3 = 239 HZ. Predictions from the vesicle density are: STN = 38 Hz, INT1 = 120 HZ, INT2 = 170 Hz, INT3 = 360 Hz (see appendix table A31). Comparing these results to those from the mitochondrial volume density, the STN is predicted to be lower, the predictions for INT1-3 are much higher, and the order of INT1 and INT2 is switched.

In summary, the mean firing rate significantly correlates with both the vc volume density and the axon's vesicle density. However, the order of cell types differs between the two parameters, leading to different firing rate predictions for novel GABAergic interneuron types.

Golgi apparatus density

The GA is involved in protein synthesis and is primarily found in neuronal soma. Since the GA has not been segmented before, its relationship with neuronal firing rate is unknown and will be investigated in this section.

First, differences between cell types were quantified after a visual inspection revealed differences in some cell types. For example, GPi cells have a much larger GA in their large somata than MSN cells have in their small somata (see figure 3.19 a). To determine whether these differences depend on soma size or translate to differences in density, the volume and area density were calculated. Since the GA is layered and has a high surface-to-volume ratio, area density was also calculated, even though segmentation does not show individual GA stacks. Although significant differences exist in both volume and area density, they are not as striking as those observed for mitochondria or vesicles (see figure 3.19 b, d, appendix tables A26, A27).

Secondly, it was tested whether these weak differences were related to different reported firing rates. The results showed non-significant Spearman correlations for volume density ($r = 0.8$, $p = 0.1$) and significant correlations for median area density ($r = 0.9$, $p = 0.04$, appendix table A28). The correlations with the regression fit were much weaker and non-significant (volume: $r = 0.31$, $p = 0.19$, area: $r = 0.37$, $p = 0.17$, figure 3.19 c, e, appendix table A28). Although the regression fit between the parameters is weak, the ranking of the cell types differs. Due to the weak correlations, the predicted firing rates for the STN, INT1, INT2 and INT3 are not discussed further.

Overall, differences in GA volume and soma area density were observed, but only a weak, non-significant correlation was found with the reported firing rates.

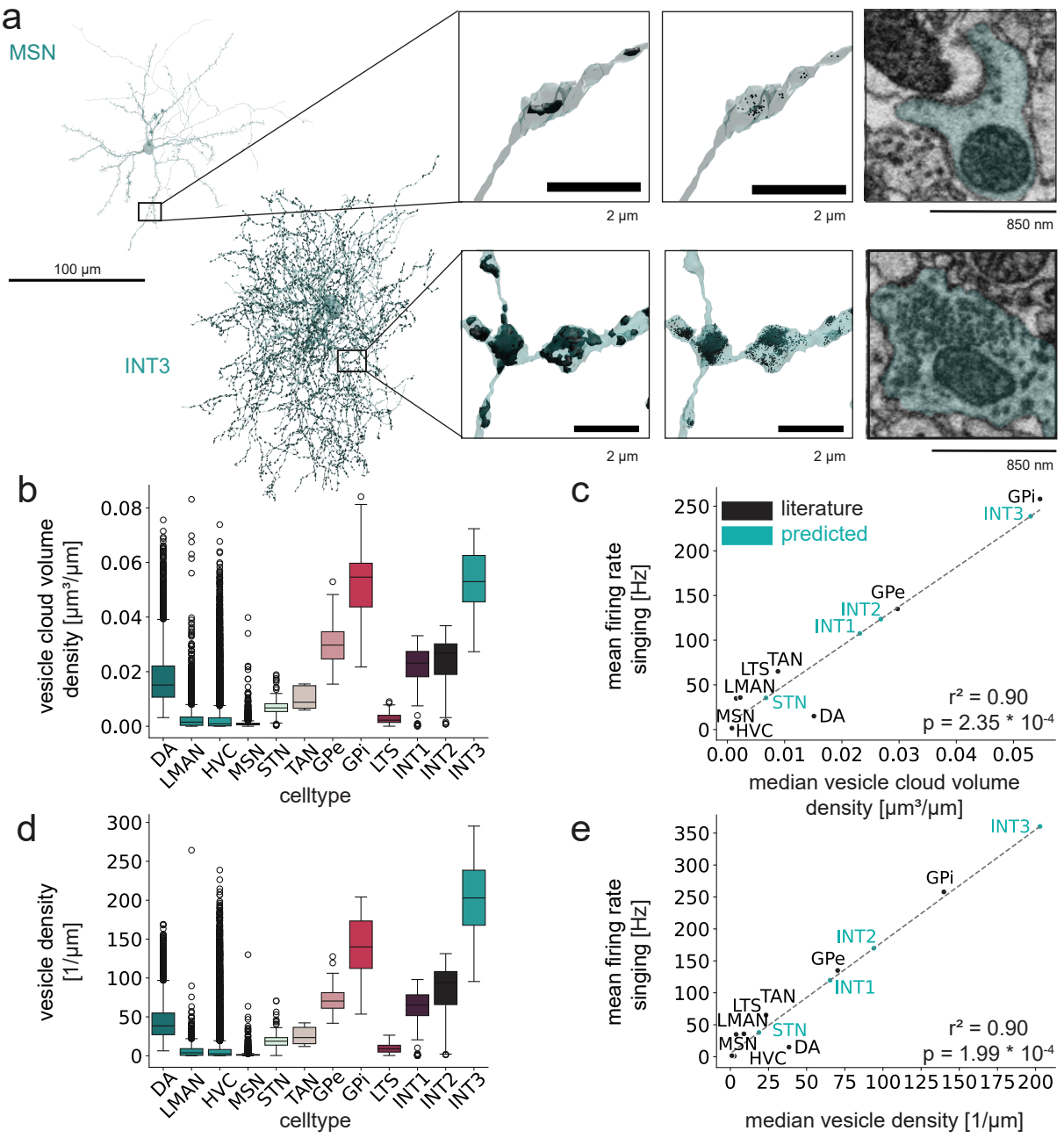

Figure 3.18: Vesicle cloud volume density and vesicle density of different cell types. a Renderings of an MSN (ID: 832232717) and an INT3 cell (ID: 24397945), both on the same scale, with axonal vesicle clouds in black. The insets show an enlarged portion of the axon with a vesicle cloud and individual vesicles, as well as the raw data from the same location (MSN: 13825, 6737, 5382; INT3: 13157, 6715, 4882). All rendered vesicles are spheres with a radius of 20 nm and are only rendered at the specific coordinate. b Axon vesicle cloud volume density in relation to skeleton length. c Mean firing rate singing predicted from the median axon vesicle cloud volume density with linear regression. Black indicates cell types for which literature values for firing rate were available; turquoise indicates cell types predicted by the linear regression line. The regression coefficient = 4393, the intercept = 5.82, the adjusted r-squared = 0.90, and the p-value = 2.35×10^{-4} d Axonal vesicle density in relation to the skeleton length. e Mean firing rate singing predicted from the median axon vesicle cloud volume density with linear regression, similar to (c). Regression coefficient = 1.75, intercept = 5.16, adjusted R-squared = 0.90, p-value = 1.99×10^{-4}. Mean firing rates see appendix table A25.

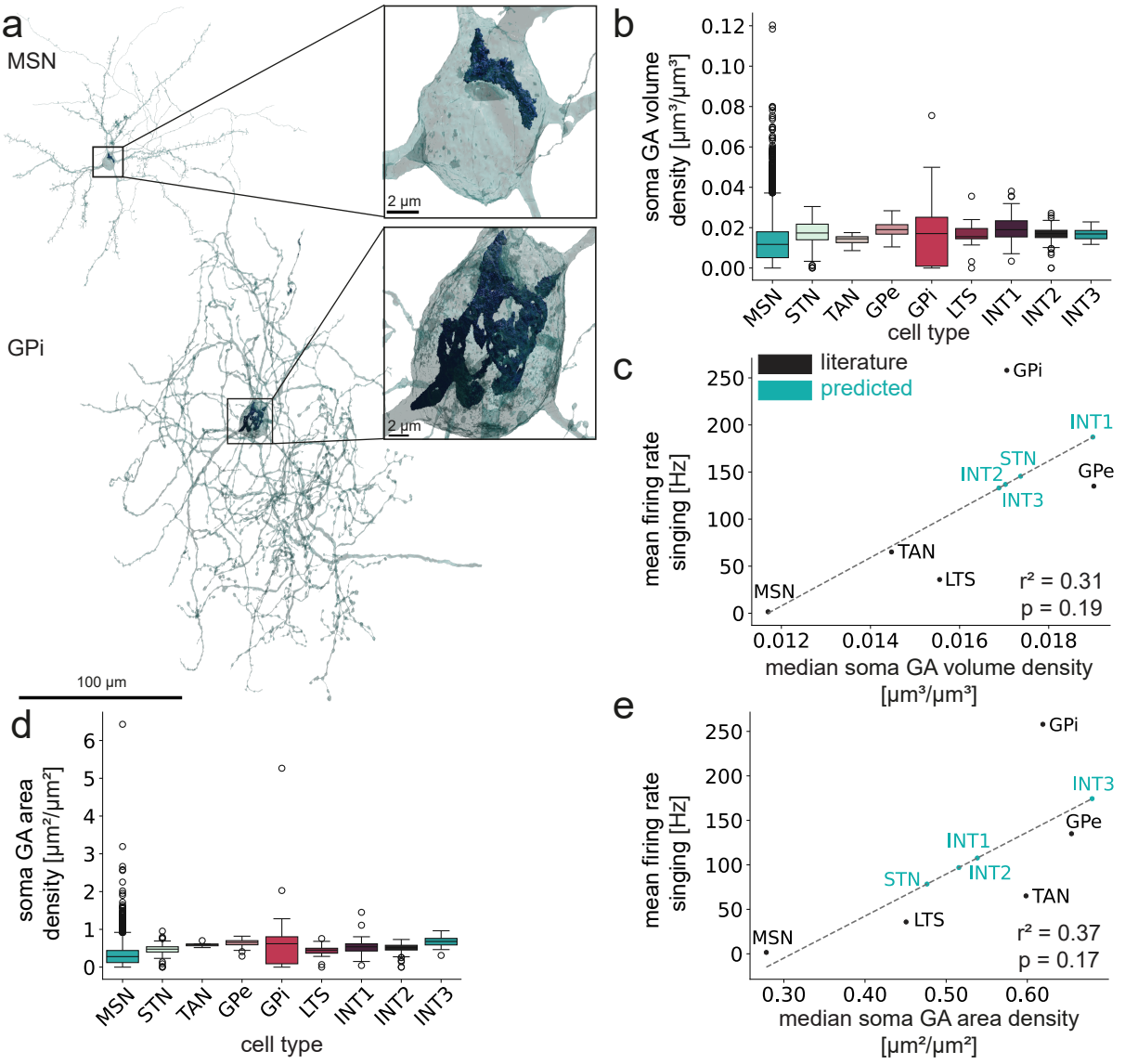

Figure 3.19: GA volume and surface area density in different cell types. a Renderings of an MSN (ID: 832232717) and a GPi cell (ID: 26790127), both on the same scale, with GA. The insets show the GA in the soma. b Soma GA volume density in relation to estimated soma volumes. c Mean firing rate singing predicted from the median soma GA volume density with linear regression. Black indicates cell types for which literature values for firing rate were available; turquoise indicates cell types predicted by the linear regression line. For values see appendix table A22. d Soma GA surface area in relation to soma surface area by ascending order. e Same as (d) with soma GA area density.

Endoplasmic reticulum density

The ER stores calcium and is therefore linked with neuronal activity (Tsuboi et al. 2021). Previously, the ER had not been segmented, so differences between cell types and their correlation with reported firing rates had not been studied in Area X. As in previous sections, first the differences between cell types are quantified and then their correlation with reported firing rates is tested.

Since the ER is organized into sheets that maximize surface area, particularly near synapses and the soma, the area density was analyzed. Due to the ER being processed as one compartment per cell, volume density could not be analyzed additionally (method sections 2.2.3, 2.3.4).

Generally, the cells exhibit a dense network of ER, with portions of the ER extending into thin axon fragments and spines (see figure 3.20 a, large renderings show only the ER). Occasionally, the ER forms sheet-like structures that resemble a classical spine apparatus (example coordinates STN: 11069, 10540, 7056, MSN: 4234, 5348, 3010).

First, differences between cell types were quantified separately for each compartment. In all three compartments, there were significant differences in ER density between cell types (see appendix table A29, see figure 3.20 a-d, appendix figure A19 d, g). GPi cells had the highest surface area in all three compartments, and INT2 cells had one of the lowest surface areas. MSNs have the smallest somata (see figure 3.15 c), so the influence of the nucleus may be proportionally high see the shadow of the nucleus in the ER-free area of the MSN soma in figure 3.20 a).

Second, ER area densities were related to reported firing rates during singing. All three compartments showed correlations with the firing rate. The highest correlation was in the axon ($r = 0.89$, $p < 0.005$), followed by the soma ($r = 0.789$, $p = 0.028$), and then the dendrite ($r = 0.71$, $p = 0.048$, see figure 3.20 e-g, appendix table A30). Note that the dendritic ER area density predicts physiologically impossible negative firing rates for INT1 and INT2 (see appendix table A31). Correlations with mean densities produced similar results for the axon and dendrite ($r = 0.90, 0.76$, $p < 0.005, 0.035$, see appendix figure A19 a, b), but the correlation for soma is lower and not significant (0.68, $p = 0.054$, see appendix figure A19 c, appendix table A30). Note that the axon prediction is also based on the most cell types due to projecting axons.

The results differ when calculating the ER area density in relation to the surface area of the axon and dendrite compartments. In both the axon and the dendrite, MSN has the highest ER densities, followed by GPi (see appendix figure A19 d, g). Thus, the correlations with the firing rate are low and not significant for both the axon and the dendrite ($r = 0.15, -0.15$, $p = 0.2, 0.5$; see appendix figure A19 e, f, appendix table A30). The high density in MSNs could be due to their thinner axons and dendrites, which are more tightly packed with ER than the thicker axons and dendrites of other cell types. This effect is less obvious when relating density to path length only.

Third, the regression results are used to predict the firing rates of the STN, INT1, INT2, and INT3. Since only the axon and soma ER density in relation to path length yielded physiologically possible results with significant correlations, only these are used to predict firing rates. The predicted firing rates range from 32 Hz to 47 Hz for STN, from 62 Hz to 73 Hz for INT1, from 28 Hz to 46 Hz for INT2, and from 115 Hz to 132 Hz for INT3 (see appendix figure A31).

In conclusion, the ER area density differs between cell types and is highly correlated with several compartments, especially the axon area density related to path length.

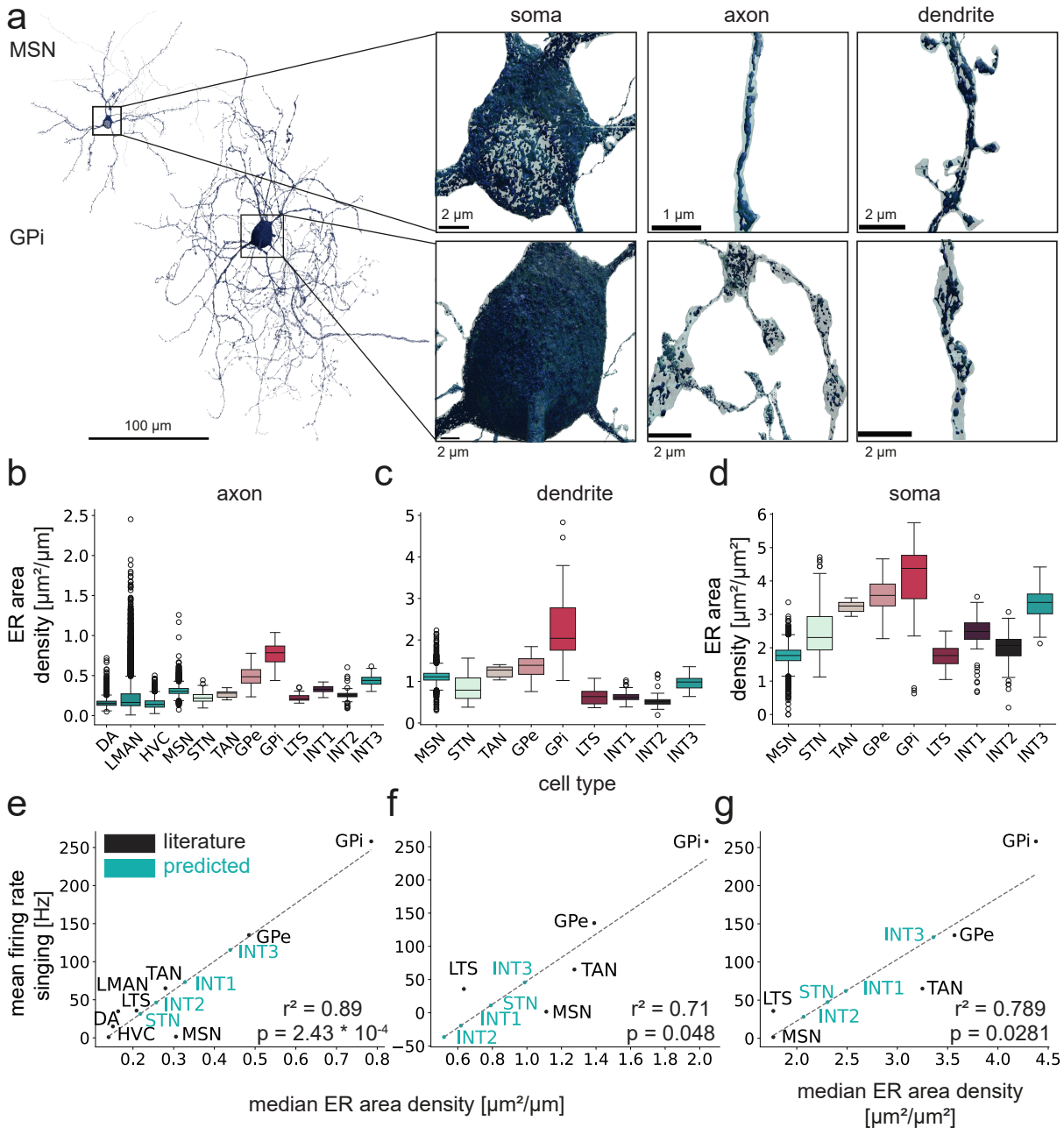

Figure 3.20: ER renderings of an MSN (ID: 832232717) and a GPi cell (ID: 26790127), both on the same scale. The insets show the ER in different compartments. The MSN soma shows an area of lower ER density, which is the nucleus. b, c ER surface area in relation to the corresponding skeleton pathlength in the axon and dendrite, respectively. d ER surface area in relation to soma surface area. e-g Median values from b-d with the corresponding mean firing rate values from the literature. INT1-3 and STN values were predicted with linear regression. The adjusted R-squared value and p-values are shown.

3.3.3 Subcellular structures in relation to cellular morphology

As shown in the previous sections, several organelle densities are related to reported firing rates, and significant differences are observed among cell types. In the SyConn pipeline, organelle information improved cell classification (Dorkenwald et al. 2017, Schubert et al. 2022). To test whether organelle densities can also aid in the separation of cell types, and to determine which parameters are the most useful, an RFC was trained using recursive feature elimination with cross-validation (RFECV; method section 2.3.4).

First, dimensionality reduction was applied to a combined set of organelle densities and morphological features to determine whether organelle densities could enhance cell classification. An UMAP was used to cluster the resulting 22-dimensional feature set, once for all cell types and once for all cell types without MSNs. The results show that most cell types cluster well together (see figure 3.21 a, b, see appendix figure A20 a, b), indicating improved clustering compared to the morphology-only approach (see figure 3.15).

The only cell type that is not well separated is the LTS, which is pooled together with some cells from the STN, INT1, INT2, and GPe. Upon manual inspection, most of the 75 non-LTS cells were potentially misclassified LTS cells (41 cells), followed by potentially misclassified MSNs (12 cells), unclear or cutoff cells (12 cells), and 10 STNs that morphologically did not differ from the rest. For comparison, vesicle density was replaced with volume density, but this did not yield different results (see appendix figure A20 c, d). Using all the parameters for axons, the resulting eight-dimensional feature space was insufficient to distinguish between projecting axon cell types (DA, LMAN, and HVC) in an UMAP (see appendix figure A21).

Since the addition of organelle densities improved the clustering, the next step was to select the most important features for clustering. To do so, an RFC was iteratively trained, leaving one feature out, while the cross-validation score determined whether the feature was selected or discarded (RFECV, method section 2.3.4). Ultimately, this procedure should select the fewest features possible before the cross-validation score decreases. Training was performed once on all cell types in Area X and once without MSNs.

In training with all cell types, nearly all parameters (21, excluding GA density) were required to achieve similar clustering to that with the 22-dimensional feature set (see figure 3.21 c-e, appendix figure A22 a, b). Accuracy of the RFC with all features was 0.991, the cross-validated accuracy with only selected features 0.99 ± 0.00 and the test accuracy with selected features on an RFC split in training and test data 0.992, so all metrics are very similar. To see the influence on the different parameters, the mean accuracy without one parameter was also calculated and did not differ much between the parameters (see appendix table A32).

When this procedure was performed without MSNs, all features were selected (see figure 3.21 f, appendix figure A22 c). The separation of cell types was similar to the UMAP of all parameters and those with MSNs (see figure 3.21 g). Accuracy scores were slightly lower overall: 0.8902 with all features, 0.89 ± 0.04 with selected features, and 0.897 with the test set. Training the RFC without one parameter produced similar performance differences, independent of the parameter (see appendix table A32).

Although a 21- or 22-dimensional feature set is necessary to distinguish eight or nine cell types, differences between specific cell types are visible with a much smaller feature set. As shown in previous sections, the three interneuron types could be separated by a PCA with four parameters (see figure 3.9).

All parameters related to organelle information were selected for classification, apart from GA area density. This demonstrates that organelle information is useful for cell classification.

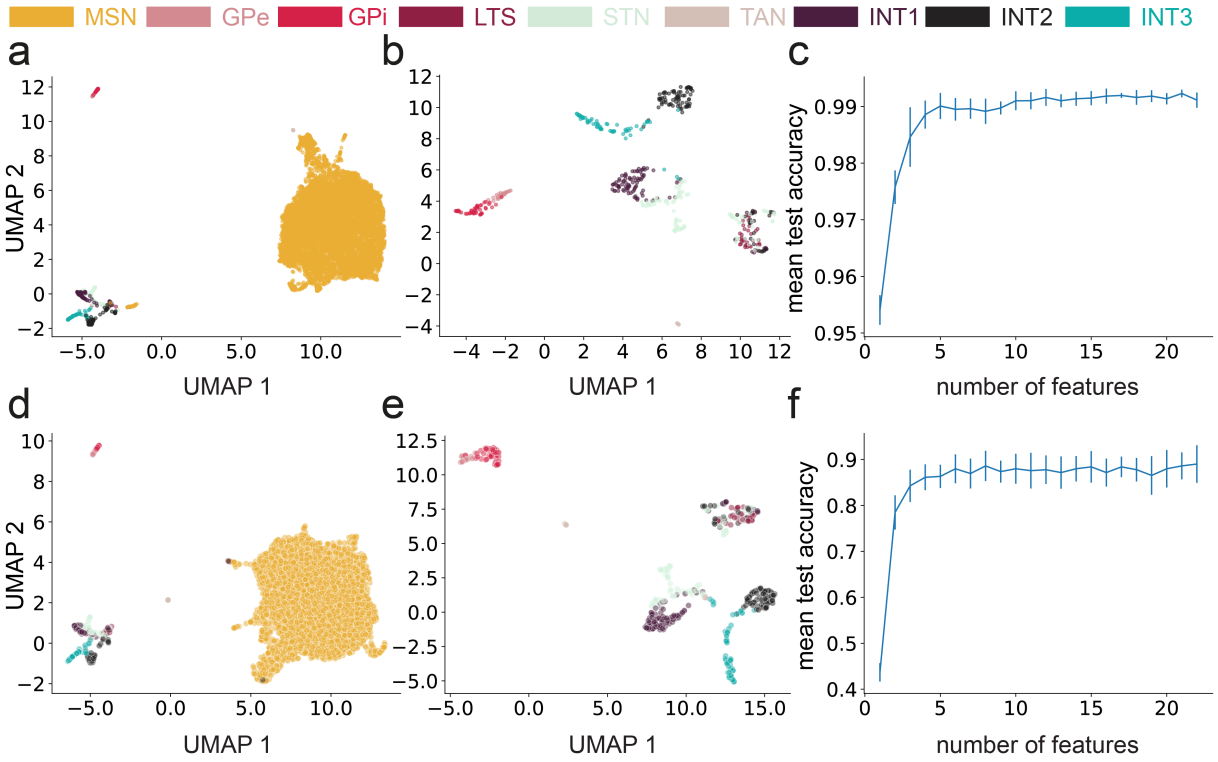

Figure 3.21: Separation of different cell types based on morphological parameters and organelle densities. a Separation of different cell types based on parameters in figure 3.15 and organelle densities, see appendix table A32. b The same as (a), but the separation is done without MSNs. c Mean test accuracy plotted against the number of features for all cell types with RFECV and an RFC. d UMAP clustering based on a 21-dimensional feature vector selected for all cell types. e Same as (d), but UMAP clustering done without MSNs. f Same as (c), but features selected without MSNs. g UMAP clustering on cell types without MSNs based on a 12-dimensional feature vector selected in (f).

3.4 Connectomic analyses of Area X

As shown in the previous section, the nine neuronal cell types and three projecting axons in Area X are morphologically distinct and exhibit unique subcellular properties. The following sections will analyze whether these differences also translate into differences in connectivity.

The connectivity will be analyzed with respect to the following: basal ganglia pathways known in mammals (section 3.4.1), interneuron connectivity (section 3.4.2), and connectivity in the context of motor channels (section 3.4.3).

3.4.1 Basal ganglia pathways in Area X

The three classical basal ganglia pathways in mammals consist of direct, indirect, and hyperdirect pathways. The following sections analyze the connectivity between neurons in Area X in relation to these three pathways, how they are separated, and their relative connective strength.

Separation of GPe and GPi based on morphology

The cell types central to the basal ganglia pathways are MSNs, GPe, GPi, and STN. MSNs differ substantially in number and morphology from the other cell types (section 3.3). STN can be identified by the presence of asymmetric synapses, making it the only glutamatergic cell type in Area X, in addition to connectivity differences.

The aforementioned analyses of morphological features revealed that GPe and GPi are morphologically distinct from each other and from other neuronal cell types in Area X, as demonstrated in a UMAP (section 3.3.3). Due to their central role in basal ganglia pathways and proximity in UMAPs, their different morphologies were examined more closely. Previous studies have only distinguished them based on their electrophysiological properties or their ability to project outside of Area X (Goldberg et al. 2010, Farries et al. 2005).

The results show that GPe and GPi cells can be separated based on a four-dimensional feature set in a PCA with one principal component. These features are axon mitochondrial volume density, axon median radius, axon myelin fraction, and soma diameter (see figure 3.22). The presence of myelinated axons extending beyond the dataset boundaries aligns with the idea that the GPi is the putative projecting neuron type of Area X (see figure 3.22 b, 3.15 d).

In conclusion, GPe and GPi cells differ in morphology, reflecting their functional differences. Thus, they can be separated based on morphology alone.

Direct and indirect pathways at the MSN level

Both the direct and indirect pathways start with cortical innervation of MSNs in the striatum. The two pathways diverge based on their next target: the direct pathway involves direct innervation of the GPi, while the indirect pathway involves initial targeting of the GPe.

To determine whether the direct and indirect pathways exist at the level of MSNs, their input and output connectivity was analyzed. MSNs receive most of their input from HVC (68.2 %), followed by LMAN (15.6 % , see figure 3.23 a, b). Their main output targets are GPi (62.9 %) and GPe (21.1 %). This is consistent with the connectivity of a direct and indirect pathway.

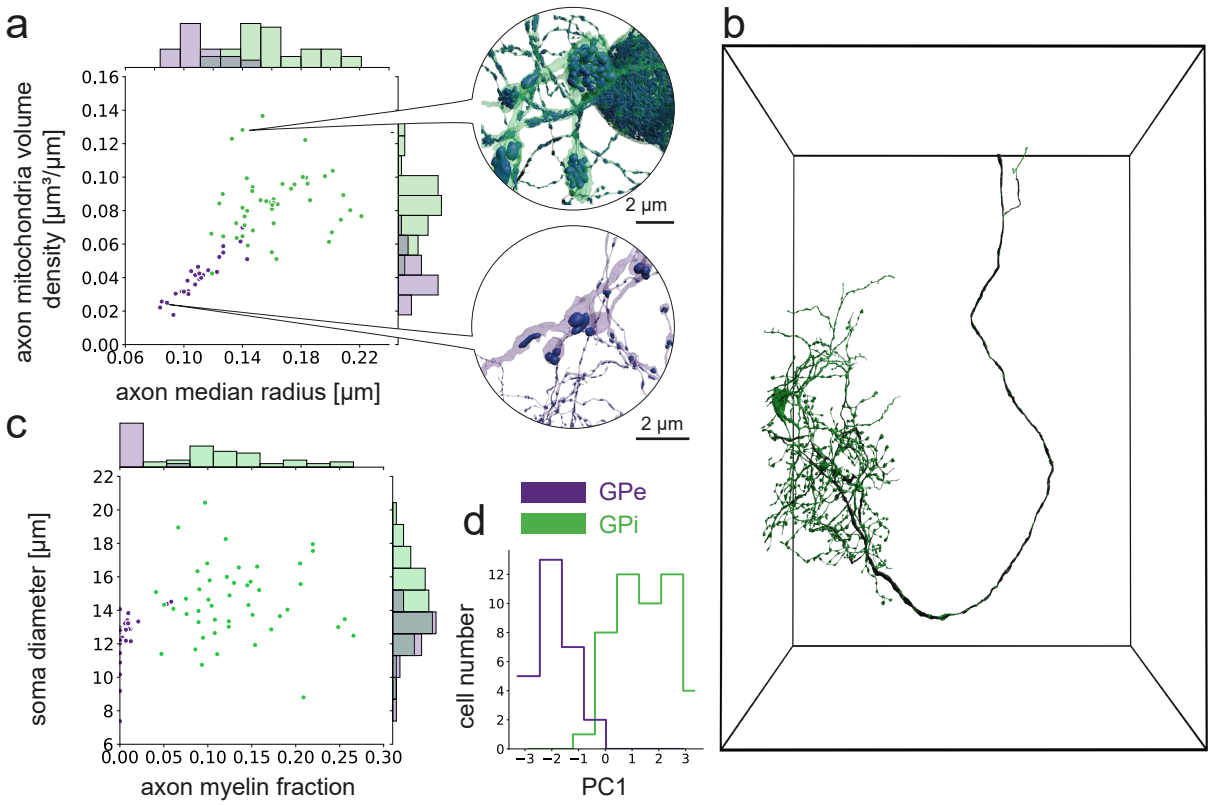

Figure 3.22: Separation of GPe and GPi based on different morpholoical parameters. a The GPe and GPi neurons differ in their axon mitochondrial volume density and axon median radius. GPi ID: 26790127; GPe ID: 32356701 b GPi with a long, myelinated axon going through the dataset. The myelinated parts of the axon are shown in black (ID: 379072583). Dimensions of the dataset: 256 x 256 x 384 µm^3. c Soma diameter and axon myelin fraction of GPe and GPi. d First principal component of PCA based on parameters in a and c.

To distinguish between the direct and indirect pathways, MSN subpopulations in mammals can be differentiated by their dopamine receptors, their output targets (either to the GPe or the GPi, with collaterals to the GPe, Wu et al. 2000), or morphological differences, e.g., spine density and dendritic length (Gagnon et al. 2017, Gertler et al. 2008).

To determine if this data set contains two MSN subpopulations, it was tested whether morphological differences could predict which MSNs project to the GPe and which to the GPi. An UMAP analysis of a 22-dimensional feature set revealed no morphological separation of MSNs (parameters from appendix table A32, see appendix figure A23 a). Focusing on the literature-reported features of spine density and dendritic length revealed differences between MSN cells in these features, which were also weakly correlated (r = 0.31, p-value < 0.001,3.15 e, 3.23 a, c. appendix figure A23). These morphological parameters showed only a weak association with GPe or GPi connectivity (r = 0.14 for spine density, r = -0.1 for dendritic length, p-value < 0.001, see figure 3.23 c. appendix figure A23 c). Insteatd, most MSNs (73.4 %) connected to both the GPe and the GPi, while 21 % connected to the GPi only, and only 3.1 % connected to the GPe only (2.4 % did not connect to either; n = 197)

When the analyses were performed again with only the MSNs whose dendrites were not cut off (3,052 cells, method section 2.3.1), the correlations of the morphological features with each other and with connectivity were weak (r = -0.24 to 0.15, p < 0.001, see appendix figure A23 d-f). The group of MSNs that connect only to the GPe was also smaller, with only 0.78 % (24 cells, to both GP = 80.3 %, only GPi = 18.2 %, neither = 0.69 %).

Additionally, MSNs that only connected to the GPe had shorter axons and dendrites, as well as a soma that was closer to the dataset border, compared to MSNs that connected only to the GPi or to both the GPe and the GPi (all p < 0.001, except for MSN no GPe vs MSN only GPe: p = 0.027, see appendix figure A23 g-i, appendix table A33). These results suggest that the observation of MSNs connecting only to GPe neurons may be due to reconstruction fragmentation or dataset boundaries.

In summary, most MSNs connect to both the GPe and the GPi, indicating that there is no clear separation between the direct and indirect pathways at the MSN level. A total of 94.4 % of MSN cells connect to the GPi. Therefore, the direct pathway has the strongest connectivity through Area X.

To determine whether there are differences in MSN connectivity to the GPe and GPi at the level of individual cells and synapses, synapse sizes and the number of multi-synaptic connections were analyzed. Multi-synapses refer to multiple synapses between the same presynaptic and postsynaptic cells. MSN-GPi synapses are larger, and there is a greater tendency to form multi-synaptic connections with GPis. This results in MSN-GPi connections with larger total synaptic areas compared to MSN-GPe connections (p < 0.001, see figure 3.23 d-f, appendix table A33). These results demonstrate that MSN-GPi connectivity is significantly stronger than MSN-GPe connectivity.

Although there is a lack of evidence for distinct MSN populations, these connectivity differences could be accompanied by MSN selectivity for targeting the GPi or GPe. To test this theory, the ratio of GPi to GPe synaptic area was calculated for each MSN cell, and the synapses were shuffled among the cells. Among the observed ratios, 35.61 % of MSN cells exhibited high selectivity for GPi outputs (GP ratio > 0.9). After shuffling the data over 100 iterations, only $17.57 \pm 0.35\%$ of MSNs randomly exhibited the same degree of selectivity (see figure 3.23 g, methods section 2.3.5). While the shuffled data shows a peak in the GPi/GPe ratio at 75 % (the observed ratio), the observed data leans more toward the GPi. This indicates that some MSN cells are selective for GPi.

MSNs generally form few synapses with GP cells (3.54 ± 5.4 to GPe, 9.55 ± 7.2 to GPi), which increases the likelihood of selective MSN cells. Indeed, a small population has a high number of synapses and a GP ratio close to 0.6 (> 40 synapses, appendix figure A24). However, most MSNs form fewer synapses,

and some MSN cells connect only to the GPi with up to 40 synapses per cell. This again shows that there is some level of selectivity to the GPi.

In summary, MSNs receive input from the HVC and LMAN and connect to GPe and GPi cells. This indicates the presence of direct and indirect pathways at the MSN level. Neither morphology nor connectivity revealed distinct subpopulations for direct or indirect pathway MSNs. Since the connectivity to the GPi is stronger than to the GPe in the entire MSN population, these results demonstrate a strong direct pathway through Area X (see figure 3.23 h).

'Short' indirect pathway between GPe and GPi

In mammals, the indirect pathway from GPe can take two routes: the "short" indirect pathway, in which GPe connects directly to GPi, or the "long" indirect pathway, in which GPe connects to STN, which then targets GPi (Shipp 2017).

First, connectivity via the "short" indirect pathway is analyzed. On average, the GPi receives three times more synaptic area from the GPe ($7.93 \pm 10.6 \mu m^2$, n = 40 GPi cells) than the GPe receives from the GPi ($2.12 \pm 1.62 \mu m^2$, n = 23 GPe cells, see figure 3.24 a-e). With similarly sized synapses ($p = 0.13$), this innervation pattern results from a greater number of multisynaptic connections from the GPe to the GPi than vice versa ($p < 0.001$, see figure 3.24 e, d, appendix table A34). Thus, there is evidence for a "short" indirect pathway.

However, in the context of general GPe and GPi connectivity, this pathway is weak. GPe cells project only 7.5 % of their outgoing synaptic area to GPi cells, and only 0.8 % of the GPi's synaptic input comes from the GPe (see figure 3.24 f,g). This small GPe input could take the form of particularly effective somatic synapses. However, only a small percentage of GPi neurons receive somatic GPe input (13/47 neurons, 28 %).

In summary, connectivity exists in the direction of the "short" indirect pathway, but it is weak. This pathway is neither a primary output target for GPe nor a primary source of input for GPi.

With the focus on the incoming and outgoing synaptic areas of the GPe and GPi, three other noteworthy results emerged.

First, both GPe and GPi cells receive a significant portion of their input from HVC. The range is from 28.7 % to 54.7 % for GPe and from 20.5 % to 46.1 % for GPi, depending on the filtering criteria (method section 2.3.1, appendix figure A28). This makes the HVC the second-largest source of input after the MSNs.

Second, GPi cells send the largest fraction of their outgoing synaptic area to STN cells (31.4 %), which will be discussed further in the following section 3.4.1 and their second largest fraction to other GPi cells (25.5 %). Other GPi neurons also constitute of 6.9 % of the incoming synaptic area to GPi cells. This level of interconnectivity between cells of the same cell type is not observed in GPe cells. When comparing these intra-GPi synapses to intra-GPe synapses, intra-GPi synapses are larger than intra-GPe synapses, establish more multisynaptic connections, and have a larger summed synaptic area per cell pair ($p < 0.001$, see appendix figure A25, appendix table A34). The summed synaptic area per cell pair is also larger in GPi-GPi synapses than in GPe-GPi synapses due to the former's higher number of multisynaptic connections ($p < 0.001$, appendix table A34). These results demonstrate the importance of a GPi-GPi network, which will be further explored in 3.4.3.

Third, GPe cells primarily target INT2 and INT3, two of the novel GABAergic interneuron types, accounting for 67.7 % of outgoing synaptic area together. Their connectivity will be discussed in detail later (section 3.4.2).

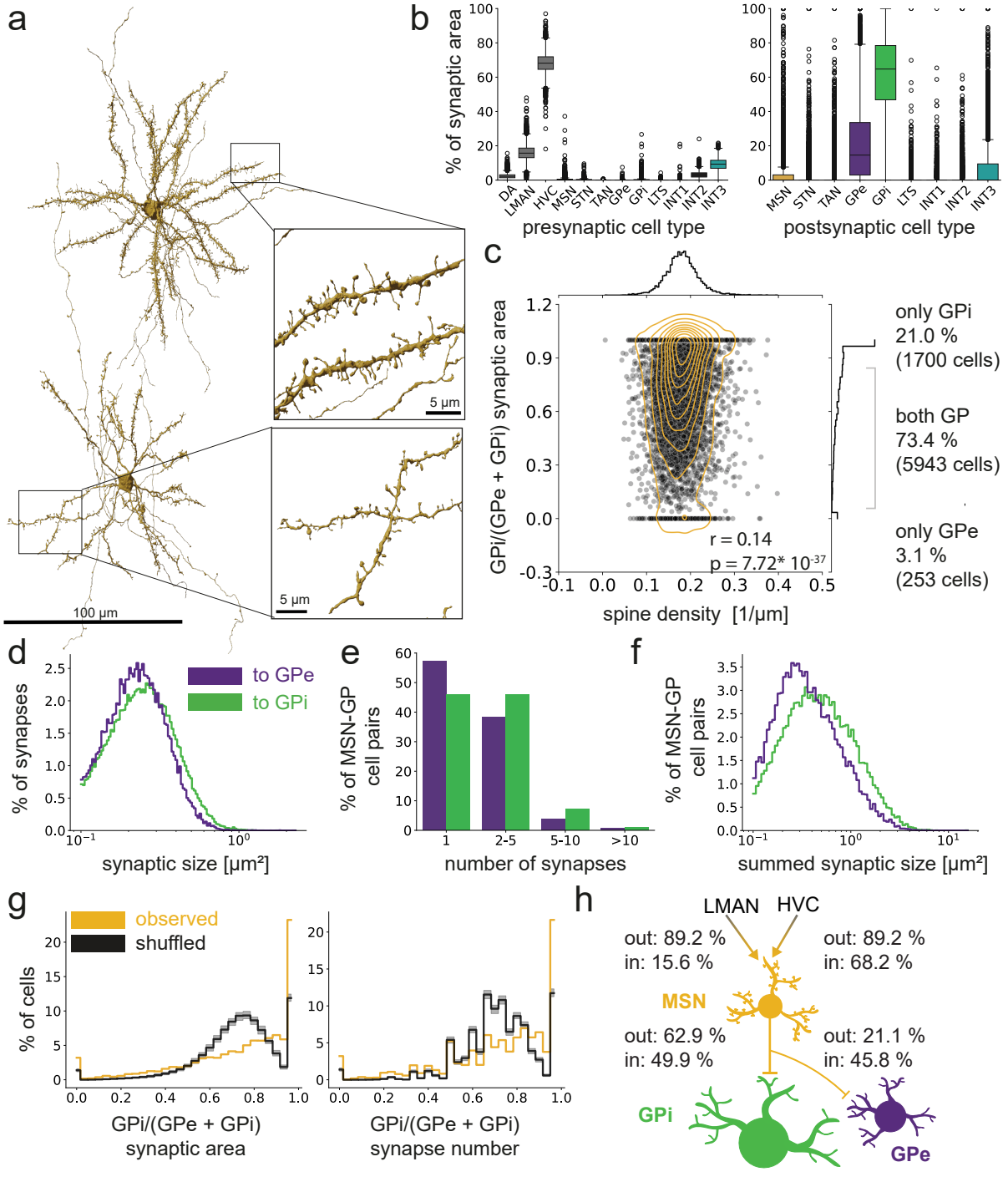

Figure 3.23: Identification of the direct and indirect pathways at the level of MSNs. a Two examples of MSNs with different spine densities on their dendrites (IDs: 662789385, 542544908). b Incoming and outgoing connectivity to and from MSNs. cMorphological parameters, such as spine density, only weakly correlate with the connectivity of MSNs to the GPe or GPi. MSNs that did not project to either the GPe or the GPi were excluded (2.4 % , n = 197). d MSNs connect to the GPi through slightly larger synapses, e, with more parallel synapses, and f, larger total synaptic area per pre-post neuronal connection. g The GPi preference of the MSNs is plotted against the shuffled synapses. The black curve shows the mean over 100 iterations and the gray curve shows the 95 % confidence interval. h Schematic representation of the direct pathway, with the synaptic area between the shown cell types normalized to their corresponding incoming and outgoing synaptic areas (see figure 3.31 a, b)

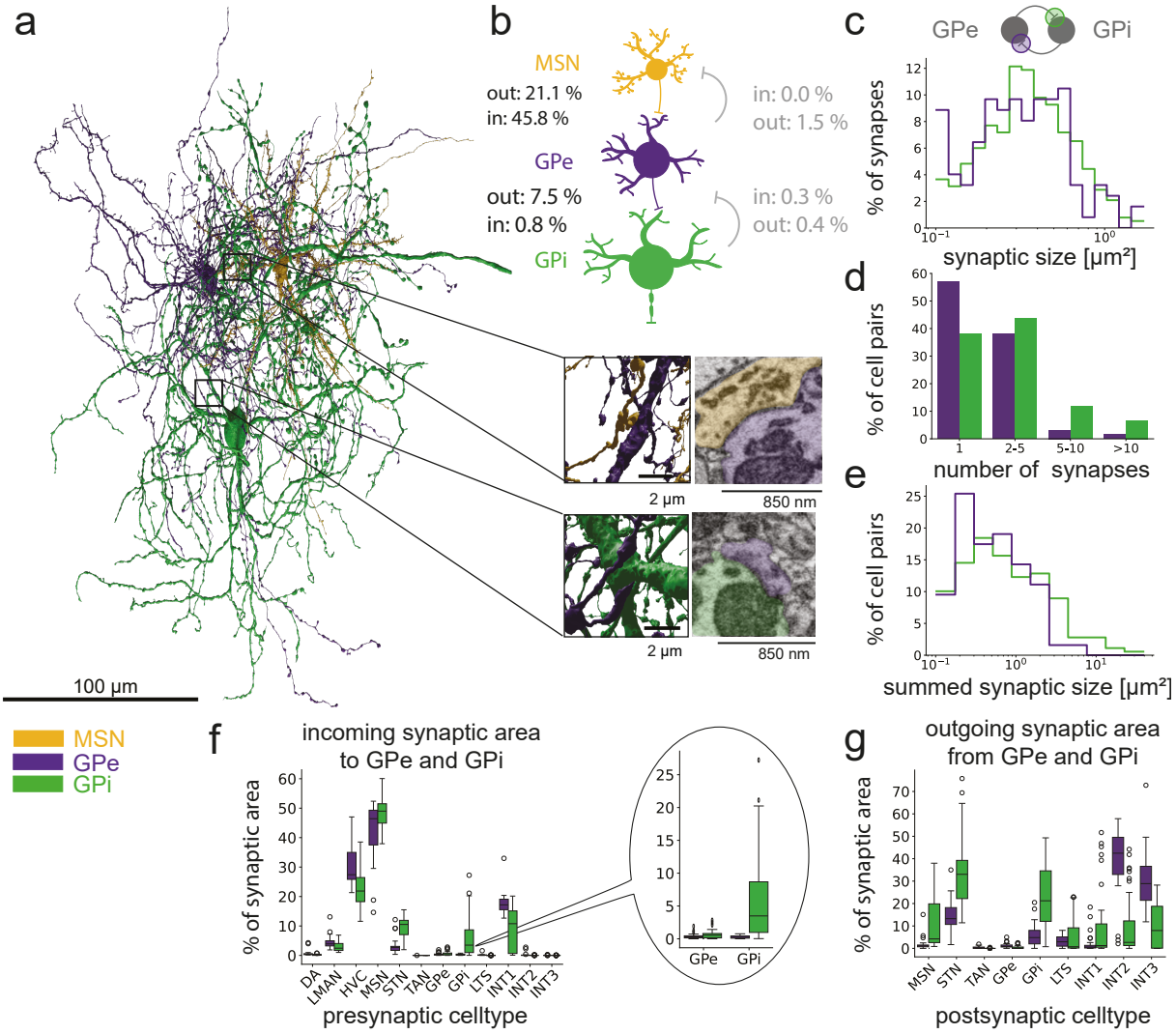

Figure 3.24: Indirect pathway at the level of pallidal cells. a Renderings of exemplary indirect pathway neurons starting at the MSN level (MSN ID: 27161078; GPe ID: 32356701; GPi ID: 26790127). The insets show an MSN-GPe synapse (top:12139, 10877, 3292) and a GPe-GPi synapse (bottom: 13502, 17089, 6174). b Schematic representation of the indirect pathway starting at the MSN level, showing the summed synaptic area in relation to the synapses in the dataset (see figure 3.31 a, b). Backward connectivity is shown in gray. c-e Comparison of the synaptic areas of individual synapses and multisynaptic connections from GPe to GPi cells (and vice versa). f,g Incoming and outgoing synaptic connectivity of GPe and GPi cells. The inset shows the incoming synaptic area to the GPe and GPi cells.

'Long' indirect and hyperdirect pathways with STN

After analyzing the "short" indirect pathway, the "long" indirect pathway is now analyzed. In this pathway, GPe does not make direct connections with GPi cells. Instead, GPe connects with STN, which then projects to GPi.

First, the connectivity from the GPe to the STN is analyzed. STN is the third-highest output target of GPe (16.8 %, see figure 3.24 g, 3.25 b), but GPe is not one of STN's major input sources (6.9 % of incoming synaptic area). STN cells' largest output target is GPi cells (64.9 %), which receive 9.8 % of their incoming synaptic area from STN. This connectivity demonstrates that the "long" indirect pathway exists in Area X.

Synaptic projections from STN to GPi cells are also part of the hyperdirect pathway, which begins with cortical input to the STN. STN neurons receive most of their input from LMAN and HVC (37 % in total, see figure 3.25 a, b, d). This demonstrates that the hyperdirect pathway also exists in Area X.

In summary, results show the existence of a direct, indirect, and hyperdirect pathway in Area X.

In addition to input from HVC and LMAN, STN cells receive a major fraction of their incoming synaptic area from GPi (34.2 %). As previously mentioned, the STN is the primary output target of the GPi (31.4 %). However, this projection from GPi to STN is not part of the classical basal ganglia pathways.

Since STN cells project to and receive synapses from both GPe and GPi, these connections are examined in more detail. While all GPe and GPi cells receive input from and project to STN, only 82 % of STN cells project to either the GPe, the GPi, or both (see appendix table A35). Those that do not project to either the GPe or the GPi mainly project to INT3 and STN cells (see appendix figure A26). Since the analysis focuses on the connectivity between "complete" cells in Area X (method section 2.3.1), and since individual dendrites that are not connected to any soma constitute a large fraction of the dendritic pathlength in Area X (see appendix table A1), this population could be a dataset artifact.

When comparing the connections from and to STN with those from and to GPe and GPi, the connections from and to GPi consist of larger individual synapses and more multisynaptic connections. Thus, the summed synaptic area per cell pair for STN-GPi connections is larger than for STN-GPe connections, and vice versa ($p < 0.01$, see figure 3.25, appendix table A36).

In summary, these results demonstrate that STN-GPi connectivity is stronger than STN-GPe connectivity. Along with the stronger innervation of STN cells by LMAN and HVC than GPe, it demonstrates that the hyperdirect pathway is stronger than the "short" and "long" versions of the indirect pathway. Thus, the hyperdirect pathway is the strongest antagonist of the direct pathway in Area X in terms of connectivity.

Reciprocal connectivity of STN with GPe and GPi

The previous paragraph analyzed the reciprocal connections of STN with GPe and GPi cells in terms of differences in connectivity. However, these connections can also be analyzed with regard to their focus on cell-specific recurrent loops. From a functional perspective, network dynamics may differ depending on whether cell pairs are coupled through recurrent connections or only exist at the population level, e.g., when one STN projects to a few GPi cells and receives input from completely different cells.

First, it was determined whether a cell had the same cell as its strongest input and output partner. In other words, it was determined whether the largest sum of synaptic area came from the same cell to which the largest sum of synaptic area was projected. This binary measure is called "strongest partner

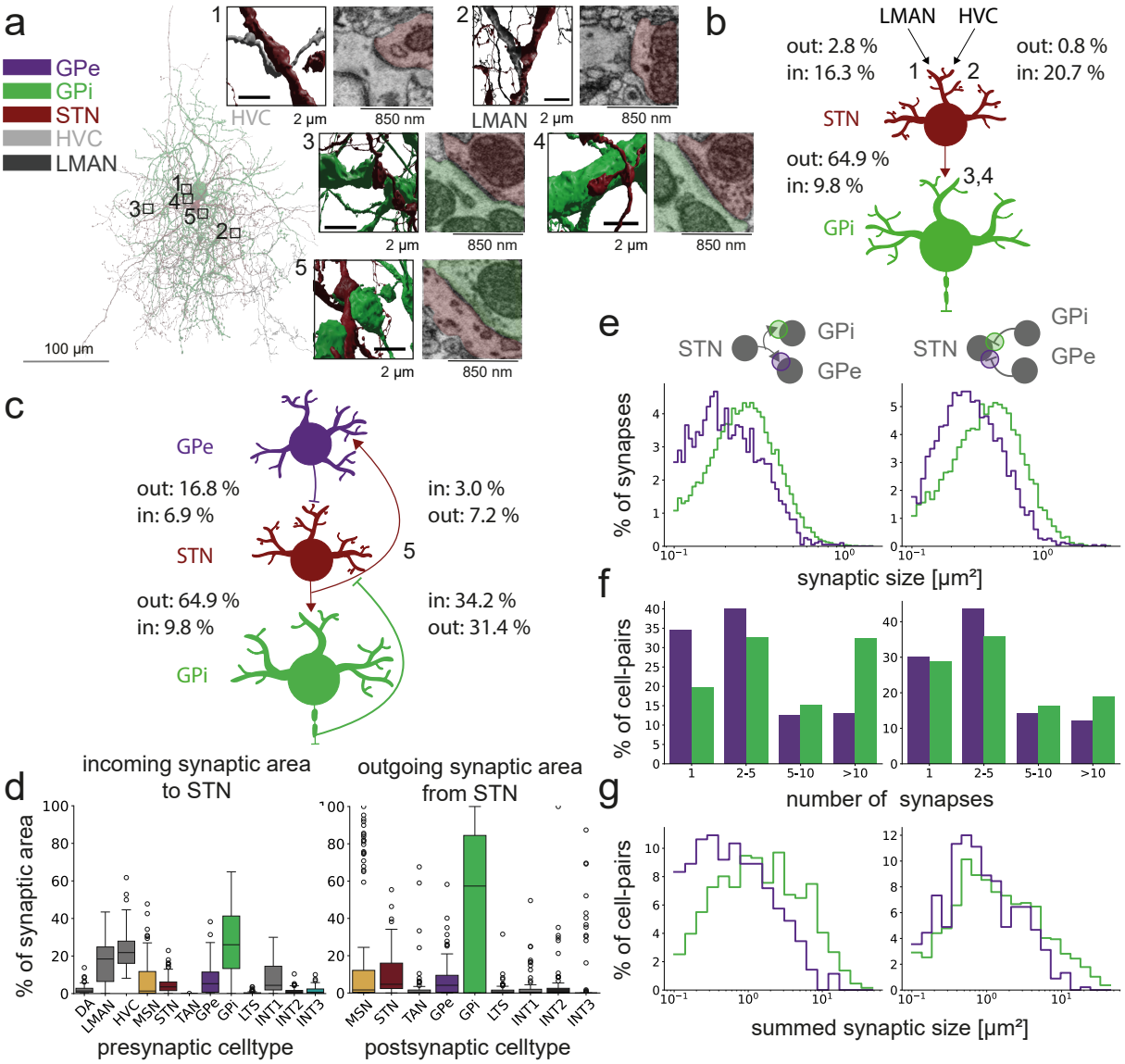

Figure 3.25: The hyperdirect pathway with STN cells. a Reconstruction of neurons in the hyperdirect pathway: HVC ID: 975932938, LMAN ID: 18222490, STN ID: 7626258, GPi ID: 26790127. Insets 1-4 show asymmetric synapses and inset 5 shows symmetric synapses. Location of insets: 1: HVC to STN synapses: 13018, 8939,7226; 2. LMAN to STN synapse: 16088, 14773, 4515; 3, 4: STN to GPi synapses: 7889, 8920, 6373; 11284, 13200, 69875; 5. GPi to STN synapse: 14381, 9867, 6235 b Schematic representation of the hyperdirect pathway with summed synaptic area in relation to the corresponding incoming and outgoing synaptic area per cell type (see figure 3.31 a, b). c Schematic representation of the long indirect pathway starting at GPe with summed synaptic area in relation to the corresponding incoming and outgoing synaptic area per cell type (see figure 3.31 a, b). a Also shows the connectivity from GPi to STN to GPe. The numbers in (b) and (c) refer to the synapses shown as insets in (a). d Cell-type-level characterization of the incoming and outgoing synaptic areas to and from STN-like neurons. e-g Comparison of the synaptic areas, numbers, and summed synaptic areas of the connections from and to the SN by the GPe and GPi.

reciprocity". For the STN-GPe connections, this exists in 18.6 % of STN neurons and 18.5 % of GPe neurons. For STN-GPi connections, this exists in 14.1 % and 19.1 %, respectively (see figure 3.26 a, b, appendix table A37).

Second, the overlap of the synaptic area from the same cell bodies on the input and output sides was determined. The fraction of synaptic area from cellids to which the cell also projects was calculated as a fraction of the total synaptic area (method section 2.3.5). For STN-GPi connections, the majority of cells have a large overlap (median: STN in 90.5 %; out 62.2 %; GPi in 75 %, out 77.9 %, see figure 3.26 c, d). In STN-GPe connections, over a quarter of STN cells have little overlap (see figure 3.26 e). In contrast, GPe cells have a higher overlap (in 81.8 %; out 49.4 %, see figure 3.26 f).

In summary, local feedback is partially conveyed via recurrent connections of individual cells in both STN-GPe and STN-GPi connections.

3.4.2 Interneuron connectivity

In addition to the cell types involved in basal ganglia pathways, five interneuron types were identified in the data. These include three novel GABAergic interneurons that morphologically resemble the "FS" type (INT1-3, section 3.1.2), as well as GABAergic LTS and cholinergic TAN.

Novel FS-like Interneurons

INT1, INT2, and INT3 were initially identified by their "FS"-like morphology, but they could be further classified into three distinct cell types (section 3.1.2). To test whether their morphological differences are accompanied by differences in connectivity, their incoming and outgoing synaptic areas were analyzed.

The three cell types differ in their incoming connectivity. INT1 cells receive the highest input fractions from LMAN (25.4 %) and other INT1 cells (22.8 %), while INT2 cells receive the highest input fraction from HVC (31.9 %), followed by GPe (23.0 %). INT3 cells receive the majority of input from HVC (59.4 %; see figure 3.27). INT2 and INT3 are also the primary output targets of GPe at 40.8 % and 26.9 %, respectively (section 3.4.1, see figure 3.24 g). The high fractional input numbers for INT2 and the high fractional output from GPe show the relative influence of this connection on both sides.

There are also differences in their output targets. While INT1 primarily targets the GPe and GPi (29.2 % and 41.2 %, respectively), INT2 and INT3 predominantly project to the MSN (92 % and 93.7 % respectively; see figure 3.27).

These results demonstrate that the three FS-like interneuron types differ in both morphology and connectivity. Their connectivity profiles suggest strong interactions with neurons from the basal ganglia pathways: GPe, GPi, and MSN.

LTS neurons

LTS neurons exhibit long, sparse arborization of dendrites and axons (Farries et al. 2002, 3.28 a, b, see table 2.6). They receive the highest input fraction (29.6 %) from the GPi and project mostly to MSN neurons (68.1 %, see figure 3.28 c).

Thus, the LTS connectivity differs from any of the cell types previously described and could demonstrate a GPi-LTS-MSN feedback loop.

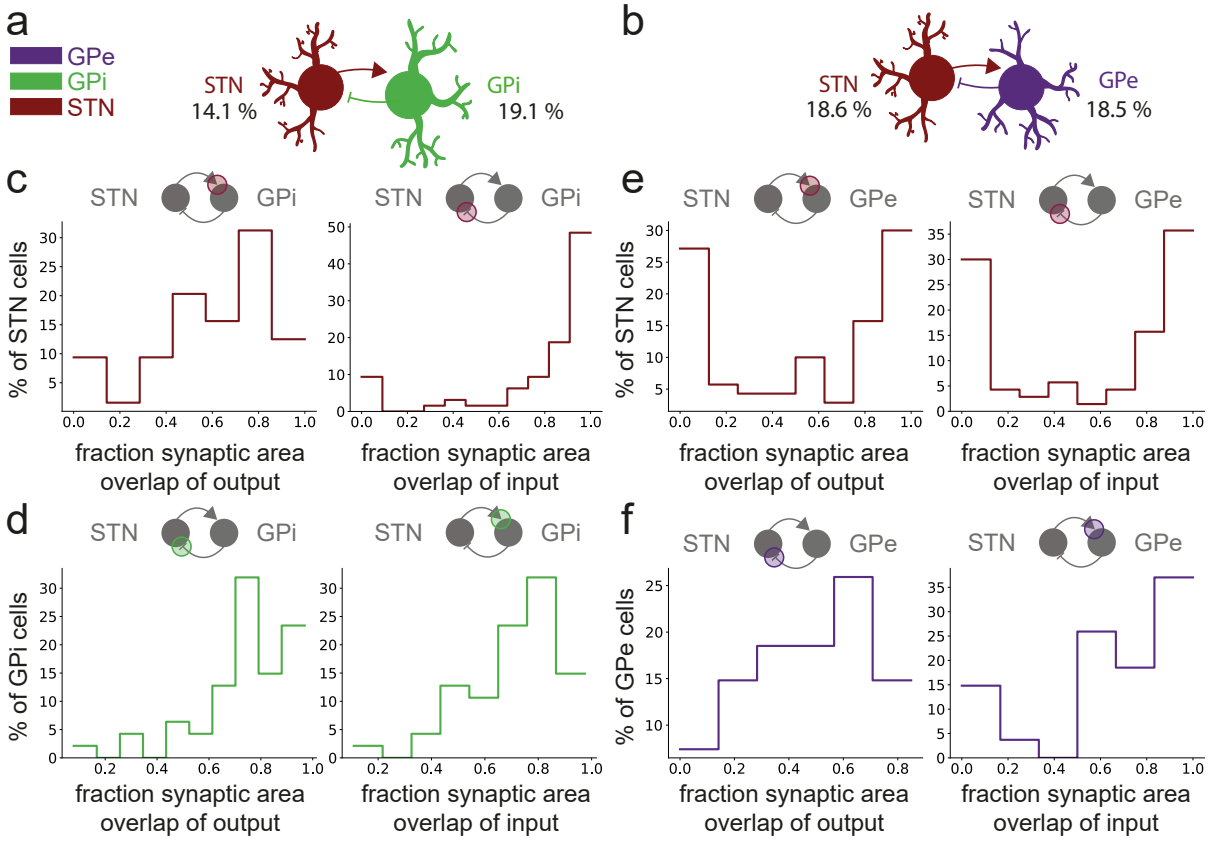

Figure 3.26: Cell-specific recurrency between STN, GPe, and GPi. a Fraction of STN and GPi cells that have their largest synaptic input area coming from the cell to which their largest synaptic outgoing area is directed, in specific connections. bSame as (a), but for STN and GPe cells. c -f Fraction of synaptic area from cells that are both inputs and outputs, calculated in comparison to the total summed synaptic area for all cells that are potential targets for recurrent connections, either incoming or outgoing. The results are also summarized in appendix table A37.

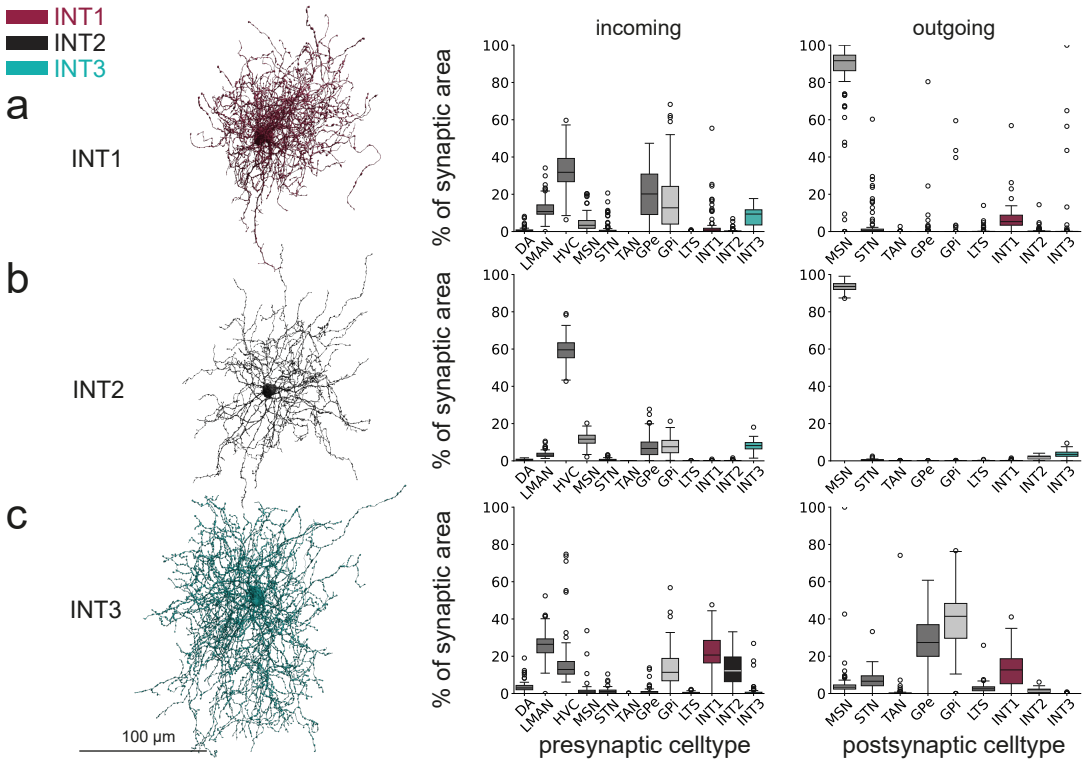

Figure 3.27: Connectomic analysis of GABAergic interneurons INT1-3. Renderings of three example cells: INT1 (ID: 1080627023), INT2 (ID: 126798179), and INT3 (ID: 24397945). The incoming and outgoing synaptic areas for INT1 (a), INT2 (b), and INT3 (c).

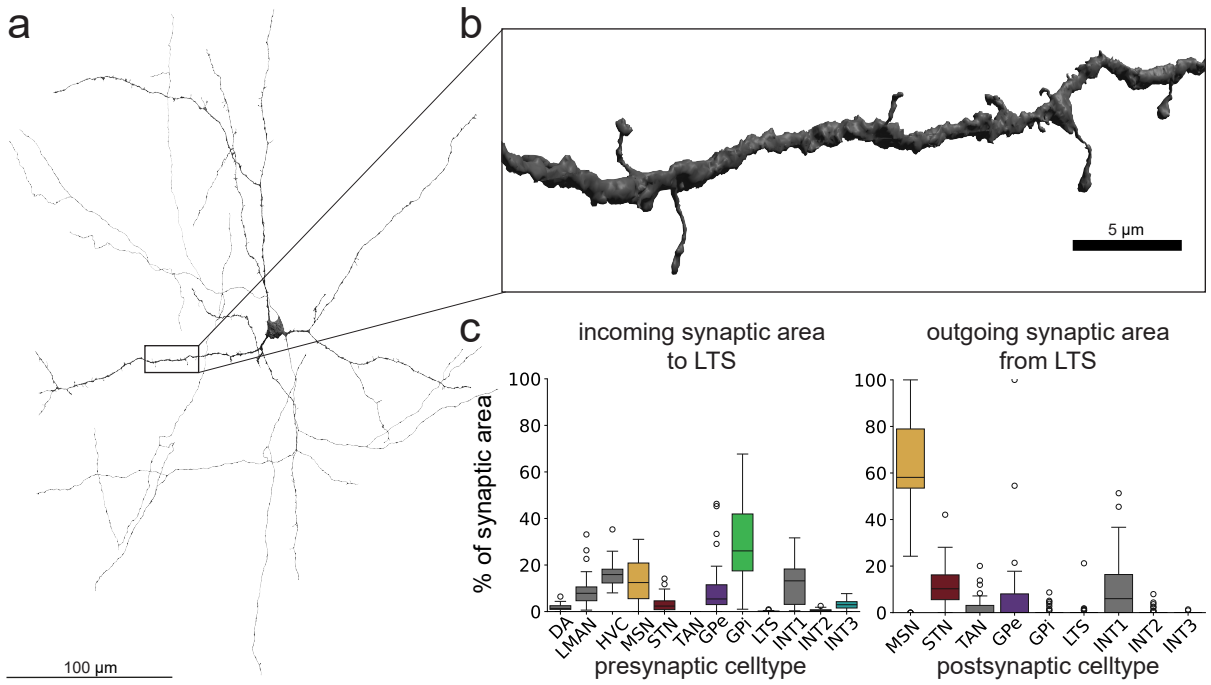

Figure 3.28: Connectivity of LTS. a Rendering of an example LTS cell (ID: 15521116). b Sparsely spiny dendrites of the LTS cell. c Incoming and outgoing synaptic areas of LTS cells.

Cholinergic interneurons

Cholinergic interneurons (TANs) are described as having large somata and sparsely spiny dendrites (Farries et al. 2002; see table 2.6), but this dataset shows that they have spines and spiny somata (see figure 3.15, 3.29 a, b).

They receive synaptic input almost exclusively from MSN (46.3 %) and HVC (36.8%), and they almost exclusively target MSN (96.2 %; see figure 3.29 c). Due to their large size, only eight TANs fulfilled the filtering criteria and were included in the dataset, which could partially explain the focused connectivity profile.

The connectivity with MSN as the strongest input and output could potentially be facilitated by recurrent connections at the level of individual cells, similar to STN-GPe or STN-GPi. To test this theory, strongest partner reciprocity and overlap of the same cell IDs on the input and output sides were calculates (method section 2.3.5). While all eight TAN cells receive input from MSN and project to MSN, only 29 MSN cells ($< 0.5\%$) project to TAN cells and receive input from them (see appendix table A37). Even with this small subset of MSN cells, only 27.6 % of MSN cells and no TAN cells showed the strongest partner reciprocity.

When analyzing the overlap of synaptic areas between the same incoming and outgoing cells, MSN cells have little synaptic overlap. About a fifth of these MSN cells seem to synapse exclusively with one TAN cell and receive synapses exclusively from that same TAN cell (see figure 3.29 e). For TANs, synaptic area overlap is generally very small, especially compared to the total synaptic area of output (up to 0.02 %, see figure 3.29 f). This is because TANs receive input from many more MSN cells (median: 236.5) than they project to (median: 18.5, see appendix table A37).

In conclusion, TANs receive input from a large number of MSN cells, which converge onto a smaller number of different cells. This distributes synapses among the MSN population rather than forming recurrent loops.

Basal ganglia pathways overview

Overall, the results show that the dataset contains nine morphologically distinct neuronal cell types that differ in connectivity. Analysis shows that the three basal ganglia pathways—the direct, indirect, and hyperdirect pathways—exist. When comparing synaptic areas, the strongest pathway is the direct pathway, followed by the indirect and hyperdirect pathways. The indirect pathway has little synaptic connectivity (see figure 3.30 a).

The three newly discovered FS-like GABAergic interneuron types are innervated differently from LMAN and HVC, and they interact with different cell types from basal ganglia pathways (see figure 3.30 b). These differences demonstrate three distinct connectivity patterns for each cell type. INT1 cells receive the largest fraction of their input from LMAN. They project to the GPe and GPi, forming a connectivity pattern that resembles potential feed-forward inhibition from LMAN. INT2 cells receive input mainly from HVC and GPe, and project to MSN. The MSN-GPe projection gives rise to an MSN-GPe-INT2 feedback loop. INT3 cells receive most of their synaptic input from HVC and project mainly to MSN. This resembles a feedforward inhibition from HVC onto MSNs.

The dataset's resolution allows not only the analysis of connectivity between cells and cell types, but also their target selectivity. MSNs have the highest number of dendritic spines and are the only cell type that receives a majority of input from one of their inputs, HVC, onto spine heads (see appendix figure A27 a). This is similar to previous observations of connectivity to MSNs (Kornfeld et al. 2020). However,

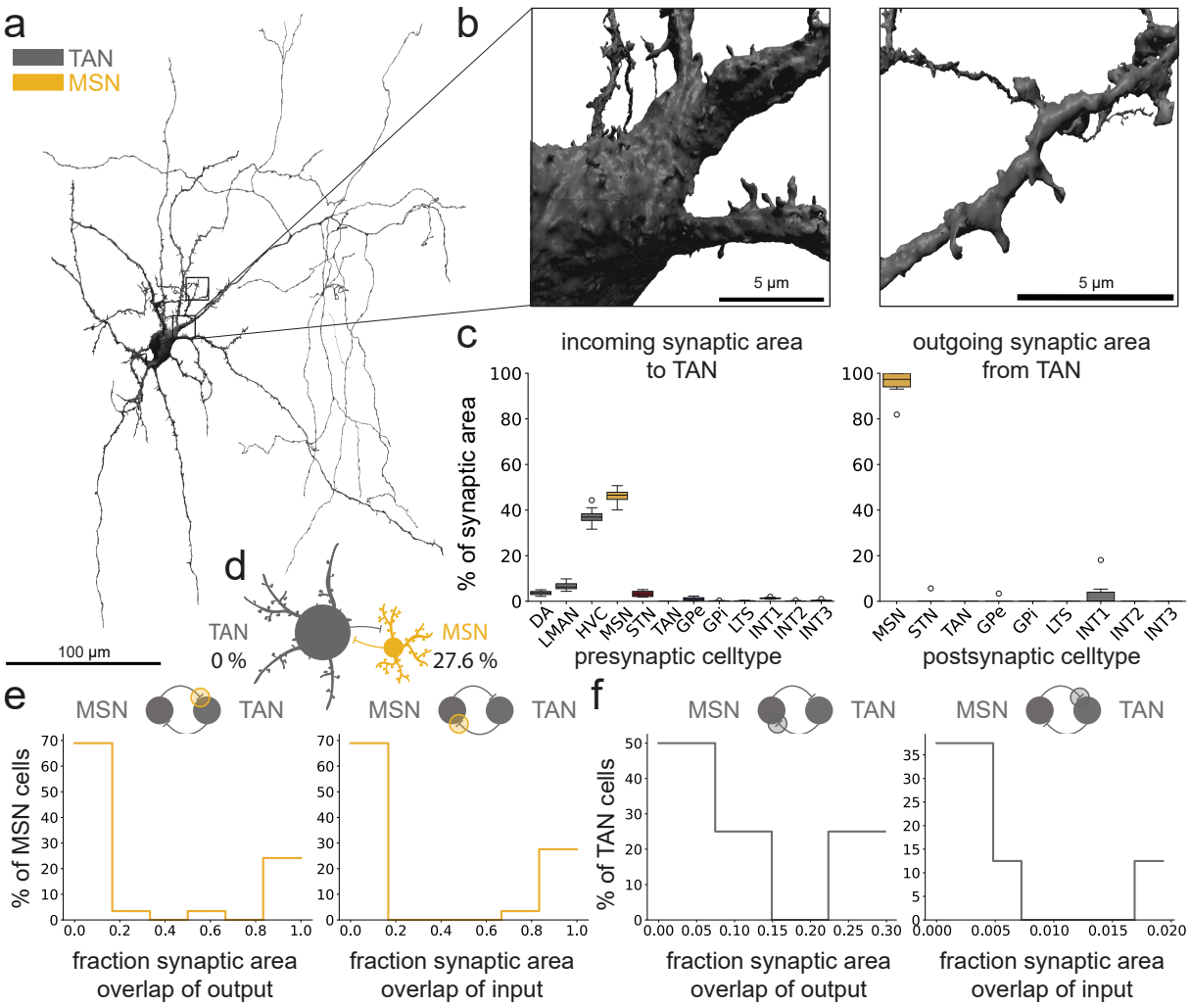

Figure 3.29: Connectivity of TAN cells. a Rendering of a TAN cell (ID: 10157981). b Spiny soma and dendrite of the TAN example cell. c Incoming and outgoing synaptic areas of TAN cells. d Binary specificity of TAN and MSN cells (largest synaptic input and output from the same cell). Note that only 29 out of 8,093 MSN cells (< 0.5 %) project to TANs and receive input from them, whereas all eight TANs do so. e, f The fraction of the synaptic area from cells that act as both inputs and outputs is calculated in comparison to the total summed synaptic area for all cells that are potential targets for recurrent connections, either incoming or outgoing. The results are also summarized in appendix table A37.

most of the input in Area X goes to the synaptic shaft of cells (see appendix figure A27).

For some cell types, larger fractions of their inputs go to different compartments. For example, the STN receives 15 % of its GPi input on the soma and a similar fraction from the LMAN and HVC on their spine heads (median 15 and 13 % respectively, see figure 3.30 c, see appendix figure A27 d). GPe and GPi generally direct a portion of their input to the soma of their target cells, but for INT2, 16 % of GPe input goes to spine heads—a similar amount to LMAN input, but higher than HVC input (median: 17 and 9 % , respectively, see figure 3.30 d, appendix figure A27 h).

In summary, this shows that different cell types have different connectivity profiles and are selective to the compartment to which they project.

The connectivity described above can be visualized using connectivity matrices of the different cell types. Depending on the normalization, different aspects can be highlighted. Normalizing to outgoing or incoming cell types shows the main output targets and input sources (see figure 3.31 a, b), while normalizing across the entire dataset shows the major pathways of connectivity (see figure 3.31 c).

Normalization across the dataset is helpful when the flow of information through the entire dataset is more interesting than the characteristic connectivity of individual cell types. Here, input to MSN from LMAN, HVC, and INT3, as well as output from MSN to GPi, are visible. This again demonstrates that the direct pathway is the strongest pathway through the dataset in terms of synaptic area.

The strong direct pathway and the structures of the classical basal ganglia pathways, feedback loops, and feedforward inhibitions remain the same when including all cells in GPe, GPi, LTS, TAN, and STN without manually reviewing cells for mergers or completeness. This remains also true when different thresholds are applied to filter projecting axon fragments in regard to their path length (see appendix figure A28). The filter criteria mainly influence the fraction of synaptic area from projecting axons relative to cell types within Area X. Since there are more, longer LMAN axons in the dataset (see figure 3.7), applying different filtering criteria affects the incoming normalized matrix in respect to the influence of HVC vs LMAN connectivity.

Additionally, these matrices show that, although cell types have distinct connectivity profiles, some cell types (DA, TAN, and LTS) have limited influence on all other cell types based on their overall synaptic connectivity (see figure 3.31, see appendix figure A28).

In summary, to get full connectivity profiles of the cells and depict the complexity of connectivity in Area X, several connectivity matrices are necessary. Although normalization to fractional incoming synaptic area is susceptible to the filtering criteria of projecting axons, the connectivity motifs remain consistent independent of the applied thresholds regarding skeleton path length.

3.4.3 LMAN - MSN - GPi - DLM Loop

The aforementioned analysis of basal ganglia pathways revealed that the direct pathway via HVC/LMAN-MSN-GPi connections is the strongest in terms of synaptic connectivity. In songbirds, it is hypothesized that song learning occurs in motor channels, each of which is responsible for different muscles (introduction section 1.3.2, Fee et al. 2011). The following sections analyze the direct pathway with respect to these channels, focusing on LMAN-MSN-GPi connectivity within the context of topographical loops, GPi-GPi connectivity, and GPi autapses.

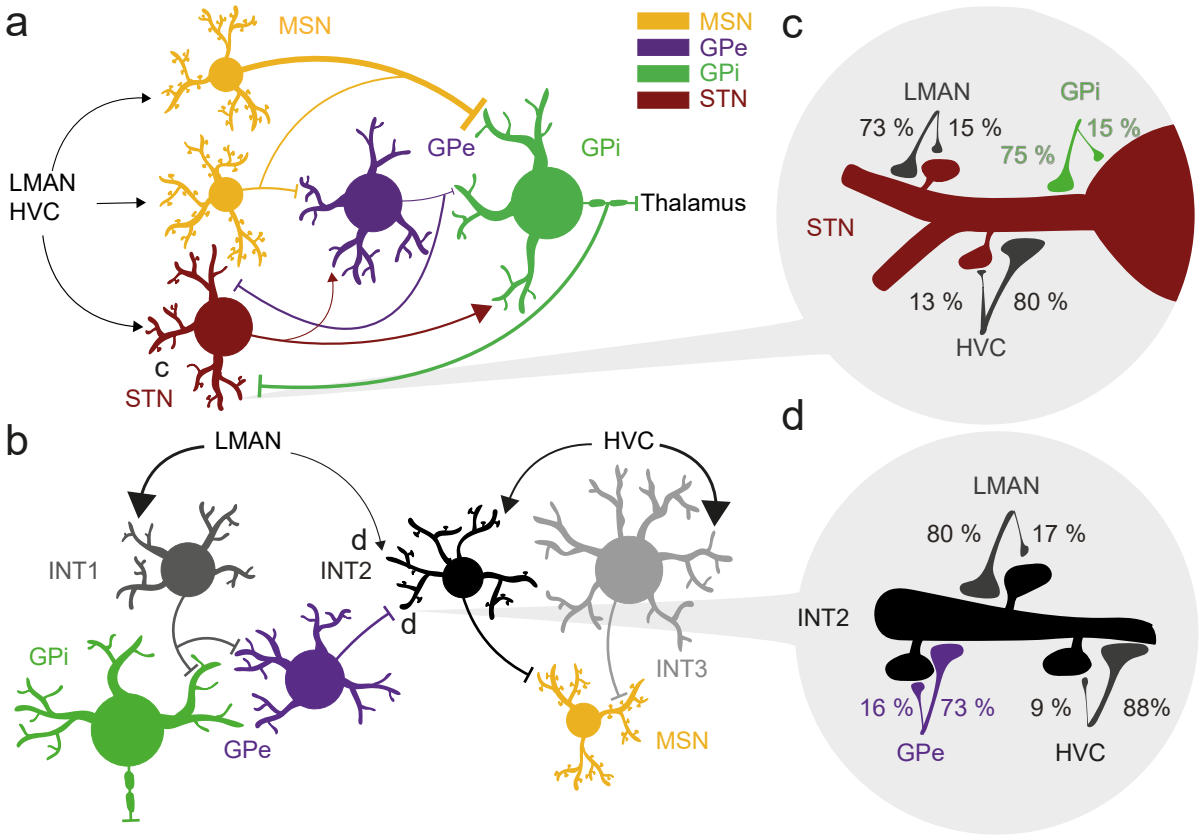

Figure 3.30: Overview of Pathways in Area X. a Schematic of the direct, indirect, and hyperdirect basal ganglia pathways identified in Area X. Arrow thickness is scaled to reflect the percentage of input to GPi. b Schematic overview of inputs to INT1-3 and their major outputs. c Compartment-specific connectivity to INT2. Numbers show the median percentage of the compartment for the connection between two cell types. For example, 80 % of the LMAN-INT2 synapses are on the INT2 shaft. d Summary of compartment-specific connectivity for connections to the STN, similar to (c). Detailed results of (c) and (d) are shown in appendix figure A27.

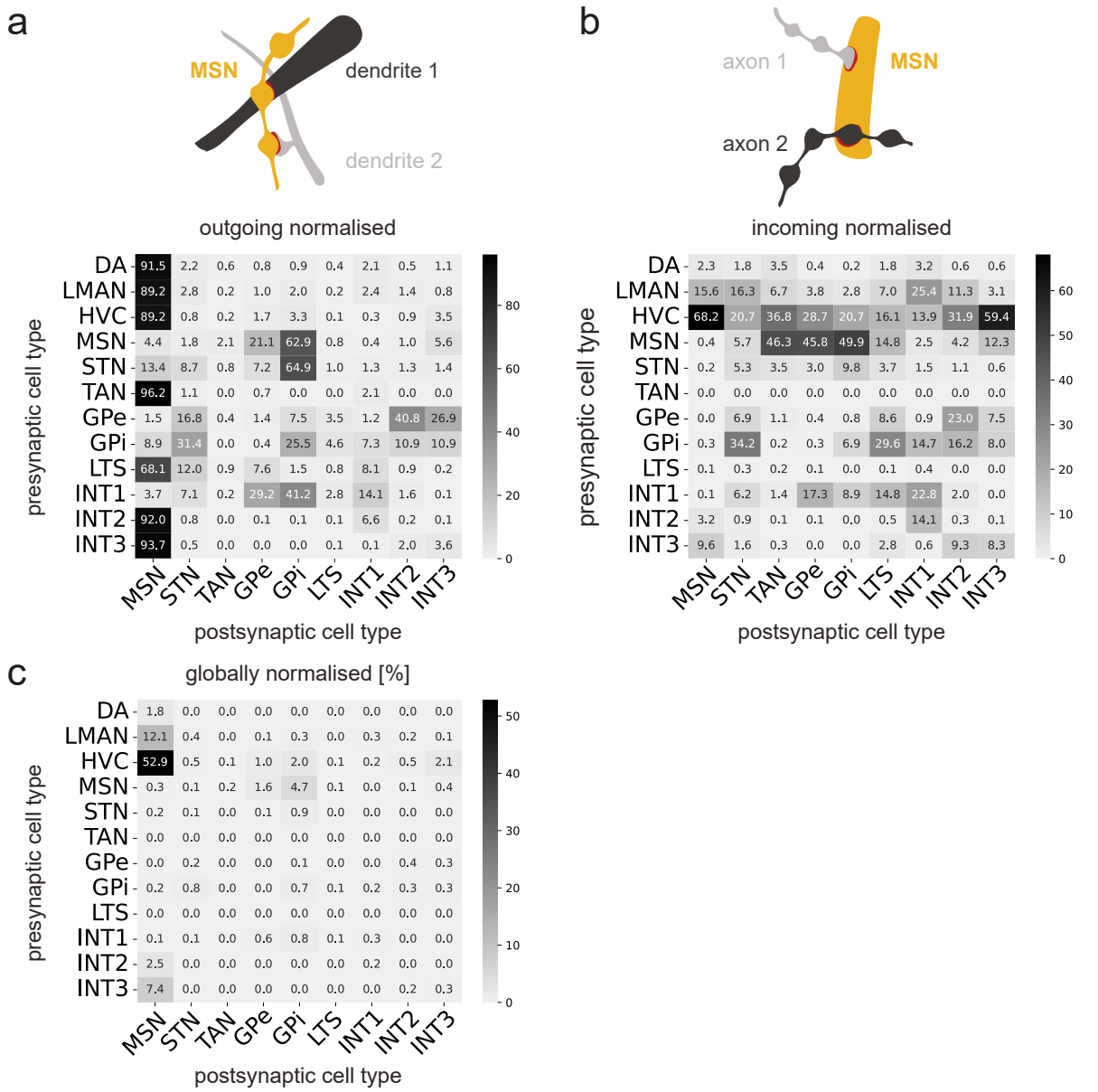

Figure 3.31: Connectivity matrices with different normalizations. a Cell-type level connectivity matrices are normalized by outgoing synaptic area (rows). The schematic shows an MSN making synapses onto two different dendrites. b Cell-type level connectivity matrices normalized to incoming synaptic area (columns). The schematic shows an MSN dendrite receiving input from two different axons. e Cell-type connectivity normalized to the synaptic area of the entire dataset.

LMAN - MSN - GPi specificity

In songbirds, the connectivity from LMAN, Area X, and DLM forms a microscopically closed topographic loop which biases learning. Different topographies correspond to associations with different muscles or subdomains of them (Luo et al. 2001, see figure 3.32 a). With eight muscles in the syrinx (Adam et al. 2021), that are learned in Area X ((Fee et al. 2011), the j0251 dataset is likely too small to depict the connectivity of different muscle domains. However, there are different hypotheses regarding connectivity within one topographical domain.

Within a topographical domain, the elements of the loop can be connected in a "focused" or "unfocused" manner. With "focused" connectivity, different LMAN cells project only to MSNs that project to one GPi neuron, allowing direct information flow over the entire topographical loop (see figure 3.32 b, left). In an "unfocused" loop, LMAN cells indirectly target several GPi neurons in their surrounding area, distributing the information more widely while maintaining the closed loop (see figure 3.32 b, right).

To test whether the loop in Area X is "focused" or "unfocused," the number of GPi cells indrectly innervated by one LMAN axon via MSN connectivity is analyzed. In a "focused" loop, one LMAN should target only a small number of GPi cells in the dataset. To address this question, a subset of large (> 5 mm) LMAN axons that were manually reviewed and entered the dataset myelinated and branched out inside the dataset, were used for analysis (method section 2.3.5). This was done to include only large axons that likely originate from different cells within LMAN.

A median LMAN axon targets a large number of MSNs (235), while a median MSN cell receives input from only two of these large LMAN axons (see figure 3.32 d). A median MSN cell connects to only four different GPis, but a median GPi cell receives input from 396 different MSNs. Thus, a median LMAN cell connects to 42 GPis via MSN, and each GPi receives input from 40 different LMAN cells via MSN. All LMAN cells project to at least 25 GPi cells indirectly, and all GPi cells receive indirect input from at least 20 large LMAN axons (see figure 3.33 a, b).

In conclusion, LMAN axons project to a large fraction of GPi cells, thereby rejecting the hypothesis of a strictly "focused" loop.

While the loop is not strictly "focused" in terms of individual cells, each LMAN axon may favor a few GPi cells by projecting to MSNs that primarily target those cells. In this case, a large fraction of the targeted MSNs should project to the same GPi cell. However, in contrast to this hypothesis, the largest MSN group that projects to the same GPi cell makes only up to 16 % of the synaptic area from one LMAN axon (see figure 3.33 c). Similarly, most GPi cells have up to 15 % of their MSNs innervated by the same LMAN axon. Thus, the loop is "unfocused" at the cellular level.

To determine whether one GPi is favored in terms of synaptic area, the fraction of synaptic area that one GPi receives indirectly from one LMAN axon via MSN is analyzed. The five GPi cells with the largest indirect synaptic area receive 5-15 % from most LMAN cells (see figure 3.33 e). This shows that the loop is also "unfocused" in terms of synaptic area.

In summary, information from LMAN is transferred to the GPi cells via MSN cells in "unfocused" topographical loops. This means that each LMAN cell targets most of the GPi cells in the dataset.

GPi - GPi inhibition

The GPi, the output cell type of Area X, receives a large number of converging inputs. The outputs of GPi cells are influenced not only by inputs from other cell types, but also by interactions within the population.

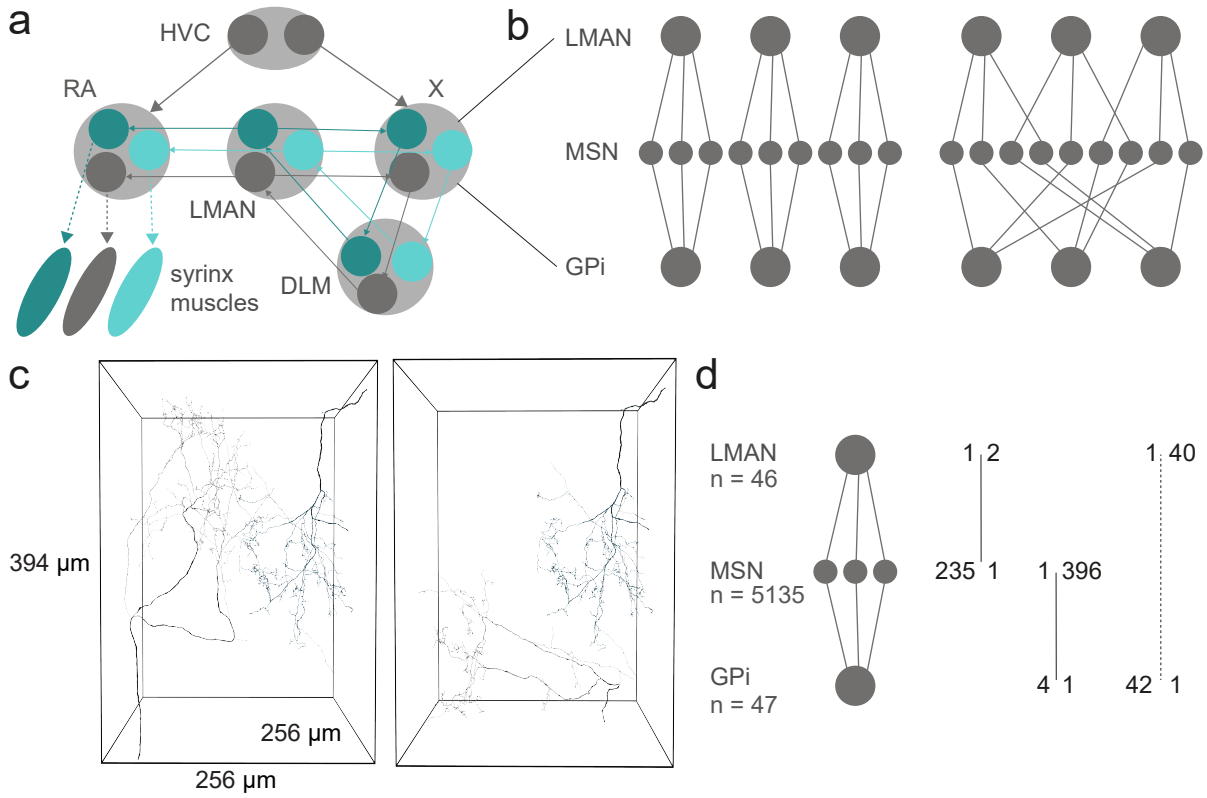

Figure 3.32: LMAN - MSN - GPi connectivity. a Model of topographical loops between LMAN, Area X, and DLM, as well as topographical connectivity of LMAN to RA, according to Luo et al. 2001. b Potential hypothesis regarding connectivity within Area X within closed topographical loops: a "focused" or "unfocused" loop. c Examples of the manually selected LMANs used for the analysis are displayed with the dataset boundaries (LMAN IDs: turquoise: 436157555; left gray: 96194764; right gray: 18222490). d Median cell numbers of connectivity between LMAN, MSN, and GPi cells. For example, one median LMAN cell connects to 235 different MSN cells, while a median MSN cell receives input from two different LMAN cells.

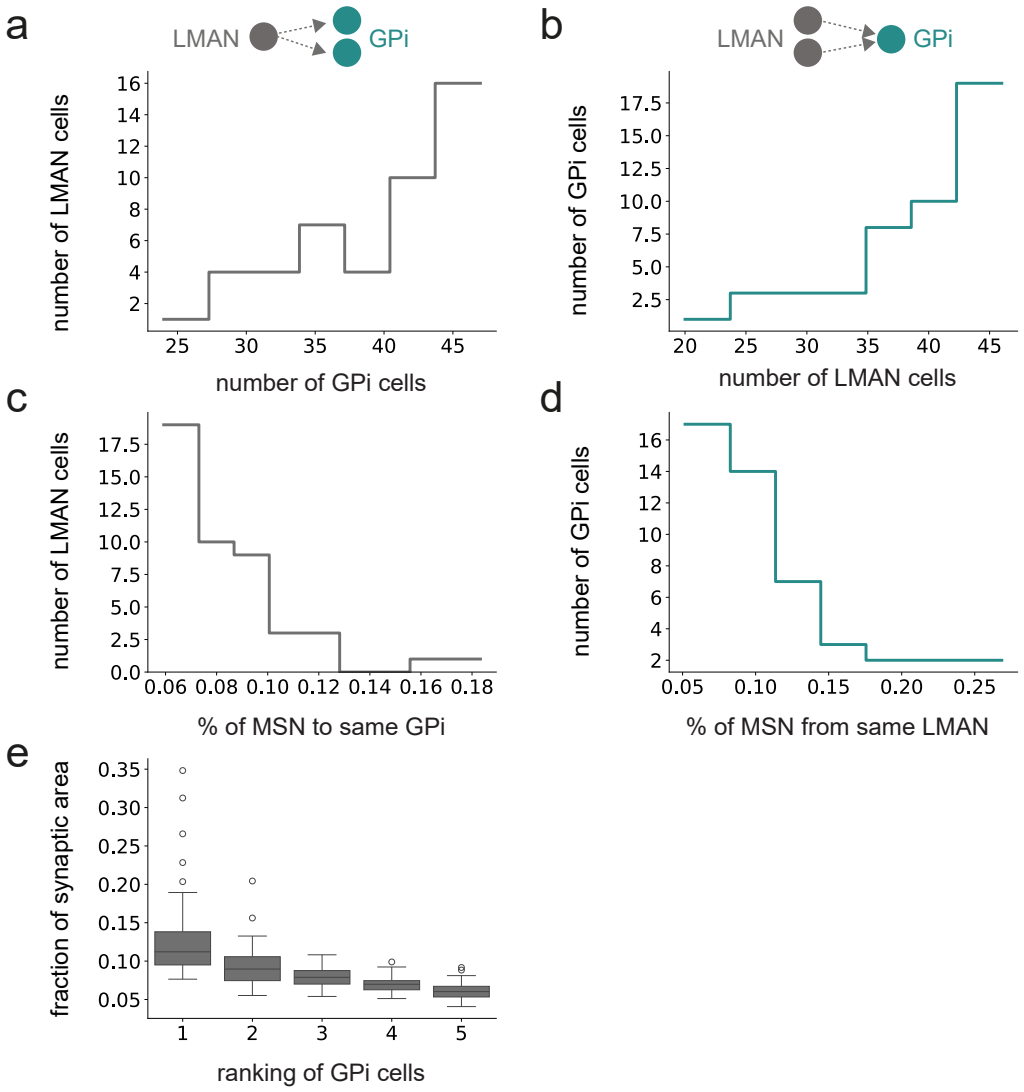

Figure 3.33: Indirect GPi innervation by LMAN. a Number of different GPi cells innervated by one LMAN axon. b Number of LMAN axons that one GPi receives input from. c Percentage of MSNs that receive input from one LMAN axon and project to the same GPi cell from the perspective of the outgoing LMAN axon. d Percentage of MSNs that receive input from the same LMAN axon and project to one GPi cell from the perspective of the GPi cell. e Fraction of the synaptic area to the five GPi cells with the highest synaptic area from one LMAN axon.

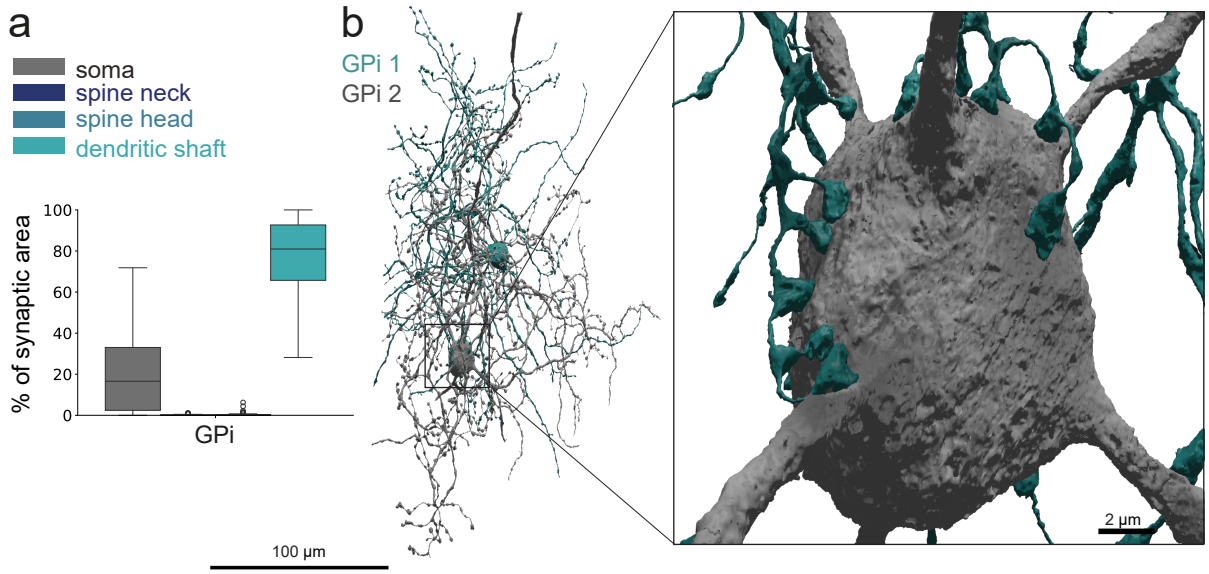

Figure 3.34: GPi - GPi inhibition via soma "claws". a Compartment-specific connectivity between GPi neurons (see appendix figure A27 c). b GPi 1 (turquoise, ID: 453097983) inhibits GPi 2 (gray, ID: 11675355) via several soma synapses.

With 25.5 % of outgoing synaptic area, the GPi is the second-highest output target for the GPi. With 6.9 % of incoming synaptic area, the GPi is the fifth-highest input source (section 3.4.1, see figure 3.24 f, g). $19.84 \pm 18\%$ of these GPi-GPi synapses are located on the soma (see figure 3.34 a, appendix figure A27 c). Manual reviews of GPi somata revealed that these connections are often facilitated by several large synapses arranged around the soma in "claws" (see figure 3.34 b).

These results demonstrate the existence of interactions among GPi neurons via "claw"-like soma synapses, which enable the GPi to strongly inhibit neighboring GPi neurons.

GPi autapses

In addition to being inhibited by other GPi cells, GPi cells may be able to influence themselves via somatic autapses. To test this theory, all GPi cells were manually inspected for autapses to the soma or the surrounding area (methods section 2.3.5). Twenty out of 47 GPi cells (40.5 %) make at least one autapse (see figure 3.35 a, appendix table A18).

Upon manually reviewing all GPe, LTS, TAN, STN, INT1, INT2, and INT3 cells, as well as a subset of MSN cells, the results revealed that, while most cell types exhibited few, if any, autapses, 30.8 % of GPe cells and 54.0 % of INT3 cells contained autapses (see appendix table A18). Thus, GPi is one of three cell types in Area X in which at least one-third of the cells contain autapses.

To determine whether there are differences between GPi cells with and without autapses, several morphological parameters, including axonal mitochondria and vesicle density and connectivity, were analyzed. There were no differences in morphology or connectivity between GPi cells with and without

autapses (see figure 3.35 b-f, appendix figure A29). Similar analyses of GPe cells revealed no differences in morphology or connectivity, except for slightly higher axonal and dendritic surface areas with autapses (p-values = 0.033, 0.049, see figure A30).

In conclusion, 40.5 % GPi of GPi cells can self-regulate via autapses. There was no difference in morphology or connectivity between cells with and without autapses.

3.5 Synaptic and non-synaptic vesicles

This thesis further inspects individual vesicles with two goals. The first is to investigate whether there is a correlation between the number of presynaptic vesicles and the synaptic area (section 3.5.1). The second goal is to determine if traces of volume transmission, e.g., in the presence of non-synaptic vesicles, exist in the dataset (section 3.5.3).

To analyze volume transmission, first, the presence of vesicles outside of clear synaptic loci is verified, then, their surroundings are analyzed.

3.5.1 Synapse size and number of presynaptic vesicles

Vesicle density is related to the firing rate reported for different cell types, and it has also been related to synaptic area (Harris et al. 1989). Examples of synapses of different sizes can be seen in HVC (see figure 3.36 a) and GPi (see figure 3.36 b,c). Figure 3.36 b shows the GPi synapse with the largest number of vesicles, which is a 0.21 µm^2 large, round synapse with 1,248 vesicles within 500 nm of the synapse. Figure 3.36 c shows the largest outgoing GPi synapse (3.4 µm^2) with 421 vesicles within 500 nm of the synapse. Another small synapse is indicated by a white asterisk at the bottom of the bouton. Compared to HVC synapses, these extreme GPi examples show that large, vesicle-filled boutons can make associating vesicles with synapses difficult in these data.

To determine whether there is a correlation between the number of vesicles and synapse size, the number of vesicles within 1 µm of the synapse is counted. When all synapses are pooled together, no correlation is observed between synaptic size and vesicle number (see figure 3.36 b, r-squared = 0.03, p-value $<$ 0.005, appendix table A38). However, when the correlation is analyzed separately for each cell type, the correlation values are higher. The highest correlation is found in INT1 (see figure 3.36 e, r-squared = 0.45, all p $<$ 0.005, appendix table A38).

For membrane-close vesicles (within 10 nm distance from the closest membrane, method section 2.3.6), correlations are generally lower (all synapses: r-squared = 0.003, p-value $<$ 0.005, appendix table A39). However, there are also cell-type-specific differences (see figure 3.36 g-i, appendix table A39). The highest correlation is found in HVC (r-squared = 0.35, p $<$ 0.005).

Since it is unclear in all cases how to assign vesicles to a synapse and there is no clear distance threshold, the analysis was also performed with vesicles within a distance of 0.5 to 2 µm from the synapse. This yielded similar results, with slightly higher correlation coefficients for all vesicles within 0.5 µm. INT1 had the highest correlation coefficient (r-squared = 0.59, p $<$ 0.005, see appendix figure A32).

Some cell types, such as GPi and INT3, have large, vesicle-filled boutons with multiple synapses, which can partially explain the lower correlations. However, high synapse or vesicle density leading to short distances between synapses (see figure 3.16, 3.18, appendix table A40) does not necessarily lead to worse correlations, as GPe is also among the cell types with higher correlations. Conversely, cell types such as LTS, which have low synapse and vesicle densities, do not have higher correlations. Therefore,

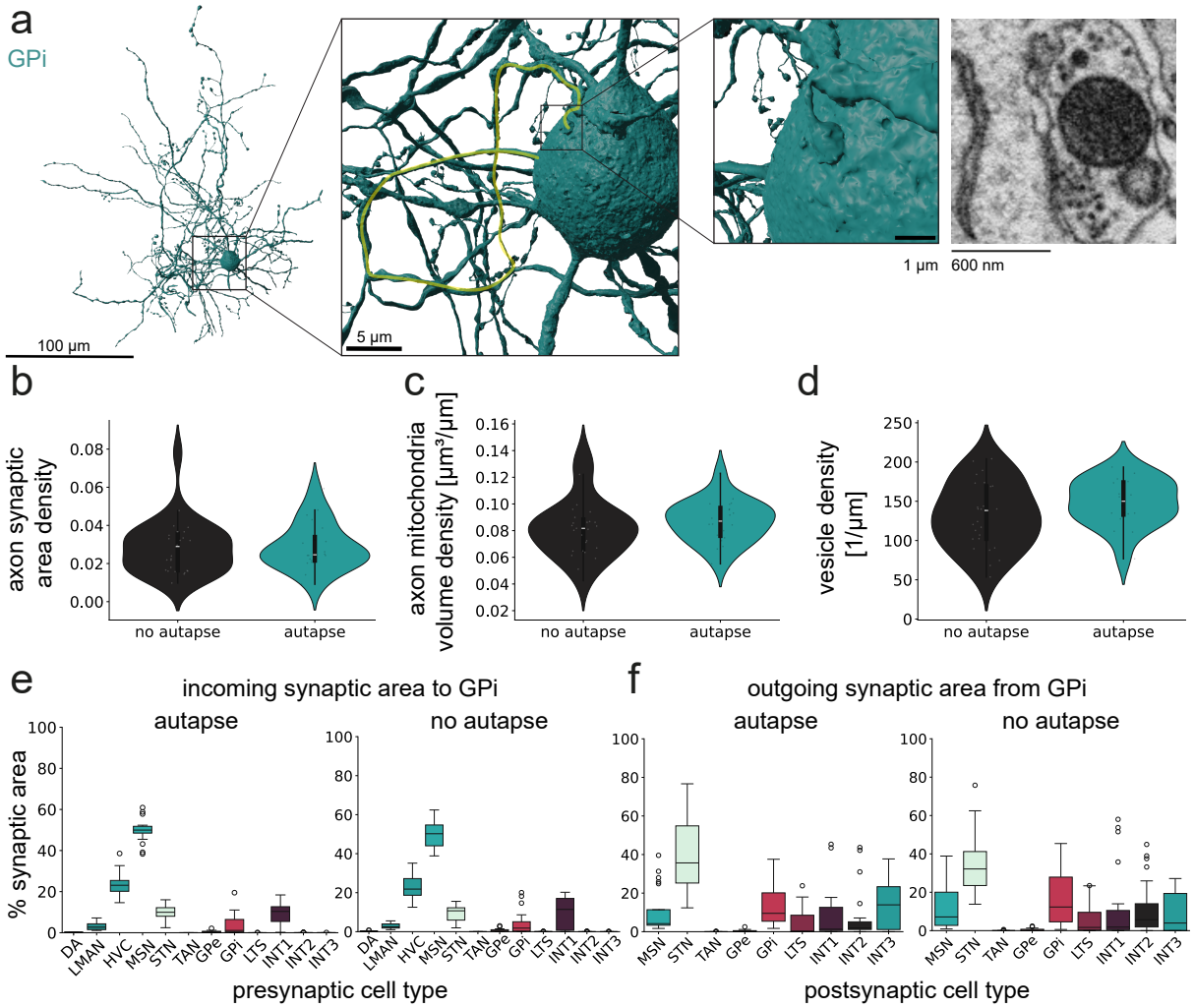

Figure 3.35: Comparison of GPi cells with and without autapses. a GPi example cell with an autapse (ID: 83542452). The loop from the axon to the autapse is highlighted in yellow in the first inset. Raw data coordinates of the autapse: 8901, 24810, 5485. b Synaptic area of the axon in relation to the axon's surface area. c Axon mitochondrial volume in relation to the axon's path length. c Number of axonal vesicles in relation to the axon's path length. e, f Incoming and outgoing connectivity of GPi cells with and without autapses.

the effects leading to cell type differences seem to be more related to the properties of specific cell types.

In summary, there are cell-type-specific differences in the correlation between synaptic size and synaptic vesicles. Some cell types show moderate correlations, but no global trend emerges across all synapses.

3.5.2 Membrane-close vesicles

Neurotransmitter-containing vesicles are found not only in proximity to synapses, but also along the axon in cases of volume transmission (see figure 3.37 a). Volume transmission has been reported for some cell types in the mammalian basal ganglia, such as DA and TAN (Abudukeyoumu et al. 2019, Arbuthnott et al. 2007).

To test whether these cell types could signal via volume transmission in Area X, the presence of non-synaptic vesicles close to the membrane was first verified. All vesicles within 10 nm of the membrane and at least 3 µm from the next synapse were analyzed as non-synaptic and membrane-close (method section 2.3.6). These were then compared to synaptic vesicles within 500 nm of a synapse.

The results show that non-synaptic, close-membrane vesicles exist and they account for a significant proportion of vesicles in DA and TAN cells (see figure 3.37 c). Their density is higher than that of synaptic vesicles in these cell types, which was not the case for the other cell types (see figure 3.37 d, appendix table A41). In LTS cells, the fraction of synaptic and non-synaptic vesicles was similar. In cell types with large boutons, such as the GPi, the density of non-synaptic vesicles is high, though still lower than the density of synaptic vesicles (see figure 3.37 b, d).

Control analyses with different thresholds for non-synaptic vesicles produced similar results. GPi non-synaptic density was higher than its synaptic density when the threshold was lowered to 1 µm.

In summary, membrane-close vesicles are found in non-synaptic locations, especially those in DA and TAN axons. Therefore, the results are consistent with DA and TAN signaling via volume transmission, which will be analyzed further in the next sections.

3.5.3 TAN and DA non-synaptic vesicles

Volume transmission from DA and TAN axons can reach receptors located several micrometers away, allowing for a more widespread signal (Beyene et al. 2019, Özçete et al. 2024). The dataset includes 4,767 DA axon fragments and eight TAN cells for analysis (see table 3.6). Since TAN cells have large axonal arborizations, their axons still span the entire dataset (see figure 3.38 a). Taken together, this means that TAN and DA vesicles in the selected axons are spread across the dataset.

Although the EM dataset lacks information on potential release sites for volume transmission, it is possible to analyze the spatial surroundings of non-synaptic vesicles. The following sections analyze the surrounding cell types, synapses, and synapse sizes to test for potential correlations within a 2 µm distance of the vesicles. As in previous analyses, vesicles within 3 µm of the closest synapse are considered non-synaptic, and those within 10 nm of the closest membrane are considered membrane-close (method section 2.3.6).

In TAN cells, 22,431 out of 607,344 vesicles are membrane-close (3.69 %), and 20,776 of those are non-synaptic (92.62 %). In DA cells, 2,481,905 out of 73,022,373 vesicles are membrane-close (3.40 %), and 1,896,142 are membrane-close non-synaptic (76.40 %).

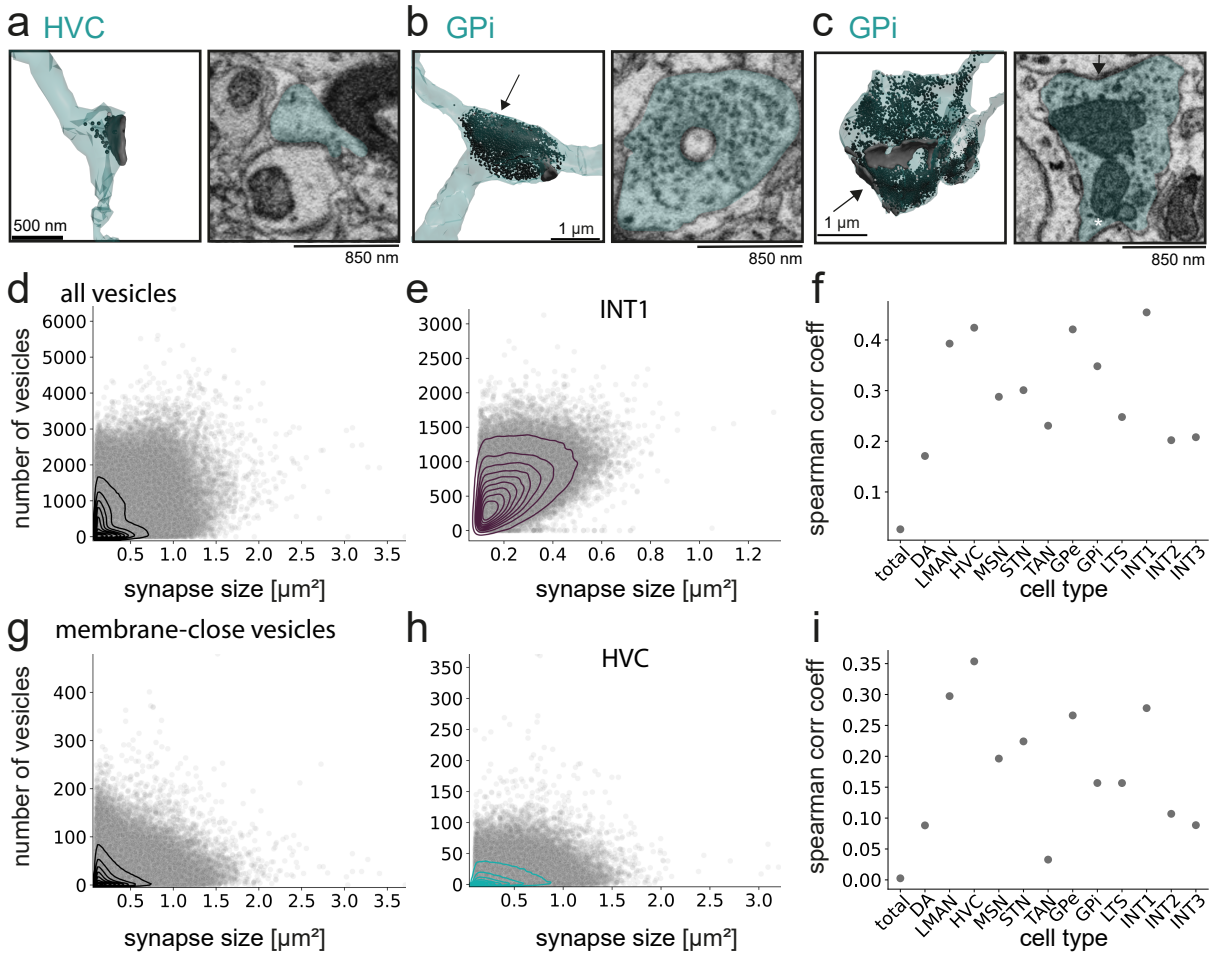

Figure 3.36: Relationship between presynaptic vesicle number and synaptic area. a Image of an example HVC axon (ID: 820388630; Location: 14641, 9127, 9375). Close-membrane vesicles are shown in white and other vesicles are shown in black. The vesicles were rendered with a radius of 20 nm. b GPi synapse with the highest number of vesicles (cell ID: 26252706; location: 6485, 6222, 6410). The arrow indicates the location of the hidden round synapse beyond the vesicles. The synapse size is 0.21 µm^2 large and contains 1,283 vesicles within 500 nm of the synapse. c The largest GPi synapse (cell ID: 33643243; location: 9363, 17419, 170) is 3.4 µm^2 large, has 421 vesicles within 500 nm, and is indicated by an arrow. Another, smaller synapse is located on the opposite side of the bouton and is indicated by a white asterisk. d Synaptic area and number of vesicles within 1 µm of all synapses. e Synaptic area and number of vesicles within 1 µm of all HVC synapses. f Spearman correlation coefficient for the correlation between synaptic area and number of vesicles in different cell types. g-i Same as d-f, but only membrane-close vesicles.

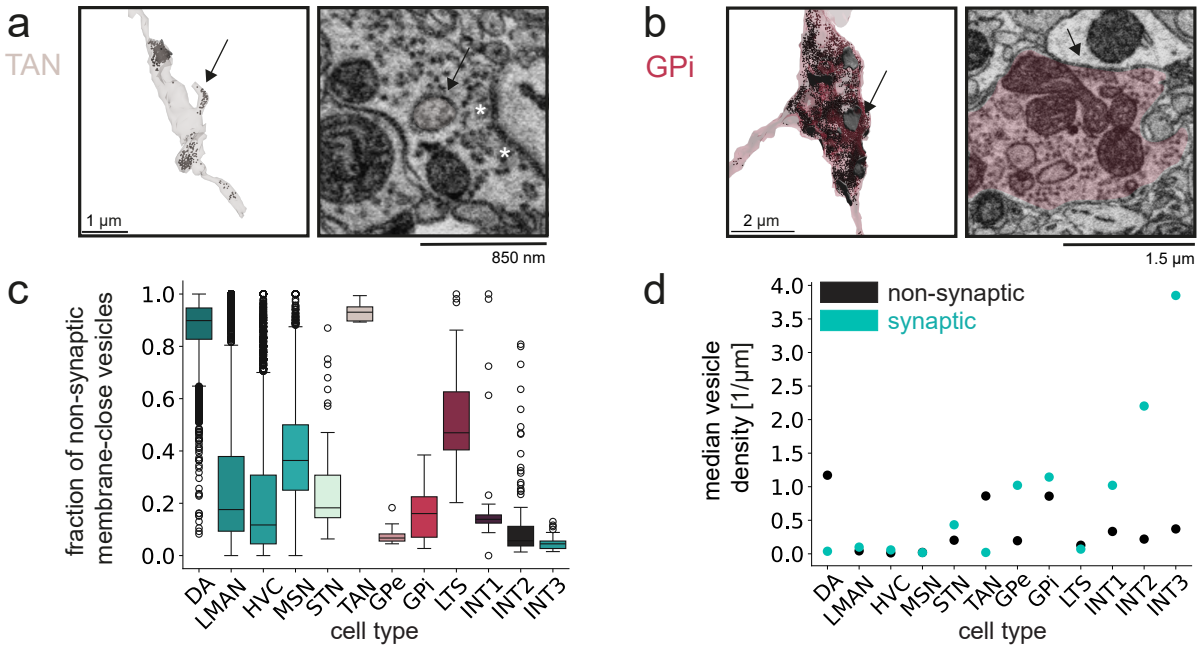

Figure 3.37: Synaptic and non-synaptic membrane-close vesicles. a TAN vesicles outside of a synapse, as indicated by the arrow (cell ID: 10157981; location: 20696, 20265, 4927). Next to the TAN axon is a synapse from an HVC axon fragment to the spine head of an MSN cell (white asterisks indicate the presynaptic axon). Membrane-close vesicles are shown in white and others in black. All vesicles were rendered with a 20-nm radius. The tip of the TAN axon is in the center of another axon labeled in rose in the raw data. b A GPi bouton with multiple vesicles (cell ID: 26790127, location: 16968, 9981, 6964). The synapse shown in the raw data is indicated by a black arrow. c Fraction of non-synaptic membrane-close vesicles in different cell types. Vesicles were non-synaptic if they were located more than 3 µm away from the synapse and synaptic if they were located within 500 nm of the synapse. d Median vesicle density non-synaptic and synaptic. Median vesicle density in non-synaptic and synaptic regions. For full density distributions, see appendix figure A32 a, b.

Modulatory vesicles in proximity to different cell types

Since different cell types have different neurotransmitter receptors, those with cholinergic (ACh) and dopaminergic receptors may be found in closer proximity to TAN and DA non-synaptic vesicles. To test for spatial correlation, the surface area of different cell types in proximity to non-synaptic, membrane-close TAN and DA vesicles is analyzed 3.38 b.

Large cell types, such as GPi and INT3, have a higher surface area per cell in proximity to TAN vesicles (see figure 3.38 c). However, MSN, the most prevalent cell type in Area X, has the highest surface area in proximity to TAN vesicles among all cell types (see figure 3.38 d). When normalized to the total surface area per cell and cell type (see appendix figure A33 a), all cell types occur in a similarly low range in proximity to TAN vesicles, with GPi slightly underrepresented (see figure 3.38 e, f).

For DA, the results are similar in that there is little difference between the cell types. However, generally, a larger fraction (> 40 %) of cells are within 2 µm of DA than of TAN vesicles (see figure 3.38 g-i, appendix figure A33 b). The results are similar when looking at the surface areas of cells at 1 µm or 5 µm distances. GPi is more strongly underrepresented at 1 µm than at 2 or 5 µm (see appendix figure A33 c-f). The selected DA fragments span a much tighter network across the dataset since almost the entire surface area of all cells lies within 5 µm of the DA membrane-close, non-synaptic vesicles (see appendix figure A33 f). In comparison, only 6-7 % of the surface area of the other cell types lies within 5 µm of the TAN membrane-close non-synaptic vesicles

In summary, there is no spatial correlation between TAN and DA non-synaptic membrane-close vesicles and a specific cell type. GPi cells are slightly underrepresented in close proximity to the vesicles. DA axons form a dense network throughout the dataset, with all cells lying within 5 µm of a DA membrane-close non-synaptic vesicle. Since most predicted fragments are shorter than the selected fragments ($>$ 200 µm, see figure 3.7 e), this number is probably an underestimation of the distances.

Modulatory vesicles in proximity to different synapses

As in the previous analysis, the spatial correlations of synapses in proximity to membrane-close non-synaptic TAN and DA vesicles is examined. If there were a correlation, these vesicles would be closer to the synapse between the two specific cell types (see figure 3.39 a). To visualize the results, a connectivity matrix was prepared with synaptic areas within a 2 µm distance of the vesicles, similar to the general connectivity in the dataset (see figure 3.31).

In proximity to TAN vesicles, the synaptic areas are highest for HVC-MSN synapses, which generally have the largest synaptic area in the dataset (see figure 3.38 b, 3.31 c). When the synaptic area close to the vesicles is normalized to the synaptic area in the dataset, all connections fall within a similar range of 0 to 2.5 %. Some connections with very few synapses are slightly overrepresented, e.g., GPi-TAN.

Similar results were found for DA: synaptic areas close to the vesicles generally reflect synapse size distribution. Variations involving lower or higher synaptic areas generally involve connections with smaller synapses, e.g., INT3-LTS (16.0 %) vs. INT3-INT (59.6 %)

As for cell surface areas, a much larger fraction of synapses are generally close to DA vesicles. For example, 37.6 % of all synapses are within 2 µm, and 93.4 % are within 5 µm. In contrast, for TAN, only 0.7 % and 5.8% , respectively, are within these distances (see appendix table A42). Similar results were found for distances of 1 and 5 µm to vesicles, indicating no preference for specific synapses (see appendix figure A34).

In conclusion, the distribution of synapses around the TAN and DA membrane-close, non-synaptic

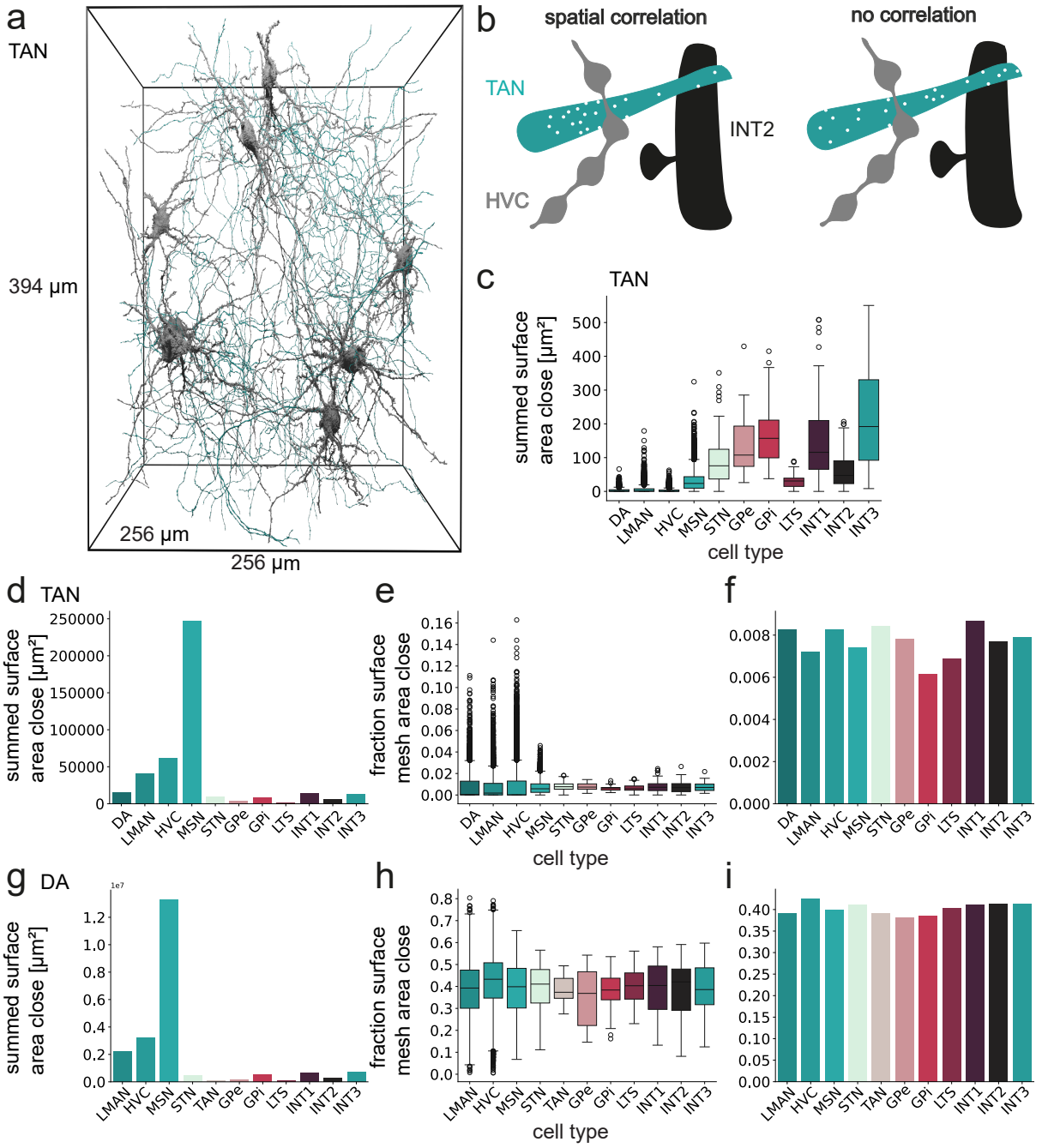

Figure 3.38: TAN and DA non-synaptic, membrane-close vesicles in proximity to cells of different cell types. a Rendering of the eight suitable TAN cells in the dataset (cell IDs: 25372570, 26353030, 26958335, 28209513, 33605129, 45452841, 52904364, 175077676). The soma and dendrite are shown in gray and the axons are shown in turquoise. b Schematic drawing of 1) a spatial correlation for one cell type, where more vesicles are close to the surface of a specific cell type, and 2) no correlation. c Summed surface area within 2 µm of TAN non-synaptic, membrane-close vesicles. d (c), summed per cell type. e,f (d) (c) in relation to the cell or cell type surface areas (see appendix figure A33 a). g-i (d) (f) for non-synaptic, close-membrane DA vesicles. The surface areas of TAN and DA were not counted when analyzing their own vesicles

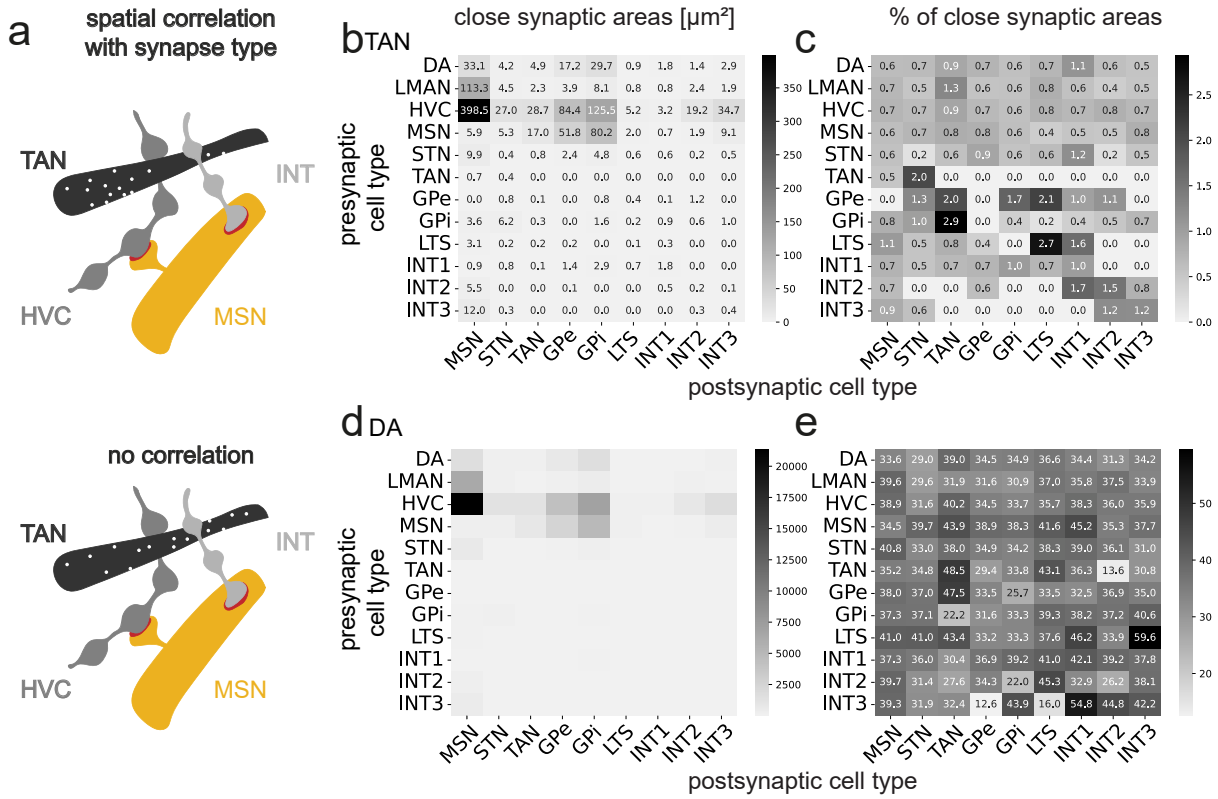

Figure 3.39: TAN and DA non-synaptic, close-membrane vesicles in proximity to synaptic areas between different cell types. a A schematic drawing showing a preference for synapses between two cell types, where more vesicles are close to these synapses, or no preference. b Summed synaptic areas within 2 µm of TAN non-synaptic membrane-close vesicles. c (b) normalized with the summed synaptic area between two cell types (see figure 3.31 c). d, e (b), (c) with DA non-synaptic membrane-close vesicles.

vesicles reflects the general distribution of synaptic areas across the dataset. As with cell surface area, most synapses are within 5 µm of membrane-close, non-synaptic DA vesicles.

Modulatory vesicles in proximity to small and large synapses associated with different basal ganglia pathways

Previous analyses showed that the non-synaptic vesicles of DA and TAN neurons are not close to a specific synapse or cell type. However, there could be spatial correlations between the size of specific synapses.

The hypothesis is that if the released neurotransmitters (ACh or DA) acted to enhance synapses between two cell types, there would be more vesicles around large synapses than small ones. Conversely, if ACh or DA were suppressive, there would be more vesicles in proximity to smaller synapses (see figure 3.40 a).

For this analysis, all non-synaptic vesicles were considered independent of their membrane distance. The distance of the vesicles was calculated from the smallest and largest quantiles of the synapses (labeled "small" and "large"), so the number of synapses would not affect the surrounding number of vesicles. Distances were then measured up to 5 µm around the synapses, and the distributions of small versus large synapses were compared (method section 2.3.6).

Although the number of small and large synapses per connection is the same, the number of synapses between different cell types is not, which affects the general shape of the curves. For high synapse numbers, there is a peak in the distribution, as seen with HVC-MSN synapses, for example (see figure 3.40 b, c).

To see how the number of vesicles and the shape of the distribution depend on the number of synapses, an analysis was performed on randomly selected subsets of HVC-MSN synapses, and the distance to the closest TAN vesicles was calculated. For small numbers of synapses, the number of vesicles increases up to 5 µm distance (see appendix figure A35 a-c). For higher synapse numbers, the vesicle number approach a peak, with the peak becoming closer to the synapse as the synapse number increases (see appendix figure A35 d-g). The overall number of vesicles within 5 µm of the synapses also increases proportionally to the number of synapses (see appendix table A43, appendix figure A35 h).

In summary, these results demonstrate that the number of vesicles, and consequently the shape of the distributions, depends solely on the number of synapses.

The number of vesicles surrounding the analyzed synapses ranges from 2,444 (TAN, GPi-STN, spine only) to over 40 million (DA, HVC, LMAN-MSN, appendix table A44). With these high sample sizes, statistical tests generally showed low p-values and if curves are similarly shaped, also low effect sizes (see appendix table A44, methods section 2.3.6). In this case, the similar shape of the distribution for vesicles in proximity to small and large synapses is explained by their overall dependence of the synapse number as explained above. However, large effects should still be measurable and apparent by a shift in the curves. Since high sample sizes bias p-values toward lower numbers, a bootstrapping approach was selected to more accurately determine statistical effects. Over 1,000 iterations, 1,000 samples were randomly drawn from each distribution. Then, the Wilcoxon rank-sum test was calculated for each round, and the median was selected to rate potential effects (method section 2.3.6). For high sample sizes, this procedure was performed with a higher number of samples per iteration.

This analysis focuses on the major connections of the basal ganglia pathways and feedback loops (section 3.4.2). All connections from and to MSN (i.e., parts of the direct and indirect pathways) did not show significant differences between small and large synapses (effect sizes = 0 - 0.3, see figure 3.40 b, c, appendix figures A36 a- i, A37 a-j, appendix tables A44, A45, A46, A47). These results remained consistent when combining HVC and LMAN as major glutamatergic inputs and when focusing only on synapses onto dendritic spines.

For the few GPe-GPi connections that indicated a weak indirect pathway (see figure 3.24), TAN vesicles were more frequent around small synapses (see figure 3.40 d, appendix table A45). This was not observed with DA (see appendix figure A37 k, appendix table A46).

For connections of the hyperdirect pathway, there was a trend toward more TAN ($p = 0.056$), but not DA vesicles around the small synapses (see figure 3.40 e, appendix figure A37 l, appendix tables A45, A46, A47). Other hyperdirect pathway connections (LMAN-STN and STN-GPi) did not show effects in either TAN or DA (see appendix figures A36 j, n, A37 m, A38 b). Combining HVC and LMAN to STN synapses weakened this effect, which disappeared when focusing only on HVC and LMAN to STN spine synapses (see appendix figures A36 k,l, A37 n,o).

For connections from GPi to STN cells, which were one of the strongest inputs to the STN alongside

cortical inputs (see figure 3.25), there were also more vesicles close to small synapses for TAN (see figure 3.40 f, appendix table A45). However, there was no effect when examining spine synapses or DA vesicles (see appendix figures A36 m, A37 p, A38 a, appendix tables A46, A47).

Two of the new interneurons, INT2 and INT3, were major output targets of GPe cells (see section 3.4.1), so their inputs and outputs were analyzed as well. While there were no effects on synapses with their major output target, MSN (see appendix figures A36 e-g, A37 e-g, tables A45, A46, A47), there were different effects on the input side. For INT2, TAN vesicle numbers increased near larger synapses from GPe but decreased directly adjacent to GPi (see figure 3.40 g,h). For INT3, there was no effect with GPe synapses, but a strong increase in vesicle number was observed with GPi inputs (see figure 3.40 i, appendix figure A36 o). None of these effects were visible with DA vesicles (see appendix figures A38 c-f). Note that the direction of the reported effects depends on the pre- and postsynaptic cell types. For instance, TAN vesicles exhibit distinct effects for INT2, as well as with GPi (see figure 3.40 g, h). Additionally, the effect with presynaptic GPi varies in connection with STN, INT2, and INT3 (see figure 3.40 f, h,i).

There were no effects with HVC inputs to either INT2 or INT3 with TAN vesicles (see appendix figure A36 p,q). For LMAN input to INT2, a higher number of TAN vesicles were found in close proximity to small synapses (see figure 3.40 j). A similar trend was observed for DA, but it was only significant when bootstrapping with 10,000 samples per iteration (see figure 3.40 k, appendix table A47). There was also an increase around small synapses for LMAN-INT3, which was the only measured effect with DA vesicles (bootstrap n = 2000, see figure 3.40 l, A46).

In summary, although the differences between small and large synapses for TAN and DA vesicles were minimal, some connections exhibited effects that supported both the enhancement and suppression hypotheses, depending on the neurotransmitter and the pre- and postsynaptic cell types.

3.6 Glial cells and migratory neurons in Area X

In addition to analyzing neuronal cell types, the following sections focus on differences in organelle density and contact area with neuronal cell types in glial cells and migratory neurons.

3.6.1 Subcellular structures in glia and migratory neurons

Mitochondria, GA, and ER were predicted in glial cells and migratory neurons. As mitochondria relate to energy consumption, the mitochondria density is analyzed now with respect to glial cells and their potential differences in energy consumption. Additionally, also the densities of ER and GA are analysed for comparison.

Different glial cell types exhibit variations in shape, number, and volume. For example, astrocytes have long mitochondria, especially in their endfeet around blood vessels. In contrast, migratory neurons have few, small, round mitochondria (see figure 3.41).

To see if there are differences between the different glial cell types, migratory neurons and neuronal cell types, the organelle densities of mitochondria, GA and ER were calculated. As comparison with neurons, a neuronal cell type with low firing rates and organelle densities, the MSN and one with a high reported firing rate and high organelle densities, the GPi, were selected (see figures 3.17, 3.19, 3.20). As glial cell types do not have the same compartments as neurons, the densities were calculated for the whole cell in relation to the cells volume (method section 2.3.7).

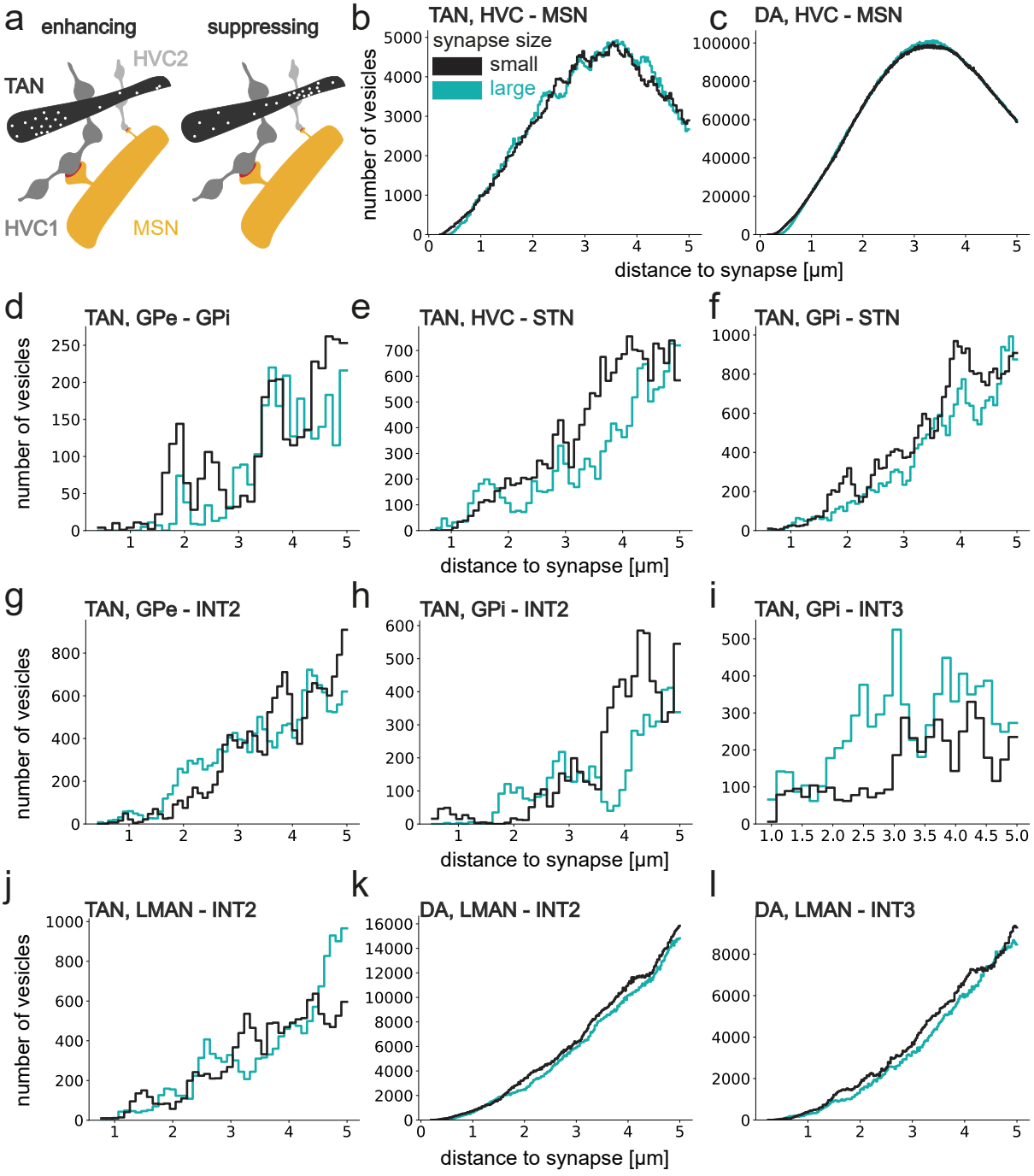

Figure 3.40: TAN and DA non-synaptic vesicles in proximity to small and large synapses of different cell types. a Schematic showing the hypothesis that, when TAN vesicles enhance the growth of a synapse between two other cell types, more vesicles will be found closer to large synapses. Conversely, if they acted suppressive, there would be more vesicles closer to the smaller synapse. b Distance of non-synaptic TAN and DA vesicles to the smallest and largest quantiles ("small" and "large," respectively) of synapses between different cell types. The number of synapses and vesicles, as well as the relevant statistics, are shown in the appendix tables: A44, A45, A46, A47.

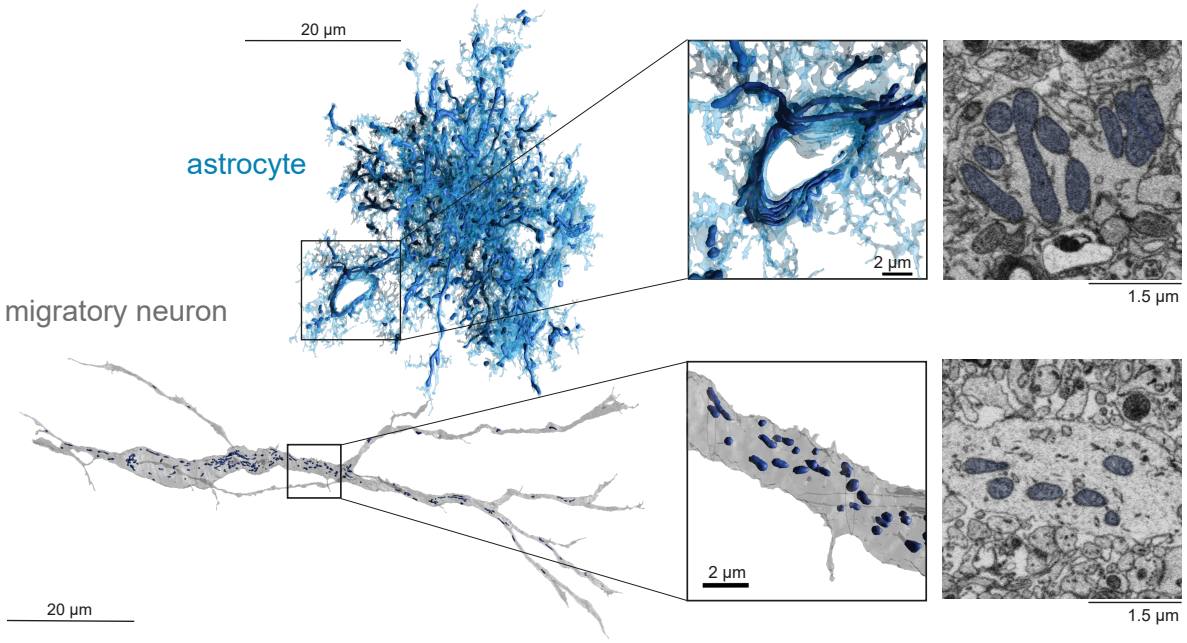

Figure 3.41: An example astrocyte (ID: 2069615083) and a migratory neuron (ID: 1644151292), as well as their respective mitochondria. The location of the mitochondria in the insets is shown in blue. The coordinates of the insets: 7811, 8655, 10721 (astrocyte), 4390, 3567, 9168 (migratory neuron).

First, the density of mitochondria was analyzed. Previous results from this lab, based on a different cell classification (Schick 2023) and different cell IDs (Schick et al. 2024, shared conference poster), showed differences in mitochondrial density between glial cell types. The results here also show differences between glial cell types, with astrocyte mitochondrial densities comparable to those of GPi. All other glial cells and migratory neurons have lower densities than MSN. Oligodendrocytes, microglia, and OPCs have similar levels of mitochondrial density that do not differ significantly from each other (see figure 3.42 b, appendix table A48).

Second, GA densities were compared among cell types. GA densities differed significantly between glial cell types and migratory neurons, but not between the two neuronal cell types (see figure 3.42 c, appendix table A48). Oligodendrocytes had the highest densities and migratory neurons had the lowest. Note that, due to their short processes, the soma of oligodendrocytes is overrepresented in the cell's volume.

Third, the ER densities were analyzed. While the ER density of all cell types appeared dense visually, analysis showed significant differences among the cell types (see figure 3.42 d). MSN cells had the highest levels of ER volume density, followed by oligodendrocytes and OPCs, which did not differ significantly (see appendix table A48). Microglia followed, and they did not differ significantly from oligodendrocytes. Migratory neurons exhibit the lowest ER densities. As mentioned before, there are differences in the ER densities of different compartments and depending on the parameter for normalization (section 3.3.2), the high ER volume density of MSNs and the lower density of GPi differ from the ER surface area densities calculated in relation to the corresponding compartment path length. However, these results are similar to the ER area densities calculated in relation to the dendritic surface area (see figure 3.20, appendix figure A19).

In summary, different glial cell types and migratory neurons have different levels of mitochondrial, GA, and ER volume density. Compared to both glial and neuronal cell types, migratory neurons showed the lowest density across all organelles. Glial cell types did not consistently have higher or lower densities than neuronal cell types; results varied among organelles. For example, astrocytes had comparable mitochondrial densities to GPi, but lower GA densities.

3.6.2 Contact site analysis of glial cells

Glial cells can interact with each other and neuronal cell types via gap junctions, the release of gliotransmitters, or synapses (Buchanan et al. 2022, Durkee et al. 2019, Elbaz et al. 2019, Peng et al. 2023, Umpierre et al. 2021). Since synapses and vesicles were specifically trained and evaluated for neurons, for glial cells, their contact sites are analyzed to examine potential interactions (method section 2.3.7). Delta Schick performed this analysis under my supervision as part of a shared conference poster (Schick et al. 2024) and a previous version was included in his master's thesis (Schick 2023, supervised by me).

To analyze preferences independently of the frequency and size of specific cell types, the contact site ratio was calculated. This ratio is the sum of the contact site mesh areas divided by the sum of the surface area for a given cell type (method section 2.3.7, figure 3.43 a).

First, contacts with neuronal cell types were analyzed. In general, different glial cells have different contact site ratios across cell types. Astrocytes have the highest contact ratios, followed by microglia, OPCs, and oligodendrocytes (see figure 3.43 b). Additionally, there are differences among neuronal cell types. For example, MSN cells have high contact areas with all glial types, while LTS cells have high contact areas with astrocytes, microglia, and OPCs.

Second, the contact areas between glial types were analyzed. While microglia and OPC have the

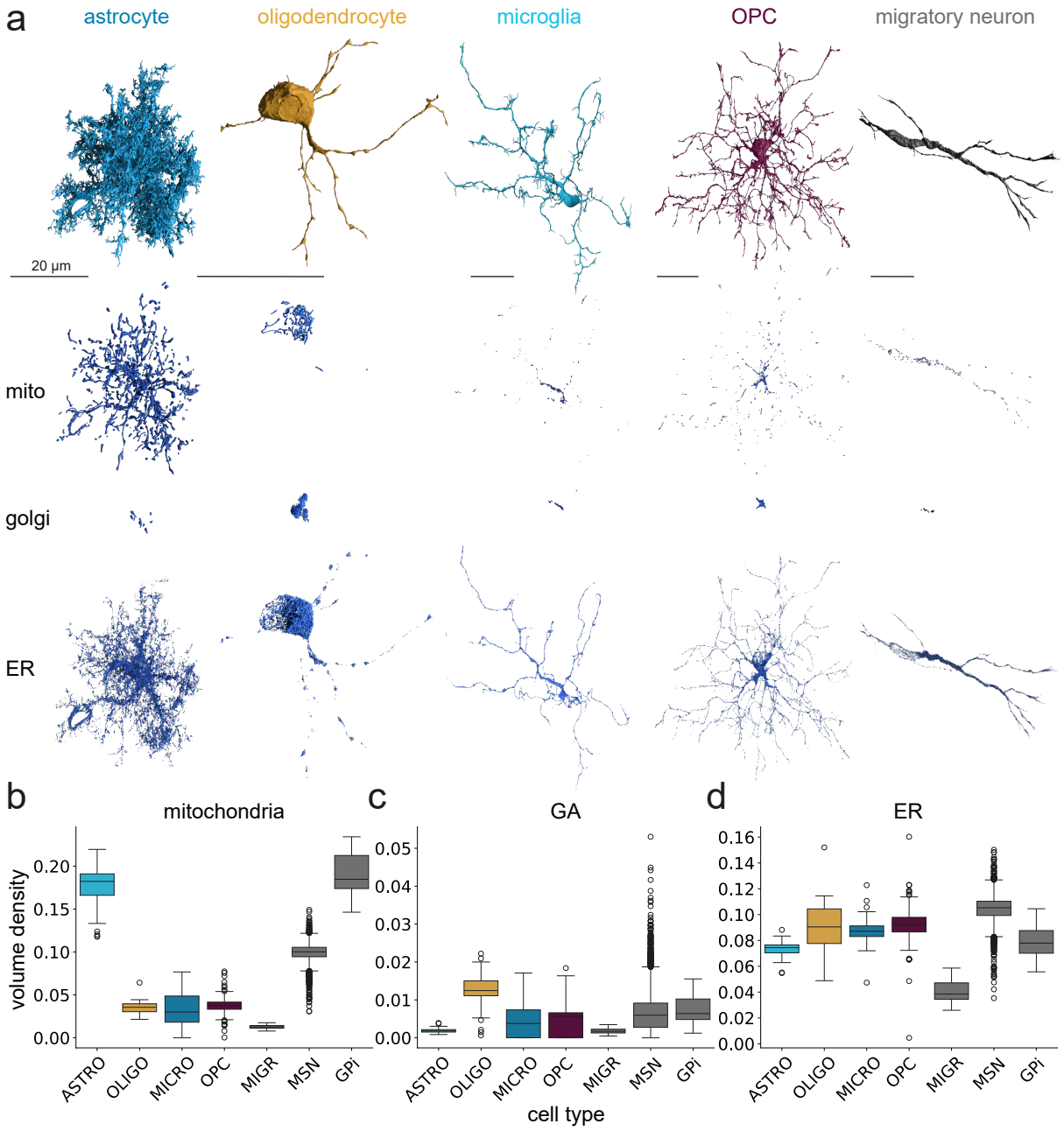

Figure 3.42: Organelle densities of glial cell types and migratory neurons. a Examples of cells from each cell type: once as a mesh and then different organelles only, such as mitochondria (mito), GA, and ER. All scale bars show 20 µm. The organelles and surface mesh of the same cell are on the same scale. Example cell IDs (left to right): 2069615083, 1190822162, 1143990345, 2017622103, and 1644151292. b Mitochondria volume densities in glial cells, migratory neurons, MSN, and GPi. c GA volume densities in glial cells, migratory neurons, MSN, and GPi. d ER volume densities in glial cells, migratory neurons, MSN, and GPi. Volume densities were calculated as the summed volume of the organelle in relation to the cell's volume.

highest contact ratio with astrocytes, while oligodendrocytes have the lowest contact ratio with microglia (see figure 3.43 c).

Third, contacts within the same glial cell type are investigated. While microglia and oligodendrocytes have few contacts with each other, astrocytes frequently make contact with each other. Some OPCs also have contact with other OPCs (figure 3.43 d).

Across all analyses, oligodendrocytes exhibit low contact site ratios and do not demonstrate a preference for highly myelinated cell types, such as the GPi cells. The thin processes of oligodendrocytes are often not segmented, and neither is the myelin, which is not considered part of either the oligodendrocyte or the neuron. This results in contact sites of myelin wrapping around a neuron not being assigned properly (see figure 3.44). When visualized in 3D, it appears as if there is a gap between the cells; however, in the raw data, the cell touches the axon. Note that in the raw data, membrane that is not myelinated is also not properly assigned to the oligodendrocyte. In this example, the oligodendrocyte wraps the axon next to the myelinated region, which could indicate a snapshot of the myelination process. Unfortunately, this is not captured by the aforementioned analysis of contact areas.

In summary, glial cell types exhibit similar contact preferences for MSNs and LTS. Astrocytes demonstrate the highest contact ratios among all cell types. Additionally, astrocytes make contact with other glial cell types and with each other. Due to the incomplete mapping of myelin and the segmentation of oligodendrocytes in the SyConn processing pipeline, their contact sites are generally underestimated.

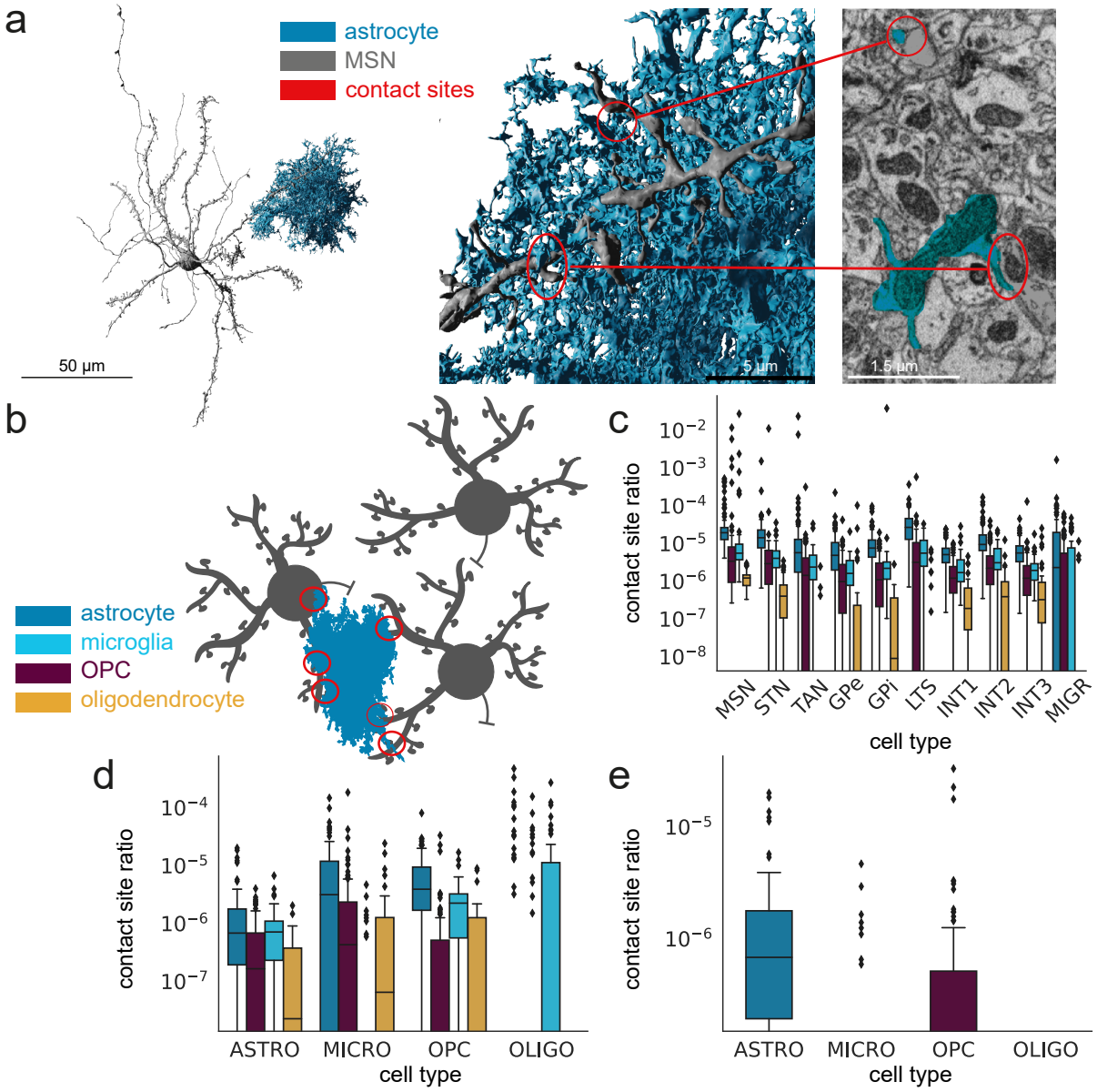

Figure 3.43: Contact sites of glial and neuronal cell types. An example of an MSN cell (ID: 1469986452) and an astrocyte (ID: 2069615083) with different contact sites. a Electron microscopy image with cells indicated by Delta Schick. b Schematic of MSN-astrocyte contacts. c Contact site ratio for glial cells with other glial cells. c Contact site ratio for glial cells with other glial cells. d Contact site ratio with other cells from the same cell type. c-e Y-axis is displayed in log scale.

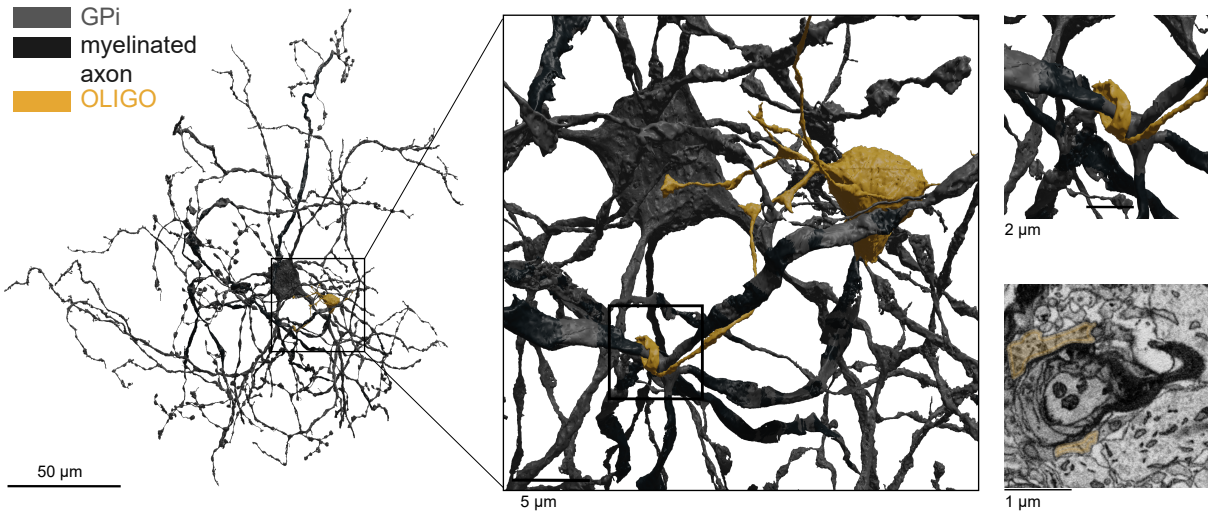

Figure 3.44: An oligodendrocyte wraps one of its processes around the axon of a GPi neuron. The myelinated part of the axon is shown in black. Since myelin is not segmented, the oligodendrocyte and the GPi are not in direct contact in the 3D rendering. The oligodendrocyte ID: 700174676, GPi ID: 63431281. Coordinates of the inset: 9841, 25211, 3117.

Discussion

4.1 EM raw data quality and artefacts

The dataset discussed in this thesis, j0251, was acquired using serial block-face electron microscopy (SBEM, Kornfeld 2017) and includes neurons, glial cells, their subcellular structures, blood vessels, and an estimated 9.6 % extracellular space (ECS).

In the native brain, the ECS content is around 15 % which can be measured with cryo-fixation (Korogod et al. 2015). To stain and image samples over 200 µm thickness in EM, cryo-fixation is insufficient and samples are commonly fixed with aldehydes (Korogod et al. 2015, Studer et al. 1995). During aldehyde fixation, ions from the ECS enter the cellular compartments, causing the ECS to shrink and the compartments to swell, a process similar to oxygen deprivation (Harreveld et al. 1967, Harreveld et al. 1967, Harreveld et al. 1968). Increasing the pressure during perfusion or the osmolality of the fixative buffer during immersion fixation (Cragg 1980, Pallotto et al. 2015) can counteract this effect in small samples and was used to prepare this dataset. With 9.5 %, the current dataset has a higher ECS than without these measures (2.5 %, Korogod et al. 2015) but it does not reach the level of the native brain. Although the goal is to preserve the native brain as much as possible, only 6 % of the ECS is sufficient to improve automated segmentation (Pallotto et al. 2015).

Among the aforementioned approaches, only the unbuffered sucrose solution was able to preserve the ECS and its contents in larger (2.5 mm) zebra finch samples. This approach had previously only been used on mouse retina samples (Pallotto et al. 2015). A recent approach involving a mannitol gradient during perfusion enabled ECS preservation in the entire mouse brain (Lu et al. 2023). Together with other protocols that allow for whole-brain staining in mammals (Lu et al. 2023, Mikula et al. 2015, Song et al. 2023), this could be a promising approach to stain larger samples in songbirds as well.

In both the current dataset and larger samples, artifacts remained, showing damaged tissue around the blood vessels. These artifacts have also been reported during whole-brain staining (Song et al. 2023) and may be more common as most staining papers do not discuss blood vessels. Light microscopy experiments have shown that these artifacts appear during fixation. These artifacts did not appear in the current experiments or published datasets with low or no ECS (The MICrONS Consortium 2025, Turner et al. 2022). Neither the artifacts around the blood vessels nor the rare cutting artifacts hindered the analysis, nor did the distribution of synapses indicate that a specific synapse type was more frequent around blood vessels. However, to preserve the brain as close to its native state as possible and avoid missing information, future protocols should aim to prepare samples that preserve ECS without introducing artifacts around blood vessels.

4.2 Data processing for connectomics

To enable biological analysis of the data set, several steps of the existing processing pipeline had to be updated. These steps included synapse, mitochondria, and cell type prediction. Additionally, new organelles, such as the ER, GA, and individual vesicles, were predicted to allow for further analysis of cellular morphology.

4.2.1 Improvement of synapse and mitochondria segmentation and cell type classification

Compared to the initial release of the dataset (Schubert et al. 2022), the synapses, mitochondria and cell types were updated.

Synapse segmentation

For synapses, a new ground truth was used for prediction of their segmentation and for the RFC. This ground truth and the RFC included synapses from all adult neuronal cell types identified in j0251 to avoid biasing the prediction toward more frequent cell types. The resulting RFC confidence was manually verified, leading to fewer synapses overall and greater accuracy of the predicted synapses. The synaptic area was used for analysis because it has been shown to correlate with synapse strength in vivo (Holler et al. 2021).

Based on their appearance in EM of vertebrate tissue, synapses can be categorized as either asymmetric (excitatory) or symmetric (inhibitory) (Colonnier 1968, Gray 1959). In j0251, the different appearances of synapses were used to manually verify the indentity of cell types and collect ground truth data but was not used on the level of individual synapses to predict their sign. Thus, all circuit mechanism assumptions assumed that synapses within one cell type are either all symmetric or all asymmetric.

While the aforementioned categorization is useful for identifying glutamatergic and GABAergic synapses, it is less effective for identifying ACh or DA synapses. In this dataset, as well as in reports from rodents and reptiles, both ACh and DA neurons make symmetric synapses (Cragg et al. 2004, Henselmans et al. 1994, Izzo et al. 1988). The effect on the postsynaptic cell type depends on the postsynaptic receptor. For TANs, the effect on MSNs is excitatory, while for DA, the effect on STN and MSNs of the direct pathway is excitatory. The effect of DA on MSNs of the indirect pathway, however, is inhibitory (Abudukeyoumu et al. 2019, Cragg et al. 2004, Gerfen et al. 1990).

Additionally, co-release with other neurotransmitters has been reported for TAN and DA neurons (Hnasko et al. 2012, Morales et al. 2017). DA-glutamate co-release has been found in different locations on the same axon, where glutamate-containing vesicles are in axon terminals that form asymmetric synapses (Zhang et al. 2015). Neurotransmitter release independent of synapses has also been reported for TAN and DA neurons, which will be discussed later (section 4.5.2). Due to the assumption that the sign of all synapses is similar within one cell type, the discussed results would not be suitable to identify differences based on co-release.

Having more exact measures of the synaptic effect would mean having more information about the type of neurotransmitter at a specific synapse. In drosophila, six different neurotransmitters were identified from EM images alone (Eckstein et al. 2024). Although this study did not address potential co-release, it demonstrates the potential for future studies to predict neurotransmitter types at the synapse level.

The synapses were trained and evaluated for axo-dendritic and axo-somatic connections between

different neurons. Although potential axo-axonic and glia-neuron synapses were predicted, their certainty has not yet been evaluated. References for axo-axonic and glia-neuron synapses are needed. To analyze these connections, future work must first evaluate the performance of the predictions. Additionally, the SyConn framework does not allow for autapses, which were manually identified and could be included in the framework for future analysis (further discussion in section 4.4.2).

Mitochondria segmentation

The mitochondria segmentation was adapted to more effectively distinguish between mitochondria with updated ground truth data and an additional step to erode the outmost layer of the segmentation, resulting in a lower overall volume of mitochondria than before (Schubert et al. 2022). Therefore, the values for mitochondrial volume density are slight underestimations.

Mitochondria exhibit varying shapes and sizes within different neuronal compartments (Thomas et al. 2023, Turner et al. 2022), as well as in astrocytic endfeet in proximity to blood vessels compared to other astrocytic regions (Salmon et al. 2023). In this thesis, differences in mitochondrial density are analyzed and will be discussed later (section 4.3.2). However, differences at the level of individual mitochondria were not analyzed. Although mitochondria are processed as individual meshes, and their surface areas and volumes are readily available, shape descriptors must be extracted from the meshes for further analysis. Future studies should employ these descriptors to analyze differences in individual mitochondria across neurons and glial cells.

Cell type classification

The cell type classification was updated with respect to three changes: 1) improved classification of projecting axons, 2) identification of novel GABAergic interneuron types, and 3) inclusion of four glial cell types and migratory neurons. All these updates resulted from changes in ground truth only, while the neuronal network architecture based on point clouds (Schubert et al. 2022) remained unchanged. Adding these new classes did not affect the network's performance.

Improving the classification of different projecting axon types required generating a more balanced ground truth with respect to fragment length. This was necessary because, compared to neurons in Area X, the ground truth could only be based on fragments that were cut off due to entering the dataset or due to the segmentation's fragmentation because of their thinness. In addition to axons from HVC, LMAN, and VTA, Area X receives thalamic input in Bengalese finches (Nicholson et al. 2018) and thalamic input has also been reported for the mammalian striatum (Powell et al. 1956). These may be included in one of the other projecting axon types, and further studies are needed to identify their morphology in this dataset and predict them as a separate cell type.

The three novel GABAergic interneuron types were identified based on morphological differences. All of them resemble the previously reported fast-spiking (FS) cell type (Farries et al. 2002) and will be discussed in detail later (section 4.3.3).

The glial cell types analyzed in this dataset include astrocytes, microglia, oligodendrocytes, and oligodendrocyte precursor cells (OPCs). These cells were introduced alongside migratory neurons and will be discussed further later (section 4.6). Of all the novel cell types, the only ones analyzed in this thesis that were not predicted by the cell type classifier, but rather identified manually, were the OPCs. Future analyses should include OPCs and rerun the cell type prediction with additional cell classes.

4.2.2 Prediction of ER, GA and individual vesicles

To take advantage of staining several organelles with double-layered membranes and to allow for more analysis of neuronal subcellular structures, the endoplasmic reticulum (ER), the Golgi apparatus (GA), and individual vesicles were segmented. Manual evaluation proved the prediction to be highly accurate, especially with additional filtering for specific compartments, e.g., the axon for individual vesicles.

Reconstructions using machine learning have been performed on individual vesicles and mitochondria in a semi-automated (Kasthuri et al. 2015) or automated manner (Simon et al. 2021), as well as on subsets of ER (Uytiepo et al. 2025). Together with GA and other organelles, automated reconstructions have also been used on individual non-neuronal cells in cell culture (Heinrich et al. 2021), which revealed different organelle distributions in different cell types. However, this dataset is the first available volume EM dataset containing dense reconstructions of cells, synapses, mitochondria, ER, GA and individual vesicles together, spanning several thousand cells. This allows for comparisons of these organelles in several neuronal cell types.

While the ER is a connected network throughout all neuronal compartments (Terasaki 2018, Tsuboi et al. 2021), in this dataset, it could only be processed as individual fragments. Similarly, stacks of cisternae could not be recovered individually, thus underestimating the surface area of these organelles. This is likely due to a resolution limit, as other studies have shown that thin ER, including its membrane contacts with mitochondria, and individual cisternae could only be recovered with a 4-nm voxel size, which was already difficult with an 8-nm voxel size (Xu et al. 2021). However, the voxel size in this dataset is $10 \times 10 \times 25$ nm^3.

For GA, the focus of prediction, evaluation and analysis was on the somatic form. Golgi outposts have also been identified in one or two dendrites, or in the apical dendrite, in the hippocampus (Horton et al. 2005), and rarely in astrocyte endfeet (Kemal et al. 2022). While some GA structures were identified outside of the soma, further work is needed to determine whether they are Golgi outposts or other misclassified organelles.

At the given resolution, most individual vesicles are clearly identifiable, but some cell types, e.g., INT3, have very dense vesicle clouds (see figure 3.18 a) that overlap, and not every individual vesicle may have been recovered. Additionally, glutamate- and GABA-containing vesicles exhibit distinct shapes at high resolution (Korogod et al. 2015), though these differences were not apparent in this dataset.

Although this resolution is sufficient for predicting the ER and Golgi apparatus, as well as individual vesicles, future studies with higher resolution are needed to analyze a connected ER network, resolve individual GA cisternae, and observe different vesicle morphologies based on neurotransmitter content.

4.3 Morphological and organelle differences in neuronal cell types

Updates on cell type classification and organelle prediction were used to analyze differences in neuronal cell type morphology and organelle density.

To evaluate the effectiveness of morphological parameters and organelles in clustering, all adult neuronal cell types within Area X were analyzed collectively. While projecting axons differed in some morphological and organelle density differences and these are enough to classify them (Schubert 2022), these were not as strong as between neuronal cell types within Area X. As they are restricted to one compartment, they could not be separated into different clusters based solely on these characteristics.

4.3.1 Morphological differences in neuronal cell types

To not only classify the cell types based on morphology but also quantify their morphological differences, several morphological parameters were analyzed, such as axon myelination, spine density, and soma area. While these features differed among the cell types, they alone were insufficient for classifying all 12 neuronal types. Including information on the density of subcellular structures in different compartments, such as axon, mitochondria, and synaptic area densities, allowed for the classification of all 12 cell types. Using a recursive feature selection algorithm to select optimal features showed that nearly all additional organelle information was necessary for classification.

The selected feature set is not entirely composed of independent parameters. Parameters such as the median radius and surface area of an axon or dendrite depend on each other directly. The fraction of axon myelination also depends on axon diameter because oligodendrocytes initiate myelination only when a certain diameter threshold is reached (Lee et al. 2012, Matthews 1968). In cultured oligodendrocytes, this threshold is 0.4 µm (Lee et al. 2012). Thus, the feature set could be further improved by selecting only independent parameters.

Although the final selection of features is not universal, the approach of combining morphological information and subcellular densities is sufficient to distinguish these neuronal types. One cell type was not separated as well as the others: LTS. Upon manual inspection, several cells of other neuron types in the same cluster were misclassified. LTS had the fewest ground truth cells of all the cell types. Retraining the cell type classifier with more LTS ground truth cells may improve classification and should be attempted in future studies.

In addition to identifying misclassified cells, manual inspection revealed that some MSN cells in another cluster were mergers. This demonstrates that, even with a classifier in place, this approach can assist in identifying mergers and misclassified cells.

That organelle features help classification and that morphological features can separate these cells has been shown before on a smaller Area X dataset (Dorkenwald et al. 2017, Kornfeld et al. 2020). Clustering based on a latent space extracted by a neural network has also been able to classify neuronal cell types in the same dataset (Schubert et al. 2022). Unlike the current approach, the latent space feature set does not provide clear, quantifiable parameters that could be used to identify these cell types in other datasets or with different techniques.

The feature set selected for this thesis relied on nearly complete neurons, as several features relate to axon and dendrite morphology. It has been demonstrated for several cortical cell types that a feature set based solely on nuclear and somatic features, without information from additional somatic organelles, can distinguish between excitatory, inhibitory, and glial cell types in a connectomics dataset derived from the mouse cortex (Elabbady et al. 2025). In combination with somatic features and features from spines up to 60 µm away, several inhibitory classes could be predicted. Thus, the classification approach is not dependent on complete reconstructions. This approach is based on a hierarchical clustering system that first separates neurons from glial cells and then classifies neuronal subtypes further (Elabbady et al. 2025).

In this dataset, some cell types also express different nuclear morphologies. For example, half of the GPis had wrinkled somata, and 29 % of the STNs had nuclear infoldings. Therefore, including a nucleus segmentation that quantifies these features could also aid in classifying cells in this dataset or in Area X in general. Additionally, organelle information from and around the soma could be used to incorporate more parameters into this approach.

4.3.2 Organelle densities in different neuronal cell types

The density of synapses, mitochondria, vesicles, ER, and GA were analyzed for neuronal cell types in different compartments. Significant differences were observed among all of these cell types. Mitochondria volume density in the axon, dendrite, and soma; vesicle cloud volume density; vesicle density; and axon ER surface area density showed strong correlations with reported firing rates during singing. This has been shown for axon and dendrite mitochondrial volume density, as well as for vesicle cloud volume density, in a smaller dataset of Area X for three coarse classes: MSN, INT, and GP (Dorkenwald et al. 2017). Note that the correlation with axon density was the highest, possibly because the inclusion of projecting axon classes made more cell types available (eight cell types versus five). Nevertheless, the strong correlation between axon ER area density and firing rate, as well as the density of individual vesicles and firing rate, has not been measured before. The reason only the axonal ER density (when normalized to the skeleton pathlength) is correlated to the reported firing rates but not the dendritic density is also in part due to the dense ER in MSN dendrites, which have a low reported firing rate (see table 2.11, Goldberg et al. 2010). As this is the first time MSN ER densities are analyzed in this matter, the reason for their high ER densities remains to be elucidated.

Mitochondria are related to energy production, and both mitochondria and the and ER are related to Ca^{2+} storage (Devine et al. 2018, López-Doménech et al. 2023, Tsuboi et al. 2021). In mouse pyramidal cortex neurons, higher spike frequencies have also led to increases in mitochondrial Ca^{2+} (Stoler et al. 2022). Conversely, GA has been associated with protein sorting and modifications (Chen et al. 2023, Mohan et al. 2023). Thus, the correlation between mitochondria and ER and the firing rate that is absent for GA is in line with the literature. However, as discussed previously (section 4.2.2), GA is not predicted as stack of individual cisternae; thus, the surface area is not predicted accurately, which may influence these results. GA has been correlated with morphology because it is oriented toward the apical dendrite in hippocampal pyramidal neurons, but not in symmetric GABAergic interneurons (Horton et al. 2005). Further analysis could examine the relationship between GA and cellular morphology in the current dataset.

Other than overall power demand, in drosophila larvae it was shown that across the axon, mitochondria are larger and have a higher density in terminals with higher power demands (Justs et al. 2022).The distribution of mitochondria along the axon has not been analyzed in this thesis. In some cell types, such as GPi (3.17 a), mitochondria seem to be concentrated mainly in the boutons. Whether there are differences in shape or density between boutons needs to be determined by further analysis. In addition to local changes in density, changes in mitochondrial ultrastructure have been reported in faster-spiking cells in the hippocampus (Cserép et al. 2018). These mitochondria have a higher crista surface area density and are more elongated. Whether these differences in mitochondrial ultrastructure can be analyzed within the resolution of this dataset needs to be investigated further.

The high correlation between axon mitochondria and ER density and the reported firing rates in the literature enabled prediction of the firing rates of three novel GABAergic interneuron types (further discussed in section 4.3.3) and STN. Previously, STN had only been recorded at 20 Hz in Area X brain slices, but not during song (Budzillo et al. 2017). While the total mitochondria volume density indeed predicted a firing rate of 20 Hz for the STN, this prediction is not likely due to the physiologically not possible prediction of less than 0 Hz for INT2 with the same parameter. All other predictions with parameters that were both highly correlated with the firing rate and physiologically plausible ranged from 31.5 to 62 Hz (see appendix table A31). Future studies with STN recordings during singing will need to determine the exact firing rate and clarify which parameter best correlates with it.

4.3.3 Novel GABAergic interneuron types

Three novel GABAergic interneuron types, INT1-3, were identified in Area X based on different morphologies and organelle densities. These types resemble previously identified FS-type interneurons (Farries et al. 2002). They also have distinct connectivity profiles that differ from those of other GABAergic cell types in the dataset, such as MSN, LTS, GPe, and GPi. Thus, together with LTS neurons, Area X includes four GABAergic interneuron types. However, this finding differs from a recent single-nucleus RNA sequencing study that identified eight non-pallidal GABAergic interneuron types in Area X (Xiao et al. 2021). Without further morphological quantification, it is unclear whether the other four interneuron types were overlooked in this study or if they correspond to morphologically and connectivity-wise similar subpopulations of the described interneuron types.

The morphology and connectivity of the three novel GABAergic interneuron types, together with firing rate predictions from the different organelle densities, allow for a detailed description.

INT1 neurons have a medium-sized soma, low spine density, and localized, dense axonal arborizations. They are mostly innervated by LMAN, depending on the filtering criteria of the projecting axons (section 4.4.1). They also receive input from other INT1 neurons, and their targets mainly include GPe and GPi neurons. Predicted firing rates range from 35 to 120 Hz. Since striatal interneurons do not project outside the striatum by definition, neurons that mainly target the GPe and GPi are unlikely to be similar to striatal interneurons. Several neuronal subtypes have been identified in both the GPe and the GPi, apart from the projecting neurons of the basal ganglia pathways (Courtney et al. 2023, Miyamoto et al. 2022, Saunders et al. 2018). Both the GPe and the GPi also receive cortical projections (Naito et al. 1994). Future studies of the mammalian pallidum and Area X are needed to determine whether INT1 neurons are similar to these cell types in terms of molecular markers, morphology, and connectivity.

INT2 neurons have small somata and spiny dendrites with denser and larger arborizations than MSNs. Their main input comes from HVC, GPe, and GPi neurons, and they almost exclusively target MSNs. The predicted firing rate is lower than that of INT1 and INT3 neurons, except for vesicle cloud or density, and ranges from 14 to 170 Hz. In the mammalian striatum, apart from FS and LTS interneurons, neurogliaform (NGF) interneurons and arkypallidal neurons in GPe are GABAergic and target mainly MSNs (Ibáñez-Sandoval et al. 2011, Mallet et al. 2012). NGF neurons express neuropeptide Y, have round somata, dense, highly branched, and sparsely spiny dendrites, as well as dense axonal arborizations. They receive input from the cortex (Ibáñez-Sandoval et al. 2011). Arkypallidal neurons in the GPe express preproenkephalin and have branched, spiny dendrites with short, local axon collaterals in the GPe and large, dense axonal arborizations in the striatum (Mallet et al. 2012). They receive input from prototypical GPe neurons and become disinhibited when MSNs are activated via those inputs (Aristieta et al. 2021). In addition to MSNs, they target other striatal GABAergic interneurons and TANs (Mallet et al. 2012).In vivo, their activity is sufficient to inhibit movement in mice (Aristieta et al. 2021).

In addition to targeting MSNs, INT2 neurons exhibit characteristics of both NGF and arkypallidal neurons. Their HVC input and dense axonal arborization resemble NGF, while their spiny dendrites and prototypical GPe innervation, which place them in an MSN-GPe-INT2 feedback loop, resemble arkypallidal neurons more. Further studies measuring their electrophysiological properties and molecular markers are needed to determine whether they are analogous to either of these mammalian cell types or if they are a unique type of interneuron found only in birds.

INT3 neurons have large somata, spiny dendrites, and large, dense arborizations with frequent, large boutons that are densely filled with vesicles. 54 % of these neurons also form at least one autapse. They receive input primarily from HVC and target MSNs almost exclusively. They have the highest

predicted firing rates, ranging from 100 to 360 Hz. In the mammalian striatum, FS neurons, identified by parvalbumin expression, have spiny dendrites, dense axonal arborizations, and a high firing rate of up to 199 Hz. Around half of these cells form autapses (Wang et al. 2023). FS neurons are the primary source of feedforward inhibition from the cortex to MSNs in the mammalian striatum. They also receive thalamic input (Gittis et al. 2010, Johansson et al. 2020, Owen et al. 2018). They are reported to synapse onto MSNs from both the direct and indirect pathways; however, results vary as to whether they prefer MSNs from the direct pathway (Gittis et al. 2010) or not (Johansson et al. 2020, Owen et al. 2018). In this dataset, INT3 cells are the strongest source of feedforward inhibition to MSNs, but only from HVC and not LMAN. As discussed previously (see section 4.2.1), thalamic input to Area X has been reported, but the projecting axon types have not been identified separately.

Overall, there is strong evidence suggesting that INT3 is analogous to the mammalian FS type and that it drives feedforward inhibition from HVC to MSN.

4.4 Connectomic analyses of the Area X dataset

The connectivity of novel GABAergic interneuron types was analyzed alongside known interneuron and projecting neuron types to provide a comprehensive overview of connectivity in Area X. Additionally, the analysis focused on the direct pathway and topographic loops in Area X.

4.4.1 Connectivity between neuronal cell types in Area X

Basal ganglia pathways

In the canonical view of basal ganglia in vertebrates, there are three main basal ganglia pathways: direct, indirect and hyperdirect pathway. Connectivity analysis revealed that analogues of all three pathways also exist in Area X.

While previous single-nucleus RNA sequencing in Area X found separate MSN populations (Xiao et al. 2021), which have also been found in zebrafish (Tanimoto et al. 2024) and in mammals are separable also based on morphology (Gertler et al. 2008, Gagnon et al. 2017), MSN could not be separated based on morphology or connectivity in this study. Since 73 % of MSNs in this dataset project to both GPe and GPi, there is no clear separation between the direct and indirect pathways at the MSN level in this dataset. Consistent with this in one study over half of the MSNs in Area express both D1 and D2 receptors (Kubikova et al. 2010) and pharmacological measurements suggest DA receptor colocalization in a large number of MSNs (Ding et al. 2002). In single-cell nucleus sequencing however, only 18 % of MSNs expressed both receptor types, while 33 % did not express either (Xiao et al. 2021).

Most of the remaining MSNs were selective for GPi, with only a small population (3 %) that projected to GPe. Even fewer neurons projected to GPe when considering only MSN cells with complete dendrites in the dataset. Along with their generally shorter axons and somata closer to the border of the dataset, it is unclear whether there is a small population of MSNs that specifically target the GPe or if this is a dataset artifact. While previous studies also found that the MSN population only expressing the D2 receptor is the smallest group of MSNs, the reported numbers of 14-15 % were still higher than MSNs that project to the GPe in this dataset. (Kubikova et al. 2010, Xiao et al. 2021).

However, the preference for GPi differs from that of mammals, in which 36 % of MSNs project to the GPe only, and all direct pathway MSNs send axon collaterals to the GPe (Wu et al. 2000). MSNs

that express both D1 and D2 receptors project exclusively to the GPe (Bonnavion et al. 2024). The population of MSNs that express both D1 and D2 receptors makes up between 2 and 17 % of MSNs in the striatum, depending on the region and measurement technique (Bonnavion et al. 2024, Gagnon et al. 2017). The existence of this D1/D2 MSN population and the projection of all MSNs to the GPe in mammals suggests that the lack of separation between the direct and indirect pathways at the MSN level may not be specific to the zebrafinch. The difference in preference for the GPe and GPi may be partially explained by the different spatial arrangements in Area X compared to the mammalian basal ganglia. In mammals, the GPe is located next to the striatum, while the GPi/SNr is farther away (see figure 1.3). In Area X, however, distance is not a constraint. Further studies are needed to investigate the shift to GPi-default connectivity, as well as to determine if a GPe-specific population exists in Area X and which dopamine receptors are expressed there.

Based on the overall connectivity throughout the dataset and the influence of MSN connectivity on the GPi, the "gatekeepers" of Area X's output, the direct pathway is the strongest through Area X. The hyperdirect pathway is the second strongest, while the indirect pathway (either the long version via the STN or the short version) is the weakest (see figure 3.30).

This connectivity establishes the hyperdirect pathway as the strongest antagonist of Area X. The weak connectivity and lack of separation from the direct pathway at the level of MSNs raises the question of whether learning with the direct and hyperdirect pathways is sufficient in Area X and the indirect pathway is not needed in its function as an additional inhibitor of movement.

This view is supported by analyses showing that both the MSN and the STN prefer the GPi over the GPe, both in terms of connectivity and synapse size. Meanwhile, the GPe's main output targets are the INT2 and INT3. As previously discussed (see section 4.3.3), these predominantly target MSNs, placing GPe at the center of an MSN-GPe-INT2/3 feedback loop partially mediated by GPe-INT2 spine synapses (see figure 3.30). Since GPe projecting neurons (or prototypical GPe neurons) also project to arkypallidal neurons, a similar feedback loop has been described in mammals that leads to the inhibition of MSNs and locomotion (Aristieta et al. 2021). Along with cortical and dopaminergic input to the GPe, the traditional view of the GPe as primarily part of the indirect pathway has also recently been challenged in mammals (Naito et al. 1994, Courtney et al. 2023).

Due to the strong synaptic output from the GPe to the INT2 and INT3, the weak connectivity of the indirect pathway, and the lack of MSN separation, being part of the MSN-GPe-INT2/3 feedback loop appears to be the primary function of the GPe in Area X, rather than an additional function. Potential roles for this feedback loop could be to reset MSNs to a default state after their inhibition or synchronization of MSNs.

Functional studies in Area X are needed to determine whether this connectivity pattern has functional implications and what role it fulfills. Connectomic studies of the mammalian basal ganglia must test whether a closer examination of the GPe would reveal a similar connectivity pattern or whether this pattern is specific to Area X.

Further connectivity in Area X

The role of GPe neurons as part of a feedback loop rather than as part of a feedforward pathway is not the only connectivity pattern that arose outside of basal ganglia pathways.

A second finding is the back projection from GPi to STN, which is partially mediated by somatic input and cell-specific recurrency. This has not been previously reported in the mammalian literature (Shipp 2017, Tisch et al. 2004). Since DA can reduce GABAergic inhibition to the STN (Cragg et al.

2004) and high, tonic firing of GPi (Goldberg et al. 2010), this could result in STN inhibition in the default state, which restricts STN firing in the absence of DA input during learning.

Another potential role is the lateral inhibition of neighboring GPis. In this case, once a GPi is inhibited by MSNs, an STN cell is released from inhibition and can excite surrounding GPis. In the DLM, MSN activation leads to disinhibition. There, MSN activation mainly excites a DLM neuron activated by a specific GPi while silencing others that are more controlled by neighboring GPis. Therefore, if a GPi inhibits an STN that projects mainly to its neighbors, it could lead to a more defined signal in the DLM. To test this theory, a larger Area X dataset combined with synaptic information about DLM innervation would be necessary.

The connectivity profile of TANs revealed that they primarily receive input from MSN and HVC, and their main output target is also MSN. This is consistent with the mammalian striatum, where TANs receive input from cortical and thalamic regions, as well as from MSN. However, TANs also target other striatal interneurons (Abudukeyoumu et al. 2019, Johansson et al. 2020). As discussed previously (see section 4.2.1), thalamic input was reported for Area X, though it was not classified separately in the data.

Rather than forming recurrent connections with MSNs, TANs target many and only receive feedback from a few. This is consistent with the suggested coordinating role of TANs in the striatum (Graybiel et al. 1994).

Together with DA and LTS, TAN belongs to a group of cell types with low synaptic density that exerts little synaptic influence on other cell types (see figure 3.31). For TAN and DA, this relates to their modulatory role using volume transmission, which will be discussed later (see section 4.5.2).

For LTS, low synapse density and little synaptic influence on other cell types are consistent with findings in the mammalian striatum (Gittis et al. 2010, Ibáñez-Sandoval et al. 2011). While their major output target there is also MSN, results in this dataset show GPi as one of the major input sources, next to the reported cortical input. These results suggest a potential feedback and feedforward role; however, due to the small number of synapses, it may be difficult to test this functionally. Similar to DA and TAN, which have known modulatory roles, a modulatory role has also been suggested for LTS due to its low synapse density, potentially to release somatostatin or neuropeptide Y (Gittis et al. 2010, Ibáñez-Sandoval et al. 2011). In line with this, half of the very few vesicles in LTS axons are non-synaptic in this dataset (see figure 3.37). Further studies are needed to verify this modulatory role and identify the released neurotransmitter.

Although there are differences in innervation from the HVC and the LMAN, connectivity analyses in this thesis have focused primarily on Area X cell connectivity. These differences include the fact that HVC predominantly innervates MSN spines while LMAN innervates MSN spines and shafts to a similar degree, as previously reported (Kornfeld et al. 2020), and that INT1 is the only cell type that is innervated more by LMAN than by HVC. The reason for this focus is that, due to axon fragmentation, the fractional connectivity input from the LMAN and HVC to other cell types depends on the filtering criteria. When only long axons are included, LMAN axons are favored due to their branching morphology, and connectivity with cell types within Area X is underestimated because most synapses in the dataset are excluded. Conversely, when all fragments are included, every cell type receives input mainly from HVC, and the input relative to the filtered cells within Area X is overestimated. Apart from these differences, all connectivity patterns remain stable regardless of the filtering criteria. Further studies are needed to investigate the importance of cortical inputs relative to neurons within Area X.

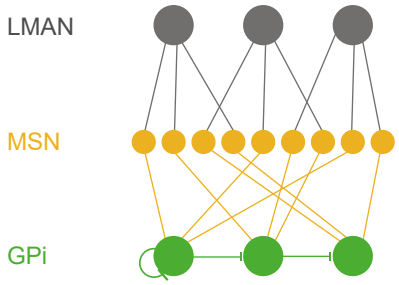

Figure 4.1: Current model of LMAN-MSN-GPi connectivity within the Area X dataset. The LMAN indirectly synapses with a significant portion of the GPi via MSN connections. The GPi is controlled by inhibition from other GPi cells via "soma claws." More than one-third of GPi cells form autapses.

4.4.2 LMAN - MSN - GPi specificity

To investigate axon projection in more detail, a small sample of large LMAN axons was selected for analysis of connectivity in Area X with respect to topographical loops.

In comparison to HVC, LMAN projects to Area X topographically onto Area X. Along with connections from Area X to DLM and from DLM back to LMAN, these form closed loops in light microscopy (Luo et al. 2001, Fee et al. 2011). With large LMAN axons entering the dataset and branching there, it is possible to analyze and determine how "focused" this loop is. Since the direct pathway is strongest pathway through Area X in terms of synaptic area, information flow from LMAN is most likely to lead over MSN to GPi. In a "focused" loop, one LMAN axon indirectly projects to only one GPi cell. In an "unfocused" loop, however, it indirectly projects to all GPi cells in the region (see figure 3.32).

The results show that the loop is "unfocused," with each LMAN axon projecting indirectly to most of the GPi, and there is no clear "winner" in terms of synaptic area. Additionally, the GPi synapses onto itself with multiple soma synapses, resulting in "claws" or "baskets". These have been previously observed from the GPi to the DLM and to the GPi soma. However, it was unclear whether GPi neurons were the source of these connections to other GPi neurons (Luo et al. 1999). To complete the picture of GPi connectivity, approximately a third of the GPis also form autapses (see figure 4.1).

Area X is estimated to contain 500,000 cells (Burek et al. 1991). If 94 % of these cells are MSN cells, as in this dataset, then there are an estimated 470,000 MSNs in Area X. Together with approximately 2,300 GPi cells (Farries et al. 2005), this leads to massive convergence within Area X. This convergence can be measured in the data, with each GPi neuron receiving over 1,000 synapses from nearly 400 different MSNs. The number of MSNs is estimated to be high enough, so that each muscle fibre could be represented with up to 100 time points in the song (Fee et al. 2011), while maintaining temporal precision through convergence to the GPi by activating different GPis at different time points.

Following the feedback loop through the anterior forebrain pathway (AFP), the GPi projects to approximately 3,750 neurons in the DLM (Farries et al. 2005) which project to 6,000 - 10,000 LMAN neurons. In juveniles that are still learning their song, this number is doubled, leading to 12,000 - 20,000 LMAN neurons (Burek et al. 1991, Bottjer et al. 1989). The LMAN neurons, in turn, project topographically to 15,000 – 17,000 RA neurons (Burek et al. 1991, Gurney 1981). To innervate the approximately

7,000 muscle fibers in the syrinx (Adam et al. 2021), the RA innervates 800–1,100 neurons in the tracheosyringeal branch of the hypoglossal nerve (NXIIts, Adam et al. 2021, Gurney 1981, Lissandrello et al. 2017). With 50 % of the motor neurons in NXIIts innervating $\leq$ 3 muscle fibers, the motor pathway exerts extremely fine control over the vocal muscles (Adam et al. 2021). Since the topographical loop is closed and muscle control is high, if this pattern were maintained in the AFP, up to 20 neurons in the RA and LMAN, as well as a few GPis, would be responsible for one muscle fiber. Synaptic connectivity would favor only up to three GPi that one LMAN axon indirectly synapses to. However, this level of topography is not reflected in the data. Given the number of neurons in NXIIts, it seems too high a number for one LMAN to synapse to over 40 GPis indirectly in order to separate individual muscle fibers throughout the whole AFP. It is hypothesized that the topography in the AFP reflects individual motor channels (Fee et al. 2011), but it is unclear which proportion of a muscle is represented in a motor channel. Since the results did not vary across the dataset, it is likely that one motor channel spans a larger volume than the current dataset. Further analysis of a larger volume is needed to analyze connectivity with respect to motor channels and determine their size.

If the connectivity from LMAN via MSN to GPi alone does not reflect distinct units for individual muscle fibers, then additional mechanisms must be in place to strengthen the signals of additional GPis. One possibility is lateral inhibition of STNs, whereby activation of one GPi activates its neighbors, which then silence surrounding neurons in the DLM, as discussed previously (see section 4.4.1). Another mechanism could be the inhibition of GPis by each other, as seen in the form of "soma claws". Inhibiting one GPi would lead to less inhibition by its neighbors, resulting in a similar effect to lateral inhibition.

Another function of GPi-GPi inhibition could be synchronization of the network. When inhibitory neurons are recurrently coupled, they oscillate in anti-phase. If a third inhibitory neuron provides long enough input to both of these neurons, the third input can synchronize the other two neurons, even if it is weak (Belykh et al. 2008). It is unclear if any of the GABAergic inputs to GPi cells, MSN, GPe, or INT1 are able to provide the necessary input for synchronization, and this needs to be determined in further studies. Additionally, it remains to be tested whether GPi-GPi connectivity is recurrent or if each GPi inhibits other cells to form a uniform network.

Another feature influencing GPi network activity is the presence of autapses on 41 % of GPi neurons. GPi is not the only cell type that forms autapses; 31 % of GPe and 54 % of INT3 neurons also form them. While autapses have not been reported in Area X or the mammalian GPe, GPi, or SNr, they have been reported in the FS of the striatum (see section 4.3.3) and the cortex (Bacci et al. 2003).

In FS, autapses help maintain high firing frequencies (Wang et al. 2023), increase the regularity and precision of spike times (Bacci et al. 2006) and help sychronization, particularly in networks that are already coupled by inhibitory connections(Deleuze et al. 2019, Jia et al. 2023).

In mammals, FS interneurons and projecting neurons of the GPe and GPi express PV (Courtney et al. 2023, Miyamoto et al. 2022). Since these cell types have high tonic firing rates, autapses likely exist in the mammalian GPe and GPi, fulfilling similar functions as in Area X. These could include maintaining high firing rates, making firing more precise, and aiding synchronization among a coupled GPi network. Further studies are needed to investigate this.

4.5 Synaptic and non-synaptic vesicles

In addition to analyzing the connectivity and overall density of the different organelles, we examined the relationship of individual vesicles with synapses, as well as those distant from synapses, to study volume

transmission from TAN and DA axons.

4.5.1 Synapse size and relationship to number of vesicles

There is no global correlation between synaptic size and the number of synaptic vesicles across the dataset, nor for those close to the membrane. However, some cell types, such as HVC and INT1, show correlations when analyzed individually.

Previous reports on rat hippocampal neurons have shown that the number of vesicles correlates with synaptic area (Harris et al. 1989) , that only the number of docked vesicles, but not the total number of vesicles, correlates with synaptic area (Branco et al. 2010), or that both the number of vesicles and the number of docked vesicles correlate with synaptic area (Murthy et al. 2001). In the mouse neocortex, larger synapses have been shown to also have more synaptic vesicles (Kasthuri et al. 2015).

One reason the membrane-close vesicles do not correlate with the synaptic area is that membrane closeness does not indicate whether the vesicles touched the membrane. Thus, they are not comparable to reports about docked vesicles. Some vesicles that touch the membrane may also be excluded by the filtering criteria. Further analysis may be needed to determine whether using the mesh of the synapse object and the distance of the vesicle from it can indicate whether a vesicle is touching the synaptic membrane.

Furthermore, fixation with aldehydes may result in a depletion of docked vesicles because this tissue exhibits fewer vesicles in close proximity to the synapse than cryo-fixed tissue (Korogod et al. 2015, Maus et al. 2020). However, since previous papers reporting correlations also used aldehyde fixation on their samples (Branco et al. 2010, Harris et al. 1989, Murthy et al. 2001), it is unclear whether this explains the differences in correlation.

One difference from the reported studies is that the synapses analyzed were exclusively on spines. In the present dataset, all cell types except MSNs have more synapses on their dendritic shafts. Additionally, if a bouton has more than one outgoing synapse, the number of vesicles is higher (Harris et al. 1989, Kasthuri et al. 2015, Uytiepo et al. 2025). This may explain why synapses from HVC are among the most highly correlated and primarily target MSN spines. However, INT1 mainly targets the dendritic shaft of the GPe and GPi, upon manual inspection often shows more than one synapse per bouton and also exhibits high correlations. Therefore, further analysis should control for the number of synapses on the presynaptic bouton and the different postsynaptic compartments when testing for correlation.

In addition to vesicles, mitochondria and ER are also located close to synapses, on both the presynaptic and postsynaptic sites.

At the presynaptic site, boutons containing mitochondria exhibit lower levels of cytosolic Ca^{2+}, reduced neurotransmitter release, and larger vesicle pools compared to boutons lacking mitochondria (Kwon et al. 2016). One study using EM showed that boutons with mitochondria had higher vesicle numbers and were weakly correlated with larger spine heads in the mouse neocortex (Kasthuri et al. 2015), while another study in mouse hippocampus showed that the synaptic area does not correlate with the presence of presynaptic mitochondria but with the presynaptic mitochondria volume (Cserép et al. 2018). Mitochondria were also more prevalent in boutons with multiple synapses, and their volumes increased during learning (Uytiepo et al. 2025).

Along the dendrite, mitochondria are present on the postsynaptic site and rarely inside spines (under 1 % of spines, Kasthuri et al. 2015). ER is present in the dendritic shaft and inside spines, sometimes forming multiple cisternae as the spine apparatus (SA). Generally, the volume of the spine head is correlated with the synaptic area onto the spine (Harris et al. 1989, Holler et al. 2021). Dendritic mitochondrial volume

density is also correlated with spine density (Turner et al. 2022). When an action potential backpropagates into the dendrites and coincides with an excitatory postsynaptic potential (EPSP) there, mitochondrial Ca^{2+} elevates in close proximity to active spines (Stoler et al. 2022).

Mitochondria in dendritic shafts are not correlated with synaptic areas on spines. However, spines with mitochondria tend to have larger volumes and larger synaptic areas (Thomas et al. 2023). ER reaches at least partially into 50 % of spines (Spacek et al. 1997, Wu et al. 2017). Spines with ER, in the form of an SA, are larger (Dorkenwald et al. 2022, Wu et al. 2017), and ER is present in 80 % of large mushroom spines (Cooney et al. 2002, Spacek et al. 1997). The synaptic area of a spine also correlates with the number of cisternae in the SA, and measurements of four spines suggest a potential correlation between SA volume and surface area (Spacek et al. 1997).

There are conflicting reports about SA in learning. One study of the mouse hippocampus reported an enlargement of spines accompanied by a loss of SA in spines (Uytiepo et al. 2025), while another study of the rat hippocampus found that only synapses with SA present enlarged during long-term potentiation (LTP, Chirillo et al. 2019). Some enlargement was also observed in spines with polyribosomes, but it was smaller than that observed in spines with SA. Additionally, LTP led to an increase in ER volume in spines with SA and redistributed ER to areas with at least one spine with SA (Chirillo et al. 2019).

In addition to their relationship with synapses, the ER and mitochondria are reported to establish connections in all neuronal compartments (Wu et al. 2017).

Together, the reported studies suggest a relationship between the presence of mitochondria and ER and the larger volume and surface area of these organelles in larger synapses, at least in spines. Whether the ER area is larger close to larger synapses in presynaptic boutons and if there is a relationship with the number of synapses similar to that of mitochondria is unclear. Further investigation is needed to determine whether the reported correlations for the ER, mitochondria, and vesicle number with synapse size in spines are similar in birds and whether similar correlations can be found with synapses on dendritic shafts.

4.5.2 Single vesicles in TAN and DA axons

TAN and DA are cell types that have been reported to signal via volume transmission (Abudukeyoumu et al. 2019, Arbuthnott et al. 2007). Consistent with this, the axons of TAN in DA exhibit low synapse density and a high proportion of vesicles close to the cell membrane distant from synaptic locations.

Environment of TAN and DA non-synaptic vesicles

The surroundings of these vesicles mirrored the distribution of cell types and synapses in the dataset, with MSN cells and HVC-MSN synapses as the most prevalent. Within a 1 µm distance, GPe and GPi surface areas were slightly underrepresented for both TAN and DA. Overall, the results for TAN and DA are similar. This is interesting since DA axons are known to project to all of the aforementioned basal ganglia nuclei (Cragg et al. 2004, Tisch et al. 2004), while cholinergic modulation has only been reported in the striatum and GPe so far (Courtney et al. 2023, Dong et al. 2021, Ratna et al. 2025).

In general, DA axons form a dense network. 93.4 % of all synapses and over 90 % of all cell surface area are within a 5 µm radius of a close-membrane, non-synaptic DA vesicle. However, as most predicted DA axons are shorter than the minimum length of 200 µm, this number is likely an underestimation. Conversely, ECS shrinkage due to chemical fixation during sample preparation could result in an underestimation of the measured distances compared to those in a living brain (Korogod et al. 2015).

To ensure TAN classification certainty, the analysis included only TAN axons from cells within the dataset. This explains why only around 6 % of all synapses and cell surfaces are within 5 µm of TAN axons. Since these represent only 4 % of the axon path length in the dataset, it is possible that TAN cells form a similarly dense network throughout the dataset. However, a recent study found that, in the mammalian striatum, individual DA axons cover three times the area that TAN cells do, and that TAN cells can activate DA release independently of soma activity (Liu et al. 2022). When multiple TANs are active simultaneously, they can leverage the DA network to extend their reach. If the DA network is indeed denser than the TAN network, this mechanism could compensate for that.

Results showing synapses and cell surfaces within 5 µm of DA vesicles align with a volume transmission model assuming DA acts within a 7 µm sphere of influence (Cragg et al. 2004), which is temporally, but not spatially, limited (Arbuthnott et al. 2007). In this model, the dense network of DA ensures that all receptors can be reached, and specific synapses and receptors can be targeted with temporal precision. This means that the effects on receptors, whether on- or off-synaptic, are due to previous changes in the membrane potential of postsynaptic cells.

This is all under the assumption that membrane-close vesicles could potentially be released at this spot, even though manual verifications showed that only half of these vesicles touch the membrane, and there are no markers indicating docking of the vesicles. A more recent study found that DA is not released at all vesicle-filled varicosities, but rather, only at around 30 % (Liu et al. 2018). These release sites cannot be identified using EM alone, but rather require protein markers.

Additionally, measuring DA release in the mammalian striatum with nanosensors revealed hotspots with a median size of 2 µm, suggesting a potentially smaller effective radius (Beyene et al. 2019). In this dataset, 35-40 % of surface areas and 37.5 % of synapses were within 2 µm of DA vesicles. If only 30 % of the vesicles were at active sites, then only around 10 % of the cell surface area or synapses would be within reach of one release. Consistent with this, a more recent model, the "dopamine-overlap" model, assumes that, for tonic release, which is responsible for steady DA concentrations, most receptors are not reachable by release from individual active sites (Liu et al. 2021). This model proposes that, for phasic dopamine release driven by excitatory inputs that lead to fast changes in DA concentration, several dopamine axons must be active simultaneously to reach receptors for learning signals. To better understand the dynamics of DA volume transmission, further analysis must identify active sites with synapse resolution, either by finding markers visible in EM or by staining them to analyze with light microscopy-based connectomics (Tavakoli et al. 2025).

For both DA and TAN neurons, co-release with glutamate and, for DA, with GABA, has been reported (Hnasko et al. 2012, Morales et al. 2017). In this study, all vesicles were assumed to contain the same neurotransmitter and were classified only by cell type. Although it has been reported that, as an effect of chemical fixation, presumed GABA-containing vesicles have a more oval shape than glutamatergic vesicles (Korogod et al. 2015), the resolution of the raw data was insufficient to detect these differences in this dataset. Furthermore, it is unclear whether DA- or ACh-containing vesicles could be differentiated based on their shape. Thus, future studies should also verify the neurotransmitter identity when investigating DA or ACh volume transmission.

TAN and DA non-synaptic vesicles and surrounding synapse sizes

Changes in synaptic size can be influenced by modulatory activity from both TAN and DA neurons (Abudukeyoumu et al. 2019, Yagishita et al. 2014). To determine whether these effects are evident in EM, the proximity of non-synaptic vesicles to smaller or larger synapses of different presynaptic and

postsynaptic cell types was studied. The focus was on connections that had been studied in the context of basal ganglia pathways and feedback loops. There was no difference in proximity between most cell type pairs, and if there was a difference, it was small. Most of the reported effects were related to TANs in relation to synapses that were not among the most frequent, which could indicate that these effects were due to smaller sample sizes.

The two effects on more frequent synapses that were discussed as part of the basal ganglia pathways were TAN vesicles, which are more associated with smaller HVC-STN and GPi-STN synapses, but not DA. As mentioned above, there are no reports of cholinergic modulation of the STN thus far (Prasad et al. 2024, Tisch et al. 2004), but DA modulation can reduce GABAergic transmission to the STN (Cragg et al. 2004), which is in contrast to these results. The incorporation of these cells into Area X, in close proximity to TAN neurons, raises the question of whether other cell types have cholinergic receptors in the songbird. Future studies are needed to elucidate the effects of ACh on STN and GPi neurons in Area X.

The small differences were mostly cell type-specific for pre- and postsynaptic partners, e.g., more TAN vesicles were associated with smaller GPi-INT2 synapses, while larger synapses were associated with more vesicles for GPi-INT3 synapses, and slightly more vesicles were associated with larger synapses for GPe-INT2 synapses. INT2 and INT3 are newly identified cell types in Area X, so these results could provide additional insight into their functions, which should be explored further in functional studies.

As mentioned above, this analysis has the limitation of being oblivious to actual release sites, which have been shown for DA (Liu et al. 2018) and could be similar in TAN. This means that if DA only affects synaptic size in proximity to active-like zones, these effects would be missed in the data. Additionally, small differences detected could be spatial artifacts rather than functionally relevant differences. Therefore, all potential effects must be interpreted with caution and verified in future studies using functional analysis or analysis that labels active-like zones.

4.6 Glia and migratory neurons

In addition to several types of adult neurons, astrocytes, microglia, OPCs, oligodendrocytes, and migratory neurons have been identified and analyzed based on their organelle densities and contact areas with neuron types.

The morphology of the aforementioned cell types is consistent with previous literature (Baldwin et al. 2024, Buchanan et al. 2022, Salmon et al. 2023, Xu et al. 2008). However, there are differences between the glial cells described here and those in the living brain.

First, oligodendrocytes have several processes that extend to axons. Due to their thinness, these processes could not be properly segmented in our data and were not properly linked to myelin segments. This restricts the analysis of organelles to primarily the soma and omits most of their contact sites. In a recent connectomics study from mouse neocortex, more of these processes could be segmented (Buchanan et al. 2022, Turner et al. 2022). The current segmentation could potentially be improved by adjusting it specifically for thin oligodendrocyte processes or by adding more to the ground truth segmentations.

Second, chemical fixation alters the morphology of astrocytes, resulting in increased coverage of spines, more intricate morphology with thinner processes between neurites, and greater coverage of blood vessels compared to cryo fixation (Korogod et al. 2015). Therefore, astrocyte contact areas are overestimated in comparison to the living brain.

4.6.1 Organelles in glia and migratory neurons

This is the first analysis comparing the densities of mitochondria, GA, and ER in different glial cell types and migratory neurons. The analysis shows that glial cell types differ in their organelle densities, as well as in comparison to neurons. Astrocytes had similarly high mitochondrial densities as tonically active GPi; however, oligodendrocytes, OPCs, microglia, and migratory neurons had lower mitochondrial densities than MSNs. Regarding GA and ER densities, glial cell types were similar to neuronal cell types, with astrocytes having lower densities than the other glial cell types. Migratory neurons had the lowest densities of mitochondria, GA, and ER. Oligodendrocytes had the highest GA densities, even compared to neurons, but their processes are often cut off, which could lead to an overrepresentation of the soma compared to other cell types.

Since 5-15 % of ATP demand is estimated to be required for astrocyte metabolic processes, high mitochondrial density aligns with high metabolic demand, even though astrocytes are not dependent on mitochondria for energy supply through glycogen stores (Rose et al. 2020). In contrast, a previous study of only four astrocytes and microglia cells did not observe significant differences in mitochondrial density in the somatosensory cortex of rats (Calì et al. 2019). Whether this discrepancy is due to the small sample size or to differences in the developing brain needs to be further elucidated.

Interestingly, the high density of mitochondria in astrocytes is not correlated with high densities of ER or GA, even though astrocytes respond to neurotransmitters with changes in intracellular Ca^{2+} (Durkee et al. 2019) and higher ER density is correlated with higher firing rates in neurons (section 4.3.2). Similar to neurons, astrocytic mitochondria have been associated with modulating Ca^{2+} transients. Mitochondria interact with the ER throughout the astrocyte. Although mitochondria are longer, they make more contacts with the ER, and the ER has a higher surface area in the endfeet regions of astrocytes (Salmon et al. 2023). The ER and mitochondria are also dense near the soma (Baldwin et al. 2024).

Overall, the high mitochondrial density and the compartment-specific differences in ER density suggest that, for modulation of Ca^{2+}, ER may only be necessary at high densities in specific regions, provided that the mitochondrial density is also high. Further analysis should focus on compartmental differences in mitochondria and ER. Additionally, astrocytes have been reported to rarely have Golgi outposts in the endfeet (Boulay et al. 2017), which has not been observed in this dataset but should be analyzed systematically in the future.

Since OPCs and migratory neurons move through the tissue (Hughes et al. 2013, Shvedov et al. 2024), their low mitochondrial and overall organelle densities, respectively, could indicate that migration in the brain is more energy efficient than environmental surveillance or neuronal firing. Further studies are needed to investigate the link between energy demand and organelle density in different glial cell types and migratory neurons.

The organelle densities of microglia and OPCs were similar. These results are consistent with those suggesting that they are similar not only in morphology, but also in function and distribution throughout the brain (Buchanan et al. 2022).

The shapes of organelles differ among glial types and migratory neurons. For example, microglia have been reported to have shorter mitochondria than astrocytes (Calì et al. 2019), while the data showed small, round mitochondria in migratory neurons (see figure 3.41). Further analysis of the shapes and sizes of mitochondria among glial cell types is needed for a more detailed comparison.

4.6.2 Contact areas between glia and neurons

Since all glial cell types interact with neurons and influence the formation of neuronal synapses, contact areas between different glial cell types and neuron types in Area X were analyzed. It should be noted that the presence of a membrane contact does not indicate a functional interaction. However, since there are no established markers for glia-glia or glia-neuron interactions in EM, the contact areas were considered a preliminary estimate.

Astrocytes had the highest contact areas with all cell types, followed by microglia. When normalized to the surface areas of the different cell types, the contact areas were similar, though MSN and LTS had slightly higher normalized contact areas.

The high contact areas of astrocytes with all neuronal types align with their regular ensheathment of synapses as part of the tripartite synapse. As part of this process, individual astrocytes can release multiple neurotransmitters, the effects of which vary depending on the neuronal receptors (Durkee et al. 2019). In the mouse somatosensory cortex, 20 % of synapses were covered by 50 % or more (Yener et al. 2025), but due to the higher coverage of synapses in chemical fixation, this is probably an overestimate (Korogod et al. 2015).

Astrocyte coverage is cell-type specific, with slightly more coverage in excitatory synapses in the mouse somatosensory cortex. This coverage also depends on synapse size. Astrocyte coverage is low in small, multi-synapses, suggesting that it plays a role in LTD (Yener et al. 2025). Additionally, astrocyte coverage of axon terminals correlates with the number of outgoing synapses (Uytiepo et al. 2025). Further analysis should focus on synapse coverage to determine if there are differences in astrocyte coverage of synapses in this dataset. Furthermore, astrocytic mitochondria are closer to denser clusters of synapses (Salmon et al. 2023), so astrocyte synapse coverage should be analyzed in the context of astrocytic organelles as well.

In the mammalian striatum, astrocyte subpopulations have been found to respond specifically to direct and indirect pathway MSNs. Although the analysis of MSNs revealed no distinct subpopulations in this dataset (section 4.4.1), it is conceivable that astrocyte coverage of MSN-GPe and MSN-GPi synapses differs due to variations in synapse size or spine density across the population. These questions should be addressed in future analyses.

As mentioned above, oligodendrocyte myelination could not be properly analyzed automatically because processes were cut off and the myelin was not segmented. However, manually identifying some processes showed that oligodendrocytes were myelinating a GPi. The GPi's axons are not continuously myelinated, as was previously shown in pyramidal axons in the neocortex (Tomassy et al. 2014).

Microglia have been shown to interact with neurons on a large scale by increasing neuronal firing under anesthesia and reducing firing under hyperactivity (Umpierre et al. 2021), as well as on a small scale by influencing synapse formation. In the nucleus accumbens, mice without microglia had fewer excitatory synapses (Gongwer et al. 2025). They can also remove inhibitory synapses (Hashimoto et al. 2023) and in Chandelier cells a type of GABAergic interneuron that synapses onto the axon initial segment of a pyramidal neuron in the cortex, depletion of microglia leads to shorter cartridge length and fewer boutons (Gallo et al. 2022). Microglia can also influence synapse formation directly by contacting a dendrite. Within ten minutes, this dendritic contact is followed by a Ca^{2+}response that leads to filopodia formation and subsequently increases synapse formation, especially in feedforward circuits (Miyamoto et al. 2016). Additionally, depletion of microglia reduces spine density. These effects were demonstrated in the somatosensory cortex of mice within the first eight to ten days of life. Further analysis is needed to determine if microglia preferentially contact neuronal dendrites, if these contacts occur more frequently

in proximity to feedforward synapses (e.g., onto MSNs), and if there is a relationship with MSN spine density.

OPCs have been suggested to prune axons because they frequently form phagolysosomes containing axons, particularly excitatory ones (Buchanan et al. 2022). Further analysis is needed to determine whether they specifically target the axons of neurons within Area X and whether they make preferential contact with excitatory projecting axons.

Reminiscent of their dense surveillance network, astrocytes had the most contact with other glial cell types and with each other. This network develops in the first 15 days in mice and is coupled via gap junctions (Gutnick et al. 1981, Peng et al. 2023, Zhong et al. 2023). Although astrocytes interact with oligodendrocytes via gap junctions (Peng et al. 2023), this interaction is not evident in the data, likely due to the cutoff of oligodendrocyte processes. There are no reports on how the different glial types interact with each other, and further studies are needed to determine whether the reported contact areas are functionally relevant.

Microglia and OPCs span the entire territory with little overlap (Buchanan et al. 2022, Hughes et al. 2013, Kettenmann et al. 2011) forming few contacts with each other. Microglia can form membrane contacts with each other (Peng et al. 2023), but these contacts are rarely observed in the data. Both OPCs and microglia are often in a "satellite" position, touching the soma of other cells, mostly neuronal (Buchanan et al. 2022), which has also ben found for one example among OPCs (cell IDs: 1438305032, 1535070169, coordinate: 4320, 3208, 9284). This could potentially explain the interaction between OPCs, but further analysis is needed to determine the percentage of contacts that result from soma contact.

Overall, the analysis of this dataset provided an initial understanding of glial cell contacts with neuronal cell types, which is consistent with descriptions in mammalian literature, particularly with regard to astrocyte networks and their interactions with other cell types. Since little is known about glial interactions with each other, and whether these interactions are visible in EM, this data can provide new insights for further studies. These studies need to determine how well membrane contacts in EM translate to functional interactions.

Conclusions and Outlook

This thesis focuses on the analysis of a songbird Area X dataset with respect to the morphology and subcellular structures of neuronal and glial cells, as well as their connectivity.

A previously published pipeline (Dorkenwald et al. 2017, Schubert et al. 2022) was used to analyze the current dataset. Improvements were made to the ground truth of cell type classification and synapse prediction to remove artifacts. These improvements led to the identification of three previously undescribed interneuron types and the prediction of glial cells and migratory neurons. Additionally, the prediction and processing of single vesicles, the endoplasmic reticulum (ER), and the Golgi apparatus (GA) were added and accurate prediction of these organelles was manually verified.

The analysis of neuronal morphology and subcellular structures revealed quantifiable differences among cell types that align with existing literature. These findings can be applied to other microscopy techniques for further investigation of the three novel interneuron types. Axonal mitochondria, ER, and vesicle density were correlated with firing rates reported in the literature and led to different proposals for the firing rates of novel interneuron subtypes: INT1, INT2, and INT3. Through the analysis of connectivity, morphology, and organelle densities, the novel interneuron subtypes could be characterized. While it is unclear whether INT1 and INT2 have mammalian analogues, INT3 bears striking similarities to the mammalian FS cell type. Further studies using molecular markers and electrophysiology are needed to determine the identity of these interneuron types. Electrophysiological studies can also help determine which organelle is the best predictor of firing rates during singing.

Overall, organelle information has primarily been studied in the context of volume densities, which can improve cell classification and hint at neuronal activity, as well as glial energy demand. Further analysis is needed to investigate correlations with synaptic area. However, these results show that including organelle information allows us to gain more insight from connectomic datasets than just snapshots of morphology and connectivity.

For the first time, connectivity analyses of neurons in Area X revealed that the three known basal ganglia pathways—the direct, indirect, and hyperdirect pathways—are present with varying degrees of synaptic strength. The direct pathway is the strongest, followed by the hyperdirect pathway, which is its strongest antagonist. The indirect pathway is neither separated from the direct pathway at the level of MSNs nor supported by a large area of synaptic connectivity.

The three novel GABAergic interneuron types differ in their incoming and outgoing connectivity. This connectivity suggests potential roles for INT3 as a feedforward pathway from HVC to MSNs, for INT2 as part of a similar feedforward pathway, and for an additional feedback loop from GPe via INT2 to MSNs. INT1 acts as feedforward inhibition from LMAN onto GPe and GPi. These connectivity patterns demonstrate that these novel interneuron types interact not only with the known basal ganglia pathways

as previously described for striatal and pallidal interneurons, but also play integral roles in them.

With GPe having INT2 and INT3 as their primary output targets, the GPe's primary role, as dictated by connectivity, is to be part of the MSN feedback loop, rather than the indirect pathway, as previously described. This result positions feedback and feedforward loops as major pathways in connectivity alongside the forward basal ganglia pathways. Further studies with functional and behavioral data are needed to determine whether these results are limited to specific temporal conditions during song learning or if they are common.

While not all of the investigated neuronal cell types act primarily via synaptic transmission, hints of volume transmission were also analyzed. In fact, most of the vesicles in cholinergic and dopaminergic axons were found outside of synaptic loci. Although release sites cannot be identified with EM, the surroundings of these non-synaptic vesicles were analyzed and showed no preference for a specific synapse type or cell type. This finding is consistent with a global signal. These results suggest that, if release sites can be identified, connectomics could be a powerful tool for investigating volume transmission.

In summary, this thesis provides new insights into the cell types and connectivity within Area X. The results also demonstrate that volume EM datasets enable the study of various organelles and cell types, not just neurons and synapses. This can aid connectomic analysis by providing clues about cell properties and non-synaptic transmission. Further research on verifying relationships between organelles and cell properties will make connectomics an even more powerful tool, allowing us to bridge the gap between static and functional analyses. Most importantly, this is the first time that connectomics has allowed for a detailed analysis of a basal ganglia area, revealing novel interneurons and connectivity motifs. These results demonstrate new insights into the songbird basal ganglia and show that connectomic analysis is a powerful tool for understanding basal ganglia connectivity.

Bibliography

Abbott, Larry F., Davi D. Bock, Edward M. Callaway, Winfried Denk, Catherine Dulac, Adrienne L. Fairhall, Ila Fiete, Kristen M. Harris, Moritz Helmstaedter, Viren Jain, Narayanan Kasthuri, Yann LeCun, Jeff W. Lichtman, Peter B. Littlewood, Liqun Luo, John H.R. Maunsell, R. Clay Reid, Bruce R. Rosen, Gerald M. Rubin, Terrence J. Sejnowski, H. Sebastian Seung, Karel Svoboda, David W. Tank, Doris Tsao, and David C. Van Essen (Sept. 2020). "The Mind of a Mouse". In: *Cell* 182 (6), pp. 1372–1376. ISSN: 10974172. DOI: 10.1016/j.cell.2020.08.010.

Abudukeyoumu, Nilupaer, Teresa Hernandez-Flores, Marianela Garcia-Munoz, and Gordon W. Arbuthnott (Mar. 2019). "Cholinergic modulation of striatal microcircuits". In: *European Journal of Neuroscience* 49 (5), pp. 604–622. ISSN: 0953-816X. DOI: 10.1111/ejn.13949. https://onlinelibrary.wiley.com/doi/10.1111/ejn.13949.

Adam, Iris, Alyssa Maxwell, Helen Rößler, Emil B. Hansen, Michiel Vellema, Jonathan Brewer, and Coen P.H. Elemans (July 2021). "One-to-one innervation of vocal muscles allows precise control of birdsong". In: *Current Biology* 31 (14), 3115–3124.e5. ISSN: 18790445. DOI: 10.1016/j.cub.2021.05.008.

Adam, Iris, Katharina Riebel, Per Stål, Neil Wood, Michael J. Previs, and Coen P.H. Elemans (Dec. 2023). "Daily vocal exercise is necessary for peak performance singing in a songbird". In: *Nature Communications* 14 (1). ISSN: 20411723. DOI: 10.1038/s41467-023-43592-6.

Alcamí, Pepe and Alberto E. Pereda (May 2019). "Beyond plasticity: the dynamic impact of electrical synapses on neural circuits". In: *Nature Reviews Neuroscience* 20 (5), pp. 253–271. ISSN: 14710048. DOI: 10.1038/s41583-019-0133-5.

Andalman, Aaron S and Michale S Fee (July 2009). "A basal ganglia-forebrain circuit in the songbird biases motor output to avoid vocal errors". In: *Proc Natl Acad Sci U S A* 106 (30), pp. 12518–12523. DOI: 10.1073/pnas.0903214106. www.pnas.org/cgi/content/full/.

Arbuthnott, Gordon W. and Jeff Wickens (Feb. 2007). "Space, time and dopamine". In: *Trends in Neurosciences* 30 (2), pp. 62–69. ISSN: 01662236. DOI: 10.1016/j.tins.2006.12.003. https://linkinghub.elsevier.com/retrieve/pii/S0166223606002748.

Aristieta, Asier, Massimo Barresi, Shiva Azizpour Lindi, Grégory Barrière, Gilles Courtand, Brice de la Crompe, Lise Guilhemsang, Sophie Gauthier, Stéphanie Fioramonti, Jérôme Baufreton, and Nicolas P. Mallet (Feb. 2021). "A Disynaptic Circuit in the Globus Pallidus Controls Locomotion Inhibition". In: *Current Biology* 31 (4), 707–721.e7. ISSN: 18790445. DOI: 10.1016/j.cub.2020.11.019.

Bacci, Alberto and John R. Huguenard (Jan. 2006). "Enhancement of spike-timing precision by autaptic transmission in neocortical inhibitory interneurons". In: *Neuron* 49 (1), pp. 119–130. ISSN: 08966273. DOI: 10.1016/j.neuron.2005.12.014.

Bacci, Alberto, John R. Huguenard, and David A. Prince (Feb. 2003). "Functional Autaptic Neurotransmission in Fast-Spiking Interneurons: A Novel Form of Feedback Inhibition in the Neocortex". In: *The*

Journal of Neuroscience 23 (3), pp. 859–866. ISSN: 0270-6474. DOI: 10.1523/JNEUROSCI.23-03-00859.2003. https://www.jneurosci.org/lookup/doi/10.1523/JNEUROSCI.23-03-00859.2003.

Baldwin, Katherine T., Keith K. Murai, and Baljit S. Khakh (July 2024). "Astrocyte morphology". In: *Trends in Cell Biology* 34 (7), pp. 547–565. ISSN: 09628924. DOI: 10.1016/j.tcb.2023.09.006. https://linkinghub.elsevier.com/retrieve/pii/S0962892423002040.

Bariselli, S., W.C. Fobbs, M.C. Creed, and A.V. Kravitz (June 2019). "A competitive model for striatal action selection". In: *Brain Research* 1713, pp. 70–79. ISSN: 00068993. DOI: 10.1016/j.brainres.2018.10.009. https://linkinghub.elsevier.com/retrieve/pii/S0006899318305134.

Beaulieu, Jean-Martin and Raul R. Gainetdinov (Mar. 2011). "The Physiology, Signaling, and Pharmacology of Dopamine Receptors". In: *Pharmacological Reviews* 63 (1), pp. 182–217. ISSN: 00316997. DOI: 10.1124/pr.110.002642. https://linkinghub.elsevier.com/retrieve/pii/S0031699724009013.

Belykh, Igor and Andrey Shilnikov (Aug. 2008). "When weak inhibition synchronizes strongly desynchronizing networks of bursting neurons". In: *Physical Review Letters* 101 (7). ISSN: 00319007. DOI: 10.1103/PhysRevLett.101.078102.

Beyene, Abraham G, Kristen Delevich, Jackson Travis, Del Bonis-O'donnell, David J Piekarski, Wan Chen Lin, A Wren Thomas, Sarah J Yang, Polina Kosillo, Darwin Yang, George S Prounis, Linda Wilbrecht, and Markita P Landry (July 2019). "Imaging striatal dopamine release using a nongenetically encoded near infrared fluorescent catecholamine nanosensor". In: *Science Advances* 5 (7). DOI: 10.1126/sciadv.aaw3108. https://www.science.org.

Bonnavion, Patricia, Christophe Varin, Ghazal Fakhfouri, Pilar Martinez Olondo, Aurélie De Groote, Amandine Cornil, Ramiro Lorenzo Lopez, Elisa Pozuelo Fernandez, Elsa Isingrini, Quentin Rainer, Kathleen Xu, Eleni Tzavara, Erika Vigneault, Sylvie Dumas, Alban de Kerchove d'Exaerde, and Bruno Giros (Sept. 2024). "Striatal projection neurons coexpressing dopamine D1 and D2 receptors modulate the motor function of D1- and D2-SPNs". In: *Nature Neuroscience* 27 (9), pp. 1783–1793. ISSN: 15461726. DOI: 10.1038/s41593-024-01694-4.

Bosch, Carles, Tomas Aidukas, Mirko Holler, Alexandra Pacureanu, Elisabeth Müller, Christopher J. Peddie, Yuxin Zhang, Phil Cook, Lucy Collinson, Oliver Bunk, Andreas Menzel, Manuel Guizar-Sicairos, Gabriel Aeppli, Ana Diaz, Adrian A. Wanner, and Andreas T. Schaefer (Nov. 2023). "Non-destructive X-ray tomography of brain tissue ultrastructure". In: *bioRxiv*. DOI: 10.1101/2023.11.16.567403. http://biorxiv.org/lookup/doi/10.1101/2023.11.16.567403.

Bottjer, Sarah W. and Dale R. Sengelaub (1989). "Cell death during development of a forebrain nucleus involved with vocal learning in zebra finches". In: *Journal of Neurobiology* 20 (7), pp. 609–618. ISSN: 10974695. DOI: 10.1002/neu.480200702.

Boulay, Anne Cécile, Bruno Saubameá, Nicolas Adam, Stéphanie Chasseigneaux, Noémie Mazaré, Alice Gilbert, Mathieu Bahin, Leïla Bastianelli, Corinne Blugeon, Sandrine Perrin, Juliette Pouch, Bertrand Ducos, Stéphane Le Crom, Auguste Genovesio, Fabrice Chrétien, Xavier Declèves, Jean Louis Laplanche, and Martine Cohen-Salmon (Mar. 2017). "Translation in astrocyte distal processes sets molecular heterogeneity at the gliovascular interface". In: *Cell Discovery* 3. ISSN: 20565968. DOI: 10.1038/celldisc.2017.5.

Branco, Tiago, Vincenzo Marra, and Kevin Staras (Nov. 2010). "Examining size-strength relationships at hippocampal synapses using an ultrastructural measurement of synaptic release probability". In: *Journal of Structural Biology* 172 (2), pp. 203–210. ISSN: 10478477. DOI: 10.1016/j.jsb.2009.10.014.

Briggman, Kevin L., Moritz Helmstaedter, and Winfried Denk (Mar. 2011). "Wiring specificity in the direction-selectivity circuit of the retina". In: *Nature* 471 (7337), pp. 183–190. ISSN: 00280836. DOI: 10.1038/nature09818.

Brimblecombe, Katherine R. and Stephanie J. Cragg (Feb. 2017). "The Striosome and Matrix Compartments of the Striatum: A Path through the Labyrinth from Neurochemistry toward Function". In: *ACS Chemical Neuroscience* 8 (2), pp. 235–242. ISSN: 19487193. DOI: 10.1021/acschemneuro.6b00333.

Brini, Marisa, Tito Calì, Denis Ottolini, and Ernesto Carafoli (2014). "Neuronal calcium signaling: Function and dysfunction". In: *Cellular and Molecular Life Sciences* 71 (15), pp. 2787–2814. ISSN: 14209071. DOI: 10.1007/s00018-013-1550-7.

Buchanan, Jo Ann, Leila Elabbady, Forrest Collman, Nikolas L. Jorstad, Trygve E. Bakken, Carolyn Ott, Jenna Glatzer, Adam A. Bleckert, Agnes L. Bodor, Derrick Brittain, Daniel J. Bumbarger, Gayathri Mahalingam, Sharmishtaa Seshamani, Casey Schneider-Mizell, Marc M. Takeno, Russel Torres, Wenjing Yin, Rebecca D. Hodge, Manuel Castro, Sven Dorkenwald, Dodam Ih, Chris S. Jordan, Nico Kemnitz, Kisuk Lee, Ran Lu, Thomas Macrina, Shang Mu, Sergiy Popovych, William M. Silversmith, Ignacio Tartavull, Nicholas L. Turner, Alyssa M. Wilson, William Wong, Jingpeng Wu, Aleksandar Zlateski, Jonathan Zung, Jennifer Lippincott-Schwartz, Ed S. Lein, H. Sebastian Seung, Dwight E. Bergles, R. Clay Reid, and Nuno Maçarico da Costa (Nov. 2022). "Oligodendrocyte precursor cells ingest axons in the mouse neocortex". In: *Proceedings of the National Academy of Sciences of the United States of America* 119 (48). ISSN: 10916490. DOI: 10.1073/pnas.2202580119.

Budzillo, Agata, Alison Duffyb, Kimberly E. Millerc, Adrienne L. Fairhall, and David J. Perke (May 2017). "Dopaminergic modulation of basal ganglia output through coupled excitation-inhibition". In: *Proceedings of the National Academy of Sciences of the United States of America* 114 (22), pp. 5713–5718. ISSN: 10916490. DOI: 10.1073/pnas.1611146114.

Burek, Michael J., Kathy W. Nordeen, and Ernest J. Nordeen (1991). "Neuron loss and addition in developing zebra finch song nuclei are independent of auditory experience during song learning". In: *Journal of Neurobiology* 22 (3), pp. 215–223. ISSN: 10974695. DOI: 10.1002/neu.480220302.

Calì, Corrado, Marco Agus, Kalpana Kare, Daniya J. Boges, Heikki Lehväslaiho, Markus Hadwiger, and Pierre J. Magistretti (Dec. 2019). "3D cellular reconstruction of cortical glia and parenchymal morphometric analysis from Serial Block-Face Electron Microscopy of juvenile rat". In: *Progress in Neurobiology* 183. ISSN: 18735118. DOI: 10.1016/j.pneurobio.2019.101696.

Chen, Meilan, Lu Xu, Yi Wu, Peter Soba, and Chun Hu (Nov. 2023). "The organization and function of the Golgi apparatus in dendrite development and neurological disorders". In: *Genes & Diseases* 10 (6), pp. 2425–2442. ISSN: 23523042. DOI: 10.1016/j.gendis.2022.11.009. https://linkinghub.elsevier.com/retrieve/pii/S2352304222003105.

Chen, Ruidong and Jesse H. Goldberg (Dec. 2020). "Actor-critic reinforcement learning in the songbird". In: *Current Opinion in Neurobiology* 65, pp. 1–9. ISSN: 18736882. DOI: 10.1016/j.conb.2020.08.005.

Chen, Ruidong, Pavel A. Puzerey, Andrea C. Roeser, Tori E. Riccelli, Archana Podury, K. Maher, Alexander R. Farhang, and Jesse H. Goldberg (July 2019). "Songbird Ventral Pallidum Sends Diverse Performance Error Signals to Dopaminergic Midbrain". In: *Neuron* 103 (2), 266–276.e4. ISSN: 10974199. DOI: 10.1016/j.neuron.2019.04.038.

Chirillo, Michael A., Mikayla S. Waters, Laurence F. Lindsey, Jennifer N. Bourne, and Kristen M. Harris (Dec. 2019). "Local resources of polyribosomes and SER promote synapse enlargement and spine clustering after long-term potentiation in adult rat hippocampus". In: *Scientific Reports* 9 (1). ISSN: 20452322. DOI: 10.1038/s41598-019-40520-x.

Colonnier, Marc (July 1968). "Synaptic patterns on different cell types in the different laminae of the cat visual cortex. An electron microscope study". In: *Brain Research* 9 (2), pp. 268–287. ISSN: 00068993. DOI: 10.1016/0006-8993(68)90234-5. https://linkinghub.elsevier.com/retrieve/pii/0006899368902345.

Cooney, James R., Jamie L. Hurlburt, David K. Selig, Kristen M. Harris, and John C. Fiala (Mar. 2002). "Endosomal Compartments Serve Multiple Hippocampal Dendritic Spines from a Widespread Rather Than a Local Store of Recycling Membrane". In: *The Journal of Neuroscience* 22 (6), pp. 2215–2224. ISSN: 0270-6474. DOI: 10.1523/JNEUROSCI.22-06-02215.2002. https://www.jneurosci.org/lookup/doi/10.1523/JNEUROSCI.22-06-02215.2002.

Courtney, Connor D., Arin Pamukcu, and C. Savio Chan (July 2023). "Cell and circuit complexity of the external globus pallidus". In: *Nature Neuroscience* 26 (7), pp. 1147–1159. ISSN: 1097-6256. DOI: 10.1038/s41593-023-01368-7. https://www.nature.com/articles/s41593-023-01368-7.

Cragg, Brian (Jan. 1980). "Preservation of extracellular space during fixation of the brain for electron microscopy". In: *Tissue and Cell* 12 (1), pp. 63–72. ISSN: 00408166. DOI: 10.1016/0040-8166(80)90052-X. https://linkinghub.elsevier.com/retrieve/pii/004081668090052X.

Cragg, Stephanie J., Jérôme Baufreton, Yi Xue, J. Paul Bolam, and Mark D. Bevan (Oct. 2004a). "Synaptic release of dopamine in the subthalamic nucleus". In: *European Journal of Neuroscience* 20 (7), pp. 1788–1802. ISSN: 0953816X. DOI: 10.1111/j.1460-9568.2004.03629.x.

Cragg, Stephanie J. and Margaret E. Rice (May 2004b). "DAncing past the DAT at a DA synapse". In: *Trends in Neurosciences* 27 (5), pp. 270–277. ISSN: 01662236. DOI: 10.1016/j.tins.2004.03.011. https://linkinghub.elsevier.com/retrieve/pii/S0166223604001043.

Cserép, Csaba, Balázs Pósfai, Anett Dóra Schwarcz, and Ádám Dénes (Jan. 2018). "Mitochondrial ultrastructure is coupled to synaptic performance at axonal release sites". In: *eNeuro* 5 (1). ISSN: 23732822. DOI: 10.1523/ENEURO.0390-17.2018.

Das, Anindita and Jesse H. Goldberg (Feb. 2022). "Songbird subthalamic neurons project to dopaminergic midbrain and exhibit singing-related activity". In: *Journal of Neurophysiology* 127 (2), pp. 373–383. ISSN: 15221598. DOI: 10.1152/jn.00254.2021.

Debanne, Dominique, Emilie Campanac, Andrzej Bialowas, Edmond Carlier, and Gisèle Alcaraz (Apr. 2011). "Axon Physiology". In: *Physiol Rev.* 91 (2), pp. 555–602. DOI: 10.1152/physrev.00048.2009.-Axons. www.prv.org.

Deerinck, TJ, EA Bushong, V Lev-Ram, X Shu, RY Tsien, and MH Ellisman (July 2010). "Enhancing Serial Block-Face Scanning Electron Microscopy to Enable High Resolution 3-D Nanohistology of Cells and Tissues". In: *Microscopy and Microanalysis* 16 (S2), pp. 1138–1139. ISSN: 1431-9276. DOI: 10.1017/s1431927610055170.

Deleuze, Charlotte, Gary S. Bhumbra, Antonio Pazienti, Joana Lourenço, Caroline Mailhes, Andrea Aguirre, Marco Beato, and Alberto Bacci (2019). "Strong preference for autaptic self-connectivity of neocortical PV interneurons facilitates their tuning to -oscillations". In: *PLoS Biology* 17 (9). ISSN: 15457885. DOI: 10.1371/journal.pbio.3000419.

Denk, Winfried and Heinz Horstmann (Nov. 2004). "Serial block-face scanning electron microscopy to reconstruct three-dimensional tissue nanostructure". In: *PLoS Biology* 2 (11). ISSN: 15449173. DOI: 10.1371/journal.pbio.0020329.

Devine, Michael J. and Josef T. Kittler (Feb. 2018). "Mitochondria at the neuronal presynapse in health and disease". In: *Nature Reviews Neuroscience* 19 (2), pp. 63–80. ISSN: 1471-003X. DOI: 10.1038/nrn.2017.170. https://www.nature.com/articles/nrn.2017.170.

Ding, Long and David J. Perkel (June 2002). "Dopamine Modulates Excitability of Spiny Neurons in the Avian Basal Ganglia". In: *The Journal of Neuroscience* 22 (12), pp. 5210–5218. ISSN: 0270-6474. DOI: 10.1523/JNEUROSCI.22-12-05210.2002. https://www.jneurosci.org/lookup/doi/10.1523/JNEUROSCI.22-12-05210.2002.

Ding, Zhuokun, Paul G. Fahey, Stelios Papadopoulos, Eric Y. Wang, Brendan Celii, Christos Papadopoulos, Andersen Chang, Alexander B. Kunin, Dat Tran, Jiakun Fu, Zhiwei Ding, Saumil Patel, Lydia Ntanavara, Rachel Froebe, Kayla Ponder, Taliah Muhammad, J. Alexander Bae, Agnes L. Bodor, Derrick Brittain, Jo Ann Buchanan, Daniel J. Bumbarger, Manuel A. Castro, Erick Cobos, Sven Dorkenwald, Leila Elabbady, Akhilesh Halageri, Zhen Jia, Chris Jordan, Dan Kapner, Nico Kemnitz, Sam Kinn, Kisuk Lee, Kai Li, Ran Lu, Thomas Macrina, Gayathri Mahalingam, Eric Mitchell, Shanka Subhra Mondal, Shang Mu, Barak Nehoran, Sergiy Popovych, Casey M. Schneider-Mizell, William Silversmith, Marc Takeno, Russel Torres, Nicholas L. Turner, William Wong, Jingpeng Wu, Wenjing Yin, Szi Chieh Yu, Dimitri Yatsenko, Emmanouil Froudarakis, Fabian Sinz, Krešimir Josić, Robert Rosenbaum, H. Sebastian Seung, Forrest Collman, Nuno Maçarico da Costa, R. Clay Reid, Edgar Y. Walker, Xaq Pitkow, Jacob Reimer, and Andreas S. Tolias (Apr. 2025). "Functional connectomics reveals general wiring rule in mouse visual cortex". In: *Nature* 640 (8058), pp. 459–469. ISSN: 14764687. DOI: 10.1038/s41586-025-08840-3.

Dong, Jie, Sarah Hawes, Junbing Wu, Weidong Le, and Huaibin Cai (Mar. 2021). "Connectivity and Functionality of the Globus Pallidus Externa Under Normal Conditions and Parkinson's Disease". In: *Frontiers in Neural Circuits* 15. ISSN: 1662-5110. DOI: 10.3389/fncir.2021.645287. https://www.frontiersin.org/articles/10.3389/fncir.2021.645287/full.

Dorkenwald, Sven, Claire E. McKellar, Thomas Macrina, Nico Kemnitz, Kisuk Lee, Ran Lu, Jingpeng Wu, Sergiy Popovych, Eric Mitchell, Barak Nehoran, Zhen Jia, J. Alexander Bae, Shang Mu, Dodam Ih, Manuel Castro, Oluwaseun Ogedengbe, Akhilesh Halageri, Kai Kuehner, Amy R. Sterling, Zoe Ashwood, Jonathan Zung, Derrick Brittain, Forrest Collman, Casey Schneider-Mizell, Chris Jordan, William Silversmith, Christa Baker, David Deutsch, Lucas Encarnacion-Rivera, Sandeep Kumar, Austin Burke, Doug Bland, Jay Gager, James Hebditch, Selden Koolman, Merlin Moore, Sarah Morejohn, Ben Silverman, Kyle Willie, Ryan Willie, Szi chieh Yu, Mala Murthy, and H. Sebastian Seung (Jan. 2022a). "FlyWire: online community for whole-brain connectomics". In: *Nature Methods* 19 (1), pp. 119–128. ISSN: 15487105. DOI: 10.1038/s41592-021-01330-0.

Dorkenwald, Sven, Casey M. Schneider-Mizell, Derrick Brittain, Akhilesh Halageri, Chris Jordan, Nico Kemnitz, Manual A. Castro, William Silversmith, Jeremy Maitin-Shephard, Jakob Troidl, Hanspeter Pfister, Valentin Gillet, Daniel Xenes, J. Alexander Bae, Agnes L. Bodor, Jo Ann Buchanan, Daniel J. Bumbarger, Leila Elabbady, Zhen Jia, Daniel Kapner, Sam Kinn, Kisuk Lee, Kai Li, Ran Lu, Thomas Macrina, Gayathri Mahalingam, Eric Mitchell, Shanka Subhra Mondal, Shang Mu, Barak Nehoran, Sergiy Popovych, Marc Takeno, Russel Torres, Nicholas L. Turner, William Wong, Jingpeng Wu, Wenjing Yin, Szi Chieh Yu, R. Clay Reid, Nuno Maçarico da Costa, H. Sebastian Seung, and Forrest Collman (May 2025). "CAVE: Connectome Annotation Versioning Engine". In: *Nature Methods* 22 (5), pp. 1112–1120. ISSN: 15487105. DOI: 10.1038/s41592-024-02426-z.

Dorkenwald, Sven, Philipp J. Schubert, Marius F. Killinger, Gregor Urban, Shawn Mikula, Fabian Svara, and Joergen Kornfeld (Feb. 2017). "Automated synaptic connectivity inference for volume electron microscopy". In: *Nature Methods* 14 (4), pp. 435–442. ISSN: 15487105. DOI: 10.1038/nmeth.4206.

Dorkenwald, Sven, Nicholas L. Turner, Thomas Macrina, Kisuk Lee, Ran Lu, Jingpeng Wu, Agnes L. Bodor, Adam A. Bleckert, Derrick Brittain, Nico Kemnitz, William M. Silversmith, Dodam Ih, Jonathan Zung, Aleksandar Zlateski, Ignacio Tartavull, Szi Chieh Yu, Sergiy Popovych, William

Wong, Manuel Castro, Chris S. Jordan, Alyssa M. Wilson, Emmanouil Froudarakis, Joann Buchanan, Marc M. Takeno, Russel Torres, Gayathri Mahalingam, Forrest Collman, Casey M. Schneider-Mizell, Daniel J. Bumbarger, Yang Li, Lynne Becker, Shelby Suckow, Jacob Reimer, Andreas S. Tolias, Nuno Macarico da Costa, R. Clay Reid, and H. Sebastian Seung (2022b). "Binary and analog variation of synapses between cortical pyramidal neurons". In: *eLife* 11. ISSN: 2050084X. DOI: 10.7554/eLife.76120.

Dorkenwald, Sven et al. (Oct. 2024). "Neuronal wiring diagram of an adult brain". In: *Nature* 634 (8032), pp. 124–138. ISSN: 14764687. DOI: 10.1038/s41586-024-07558-y.

Durkee, Caitlin A. and Alfonso Araque (Jan. 2019). "Diversity and Specificity of Astrocyte–neuron Communication". In: *Neuroscience* 396, pp. 73–78. ISSN: 03064522. DOI: 10.1016/j.neuroscience.2018.11.010. https://linkinghub.elsevier.com/retrieve/pii/S0306452218307346.

Eberle, A. L., S. Mikula, R. Schalek, J. Lichtman, M. L. Knothe Tate, and D. Zeidler (Aug. 2015). "High-resolution, high-throughput imaging with a multibeam scanning electron microscope". In: *Journal of Microscopy* 259 (2), pp. 114–120. ISSN: 13652818. DOI: 10.1111/jmi.12224.

Eckstein, Nils, Alexander Shakeel Bates, Andrew Champion, Michelle Du, Yijie Yin, Philipp Schlegel, Alicia Kun Yang Lu, Thomson Rymer, Samantha Finley-May, Tyler Paterson, Ruchi Parekh, Sven Dorkenwald, Arie Matsliah, Szi Chieh Yu, Claire McKellar, Amy Sterling, Katharina Eichler, Marta Costa, Sebastian Seung, Mala Murthy, Volker Hartenstein, Gregory S.X.E. Jefferis, and Jan Funke (May 2024). "Neurotransmitter classification from electron microscopy images at synaptic sites in Drosophila melanogaster". In: *Cell* 187 (10), 2574–2594.e23. ISSN: 10974172. DOI: 10.1016/j.cell.2024.03.016.

Elabbady, Leila, Sharmishtaa Seshamani, Shang Mu, Gayathri Mahalingam, Casey M. Schneider-Mizell, Agnes L. Bodor, J. Alexander Bae, Derrick Brittain, Jo Ann Buchanan, Daniel J. Bumbarger, Manuel A. Castro, Sven Dorkenwald, Akhilesh Halageri, Zhen Jia, Chris Jordan, Dan Kapner, Nico Kemnitz, Sam Kinn, Kisuk Lee, Kai Li, Ran Lu, Thomas Macrina, Eric Mitchell, Shanka Subhra Mondal, Barak Nehoran, Sergiy Popovych, William Silversmith, Marc Takeno, Russel Torres, Nicholas L. Turner, William Wong, Jingpeng Wu, Wenjing Yin, Szi Chieh Yu, H. Sebastian Seung, R. Clay Reid, Nuno Maçarico da Costa, and Forrest Collman (Apr. 2025). "Perisomatic ultrastructure efficiently classifies cells in mouse cortex". In: *Nature* 640 (8058), pp. 478–486. ISSN: 14764687. DOI: 10.1038/s41586-024-07765-7.

Elbaz, Benayahu and Brian Popko (Apr. 2019). "Molecular Control of Oligodendrocyte Development". In: *Trends in Neurosciences* 42 (4), pp. 263–277. ISSN: 1878108X. DOI: 10.1016/j.tins.2019.01.002.

Elemans, Coen P.H., Andrew F. Mead, Lawrence C. Rome, and Franz Goller (July 2008). "Superfast vocal muscles control song production in songbirds". In: *PLoS ONE* 3 (7). ISSN: 19326203. DOI: 10.1371/journal.pone.0002581.

Farries, Michael A., Long Ding, and David J. Perkel (Mar. 2005). "Evidence for "direct" and "indirect" pathways through the song system basal ganglia". In: *Journal of Comparative Neurology* 484 (1), pp. 93–104. ISSN: 00219967. DOI: 10.1002/cne.20464.

Farries, Michael A. and David J. Perkel (May 2002). "A Telencephalic Nucleus Essential for Song Learning Contains Neurons with Physiological Characteristics of Both Striatum and Globus Pallidus". In: *The Journal of Neuroscience* 22 (9), pp. 3776–3787. ISSN: 0270-6474. DOI: 10.1523/JNEUROSCI.22-09-03776.2002. https://www.jneurosci.org/lookup/doi/10.1523/JNEUROSCI.22-09-03776.2002.

Fazl, Arash and Jori Fleisher (Apr. 2018). "Anatomy, Physiology, and Clinical Syndromes of the Basal Ganglia: A Brief Review". In: *Seminars in Pediatric Neurology* 25, pp. 2–9. ISSN: 15580776. DOI: 10.1016/j.spen.2017.12.005.

Fee, Michale S. (Apr. 2014). "The role of efference copy in striatal learning". In: *Current Opinion in Neurobiology* 25, pp. 194–200. ISSN: 09594388. DOI: 10.1016/j.conb.2014.01.012.

Fee, Michale S. and Jesse H. Goldberg (Dec. 2011). "A hypothesis for basal ganglia-dependent reinforcement learning in the songbird". In: *Neuroscience* 198, pp. 152–170. ISSN: 03064522. DOI: 10.1016/j.neuroscience.2011.09.069.

Fernholz, Martin Hans Peter (2022). "A search for functional connectivity rules in the visual thalamus and hippocampus München 2022". PhD thesis. Ludwig-Maximilians-Universität München. DOI: 10.5282/edoc.31453.

Fortune, Eric S. and Daniel Margoliash (1995). "Parallel pathways and convergence onto HVc and adjacent neostriatum of adult zebra finches (Taeniopygia guttata)". In: *Journal of Comparative Neurology* 360 (3), pp. 413–441. ISSN: 10969861. DOI: 10.1002/cne.903600305.

Frey, Terrence G. and Carmen A. Mannella (July 2000). "The internal structure of mitochondria". In: *Trends Biochem Sci* 25 (7), pp. 319–324.

Fulton, Kara A and Kevin L Briggman (Oct. 2020). "Permeabilization-free en bloc immunohistochemistry for correlative microscopy". In: *bioRxiv*. DOI: 10.1101/2020.10.07.327734. http://biorxiv.org/lookup/doi/10.1101/2020.10.07.327734.

Gadagkar, Vikram, Pavel A. Puzerey, Ruidong Chen, Eliza Baird-Daniel, Alexander R. Farhang, and Jesse H. Goldberg (Dec. 2016). "Dopamine neurons encode performance error in singing birds". In: *Science* 354 (6317), pp. 1278–1282. ISSN: 0036-8075. DOI: 10.1126/science.aah6837. https://www.science.org/doi/10.1126/science.aah6837.

Gagnon, D., S. Petryszyn, M. G. Sanchez, C. Bories, J. M. Beaulieu, Y. De Koninck, A. Parent, and M. Parent (Jan. 2017). "Striatal Neurons Expressing D1 and D2 Receptors are Morphologically Distinct and Differently Affected by Dopamine Denervation in Mice". In: *Scientific Reports* 7. ISSN: 20452322. DOI: 10.1038/srep41432.

Gallo, Nicholas B, Artan Berisha, and Linda Van Aelst (Mar. 2022). "Microglia regulate chandelier cell axo-axonic synaptogenesis". In: *Proc Natl Acad Sci U S A* 119 (11). DOI: 10.1073/pnas. https://doi.org/10.1073/pnas.2114476119.

Gerfen, Charles R., Thomas M. Engber, Lawrence C. Mahan, Zvi Susel, Thomas N. Chase, Frederick J. Monsma, J R., and David R. Sibley (Dec. 1990). "D1 and D2 dopamine receptor-regulated gene expression of striatonigral and striatopallidal neurons". In: *Science* 250 (4986), pp. 1429–1432. DOI: 10.1126/science.2147780.

Gertler, Tracy S., C. Savio Chan, and D. James Surmeier (Oct. 2008). "Dichotomous anatomical properties of adult striatal medium spiny neurons". In: *Journal of Neuroscience* 28 (43), pp. 10814–10824. ISSN: 02706474. DOI: 10.1523/JNEUROSCI.2660-08.2008.

Gittis, Aryn H., Alexandra B. Nelson, Myo T. Thwin, Jorge J. Palop, and Anatol C. Kreitzer (Feb. 2010). "Distinct roles of GABAergic interneurons in the regulation of striatal output pathways". In: *Journal of Neuroscience* 30 (6), pp. 2223–2234. ISSN: 02706474. DOI: 10.1523/JNEUROSCI.4870-09.2010.

Goldberg, Jesse H., Avital Adler, Hagai Bergman, and Michale S. Fee (May 2010a). "Singing-related neural activity distinguishes two putative pallidal cell types in the songbird basal ganglia: Comparison to the primate internal and external pallidal segments". In: *Journal of Neuroscience* 30 (20), pp. 7088–7098. ISSN: 02706474. DOI: 10.1523/JNEUROSCI.0168-10.2010.

Goldberg, Jesse H. and Michale S. Fee (Apr. 2010b). "Singing-related neural activity distinguishes four classes of putative striatal neurons in the songbird basal ganglia". In: *Journal of Neurophysiology* 103 (4), pp. 2002–2014. ISSN: 00223077. DOI: 10.1152/jn.01038.2009.

Gongwer, Michael, Fanny Etienne, Eric Moca, Megan Chappell, Sara Blagburn-Blanco, Jack Riley, Alexander Enos, Melody Haratian, Alex Qi, Rocio Rojo, Scott Wilke, Clare Pridans, Laura DeNardo, and Lindsay M De Biase (Jan. 2025). "Microglia regulate nucleus accumbens synaptic development and circuit function underlying threat avoidance behaviors". In: *Res Sq [Preprint]*. DOI: 10.21203/rs.3.rs-5837701/v1. https://www.researchsquare.com/article/rs-5837701/v1.

Götz, Magdalena, Masato Nakafuku, and David Petrik (July 2016). "Neurogenesis in the developing and adult brain—similarities and key differences". In: *Cold Spring Harbor Perspectives in Biology* 8 (7). ISSN: 19430264. DOI: 10.1101/cshperspect.a018853.

Gour, Anjali, Kevin M. Boergens, Natalie Heike, Yunfeng Hua, Philip Laserstein, Kun Song, and Moritz Helmstaedter (Jan. 2021). "Postnatal connectomic development of inhibition in mouse barrel cortex". In: *Science* 371 (6528). ISSN: 10959203. DOI: 10.1126/science.abb4534.

Gray, E G (Oct. 1959). "Axo-somatic and axo-dendritic synapses of the cerebral cortex: an electron microscope study." In: *Journal of anatomy* 93 (Pt 4), pp. 420–33. ISSN: 0021-8782. http://www.ncbi.nlm.nih.gov/pubmed/13829103%20http://www.pubmedcentral.nih.gov/articlerender.fcgi?artid=PMC1244535.

Graybiel, Ann M, Toshihiko Aosaki, Alice W Flaherty, and Minoru Kimura (Sept. 1994). "The Basal Ganglia and Adaptive Motor Control". In: *Science* 265 (5180), pp. 1826–1831. DOI: 10.1126/science.8091209. https://www.science.org.

Grillner, Sten and Brita Robertson (Oct. 2016). "The Basal Ganglia Over 500 Million Years". In: *Current Biology* 26 (20), R1088–R1100. ISSN: 09609822. DOI: 10.1016/j.cub.2016.06.041.

Gurney, ME (June 1981). "Hormonal control of cell form and number in the zebra finch song system". In: *The Journal of Neuroscience* 1 (6), pp. 658–673. ISSN: 0270-6474. DOI: 10.1523/JNEUROSCI.01-06-00658.1981. https://www.jneurosci.org/lookup/doi/10.1523/JNEUROSCI.01-06-00658.1981.

Gutiérrez, Rafael (Oct. 2023). "Gap Junctions in the Brain: Hardwired but Functionally Versatile". In: *The Neuroscientist* 29 (5), pp. 554–568. ISSN: 1073-8584. DOI: 10.1177/10738584221120804. https://journals.sagepub.com/doi/10.1177/10738584221120804.

Gutnick, Michael J, Barry W Connors, and Bruce R Ransom (1981). "Dye-coupling between glial cells in the guinea pig neocortical slice". In: *Brain Rese trch* 213, pp. 486–492.

Harreveld, A Van and S K Malhotra (Apr. 1967a). "Extracellular space in the cerebral cortex of the mouse." In: *Journal of anatomy* 101 (Pt 2), pp. 197–207. ISSN: 0021-8782. http://www.ncbi.nlm.nih.gov/pubmed/6040073%20http://www.pubmedcentral.nih.gov/articlerender.fcgi?artid=PMC1270876.

Harreveld, A. Van and B.O. Dubrovsky (Feb. 1967b). "Water and electrolytes in hydrated gray and white matter". In: *Brain Research* 4 (1), pp. 81–86. ISSN: 00068993. DOI: 10.1016/0006-8993(67)90150-3. https://linkinghub.elsevier.com/retrieve/pii/0006899367901503.

Harreveld, A. Van and F. I. Khattab (Dec. 1968). "Perfusion fixation with glutaraldehyde and post-fixation with osmium tetroxide for electron microscopy". In: *Journal of Cell Science* 3 (4), pp. 579–594. ISSN: 0021-9533. DOI: 10.1242/jcs.3.4.579. https://journals.biologists.com/jcs/article/3/4/579/58358/Perfusion-fixation-with-glutaraldehyde-and-post.

Harris, KM and JK Stevens (Aug. 1989). "Dendritic spines of CA 1 pyramidal cells in the rat hippocampus: serial electron microscopy with reference to their biophysical characteristics". In: *The Journal of Neuroscience* 9 (8), pp. 2982–2997. ISSN: 0270-6474. DOI: 10.1523/JNEUROSCI.09-08-02982.1989. https://www.jneurosci.org/lookup/doi/10.1523/JNEUROSCI.09-08-02982.1989.

Hashimoto, Akari, Nanami Kawamura, Etsuko Tarusawa, Ikuko Takeda, Yuki Aoyama, Nobuhiko Ohno, Mio Inoue, Mai Kagamiuchi, Daisuke Kato, Mami Matsumoto, Yoshihiro Hasegawa, Junichi Nabekura,

Anne Schaefer, Andrew J. Moorhouse, Takeshi Yagi, and Hiroaki Wake (May 2023). "Microglia enable cross-modal plasticity by removing inhibitory synapses". In: *Cell Reports* 42 (5). ISSN: 22111247. DOI: 10.1016/j.celrep.2023.112383.

Hayworth, K. J., N. Kasthuri, R. Schalek, and J. W. Lichtman (Aug. 2006). "Automating the collection of ultrathin serial sections for large volume TEM reconstructions". In: *Microscopy and Microanalysis* 12 (SUPPL. 2), pp. 86–87. ISSN: 14319276. DOI: 10.1017/S1431927606066268.

Hayworth, Kenneth J., David Peale, Michał Januszewski, Graham W. Knott, Zhiyuan Lu, C. Shan Xu, and Harald F. Hess (Jan. 2020). "Gas cluster ion beam SEM for imaging of large tissue samples with 10 nm isotropic resolution". In: *Nature Methods* 17 (1), pp. 68–71. ISSN: 15487105. DOI: 10.1038/s41592-019-0641-2.

Heinrich, Larissa, Davis Bennett, David Ackerman, Woohyun Park, John Bogovic, Nils Eckstein, Alyson Petruncio, Jody Clements, Song Pang, C. Shan Xu, Jan Funke, Wyatt Korff, Harald F. Hess, Jennifer Lippincott-Schwartz, Stephan Saalfeld, Aubrey V. Weigel, Riasat Ali, Rebecca Arruda, Rohit Bahtra, and Destiny Nguyen (Nov. 2021). "Whole-cell organelle segmentation in volume electron microscopy". In: *Nature* 599 (7883), pp. 141–146. ISSN: 14764687. DOI: 10.1038/s41586-021-03977-3.

Helmstaedter, Moritz, Kevin L. Briggman, and Winfried Denk (Aug. 2011). "High-accuracy neurite reconstruction for high-throughput neuroanatomy". In: *Nature Neuroscience* 14 (8), pp. 1081–1088. ISSN: 10976256. DOI: 10.1038/nn.2868.

Helmstaedter, Moritz, Kevin L. Briggman, Srinivas C. Turaga, Viren Jain, H. Sebastian Seung, and Winfried Denk (2013). "Connectomic reconstruction of the inner plexiform layer in the mouse retina". In: *Nature* 500 (7461), pp. 168–174. ISSN: 14764687. DOI: 10.1038/nature12346.

Henselmans, J. M.L. and F. G. Wouterlood (1994). "Light and electron microscopic characterization of cholinergic and dopaminergic structures in the striatal complex and the dorsal ventricular ridge of the lizard Gekko gecko". In: *Journal of Comparative Neurology* 345 (1), pp. 69–83. ISSN: 10969861. DOI: 10.1002/cne.903450105.

Hering, Heike and Morgan Sheng (Dec. 2001). "Dentritic spines : structure, dynamics and regulation". In: *Nature Reviews Neuroscience* 2 (12), pp. 880–888. ISSN: 1471-003X. DOI: 10.1038/35104061. https://www.nature.com/articles/35104061.

Hnasko, Thomas S. and Robert H. Edwards (2012). "Neurotransmitter corelease: Mechanism and physiological role". In: *Annual Review of Physiology* 74, pp. 225–243. ISSN: 00664278. DOI: 10.1146/annurev-physiol-020911-153315.

Holler, Simone, German Köstinger, Kevan A.C. Martin, Gregor F.P. Schuhknecht, and Ken J. Stratford (Mar. 2021). "Structure and function of a neocortical synapse". In: *Nature* 591 (7848), pp. 111–116. ISSN: 14764687. DOI: 10.1038/s41586-020-03134-2.

Horton, April C., Bence Rácz, Eric E. Monson, Anna L. Lin, Richard J. Weinberg, and Michael D. Ehlers (Dec. 2005). "Polarized secretory trafficking directs cargo for asymmetric dendrite growth and morphogenesis". In: *Neuron* 48 (5), pp. 757–771. ISSN: 08966273. DOI: 10.1016/j.neuron.2005.11.005.

Hua, Yunfeng, Philip Laserstein, and Moritz Helmstaedter (Aug. 2015). "Large-volume en-bloc staining for electron microscopy-based connectomics". In: *Nature Communications* 6. ISSN: 20411723. DOI: 10.1038/ncomms8923.

Hughes, Ethan G., Shin H. Kang, Masahiro Fukaya, and Dwight E. Bergles (June 2013). "Oligodendrocyte progenitors balance growth with self-repulsion to achieve homeostasis in the adult brain". In: *Nature Neuroscience* 16 (6), pp. 668–676. ISSN: 10976256. DOI: 10.1038/nn.3390.

Hyman, Steven E (Mar. 2005). "Primer Neurotransmitters". In: *Curr Biol.* 15 (5). DOI: 10.1016/j.cub.2005.02.037.

Ibáñez-Sandoval, Osvaldo, Fatuel Tecuapetla, Bengi Unal, Fulva Shah, Tibor Koós, and James M. Tepper (Nov. 2011). "A novel functionally distinct subtype of striatal neuropeptide Y interneuron". In: *Journal of Neuroscience* 31 (46), pp. 16757–16769. ISSN: 02706474. DOI: 10.1523/JNEUROSCI.2628-11.2011.

Inta, Dragos, Heather A. Cameron, and Peter Gass (Sept. 2015). "New neurons in the adult striatum: from rodents to humans". In: *Trends in Neurosciences* 38 (9), pp. 517–523. ISSN: 01662236. DOI: 10.1016/j.tins.2015.07.005. https://linkinghub.elsevier.com/retrieve/pii/S0166223615001721.

Izzo, P. N. and J. P. Bolam (Mar. 1988). "Cholinergic synaptic input to different parts of spiny striatonigral neurons in the rat". In: *Journal of Comparative Neurology* 269 (2), pp. 219–234. ISSN: 0021-9967. DOI: 10.1002/cne.902690207. https://onlinelibrary.wiley.com/doi/10.1002/cne.902690207.

Januszewski, Michał, Jörgen Kornfeld, Peter H. Li, Art Pope, Tim Blakely, Larry Lindsey, Jeremy Maitin-Shepard, Mike Tyka, Winfried Denk, and Viren Jain (Aug. 2018). "High-precision automated reconstruction of neurons with flood-filling networks". In: *Nature Methods* 15 (8), pp. 605–610. ISSN: 15487105. DOI: 10.1038/s41592-018-0049-4.

Januszewski, Michał, Thomas Templier, Kenneth Hayworth, David Peale, and Harald Hess (May 2025). "Accelerating Neuron Reconstruction with PATHFINDER". In: *bioRxiv*. DOI: 10.1101/2025.05.16.654254. http://biorxiv.org/lookup/doi/10.1101/2025.05.16.654254.

Jarvis, Erich D. (2004). "Learned birdsong and the neurobiology of human language". In: *Annals of the New York Academy of Sciences* 1016, pp. 749–777. ISSN: 00778923. DOI: 10.1196/annals.1298.038.

Jia, Yanbing, Huaguang Gu, and Yuye Li (Oct. 2023). "Influence of inhibitory autapses on synchronization of inhibitory network gamma oscillations". In: *Cognitive Neurodynamics* 17 (5), pp. 1131–1152. ISSN: 18714099. DOI: 10.1007/s11571-022-09856-5.

Johansson, Yvonne and Gilad Silberberg (Jan. 2020). "The Functional Organization of Cortical and Thalamic Inputs onto Five Types of Striatal Neurons Is Determined by Source and Target Cell Identities". In: *Cell Reports* 30 (4), 1178–1194.e3. ISSN: 22111247. DOI: 10.1016/j.celrep.2019.12.095.

Justs, Karlis A., Zhongmin Lu, Amit K. Chouhan, Jolanta A. Borycz, Zhiyuan Lu, Ian A. Meinertzhagen, and Gregory T. Macleod (Feb. 2022). "Presynaptic Mitochondrial Volume and Packing Density Scale with Presynaptic Power Demand". In: *Journal of Neuroscience* 42 (6), pp. 954–967. ISSN: 15292401. DOI: 10.1523/JNEUROSCI.1236-21.2021.

Kao, Mimi H., Brian D. Wright, and Allison J. Doupe (Dec. 2008). "Neurons in a forebrain nucleus required for vocal plasticity rapidly switch between precise firing and variable bursting depending on social context". In: *Journal of Neuroscience* 28 (49), pp. 13232–13247. ISSN: 02706474. DOI: 10.1523/JNEUROSCI.2250-08.2008.

Kasthuri, Narayanan, Kenneth Jeffrey Hayworth, Daniel Raimund Berger, Richard Lee Schalek, José Angel Conchello, Seymour Knowles-Barley, Dongil Lee, Amelio Vázquez-Reina, Verena Kaynig, Thouis Raymond Jones, Mike Roberts, Josh Lyskowski Morgan, Juan Carlos Tapia, H. Sebastian Seung, William Gray Roncal, Joshua Tzvi Vogelstein, Randal Burns, Daniel Lewis Sussman, Carey Eldin Priebe, Hanspeter Pfister, and Jeff William Lichtman (Aug. 2015). "Saturated Reconstruction of a Volume of Neocortex". In: *Cell* 162 (3), pp. 648–661. ISSN: 10974172. DOI: 10.1016/j.cell.2015.06.054.

Kemal, Shahrnaz, Hunter S. Richardson, Eric D. Dyne, and Meng-meng Fu (Oct. 2022). "ER and Golgi trafficking in axons, dendrites, and glial processes". In: *Current Opinion in Cell Biology* 78, p. 102119. ISSN: 09550674. DOI: 10.1016/j.ceb.2022.102119. https://linkinghub.elsevier.com/retrieve/pii/S0955067422000722.

Kettenmann, Helmut, Uwe-Karsten Hanisch, Mami Noda, and Alexei Verkhratsky (Apr. 2011). "Physiology of microglia". In: *Physiological Reviews* 91 (2), pp. 461–553. ISSN: 00319333. DOI: 10.1152/physrev.00011.2010.

Knott, Graham, Herschel Marchman, David Wall, and Ben Lich (Mar. 2008). "Serial section scanning electron microscopy of adult brain tissue using focused ion beam milling". In: *Journal of Neuroscience* 28 (12), pp. 2959–2964. ISSN: 02706474. DOI: 10.1523/JNEUROSCI.3189-07.2008.

Kormacheva, Maria (July 2023). "Cluster-Based Milling Method for Large-Field-of-View Volume Electron Microscopy". PhD thesis. Ludwig-Maximilians-Universität München. DOI: https://doi.org/10.5282/edoc.31985.

Kornfeld, J, M Januszewski, P Schubert, V Jain, W Denk, and MS Fee (Feb. 2020). "An anatomical substrate of credit assignment in reinforcement learning". In: *bioRxiv*. DOI: 10.1101/2020.02.18.954354. http://biorxiv.org/lookup/doi/10.1101/2020.02.18.954354.

Kornfeld, Joergen (July 2017). "Connectomic Analyses in the Zebra Finch Brain". PhD thesis. Ruprecht-Karls-Universität, Heidelberg. https://hdl.handle.net/21.11116/0000-0001-4401-1.

Kornfeld, Joergen, Sam E Benezra, Rajeevan T Narayanan, Fabian Svara, Robert Egger, Marcel Oberlaender, Winfried Denk, and Michael A Long (Mar. 2017). "EM connectomics reveals axonal target variation in a sequence-generating network". In: *elife*. DOI: 10.7554/eLife.24364.001. https://elifesciences.org/articles/24364#abstract.

Korogod, Natalya, Carl CH Petersen, and Graham W Knott (Aug. 2015). "Ultrastructural analysis of adult mouse neocortex comparing aldehyde perfusion with cryo fixation". In: *Elife*. DOI: 10.7554/eLife.05793.001. https://elifesciences.org/articles/05793#abstract.

Kozhevnikov, Alexay A. and Michale S. Fee (June 2007). "Singing-related activity of identified HVC neurons in the zebra finch". In: *Journal of Neurophysiology* 97 (6), pp. 4271–4283. ISSN: 00223077. DOI: 10.1152/jn.00952.2006.

Kubikova, Lubica, Kazuhiro Wada, and Erich D. Jarvis (Mar. 2010). "Dopamine receptors in a songbird brain". In: *Journal of Comparative Neurology* 518 (6), pp. 741–769. ISSN: 00219967. DOI: 10.1002/cne.22255.

Kubota, Yoshiyuki, Takaaki Miyazaki, Nilton L Kamiji, Tamami Honda, Motohide Murate, and Mitsuo Suga (June 2025). "A wide variety of techniques for a volume electron microscopy". In: *Microscopy*. ISSN: 2050-5698. DOI: 10.1093/jmicro/dfaf011.

Kwon, Seok Kyu, Richard Sando, Tommy L. Lewis, Yusuke Hirabayashi, Anton Maximov, and Franck Polleux (July 2016). "LKB1 Regulates Mitochondria-Dependent Presynaptic Calcium Clearance and Neurotransmitter Release Properties at Excitatory Synapses along Cortical Axons". In: *PLoS Biology* 14 (7). ISSN: 15457885. DOI: 10.1371/journal.pbio.1002516.

Lalo, Ulyana, Wuhyun Koh, C. Justin Lee, and Yuriy Pankratov (Nov. 2021). "The tripartite glutamatergic synapse". In: *Neuropharmacology* 199, p. 108758. ISSN: 00283908. DOI: 10.1016/j.neuropharm.2021.108758. https://linkinghub.elsevier.com/retrieve/pii/S0028390821003130.

Lee, Seonok, Michelle K. Leach, Stephanie A. Redmond, S. Y.Christin Chong, Synthia H. Mellon, Samuel J. Tuck, Zhang Qi Feng, Joseph M. Corey, and Jonah R. Chan (Sept. 2012). "A culture system to study oligodendrocyte myelination processes using engineered nanofibers". In: *Nature Methods* 9 (9), pp. 917–922. ISSN: 15487091. DOI: 10.1038/nmeth.2105.

Lissandrello, Charles A., Winthrop F. Gillis, Jun Shen, Ben W. Pearre, Flavia Vitale, Matteo Pasquali, Bradley J. Holinski, Daniel J. Chew, Alice E. White, and Timothy J. Gardner (Mar. 2017). "A microscale printable nanoclip for electrical stimulation and recording in small nerves". In: *Journal of Neural Engineering* 14 (3). ISSN: 17412552. DOI: 10.1088/1741-2552/aa5a5b.

Liu, Changliang, Xintong Cai, Andreas Ritzau-Jost, Paul F Kramer, Yulong Li, Zayd M Khaliq, Stefan Hallermann, and Pascal S Kaeser (Mar. 2022). "An action potential initiation mechanism in distal axons for the control of dopamine release". In: *Science* (375), pp. 1378–1385. https://www.science.org.

Liu, Changliang, Pragya Goel, and Pascal S. Kaeser (June 2021). "Spatial and temporal scales of dopamine transmission". In: *Nature Reviews Neuroscience* 22 (6), pp. 345–358. ISSN: 1471-003X. DOI: 10.1038/s41583-021-00455-7. https://www.nature.com/articles/s41583-021-00455-7.

Liu, Changliang, Lauren Kershberg, Jiexin Wang, Shirin Schneeberger, and Pascal S. Kaeser (Feb. 2018). "Dopamine Secretion Is Mediated by Sparse Active Zone-like Release Sites". In: *Cell* 172 (4), 706–718.e15. ISSN: 10974172. DOI: 10.1016/j.cell.2018.01.008.

Loomba, Sahil, Jakob Straehle, Vijayan Gangadharan, Natalie Heike, Abdelrahman Khalifa, Alessandro Motta, Niansheng Ju, Meike Sievers, Jens Gempt, Hanno S. Meyer, and Moritz Helmstaedter (July 2022). "Connectomic comparison of mouse and human cortex". In: *Science* 377 (6602). ISSN: 10959203. DOI: 10.1126/science.abo0924.

López-Doménech, Guillermo and Josef T. Kittler (Aug. 2023). "Mitochondrial regulation of local supply of energy in neurons". In: *Current Opinion in Neurobiology* 81, p. 102747. ISSN: 09594388. DOI: 10.1016/j.conb.2023.102747. https://linkinghub.elsevier.com/retrieve/pii/S0959438823000727.

López-Muñoz, Francisco, Jesús Boya, and Cecilio Alamo (Oct. 2006). "Neuron theory, the cornerstone of neuroscience, on the centenary of the Nobel Prize award to Santiago Ramón y Cajal". In: *Brain Research Bulletin* 70 (4-6), pp. 391–405. ISSN: 03619230. DOI: 10.1016/j.brainresbull.2006.07.010.

Lu, Xiaotang, Xiaomeng Han, Yaron Meirovitch, Evelina Sjöstedt, Richard L. Schalek, and Jeff W. Lichtman (July 2023a). "Preserving extracellular space for high-quality optical and ultrastructural studies of whole mammalian brains". In: *Cell Reports Methods* 3 (7). ISSN: 26672375. DOI: 10.1016/j.crmeth.2023.100520.

Lu, Xiaotang, Yuelong Wu, Richard L. Schalek, Yaron Meirovitch, Daniel R. Berger, and Jeff W. Lichtman (Sept. 2023b). "A Scalable Staining Strategy for Whole-Brain Connectomics". In: *bioRxiv*. DOI: 10.1101/2023.09.26.558265. http://biorxiv.org/lookup/doi/10.1101/2023.09.26.558265.

Luo, Minmin, Long Ding, and David J. Perkel (Sept. 2001). "An Avian Basal Ganglia Pathway Essential for Vocal Learning Forms a Closed Topographic Loop". In: *The Journal of Neuroscience* 21 (17), pp. 6836–6845. ISSN: 0270-6474. DOI: 10.1523/JNEUROSCI.21-17-06836.2001. https://www.jneurosci.org/lookup/doi/10.1523/JNEUROSCI.21-17-06836.2001.

Luo, Minmin and David J. Perkel (Jan. 1999). "Long-range GABAergic projection in a circuit essential for vocal learning". In: *Journal of Comparative Neurology* 403 (1), pp. 68–84. ISSN: 00219967. DOI: 10.1002/(SICI)1096-9861(19990105)403:1<68::AID-CNE6>3.0.CO;2-5.

Magee, Jeffrey C and Christine Grienberger (July 2020). "Annual Review of Neuroscience Synaptic Plasticity Forms and Functions". In: *Annu Rev Neurosci.* 34, pp. 95–117. DOI: 10.1146/annurev-neuro-090919. https://doi.org/10.1146/annurev-neuro-090919-.

Mallet, Nicolas, Benjamin R. Micklem, Pablo Henny, Matthew T. Brown, Claire Williams, J. Paul Bolam, Kouichi C. Nakamura, and Peter J. Magill (June 2012). "Dichotomous Organization of the External Globus Pallidus". In: *Neuron* 74 (6), pp. 1075–1086. ISSN: 08966273. DOI: 10.1016/j.neuron.2012.04.027.

Matthews, Murray A. (1968). "An electron microscopic study of the relationship between axon diameter and the initiation of myelin production in the peripheral nervous system". In: *The Anatomical Record* 161 (3), pp. 337–351. ISSN: 10970185. DOI: 10.1002/ar.1091610306.

Maus, Lydia, Choong Ku Lee, Bekir Altas, Sinem M. Sertel, Kirsten Weyand, Silvio O. Rizzoli, Jeong Seop Rhee, Nils Brose, Cordelia Imig, and Benjamin H. Cooper (Mar. 2020). "Ultrastructural Correlates of Presynaptic Functional Heterogeneity in Hippocampal Synapses". In: *Cell Reports* 30 (11), 3632–3643.e8. ISSN: 22111247. DOI: 10.1016/j.celrep.2020.02.083.

Mikula, Shawn and Winfried Denk (May 2015). "High-resolution whole-brain staining for electron microscopic circuit reconstruction". In: *Nature Methods* 12 (6), pp. 541–546. ISSN: 15487105. DOI: 10.1038/nmeth.3361.

Miyamoto, Akiko, Hiroaki Wake, Ayako Wendy Ishikawa, Kei Eto, Keisuke Shibata, Hideji Murakoshi, Schuichi Koizumi, Andrew J. Moorhouse, Yumiko Yoshimura, and Junichi Nabekura (Aug. 2016). "Microglia contact induces synapse formation in developing somatosensory cortex". In: *Nature Communications* 7. ISSN: 20411723. DOI: 10.1038/ncomms12540.

Miyamoto, Yuta and Takaichi Fukuda (July 2022). "New Subregions of the Mouse Entopeduncular Nucleus Defined by the Complementary Immunoreactivities for Substance P and Cannabinoid Type-1 Receptor Combined with Distributions of Different Neuronal Types". In: *eNeuro* 9 (4). ISSN: 23732822. DOI: 10.1523/ENEURO.0208-22.2022.

Mohan, Aurel George, Bogdan Calenic, Nicu Adrian Ghiurau, Roxana-Maria Duncea-Borca, Alexandra-Elena Constantinescu, and Ileana Constantinescu (July 2023). "The Golgi Apparatus: A Voyage through Time, Structure, Function and Implication in Neurodegenerative Disorders". In: *Cells* 12 (15), p. 1972. ISSN: 2073-4409. DOI: 10.3390/cells12151972. https://www.mdpi.com/2073-4409/12/15/1972.

Mooney, Richard (Apr. 2018). "The Song Remains the Same". In: *Trends in Neurosciences* 41 (4), pp. 167–170. ISSN: 1878108X. DOI: 10.1016/j.tins.2018.02.002.

Morales, Marisela and Elyssa B. Margolis (Feb. 2017). "Ventral tegmental area: cellular heterogeneity, connectivity and behaviour". In: *Nature Reviews Neuroscience* 18 (2), pp. 73–85. ISSN: 1471-003X. DOI: 10.1038/nrn.2016.165. https://www.nature.com/articles/nrn.2016.165.

Murthy, Venkatesh N, Thomas Schikorski, Charles F Stevens, and Yongling Zhu (Nov. 2001). "Inactivity Produces Increases in Neurotransmitter Release and Synapse Size". In: *Neuron* 32 (4), pp. 673–682. ISSN: 08966273. DOI: 10.1016/S0896-6273(01)00500-1. https://linkinghub.elsevier.com/retrieve/pii/S0896627301005001.

Naito, A. and H. Kita (Aug. 1994). "The cortico-pallidal projection in the rat: an anterograde tracing study with biotinylated dextran amine". In: *Brain Research* 653 (1-2), pp. 251–257. ISSN: 00068993. DOI: 10.1016/0006-8993(94)90397-2. https://linkinghub.elsevier.com/retrieve/pii/0006899394903972.

Nicholson, David A., Todd F. Roberts, and Samuel J. Sober (June 2018). "Thalamostriatal and cerebellothalamic pathways in a songbird, the Bengalese finch". In: *Journal of Comparative Neurology* 526 (9), pp. 1550–1570. ISSN: 10969861. DOI: 10.1002/cne.24428.

Nielsen, Morten Schak, Lene Nygaard Axelsen, Paul L. Sorgen, Vandana Verma, Mario Delmar, and Niels Henrik Holstein-Rathlou (July 2012). "Gap junctions". In: *Comprehensive Physiology* 2 (3), pp. 1981–2035. ISSN: 20404603. DOI: 10.1002/cphy.c110051.

Owen, Scott F., Joshua D. Berke, and Anatol C. Kreitzer (Feb. 2018). "Fast-Spiking Interneurons Supply Feedforward Control of Bursting, Calcium, and Plasticity for Efficient Learning". In: *Cell* 172 (4), 683–695.e15. ISSN: 10974172. DOI: 10.1016/j.cell.2018.01.005.

Özçete, Özge D., Aditi Banerjee, and Pascal S. Kaeser (Nov. 2024). "Mechanisms of neuromodulatory volume transmission". In: *Molecular Psychiatry* 29 (11), pp. 3680–3693. ISSN: 14765578. DOI: 10.1038/s41380-024-02608-3.

Pallotto, Marta, Paul V Watkins, Boma Fubara, Joshua H Singer, and Kevin L Briggman (Dec. 2015). "Extracellular space preservation aids the connectomic analysis of neural circuits". en. In: *eLife* 4, e08206. ISSN: 2050-084X. DOI: 10.7554/eLife.08206. https://elifesciences.org/articles/08206 (visited on 12/08/2024).

Peng, Hai-Rong, Yu-Kai Zhang, and Jia-Wei Zhou (Mar. 2023). "The Structure and Function of Glial Networks: Beyond the Neuronal Connections". In: *Neuroscience Bulletin* 39 (3), pp. 531–540. ISSN: 1673-7067. DOI: 10.1007/s12264-022-00992-w. https://link.springer.com/10.1007/s12264-022-00992-w.

Peters, Christian, Songwei He, Federica Fermani, Hansol Lim, Wenyu Ding, Christian Mayer, and Rüdiger Klein (May 2023). "Transcriptomics reveals amygdala neuron regulation by fasting and ghrelin thereby promoting feeding". In: *Science Advances* 9 (21). ISSN: 2375-2548. DOI: 10.1126/sciadv.adf6521. https://www.science.org/doi/10.1126/sciadv.adf6521.

Poirier, Colline, Michiel Vellema, Marleen Verhoye, Vincent Van Meir, J. Martin Wild, Jacques Balthazart, and Annemie Van Der Linden (May 2008). "A three-dimensional MRI atlas of the zebra finch brain in stereotaxic coordinates". In: *NeuroImage* 41 (1), pp. 1–6. ISSN: 10538119. DOI: 10.1016/j.neuroimage.2008.01.069.

Powell, T. P. S. and W. M. Cowan (June 1956). "A STUDY OF THALAMO-STRIATE RELATIONS IN THE MONKEY". In: *Brain* 79 (2), pp. 364–366. DOI: https://doi.org/10.1093/brain/79.2.364.

Prasad, Asheeta A. and Åsa Wallén-Mackenzie (Jan. 2024). "Architecture of the subthalamic nucleus". In: *Communications Biology* 7 (1), p. 78. ISSN: 2399-3642. DOI: 10.1038/s42003-023-05691-4. https://www.nature.com/articles/s42003-023-05691-4.

Ratna, Desh Deepak and Tanner Chase Francis (Feb. 2025). "Extrinsic and intrinsic control of striatal cholinergic interneuron activity". In: *Frontiers in Molecular Neuroscience* 18. ISSN: 1662-5099. DOI: 10.3389/fnmol.2025.1528419. https://www.frontiersin.org/articles/10.3389/fnmol.2025.1528419/full.

Ripoll-Sánchez, Lidia, Jan Watteyne, Hao Sheng Sun, Robert Fernandez, Seth R. Taylor, Alexis Weinreb, Barry L. Bentley, Marc Hammarlund, David M. Miller, Oliver Hobert, Isabel Beets, Petra E. Vértes, and William R. Schafer (Nov. 2023). "The neuropeptidergic connectome of C. elegans". In: *Neuron* 111 (22), 3570–3589.e5. ISSN: 10974199. DOI: 10.1016/j.neuron.2023.09.043.

Ronneberger, Olaf, Philipp Fischer, and Thomas Brox (May 2015). "U-Net: Convolutional Networks for Biomedical Image Segmentation". In: DOI: https://doi.org/10.48550/arXiv.1505.04597. http://arxiv.org/abs/1505.04597.

Rose, Jordan, Christian Brian, Aglaia Pappa, Mihalis I. Panayiotidis, and Rodrigo Franco (Nov. 2020). "Mitochondrial Metabolism in Astrocytes Regulates Brain Bioenergetics, Neurotransmission and Redox Balance". In: *Frontiers in Neuroscience* 14. ISSN: 1662453X. DOI: 10.3389/fnins.2020.536682.

Rundstrom, Parker and Nicole Creanza (Apr. 2021). "Song learning and plasticity in songbirds". In: *Current Opinion in Neurobiology* 67, pp. 228–239. ISSN: 18736882. DOI: 10.1016/j.conb.2021.02.003.

Salmon, Christopher K., Tabish A. Syed, J. Benjamin Kacerovsky, Nensi Alivodej, Alexandra L. Schober, Tyler F.W. Sloan, Michael T. Pratte, Michael P. Rosen, Miranda Green, Adario Chirgwin-Dasgupta, Shaurya Mehta, Affan Jilani, Yanan Wang, Hojatollah Vali, Craig A. Mandato, Kaleem Siddiqi, and Keith K. Murai (Mar. 2023). "Organizing principles of astrocytic nanoarchitecture in the mouse cerebral cortex". In: *Current Biology* 33 (5), 957–972.e5. ISSN: 18790445. DOI: 10.1016/j.cub.2023.01.043.

Saunders, Arpiar, Evan Z. Macosko, Alec Wysoker, Melissa Goldman, Fenna M. Krienen, Heather de Rivera, Elizabeth Bien, Matthew Baum, Laura Bortolin, Shuyu Wang, Aleksandrina Goeva, James Nemesh, Nolan Kamitaki, Sara Brumbaugh, David Kulp, and Steven A. McCarroll (Aug. 2018). "Molecular Diversity and Specializations among the Cells of the Adult Mouse Brain". In: *Cell* 174 (4), 1015–1030.e16. ISSN: 10974172. DOI: 10.1016/j.cell.2018.07.028.

Schick, D., A. Rother, and J. Kornfeld (2024). "Structure and interactions of glial cells and neurons in a basal ganglia connectome [Conference poster]". In: *FENS 2024, Vienna*. Science Communications World Wide. DOI: https://doi.org/10.57736/ea55-73c6.

Schick, Delta (2021). *Structural analysis of neuronal cell organelles in Area X [Bachelors Thesis]*.

— (2023). *Structure and interactions of glial cells and neurons in a basal ganglia connectome [Masters Thesis]*. Technische Universität München.

Schubert, Philipp J. (Feb. 2022). "Methods for the acquisition and analysis of volume electron microscopy data". PhD thesis. Ludwig-Maximilians-Universität München. DOI: 10.5282/edoc.29813.

Schubert, Philipp J., Sven Dorkenwald, Michał Januszewski, Viren Jain, and Joergen Kornfeld (Dec. 2019). "Learning cellular morphology with neural networks". In: *Nature Communications* 10 (1). ISSN: 20411723. DOI: 10.1038/s41467-019-10836-3.

Schubert, Philipp J., Sven Dorkenwald, Michał Januszewski, Jonathan Klimesch, Fabian Svara, Andrei Mancu, Hashir Ahmad, Michale S. Fee, Viren Jain, and Joergen Kornfeld (Nov. 2022). "SyConn2: dense synaptic connectivity inference for volume electron microscopy". In: *Nature Methods* 19 (11), pp. 1367–1370. ISSN: 15487105. DOI: 10.1038/s41592-022-01624-x.

Schultz, Wolfram, Peter Dayan, and P Read Montague (Mar. 1997). "A Neural Substrate of Prediction and Reward". In: *Science* 275 (5306), pp. 1593–1599. https://www.science.org.

Scott, Benjamin B., Timothy Gardner, Ni Ji, Michale S. Fee, and Carlos Lois (Jan. 2012). "Wandering neuronal migration in the postnatal vertebrate forebrain". In: *Journal of Neuroscience* 32 (4), pp. 1436–1446. ISSN: 02706474. DOI: 10.1523/JNEUROSCI.2145-11.2012.

Seligman, Arnold M, Hannah L Wasserkrug, and Jacob S Hanker From (Aug. 1966). "A new staining method (OTO) for enhancing contrast of lipid–containing membranes and droplets in osmium tetroxide–fixed tissue with osmiophilic thiocarbohydrazide(TCH)". In: *J Cell Biol.* 30 (2), pp. 424–432. DOI: 10.1083/jcb.30.2.424.. http://rupress.org/jcb/article-pdf/30/2/424/1618512/424.pdf.

Shipp, Stewart (Mar. 2017). "The functional logic of corticostriatal connections". In: *Brain Structure and Function* 222 (2), pp. 669–706. ISSN: 18632661. DOI: 10.1007/s00429-016-1250-9.

Shvedov, Naomi R., Sina Analoui, Theresia Dafalias, Brooke L. Bedell, Timothy J. Gardner, and Benjamin B. Scott (Feb. 2024). "In vivo imaging in transgenic songbirds reveals superdiffusive neuron migration in the adult brain". In: *Cell Reports* 43 (2). ISSN: 22111247. DOI: 10.1016/j.celrep.2024.113759.

Silver, David, Aja Huang, Chris J. Maddison, Arthur Guez, Laurent Sifre, George Van Den Driessche, Julian Schrittwieser, Ioannis Antonoglou, Veda Panneershelvam, Marc Lanctot, Sander Dieleman, Dominik Grewe, John Nham, Nal Kalchbrenner, Ilya Sutskever, Timothy Lillicrap, Madeleine Leach, Koray Kavukcuoglu, Thore Graepel, and Demis Hassabis (Jan. 2016). "Mastering the game of Go with deep neural networks and tree search". In: *Nature* 529 (7587), pp. 484–489. ISSN: 14764687. DOI: 10.1038/nature16961.

Simon, Anna, Arnd Roth, Arlo Sheridan, Mehmet Fişek, Vincenzo Marra, Claudia Racca, Jan Funke, Kevin Staras, and Michael Häusser (July 2021). "Ultrastructural readout of in vivo synaptic activity for functional connectomics". In: *bioRxiv*. DOI: 10.1101/2021.07.07.451278. http://biorxiv.org/lookup/doi/10.1101/2021.07.07.451278.

Song, Kun, Zhihui Feng, and Moritz Helmstaedter (June 2023). "High-contrast en bloc staining of mouse whole-brain and human brain samples for EM-based connectomics". In: *Nature Methods* 20 (6), pp. 836–840. ISSN: 15487105. DOI: 10.1038/s41592-023-01866-3.

Spacek, Josef and Kristen M. Harris (Jan. 1997). "Three-Dimensional Organization of Smooth Endoplasmic Reticulum in Hippocampal CA1 Dendrites and Dendritic Spines of the Immature and Mature Rat". In: *The Journal of Neuroscience* 17 (1), pp. 190–203. ISSN: 0270-6474. DOI: 10.1523/JNEUROSCI.17-01-00190.1997. https://www.jneurosci.org/lookup/doi/10.1523/JNEUROSCI.17-01-00190.1997.

Spurr, Arthur R. (Jan. 1969). "A low-viscosity epoxy resin embedding medium for electron microscopy". In: *Journal of Ultrastructure Research* 26 (1-2), pp. 31–43. ISSN: 00225320. DOI: 10.1016/S0022-5320(69)90033-1. https://linkinghub.elsevier.com/retrieve/pii/S0022532069900331.

Stoler, Ohad, Alexandra Stavsky, Yana Khrapunsky, Israel Melamed, Grace Stutzmann, Daniel Gitler, Israel Sekler, and Ilya Fleidervish (Feb. 2022). "Frequency-and spike-timing-dependent mitochondrial Ca2+ signaling regulates the metabolic rate and synaptic efficacy in cortical neurons". In: *eLife* 11. ISSN: 2050084X. DOI: 10.7554/ELIFE.74606.

Ströh, Sebastian, Eric W Hammerschmith, David W Tank, H Sebastian Seung, and Adrian Andreas Wanner (2022). "In situ X-ray-assisted electron microscopy staining for large biological samples". In: 11, p. 72147. DOI: 10.7554/eLife.

Studer, D., M. Michel, M. Wohlwend, E. B. Hunziker, and M. D. Buschmann (1995). "Vitrification of articular cartilage by high-pressure freezing". In: *Journal of Microscopy* 179 (3), pp. 321–322. ISSN: 13652818. DOI: 10.1111/j.1365-2818.1995.tb03648.x.

Südhof, Thomas C. (2004). "The synaptic vesicle cycle". In: *Annual Review of Neuroscience* 27, pp. 509–547. ISSN: 0147006X. DOI: 10.1146/annurev.neuro.26.041002.131412.

Sutton, Richard S and Andrew G Barto (Nov. 2017). *Reinforcement Learning: An Introduction*. Second edition. MIT Press.

Takamori, Shigeo, Matthew Holt, Katinka Stenius, Edward A. Lemke, Mads Grønborg, Dietmar Riedel, Henning Urlaub, Stephan Schenck, Britta Brügger, Philippe Ringler, Shirley A. Müller, Burkhard Rammner, Frauke Gräter, Jochen S. Hub, Bert L. De Groot, Gottfried Mieskes, Yoshinori Moriyama, Jürgen Klingauf, Helmut Grubmüller, John Heuser, Felix Wieland, and Reinhard Jahn (Nov. 2006). "Molecular Anatomy of a Trafficking Organelle". In: *Cell* 127 (4), pp. 831–846. ISSN: 00928674. DOI: 10.1016/j.cell.2006.10.030.

Tanimoto, Yuki, Hisaya Kakinuma, Ryo Aoki, Toshiyuki Shiraki, Shin ichi Higashijima, and Hitoshi Okamoto (Mar. 2024). "Transgenic tools targeting the basal ganglia reveal both evolutionary conservation and specialization of neural circuits in zebrafish". In: *Cell Reports* 43 (3). ISSN: 22111247. DOI: 10.1016/j.celrep.2024.113916.

Tavakoli, Mojtaba R., Julia Lyudchik, Michał Januszewski, Vitali Vistunou, Nathalie Agudelo Dueñas, Jakob Vorlaufer, Christoph Sommer, Caroline Kreuzinger, Bárbara Oliveira, Alban Cenameri, Gaia Novarino, Viren Jain, and Johann G. Danzl (June 2025). "Light-microscopy-based connectomic reconstruction of mammalian brain tissue". In: *Nature* 642 (8067), pp. 398–410. ISSN: 14764687. DOI: 10.1038/s41586-025-08985-1.

Tegethoff, Lennart and Kevin L. Briggman (2024). "Quantitative evaluation of embedding resins for volume electron microscopy". In: *Frontiers in Neuroscience* 18. ISSN: 1662453X. DOI: 10.3389/fnins.2024.1286991.

Tepper, James M., Tibor Koós, Osvaldo Ibanez-Sandoval, Fatuel Tecuapetla, Thomas W. Faust, and Maxime Assous (Nov. 2018). "Heterogeneity and diversity of striatal GABAergic interneurons: Update 2018". In: *Frontiers in Neuroanatomy* 12. ISSN: 16625129. DOI: 10.3389/fnana.2018.00091.

Tepper, James M., Fatuel Tecuapetla, Tibor Koós, and Osvaldo Ibáñez-Sandoval (Dec. 2010). "Heterogeneity and diversity of striatal GABAergic interneurons". In: *Frontiers in Neuroanatomy* (DEC). ISSN: 16625129. DOI: 10.3389/fnana.2010.00150.

Terasaki, Mark (Feb. 2018). "Axonal endoplasmic reticulum is very narrow". In: *Journal of Cell Science* 131 (4). ISSN: 14779137. DOI: 10.1242/jcs.210450.

The MICrONS Consortium (Apr. 2025). "Functional connectomics spanning multiple areas of mouse visual cortex". In: *Nature* 640 (8058), pp. 435–447. ISSN: 14764687. DOI: 10.1038/s41586-025-08790-w.

Thomas, Connon I., Melissa A. Ryan, Naomi Kamasawa, and Benjamin Scholl (Dec. 2023). "Postsynaptic mitochondria are positioned to support functional diversity of dendritic spines". In: *eLife* 12. ISSN: 2050084X. DOI: 10.7554/eLife.89682.

Tisch, Stephen, Paul Silberstein, Patricia Limousin-Dowsey, and Marjan Jahanshahi (Dec. 2004). "The basal ganglia: anatomy, physiology, and pharmacology". In: *Psychiatric Clinics of North America* 27 (4), pp. 757–799. ISSN: 0193953X. DOI: 10.1016/j.psc.2004.06.004. https://linkinghub.elsevier.com/retrieve/pii/S0193953X04000590.

Tomassy, Giulio Srubek, Daniel R. Berger, Hsu-Hsin Chen, Narayanan Kasthuri, Kenneth J. Hayworth, Alessandro Vercelli, H. Sebastian Seung, Jeff W. Lichtman, and Paola Arlotta (2014). "Distinct Profiles of Myelin Distribution Along Single Axons of Pyramidal Neurons in the Neocortex". In: *Science* 344 (6181), pp. 313–319. ISSN: 10959203. DOI: 10.1126/science.1249766.

Trueta, Citlali and Francisco F. De-Miguel (2012). "Extrasynaptic exocytosis and its mechanisms: A source of molecules mediating volume transmission in the nervous system". In: *Frontiers in Physiology* 3 SEP. ISSN: 1664042X. DOI: 10.3389/fphys.2012.00319.

Tsuboi, Masafumi and Yusuke Hirabayashi (2021). "New insights into the regulation of synaptic transmission and plasticity by the endoplasmic reticulum and its membrane contacts". In: *Proceedings of the Japan Academy Series B: Physical and Biological Sciences* 97 (10), pp. 559–572. ISSN: 13492896. DOI: 10.2183/PJAB.97.028.

Turner, Nicholas L., Thomas Macrina, J. Alexander Bae, Runzhe Yang, Alyssa M. Wilson, Casey Schneider-Mizell, Kisuk Lee, Ran Lu, Jingpeng Wu, Agnes L. Bodor, Adam A. Bleckert, Derrick Brittain, Emmanouil Froudarakis, Sven Dorkenwald, Forrest Collman, Nico Kemnitz, Dodam Ih, William M. Silversmith, Jonathan Zung, Aleksandar Zlateski, Ignacio Tartavull, Szi chieh Yu, Sergiy Popovych, Shang Mu, William Wong, Chris S. Jordan, Manuel Castro, Jo Ann Buchanan, Daniel J. Bumbarger, Marc Takeno, Russel Torres, Gayathri Mahalingam, Leila Elabbady, Yang Li, Erick Cobos, Pengcheng Zhou, Shelby Suckow, Lynne Becker, Liam Paninski, Franck Polleux, Jacob Reimer, Andreas S. Tolias, R. Clay Reid, Nuno Maçarico da Costa, and H. Sebastian Seung (Mar. 2022). "Reconstruction of neocortex: Organelles, compartments, cells, circuits, and activity". In: *Cell* 185 (6), 1082–1100.e24. ISSN: 10974172. DOI: 10.1016/j.cell.2022.01.023.

Umpierre, Anthony D. and Long-Jun Wu (July 2021). "How microglia sense and regulate neuronal activity". In: *Glia* 69 (7), pp. 1637–1653. ISSN: 0894-1491. DOI: 10.1002/glia.23961. https://onlinelibrary.wiley.com/doi/10.1002/glia.23961.

Uytiepo, Marco, Yongchuan Zhu, Eric Bushong, Katherine Chou, Filip Souza Polli, Elise Zhao, Keun-Young Kim, Danielle Luu, Lyanne Chang, Dong Yang, Tsz Ching Ma, Mingi Kim, Yuting Zhang, Grant Walton, Tom Quach, Matthias Haberl, Luca Patapoutian, Arya Shahbazi, Yuxuan Zhang, Elizabeth

Beutter, Weiheng Zhang, Brian Dong, Aureliano Khoury, Alton Gu, Elle McCue, Lisa Stowers, Mark Ellisman, and Anton Maximov (Mar. 2025). "Synaptic architecture of a memory engram in the mouse hippocampus". In: *Science* 387 (6740). ISSN: 0036-8075. DOI: 10.1126/science.ado8316. https://www.science.org/doi/10.1126/science.ado8316.

Vates, G E and F Nottebohm (May 1995). "Feedback circuitry within a song-learning pathway." In: *Proceedings of the National Academy of Sciences* 92 (11), pp. 5139–5143. ISSN: 0027-8424. DOI: 10.1073/pnas.92.11.5139. https://pnas.org/doi/full/10.1073/pnas.92.11.5139.

Vorona, Gregory A. and Jeffrey I. Berman (Sept. 2015). "Review of diffusion tensor imaging and its application in children". In: *Pediatric Radiology* 45, pp. 375–381. ISSN: 14321998. DOI: 10.1007/s00247-015-3277-0.

Walton, Judie (Oct. 1979). "Lead aspartate, an en bloc contrast stain particularly useful for ultrastructural enzymology". In: *J Histochem Cytochem* 27 (10), pp. 1337–1342. DOI: 10.1177/27.10.512319.

Wang, Xuan, Zhenfeng Shu, Quansheng He, Xiaowen Zhang, Luozheng Li, Xiaoxue Zhang, Liang Li, Yujie Xiao, Bo Peng, Feifan Guo, Da Hui Wang, and Yousheng Shu (Apr. 2023). "Functional Autapses Form in Striatal Parvalbumin Interneurons but not Medium Spiny Projection Neurons". In: *Neuroscience Bulletin* 39 (4), pp. 576–588. ISSN: 19958218. DOI: 10.1007/s12264-022-00991-x.

Weiler, Simon (2018). "Integrated circuit analysis of the mouse visual system". PhD thesis. Ludwig-Maximilians-Universität München. DOI: 10.5282/edoc.22967.

White, John Graham, Eileen Southgate, J. N. Thomson, and Sydney Brenner (Nov. 1986). "The structure of the nervous system of the nematode Caenorhabditis elegans". In: *Philosophical Transactions of the Royal Society of London. B, Biological Sciences* 314 (1165), pp. 1–340. ISSN: 0080-4622. DOI: 10.1098/rstb.1986.0056. https://royalsocietypublishing.org/doi/10.1098/rstb.1986.0056.

Willingham, Mark C and Angelina V Rutherford (Apr. 1984). "The use of osmium-thiocarbohydrazide-osmium (OTO) and ferrocyanide-reduced osmium methods to enhance membrane contrast and preservation in cultured cells". In: *J Histochem Cytochem.* 32 (4), pp. 455–460. DOI: 10.1177/32.4.6323574.

Wilson, Alyssa and Mehrtash Babadi (Apr. 2023). "SynapseCLR: Uncovering features of synapses in primary visual cortex through contrastive representation learning". In: *Patterns* 4 (4). ISSN: 26663899. DOI: 10.1016/j.patter.2023.100693.

Wu, Ying, Sandra Richard, and André Parent (Sept. 2000). "The organization of the striatal output system: a single-cell juxtacellular labeling study in the rat". In: *Neuroscience Research* 38 (1), pp. 49–62. ISSN: 01680102. DOI: 10.1016/S0168-0102(00)00140-1. https://linkinghub.elsevier.com/retrieve/pii/S0168010200001401.

Wu, Yumei, Christina Whiteus, C. Shan Xu, Kenneth J. Hayworth, Richard J. Weinberg, Harald F. Hess, and Pietro De Camilli (June 2017). "Contacts between the endoplasmic reticulum and other membranes in neurons". In: *Proceedings of the National Academy of Sciences of the United States of America* 114 (24), E4859–E4867. ISSN: 10916490. DOI: 10.1073/pnas.1701078114.

Xiao, Lei, Devin P. Merullo, Therese M.I. Koch, Mou Cao, Marissa Co, Ashwinikumar Kulkarni, Genevieve Konopka, and Todd F. Roberts (Dec. 2021). "Expression of FoxP2 in the basal ganglia regulates vocal motor sequences in the adult songbird". In: *Nature Communications* 12 (1). ISSN: 20411723. DOI: 10.1038/s41467-021-22918-2.

Xu, C. Shan, Kenneth J. Hayworth, Zhiyuan Lu, Patricia Grob, Ahmed M. Hassan, Jose G. García-Cerdán, Krishna K. Niyogi, Eva Nogales, Richard J Weinberg, and Harald F Hess (May 2017). "Enhanced FIB-SEM systems for large-volume 3D imaging". In: *Elife*. DOI: 10.7554/eLife.25916.001. https://elifesciences.org/articles/25916#abstract.

Xu, C. Shan, Song Pang, Gleb Shtengel, Andreas Müller, Alex T. Ritter, Huxley K. Hoffman, Shin ya Takemura, Zhiyuan Lu, H. Amalia Pasolli, Nirmala Iyer, Jeeyun Chung, Davis Bennett, Aubrey V. Weigel, Melanie Freeman, Schuyler B. van Engelenburg, Tobias C. Walther, Robert V. Farese, Jennifer Lippincott-Schwartz, Ira Mellman, Michele Solimena, and Harald F. Hess (Nov. 2021). "An open-access volume electron microscopy atlas of whole cells and tissues". In: *Nature* 599 (7883), pp. 147–151. ISSN: 14764687. DOI: 10.1038/s41586-021-03992-4.

Xu, Heping, Mei Chen, Ayyakkannu Manivannan, Noemi Lois, and John V. Forrester (Feb. 2008). "Age-dependent accumulation of lipofuscin in perivascular and subretinal microglia in experimental mice". In: *Aging Cell* 7 (1), pp. 58–68. ISSN: 14749718. DOI: 10.1111/j.1474-9726.2007.00351.x.

Yagishita, Sho, Akiko Hayashi-Tagaki, Graham C. R. Ellies-Davies, Hidetoshi Urakubo, Shin Ishii, and Haruo Kasai (Sept. 2014). "A critical time window for dopamine actions on the structural plasticity of dendritic spines". In: *Science* 345 (6204), pp. 1613–1620. ISSN: 10959203. DOI: 10.1126/science.1258750.

Yener, Yagmur, Alessandro Motta, and Moritz Helmstaedter (Feb. 2025). "Connectomic analysis of astrocyte-synapse interactions in the cerebral cortex". In: *bioRxiv*. DOI: 10.1101/2025.02.20.639274. http://biorxiv.org/lookup/doi/10.1101/2025.02.20.639274.

Yoo, Andy B., Morris A. Jette, and Mark Grondona (Aug. 2003). "SLURM: Simple Linux Utility for Resource Management". In: pp. 44–60. DOI: 10.1007/10968987_3. http://link.springer.com/10.1007/10968987_3.

Zeng, Hongkui (June 2018). "Mesoscale connectomics". In: *Current Opinion in Neurobiology* 50, pp. 154–162. ISSN: 18736882. DOI: 10.1016/j.conb.2018.03.003.

Zhang, Shiliang, Jia Qi, Xueping Li, Hui Ling Wang, Jonathan P. Britt, Alexander F. Hoffman, Antonello Bonci, Carl R. Lupica, and Marisela Morales (Mar. 2015). "Dopaminergic and glutamatergic microdomains in a subset of rodent mesoaccumbens axons". In: *Nature Neuroscience* 18 (3), pp. 386–396. ISSN: 15461726. DOI: 10.1038/nn.3945.

Zheng, Zhihao, J. Scott Lauritzen, Eric Perlman, Camenzind G. Robinson, Matthew Nichols, Daniel Milkie, Omar Torrens, John Price, Corey B. Fisher, Nadiya Sharifi, Steven A. Calle-Schuler, Lucia Kmecova, Iqbal J. Ali, Bill Karsh, Eric T. Trautman, John A. Bogovic, Philipp Hanslovsky, Gregory S.X.E. Jefferis, Michael Kazhdan, Khaled Khairy, Stephan Saalfeld, Richard D. Fetter, and Davi D. Bock (July 2018). "A Complete Electron Microscopy Volume of the Brain of Adult Drosophila melanogaster". In: *Cell* 174 (3), 730–743.e22. ISSN: 10974172. DOI: 10.1016/j.cell.2018.06.019.

Zhong, Shiying, Conrad M. Kiyoshi, Yixing Du, Wei Wang, Yumeng Luo, Xiao Wu, Anne T. Taylor, Baofeng Ma, Sydney Aten, Xueyuan Liu, and Min Zhou (Apr. 2023). "Genesis of a functional astrocyte syncytium in the developing mouse hippocampus". In: *GLIA* 71 (4), pp. 1081–1098. ISSN: 10981136. DOI: 10.1002/glia.24327.

Appendix

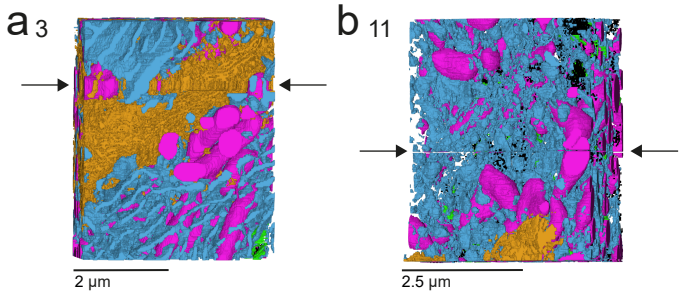

Figure A1: Annotated ground truth cubes 3 and 11 which include artifacts in the raw data. Arrows indicate location of the artefact and how it affects the annotations. Mitochondria shown in pink, ER in blue, GA in orange, synapses in green and vesicles in black.

cell type	axon pathlength ratio	dendrite pathlength ratio
GPe	0.49	0.49
GPi	0.39	0.28
INT1	0.67	0.73
INT2	0.22	0.57
INT3	0.55	0.68
LTS	0.08	0.34
MSN	0.77	0.73
STN	0.12	0.18
TAN	0.04	0.23

Table A1: The ratio of full cells versus fragments of a specific compartment per cell type in the dataset. The path length ratio calculates the path length of this compartment for all full cells versus the sum of the path lengths of all fragments in this cell type.

version	ground truth	all fragments with at least one synapse	all fragments
v4 stats	52.48	74009.93	112518.87
v4 p-value	4.02e-12	0.0	0.0
v5 stats	80.52	900698.26	1151326.87
v5 p-value	3.27e-18	0.0	0.0
v6 stats	52.75	258860.58	914903.56
v6 p-value	3.51e-12	0.0	0.0

Table A2: Test statistic and p-values calculated using the Kruskal-Wallis test for the length of projecting axons in the different versions.

	version	DA vs HVC	DA vs LMAN	HVC vs LMAN
stats	v4	-1.64	-5.63	-6.44
p-value	v4	0.10	1.84e-08	1.18e-10
stats	v5	-4.29	-6.08	-7.86
p-value	v5	1.82e-05	1.24e-09	3.82e-15
stats	v6	-0.44	-5.08	-6.74
p-value	v6	0.66	3.78e-07	1.56e-11

Table A3: P-values calculated using the ranksum test for the axon length in the ground truth for the different versions.

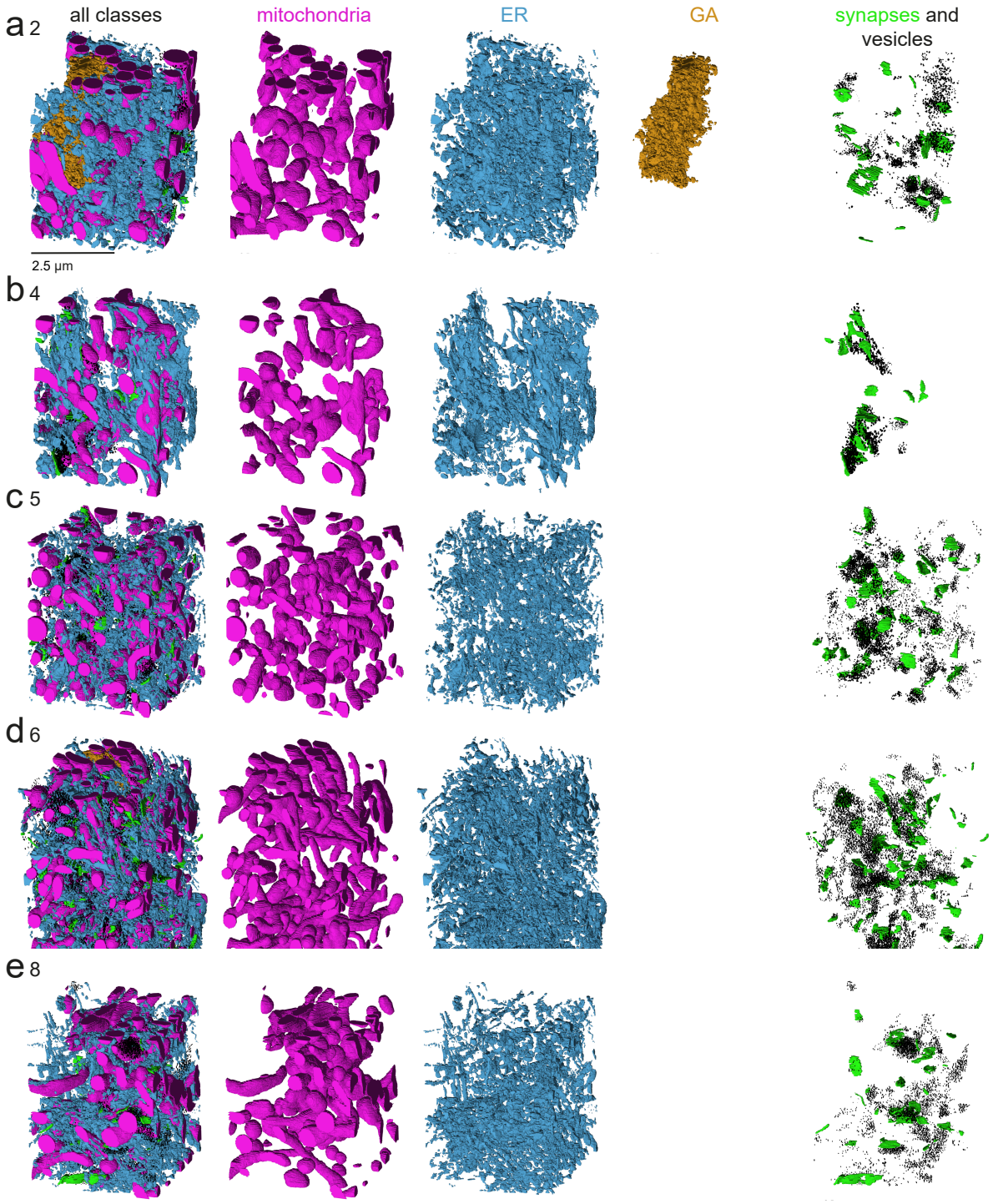

Figure A2: Annotated ground truth cubes 2, 4, 5, 6, and 8 according to table 2.10. All on the same scale. Not all cubes contain GA. d Cube 6 is over annotated in the z direction.

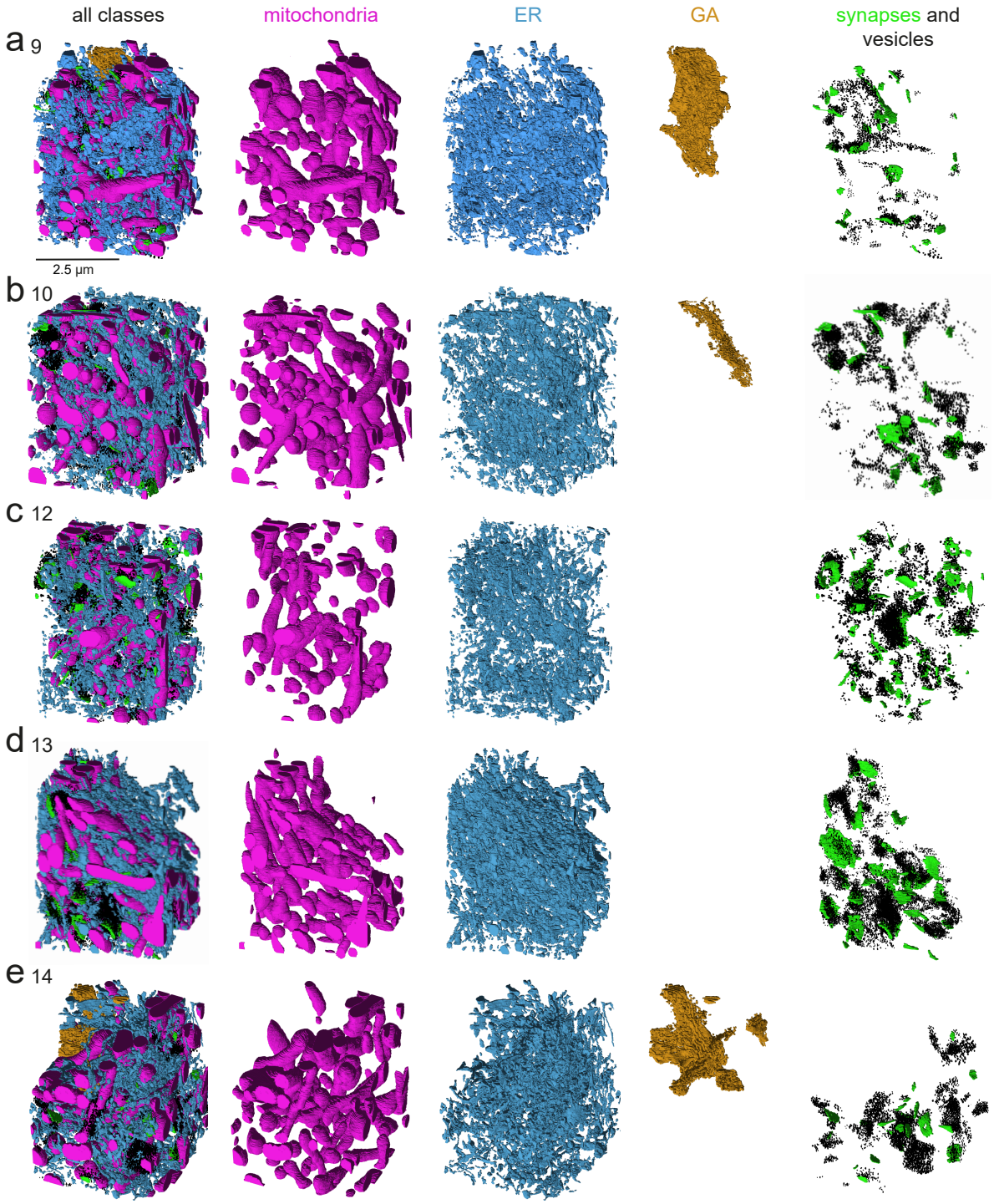

Figure A3: Annotated ground truth cubes 9, 10, 12, 13 and 14 according to table 2.10. All on the same scale. Not all cubes contain GA.

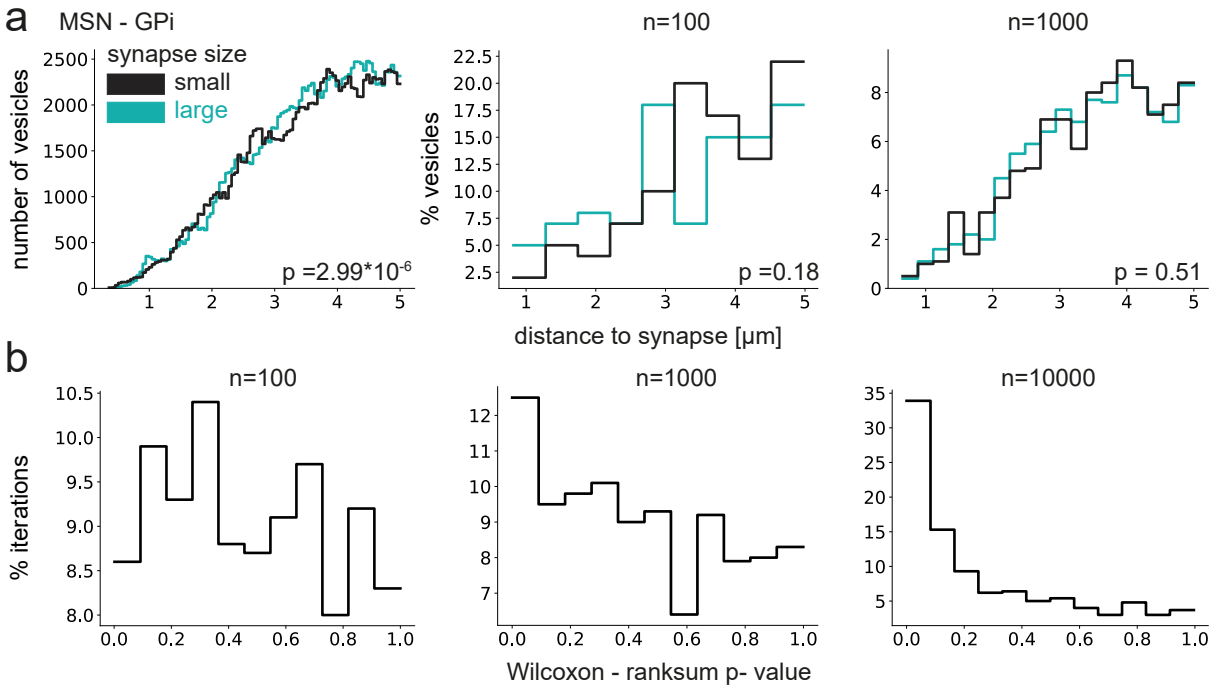

Figure A4: Non-synaptic TAN vesicles in proximity to MSN-GPi synapses. TAN vesicles were considered non-synaptic if they were at least 3 µm away from the closest synapse. "Small" and "large" synapses refer to the lowest and highest percentiles of synapses, respectively, according to synapse size. See appendix table A45 for more detail on vesicle numbers and synapse sizes. a Distance of vesicles for all MSN-GPi synapses (left); then, a random sample of 100 or 1000 vesicles was used for bootstrapping. b P-values of the Wilcoxon rank sum test across 1000 iterations of bootstrapping with different sample sizes for each iteration.

	version	DA vs HVC	DA vs LMAN	HVC vs LMAN
stats	v4	-243.72	-152.61	-114.87
p-value	v4	0.0	0.0	0.0
stats	v5	-906.41	-463.42	202.22
p-value	v5	0.0	0.0	0.0
stats	v6	-507.31	-122.53	93.65
p-value	v6	0.0	0.0	0.0

Table A4: P-values calculated using the ranksum test for axon length in the predicted axons with at least one synapse in the different versions.

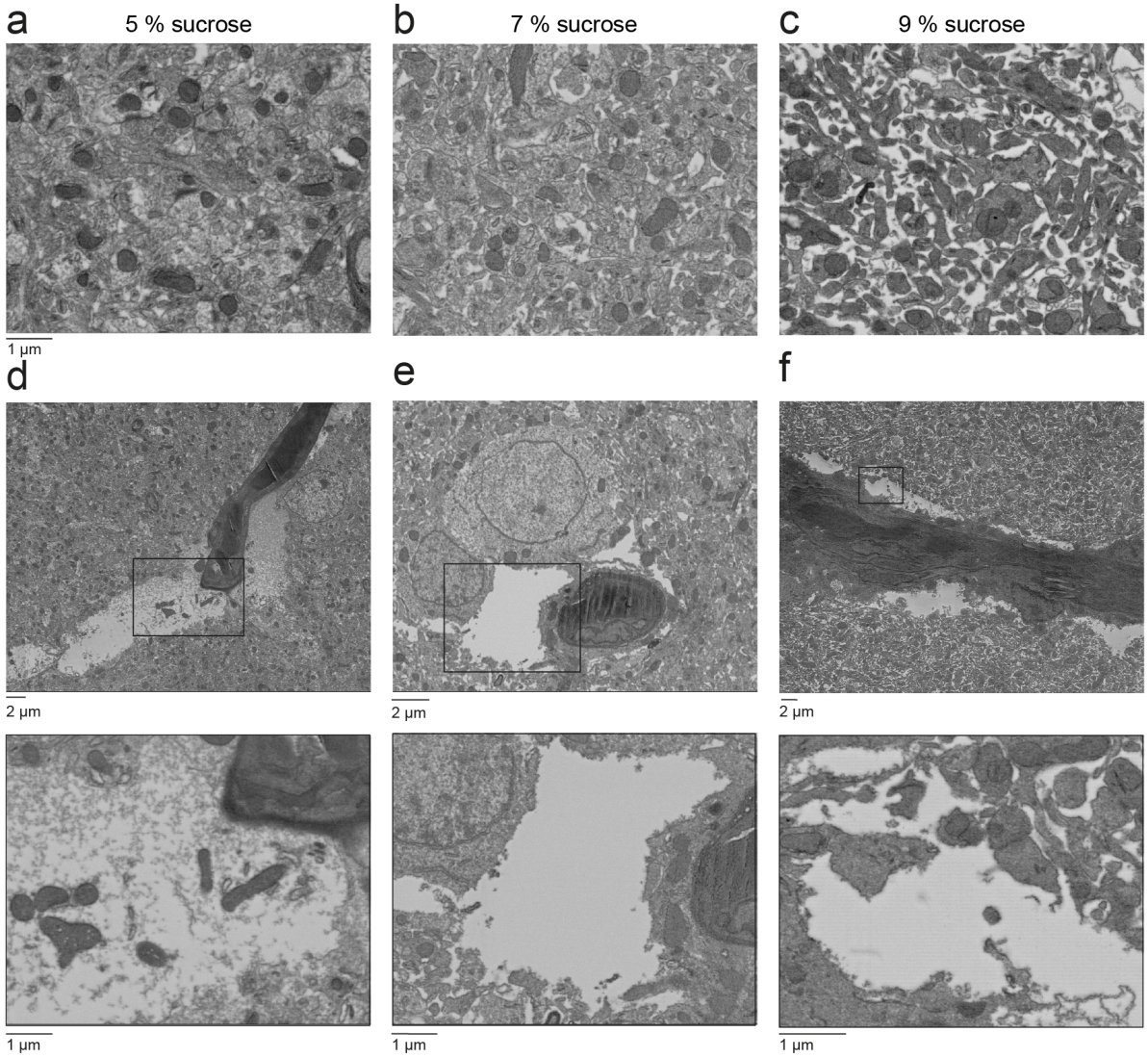

Figure A5: Different concentrations of sucrose were used for fixation of large samples. Three 2.5-mm samples of a zebra finch brain were fixed with solutions containing 5, 7, or 9 % sucrose. a-c The neuropil in the middle of the sample shows different amounts of preserved ECS depending on the sucrose concentration. All images are on the same scale. All images are on the same scale. d-f Artifacts around the blood vessels in the same samples as a-c. Insets show details of the damage around the blood vessels.

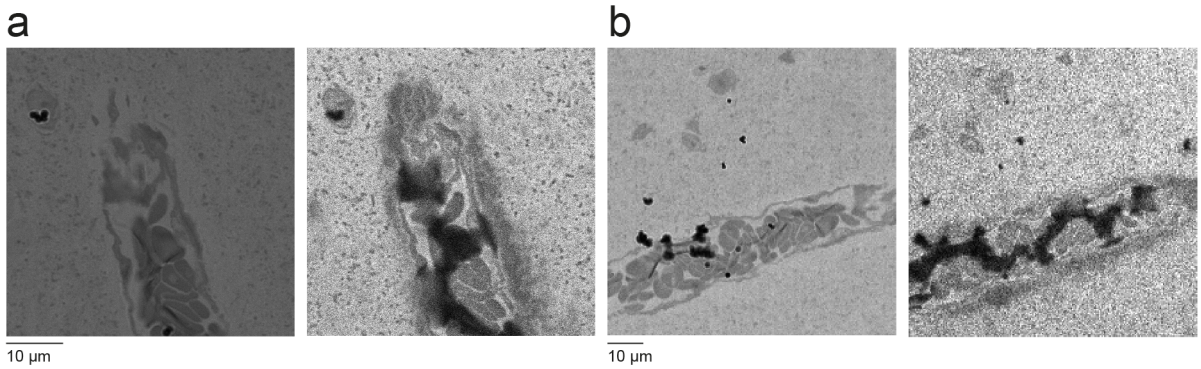

Figure A6: Light microscopy images of ETS stained samples, fixed in solution containing 7 % sucrose. The sample was fixed as a 2.5 mm block. a, b Two different locations containing blood vessels were imaged with transmitted light (left) and fluorescence (right). The area around the blood vessel shows artifacts in the unstained tissue similar to those in appendix figure A5 b.

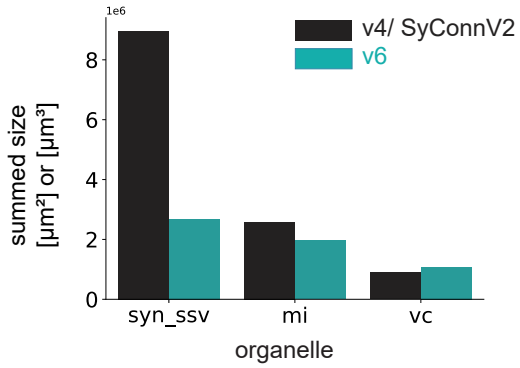

Figure A7: The summed synaptic area, summed mitochondrial volume, and summed vesicle cloud volume were compared between the versions, 'v4/SyConnV2' from Schubert et al. 2022 and the current version, 'v6'.

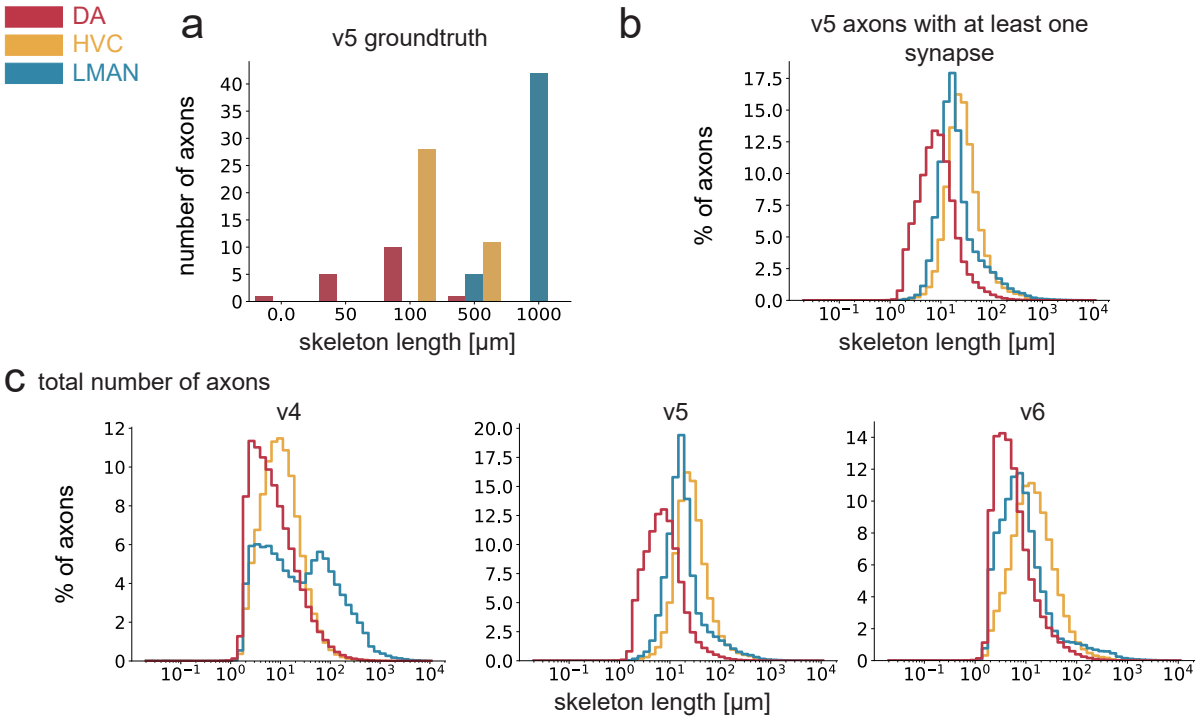

Figure A8: Projecting axons and their lengths. a v5 number of axon fragments in different length used for ground truth generation. Labels show lower end of the corresponding bin, e.g 50 indicates axon fragments with length 50 - 100 µm. b v5 percentages of axons with at least one synapse c Comparison of the lengths of predicted fragments in SyConnV2/ 'v4' (Schubert et al. 2022), 'v5', and the most recent version ,'v6'.

	version	DA vs HVC	DA vs LMAN	HVC vs LMAN
stats	v4	-307.57	-178.61	-125.57
p-value	v4	0.0	0.0	0.0
stats	v5	-1006.35	-556.32	271.62
p-value	v5	0.0	0.0	0.0
stats	v6	-953.45	-190.83	228.40
p-value	v6	0.0	0.0	0.0

Table A5: P-values calculated using the ranksum test for the axon lengths of all the predicted axons in the different versions.

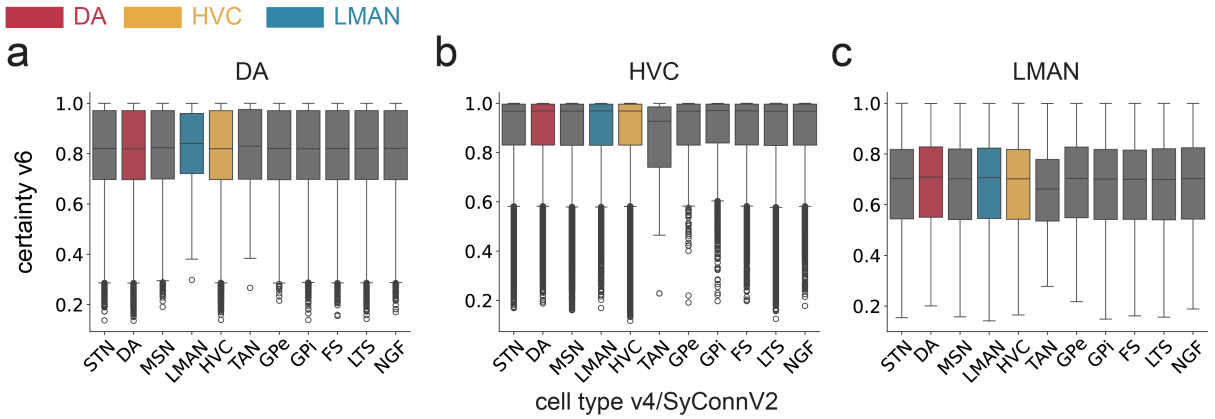

Figure A9: Certainties of different projecting axon classes in the current version v6. Putative VTA projecting axons (DA). b Putative HVC projecting axons. c Putative LMAN projecting axons.

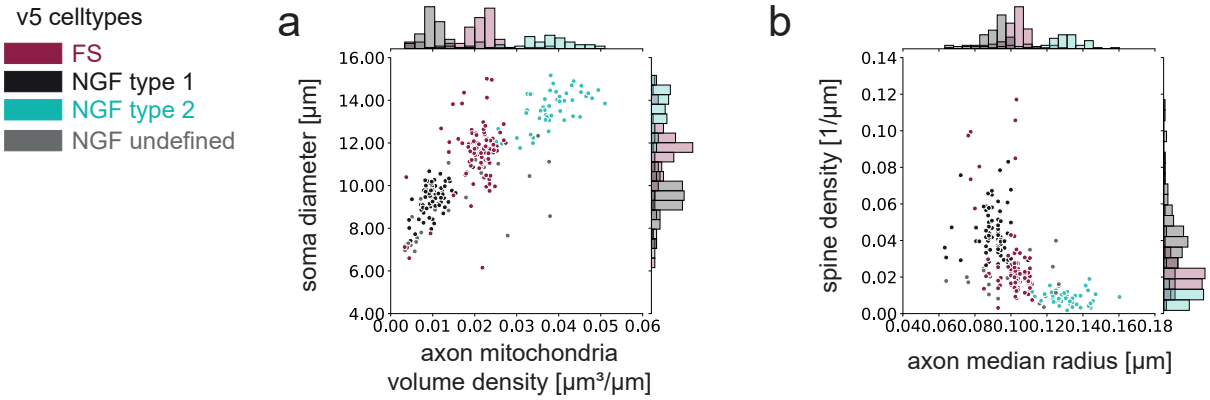

Figure A10: Interneuron morphological differences in v5. a Soma diameter and axon mitochondrial volume density. b Spine density and axon median radius of FS, NGF type 1, NGF type 2, and undefined NGF. In the following version ("v6") labeled INT1 (FS), INT2 (NGF type 1), and INT3 (NGF type 2).

cell type	number of cells v5	number of cells v6
FS/ INT1	91	96
NGF type 2/ INT2	76	100
NGF type 3/ INT3	50	66
NGF undefined	27	-
total	244	262

Table A6: Number of complete cells used to distinguish the three interneuron types: FS/INT1, NGF type 1/INT2 and NGF type 2/INT3. The cells used are filtered for completeness using the same criteria as those used for data analysis.

morphological parameters	v5 stats	v5 p-value	v6 stats	v6 p-value
axon median radius	155.87	1.42E-34	140.84	2.61E-31
axon mitochdondria volume density	172.15	4.16E-38	198.81	6.76E-44
soma diameter	151.41	1.32E-33	150.84	1.76E-33
spine density	150.51	2.07E-33	145.10	3.10E-32

Table A7: P-values calculated using the Kruskal-Wallis test for different morphological parameters between FS, NGF type 2, and NGF type 1 in v5, as well as INT1-3 in v6. The results of the post hoc test can be found in the appendix tables A8, A9.

	FS vs NGF type 1	FS vs NGF type 2	NGF type 1 vs NGF type 2
axon median radius stats	8.29	-9.80	-9.47
axon median radius p-value	1.15E-16	1.10E-22	2.68E-21
axon mitochondria volume density stats	9.87	-9.75	-9.47
axon mitochondria volume density p-value	5.84E-23	1.87E-22	2.68E-21
soma diameter stats	9.28	-8.05	-9.47
soma diameter p-value	1.73E-20	8.25E-16	2.68E-21
spine density stats	-8.64	8.83	9.47
spine density p-value	5.70E-18	1.04E-18	2.68E-21

Table A8: Results of the pairwise Wilcoxon rank sum test for FS and NGF types in v5.

	INT1 vs INT2	INT1 vs INT3	INT2 vs INT3
axon median radius stats	10.00	-3.37	-9.71
axon median radius p-value	1.52E-23	0.000762405	2.85E-22
axon mitochondria volume density stats	10.50	-9.57	-10.88
axon mitochondria volume density p-value	8.73E-26	1.05E-21	1.40E-27
soma diameter stats	9.45	-6.37	-10.06
soma diameter p-value	3.43E-21	1.84E-10	7.99E-24
spine density stats	-7.28	8.52	10.20
spine density p-value	3.22E-13	1.57E-17	2.00E-24

Table A9: Results of the pairwise Wilcoxon rank sum test for INT1, INT2 and INT3 types in v6.

	DA	LMAN	HVC	MSN	STN	TAN	GPe	GPi	LTS	INT1	INT2	INT3	ASTRO	OLIGO	MICRO	MIGR	FRAG
DA	23	0	0.67	0	0	0.67	0	0	0	0.67	1	0	0	0	0	0	0
LMAN	0	53.33	1	1	0.67	0	0	0	0	0.33	0.67	0	0	0	1	0	0
HVC	0	6	45.33	1.67	0	0	0	0	0	0	0	0	0	0	0	0	0
MSN	0	1.33	0	29.33	0	0	0	0	0.33	0	0	0	0	0	0	0	0
STN	0	1	0	0	29.67	0	0.33	0	1	1.67	0	0.33	0	0	0	0	0
TAN	0	0.33	0	0	0	9.33	0	0	0	0.67	0.67	1	0	0	0	0	0
GPe	0	0	0	0	0	0	12	0	0	1	0	0	0	0	0	0	0
GPi	0	0	1	0	0	0	2	12	0	0	0	0	0	0	0	0	0
LTS	0	0.33	1	2.33	0	0.33	0	0	3.67	1	0.33	0	0	0	0	0	0
INT1	0	1	0	0	0.67	0.33	0	0	0	22	0	0	0	0	0	0	0
INT2	0	0	0	0	0	0	0	0	0	0.33	15.67	0	0	0	0	0	0
INT3	0	0	0	0	0	0	0	0	0	0	0.67	15.33	0	0	0	0	0
ASTRO	0	0	0	0	0	0	0	0	0	0	0	0	17	0	0	0	0
OLIGO	0	0.67	0	0.67	0.33	0	0	0	0	0	0	0	0	9.33	2.33	0.67	0
MICRO	0	0	0	0	0	0	0	0	0	0	0	0	0	0	17	0	0
MIGR	0	0.33	0	0	0	0	0	0	0	0	0	0	0	0	1	12.67	0
FRAG	0.67	1.33	0.33	0.33	0	0	0	0	0	0	0.33	0	2	0.33	1.33	0	17.3

Table A10: Confusion matrix from the 10-fold cross-validation, averaged over three repetitions with redundancy 1.

	DA	LMAN	HVC	MSN	STN	TAN	GPe	GPi	LTS	INT1	INT2	INT3	ASTRO	OLIGO	MICRO	MIGR	FRAG
DA	24	0	0.67	0	0	0.67	0	0	0	0	0.67	0	0	0	0	0	0
LMAN	0	57	1	0	0	0	0	0	0	0	0	0	0	0	0	0	0
HVC	0	2.33	50.67	0	0	0	0	0	0	0	0	0	0	0	0	0	0
MSN	0	0	0	31	0	0	0	0	0	0	0	0	0	0	0	0	0
STN	0	0	0	0	33.33	0	0	0	0	0.33	0.33	0	0	0	0	0	0
TAN	0	0	0	0	0	12	0	0	0	0	0	0	0	0	0	0	0
GPe	0	0	0	0	0	0	12.33	0.67	0	0	0	0	0	0	0	0	0
GPi	0	0	0	0	0	0	0.67	14.33	0	0	0	0	0	0	0	0	0
LTS	0	0	0	0	1.33	0	0	0	6.67	1	0	0	0	0	0	0	0
INT1	0	0	0	0	2	0	0	0	0	22	0	0	0	0	0	0	0
INT2	0	0	0	0	0	0	0	0	0	0.67	15.33	0	0	0	0	0	0
INT3	0	0	0	0	0	0	0	0	0	0	0	16	0	0	0	0	0
ASTRO	0	0	0	0	0	0	0	0	0	0	0	0	17	0	0	0	0
OLIGO	0	0.67	0	0	0.33	0	0	0	0	0	0.33	0	0	9.33	2.33	1	0
MICRO	0	0	0	0	0	0	0	0	0	0	0	0	0	0	17	0	0
MIGR	0	0	0	0	0	0	0	0	0	0	0	0	0	0	1	13	0
FRAG	0	1.67	0.33	0.33	0	0	0	0	0	0	0	0	2	0.33	1.67	0	17.67

Table A11: Confusion matrix from the 10-fold cross-validation, averaged over three repetitions with redundancy 10.

	DA	LMAN	HVC	MSN	STN	TAN	GPe	GPi	LTS	INT1	INT2	INT3	ASTRO	OLIGO	MICRO	MIGR	FRAG
DA	25.33	0	0.67	0	0	0	0	0	0	0	0	0	0	0	0	0	0
LMAN	0	57	1	0	0	0	0	0	0	0	0	0	0	0	0	0	0
HVC	0	3.33	49.67	0	0	0	0	0	0	0	0	0	0	0	0	0	0
MSN	0	0	0	31	0	0	0	0	0	0	0	0	0	0	0	0	0
STN	0	0	0	0	33.33	0	0	0	0	0.67	0	0	0	0	0	0	0
TAN	0	0	0	0	0	12	0	0	0	0	0	0	0	0	0	0	0
GPe	0	0	0	0	0	0	12	1	0	0	0	0	0	0	0	0	0
GPi	0	0	0	0	0	0	1.67	13.33	0	0	0	0	0	0	0	0	0
LTS	0	0.67	0	0	1	0.67	0	0	6.67	0	0	0	0	0	0	0	0
INT1	0	0	0	0	1	0	0	0	0	23	0	0	0	0	0	0	0
INT2	0	0	0	0	0	0	0	0	0	0	16	0	0	0	0	0	0
INT3	0	0	0	0	0	0	0	0	0	0	0	16	0	0	0	0	0
ASTRO	0	0	0	0	0	0	0	0	0	0	0	0	17	0	0	0	0
OLIGO	0	0.67	0	0	0.33	0	0	0	0	0	0.33	0	0	9.67	2.33	0.67	0
MICRO	0	0	0	0	0	0	0	0	0	0	0	0	0	0	17	0	0
MIGR	0	0	0	0	0	0	0	0	0	0	0	0	0	0	1	13	0
FRAG	0.33	1.33	0.33	0.33	0	0	0	0	0	0	0	0	2	0.33	1.67	0	17.67

Table A12: Confusion matrix from the 10-fold cross-validation, averaged over three repetitions with redundancy 20.

	DA	LMAN	HVC	MSN	STN	TAN	GPe	GPi	LTS	INT1	INT2	INT3	ASTRO	OLIGO	MICRO	MIGR	FRAG
DA	25.33	0	0.67	0	0	0	0	0	0	0	0	0	0	0	0	0	0
LMAN	0	57	1	0	0	0	0	0	0	0	0	0	0	0	0	0	0
HVC	0	2.67	50.33	0	0	0	0	0	0	0	0	0	0	0	0	0	0
MSN	0	0	0	31	0	0	0	0	0	0	0	0	0	0	0	0	0
STN	0	0	0	0	34	0	0	0	0	0	0	0	0	0	0	0	0
TAN	0	0	0	0	0	12	0	0	0	0	0	0	0	0	0	0	0
GPe	0	0	0	0	0	0	12	1	0	0	0	0	0	0	0	0	0
GPi	0	0	0	0	0	0	1	14	0	0	0	0	0	0	0	0	0
LTS	0	0	0	0	1.67	0	0	0	6.33	0	1	0	0	0	0	0	0
INT1	0	0	0	0	2	0	0	0	0	22	0	0	0	0	0	0	0
INT2	0	0	0	0	0	0	0	0	0	0	16	0	0	0	0	0	0
INT3	0	0	0	0	0	0	0	0	0	0	0	16	0	0	0	0	0
ASTRO	0	0	0	0	0	0	0	0	0	0	0	0	17	0	0	0	0
OLIGO	0	0.67	0	0	0.33	0	0	0	0	0	0.33	0	0	9.67	2.33	0.67	0
MICRO	0	0	0	0	0	0	0	0	0	0	0	0	0	0	17	0	0
MIGR	0	0	0	0	0	0	0	0	0	0	0	0	0	0	0.67	13.33	0
FRAG	0	1.33	0.33	0.33	0	0	0	0	0	0	0	0	2	0.33	2	0	17.67

Table A13: Confusion matrix from the 10-fold cross-validation, averaged over three repetitions with redundancy 50.

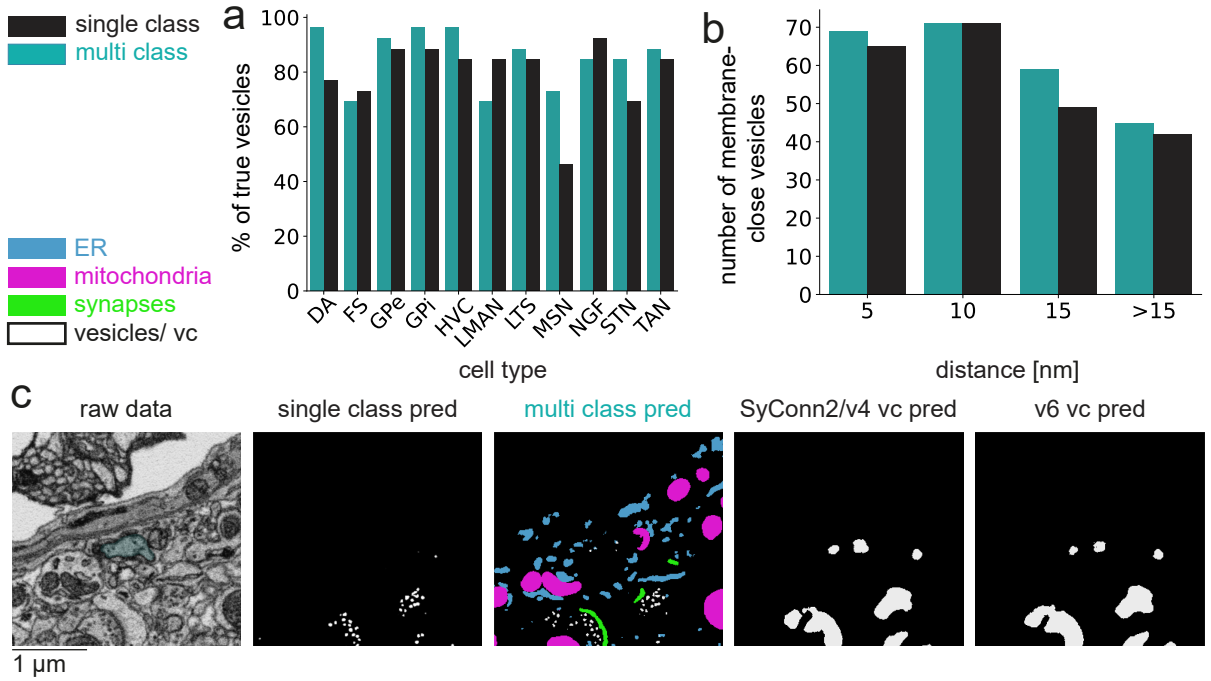

Figure A11: Evaluation of individual vesicle prediction and extraction by comparing training on individual vesicles as a single class with multi-class prediction, together with mitochondria, ER, GA, and synapses. a Fraction of true vesicles is depicted for each cell type. b Number of true membrane-close vesicles at different distances. c Astrocyte mitochondria that were misclassified as vesicles were found by Delta Schick (location: 16609, 15810, 11746; astrocyte ID: 2302353201).

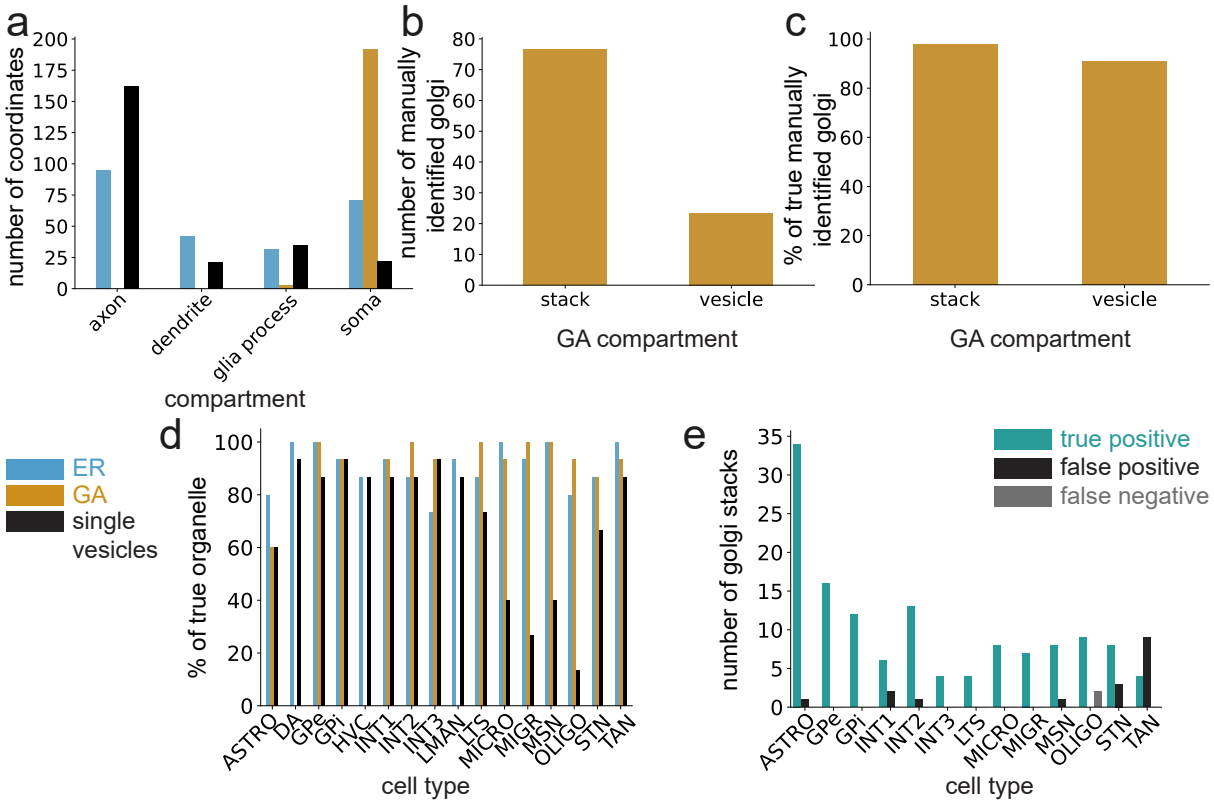

Figure A12: Evaluation of ER and Ga prediction. a Number of coordinates in each manually identified compartment. b Number of manually identified coordinates in either a GA stack or a GA vesicle. c Percentage of coordinates predicted as a GA and manually verified to be either a GA stack or a GA vesicle. d Fraction of true ER, GA, and vesicle coordinates per cell type. e Number of separated GA stacks per cell type. True positives are GA that were correctly mapped to cells. False positives are those that were mapped to cells but are not GA stacks. False negatives are stacks that are GA but were not predicted or mapped to cells.

cell type	number total	number erroneous cells	number incomplete cells	number cells with mergers	mergers per mm pathlength	number mergers with neurons	number mergers with glia
MSN	500	6	0	6	0.004	6	0
GPe	28	1	1	0	0.000	0	0
GPi	58	11	2	9	0.020	11	1
LTS	38	1	0	1	0.008	1	0
STN	108	6	2	4	0.006	5	0
TAN	13	5	1	4	0.049	5	0
INT1	10	3	0	3	0.030	2	1
INT2	10	1	0	1	0.018	1	0
INT3	10	1	0	1	0.014	1	1

Table A14: Mergers from manually reviewed cells. All reviewed cells had a predicted soma, axon, and dendrite, with a minimum path length of 200 µm for each. For MSN, a random subset of 500 cells (out of 8,093) was chosen; for INT1-3, a random subset of 10 cells was chosen because these cells have extensive axonal arborization, making manual checks time-intensive. The complete set of cells was manually inspected for the other cell types (GPe, GPi, LTS, STN, and TAN). Cells were marked as 'erroneous' if they either did not have an axon, soma, or dendrite after visual inspection ('incomplete') or were merged with another cell (>50 µm path length or >1 synapse). "Erroneous" cells were excluded from the analysis for cell types where all cells could be manually checked (method section 2.3.1). To determine the number of mergers per millimeter, all mergers involving different fragments were counted (some cells had more than one merger) and divided by the total path length of all cells of this cell type.

cell type	length mean [µm]	length std [µm]	median radius mean [µm]	median radius std [µm]	surface area mean [µm²]	surface area std [µm²]	myelin fraction mean	myelin fraction std
DA	349.39	189.35	0.09	0.010	400.43	229.69	0.000	0.000
GPe	5205.71	2016.70	0.11	0.016	8705.43	3878.51	0.009	0.015
GPi	6225.65	2201.74	0.16	0.027	14903.95	4708.35	0.132	0.056
HVC	333.84	154.10	0.09	0.018	326.31	207.83	0.000	0.003
INT1	8652.10	3948.12	0.09	0.006	11646.67	5426.67	0.000	0.000
INT2	3445.20	1761.09	0.08	0.008	3942.35	2143.13	0.000	0.000
INT3	10604.10	4759.77	0.09	0.008	20127.88	9600.45	0.003	0.006
LMAN	570.02	656.28	0.14	0.079	835.61	926.58	0.162	0.294
LTS	1619.04	1014.03	0.09	0.009	1607.07	1065.23	0.000	0.002
MSN	880.88	303.53	0.08	0.007	778.16	295.07	0.001	0.019
STN	5671.47	3877.94	0.08	0.011	6418.74	4835.05	0.004	0.010
TAN	3219.23	1737.58	0.10	0.008	4204.01	2049.72	0.000	0.000

Table A15: The mean and standard deviation of axon morphological parameters in all neuronal cell types.

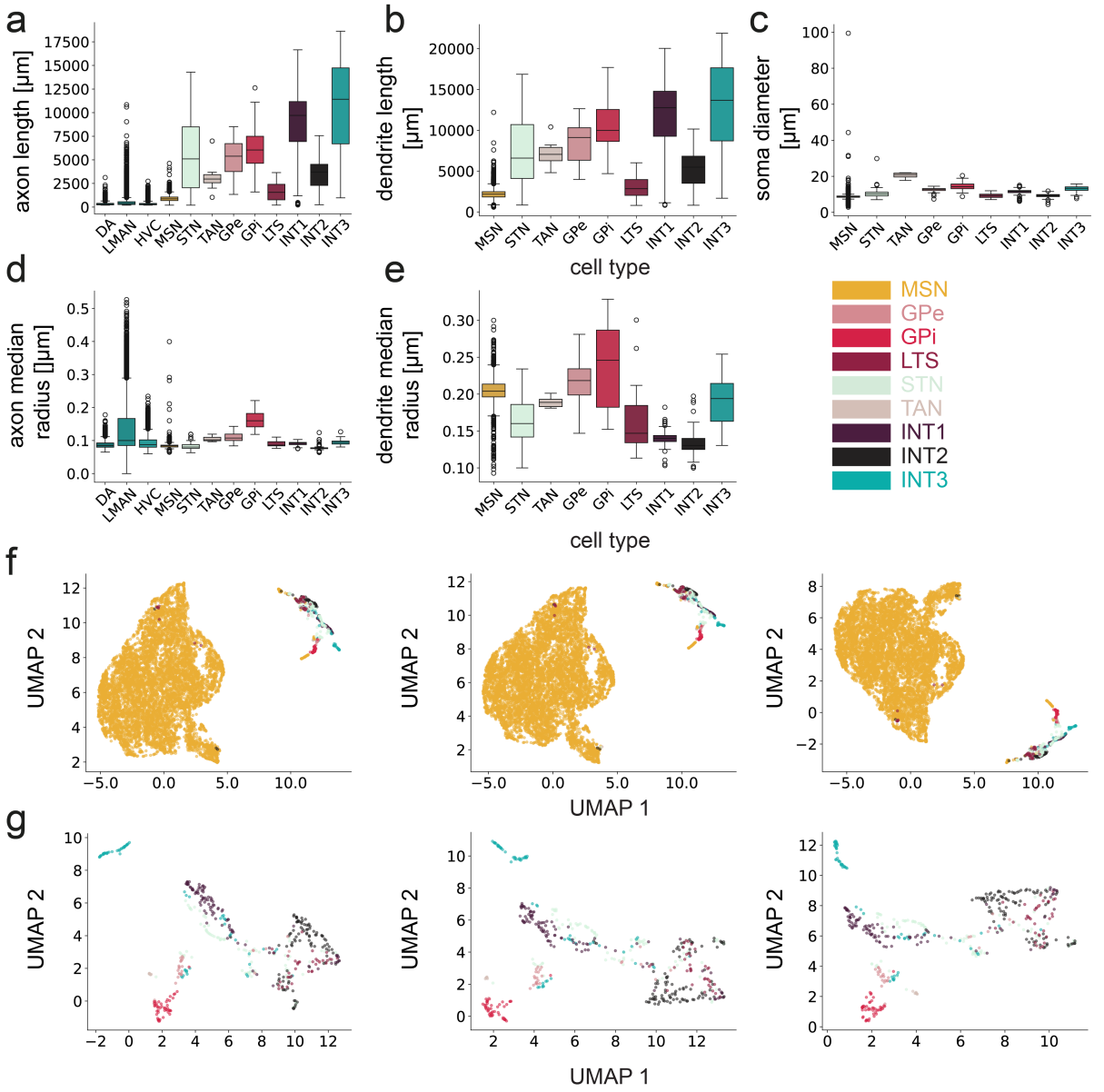

Figure A13: Different morphological parameters in neuronal cell types. a Axon skeleton pathlength. b Dendrite skeleton pathlength. c Estimated soma diameter. d Median axon radius. e Median dendrite radius. f UMAP runs of all neurons in an 11-dimensional feature space with parameters from figure 3.15 a-f and a-e, same as figure 3.15 g. g Same as f, but UMAP separation is done without MSN cells, the same as in 3.15 h.

cell type	soma diameter mean [µm]	soma diameter std [µm]	spine density mean [1/µm]	spine density std [1/µm]	dendrite length mean [µm]	dendrite length std [µm]	dendrite median radius mean [µm]	dendrite median radius std [µm]	soma surface area mean [µm²]	soma surface area std [µm²]	dendrite surface area mean [µm²]	dendrite surface area std [µm²]	cell volume mean [µm³]	cell volume std [µm³]
GPe	12.39	1.55	0.03	0.011	8309.65	2790.62	0.22	0.03	1104.17	277.04	6976.19	2526.29	3130.06	1184.74
GPi	14.52	2.24	0.01	0.007	10443.34	3101.68	0.24	0.06	1490.38	816.95	11483.55	4631.96	5856.73	1708.50
INT1	11.39	1.64	0.03	0.025	11521.39	4745.02	0.14	0.01	877.50	236.03	4617.08	1686.87	2338.41	802.45
INT2	9.21	1.14	0.04	0.026	5303.94	2243.63	0.13	0.02	554.17	157.94	3032.28	1124.85	1017.52	362.19
INT3	13.03	1.56	0.01	0.007	13011.69	5254.93	0.19	0.03	1147.40	322.33	4978.07	1671.06	3963.95	1522.97
LTS	9.36	1.33	0.04	0.023	2973.33	1251.43	0.16	0.04	622.36	179.79	2477.32	1044.77	826.58	282.34
MSN	8.77	1.38	0.18	0.038	2171.29	584.13	0.20	0.02	421.57	101.13	2942.25	939.49	729.58	165.20
STN	10.41	2.55	0.02	0.016	7588.33	4367.72	0.16	0.03	714.72	261.27	3594.38	2037.72	1547.73	850.18
TAN	20.53	1.54	0.06	0.015	7181.10	1723.76	0.19	0.01	4242.20	678.16	8015.88	1597.09	4349.92	605.97

Table A16: Mean and standard deviation of morphological parameters relating to soma and dendrite.

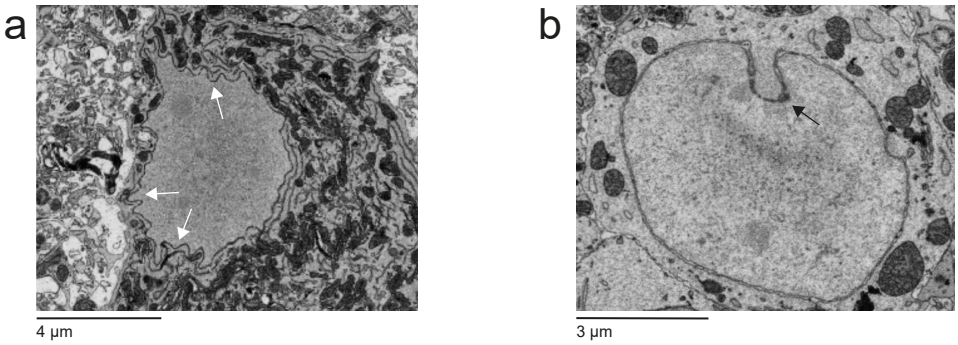

Figure A14: Specific nuclear morphologies. a An example of a wrinkly nucleus in a GPi cell. The white arrows point to the wrinkles. Coordinates: 7097, 20884, 3177. b An example of an STN cell with an infolding in the nucleus, indicated by a black arrow. Coordinates: 21482, 25063, 6136.

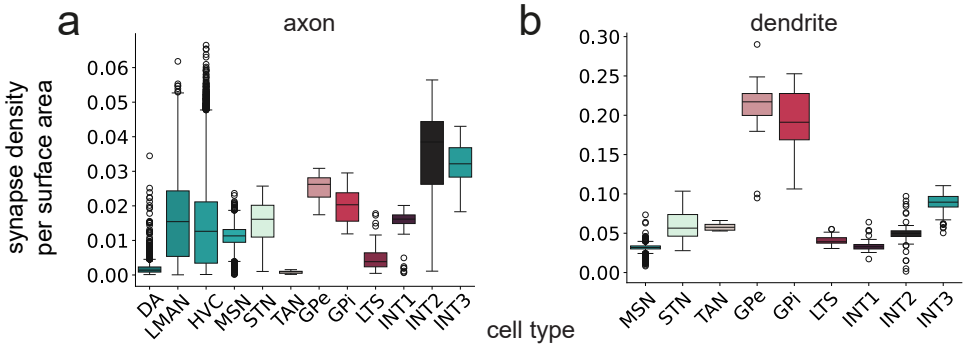

Figure A15: Synaptic area in relation to the surface mesh area of the axon and dendrite in different cell types.

parameter	Kruskal stats	Kruskal p-value
soma diameter [µm]	42662.80	0.0
spine density [1/µm]	42712.54	0.0
axon length [µm]	16827.14	0.0
dendrite length [µm]	42683.45	0.0
axon median radius [µm]	4581.13	0.0
dendrite median radius [µm]	42672.15	0.0
soma surface area [µm2]	17090.02	0.0
axon surface area [µm2]	23940.75	0.0
dendrite surface area [µm2]	42636.92	0.0
axon myelin fraction	16508.46	0.0
cell volume [µm3]	42671.59	0.0

Table A17: Results of the Kruskal-Wallis test for different parameters on all cell types. For parameters relating to axon or cell volume, projecting axon cell types (DA, HVC, and LMAN) were also included. All p-values were significant in a post hoc Kruskal–Wallis test with $p < 0.005$, except: soma diameter: GPe vs INT3 (0.03), INT2 vs LTS (0.88); spine density: GPe vs INT1 (0.17), GPe vs LTS (0.006), GPe vs STN (0.02), GPi vs INT3 (0.29), INT1 vs STN (0.03), INT2 vs LTS (0.60), INT2 vs TAN (0.006), LTS vs TAN (0.02); axon length: DA vs HVC (0.97), GPe vs GPi (0.11), GPe vs STN (0.82), GPe vs TAN (0.02), GPi vs STN (0.23), INT1 vs INT2 (0.008), INT2 vs TAN (0.46), LTS vs TAN (0.006), STN vs TAN (0.09); dendrite length: GPe vs GPi (0.009), GPe vs STN (0.27), GPe vs TAN (0.41), GPi vs INT1 (0.02), GPi vs INT3 (0.007), INT1 vs INT2 (0.09), INT2 vs TAN (0.02); axon median radius: DA vs LTS (0.07), GPe vs LMAN (0.58), GPe vs TAN (0.35), HVC vs INT1(0.23), HVC vs LTS (0.70), HVC vs TAN (0.008) , INT1 vs LTS (0.10), INT3 vs LMAN (0.01), LMAN vs TAN (0.81); dendrite median radius: GPe vs GPi (0.03), GPe vs MSN (0.005), GPe vs TAN (0.006), INT1 vs LTS (0.02), GPi vs TAN (0.05), INT3 vs TAN (0.66), LTS vs STN (0.21), LTS vs TAN (0.01), STN vs TAN (0.005); soma surface area: GPe vs INT3 (0.50), INT2 vs LTS (0.07); dendrite surface area: GPe vs TAN (0.46), GPi vs TAN (0.02), INT1 vs INT3 (0.20), INT2 vs LTS (0.01), INT2 vs MSN (0.04), INT2 vs STN (0.37), LTS vs MSN (0.006), MSN vs STN (0.04) ; axon surface area: GPe vs STN (0.01), INT2 vs TAN (0.94), STN vs TAN (0.34); axon myelin fraction: DA vs HVC (0.27), DA vs INT1 (0.89), DA vs INT2 (0.97), DA vs MSN (0.48), DA vs TAN (0.55), GPe vs INT3 (0.20), GPe vs LMAN (0.46), GPe vs STN (0.005), GPe vs TAN (0.02), HVC vs INT1 (0.97), HVC vs INT2 (0.83), HVC vs LTS (0.66), HVC vs MSN (0.74), HVC vs TAN (0.59), HVC vs INT2 (0,90), INT1 vs LTS (0.69), INT1 vs MSN(0.99), INT1 vs STN (0.006), INT1 vs TAN (0.59), INT2 vs LTS (0.63), INT2 vs MSN (0.87), INT2 vs TAN(0.56), INT3 vs LMAN (0.19), INT3 vs TAN(0.007), LMAN vs TAN (0.05), LTS vs MSN (0.64), LTS vs STN (0.09), LTS vs TAN (0.78), MSN vs TAN (0.58), STN vs TAN (0.51); cell volume: DA vs HVC (1), DA vs LMAN (1), GPe vs INT3 (0.009), INT3 vs TAN (0.63), LTS vs MSN (0.09)

cell type	**cell number**	**cells with ≥ 1 1 synapse**	**percent with autapse**	**cells with wrinkled nucleus**	**percent with wrinkled nucleus**	**cells with nucleus infoldings**	**percent with nucleus infoldings**
GPe	26	8	30.8	2	7.7	0	0.0
GPi	42	17	40.5	22	52.4	0	0.0
INT1	88	9	10.2	1	1.1	4	4.5
INT2	96	2	2.1	1	1.0	7	7.3
INT3	63	34	54.0	1	1.6	0	0.0
LTS	36	0	0.0	0	0.0	1	2.8
MSN	50	0	0.0	4	8.0	1	2.0
STN	97	0	0.0	5	5.2	28	28.9
TAN	7	0	0.0	0	0.0	0	0.0

Table A18: The fraction of cells with manually verified autapses, wrinkly somata, or soma indentations is shown for different cell types. For the GPe, GPi, LTS, STN, TAN, INT1, INT2, and INT3, all of the cells in the dataset with complete somata were inspected. For MSNs, only a random subset was inspected.

statistical test	Kruskal-Wallis statistic	Kruskal-Wallis p-value
axon synaptic density per pathlength	7496.28	0
axon synaptic density per surface area	7619.34	0
dendrite synaptic density per pathlength	991.87	8.49E-209
dendrite synaptic density per surface area	1004.90	1.30E-211
soma synaptic density	1250.90	9.63E-265

Table A19: Kruskal-Wallis test results for synaptic density in different compartments. Synaptic density was calculated twice: once as synaptic area per skeleton path length and once as synaptic area per mesh surface area. For the soma, only the synaptic area per surface area was calculated. For the projecting axon cell types (DA, HVC, and LMAN), values were only calculated for the axon. A post hoc Wilcoxon rank sum test showed p-values < 0.005 for all pairs except: axon synaptic density per pathlength: DA vs TAN (0.10), GPe vs GPi (0.10), GPe vs INT2 (0.65), GPi vs INT2 (0.008), LMAN vs STN (0.85); axon synaptic density per surface area: DA vs TAN (0.02), HVC vs STN (0.01), INT1 vs LMAN (0.97), INT1 vs STN (0.60), LMAN vs STN (0.98); dendrite synaptic density per pathlength: INT1 vs MSN (0.26), INT2 vs LTS (0.19), STN vs TAN (0.07); dendrite synaptic density per surface area: GPe vs GPi (0.06), INT1 vs MSN (0.02), STN vs TAN (0.84); soma synaptic density: GPe vs GPi (0.27), GPe vs INT3 (0.35), GPi vs INT3 (0.01), INT1 vs STN (0.81), INT2 vs TAN (0.16), STN vs TAN (0.01)

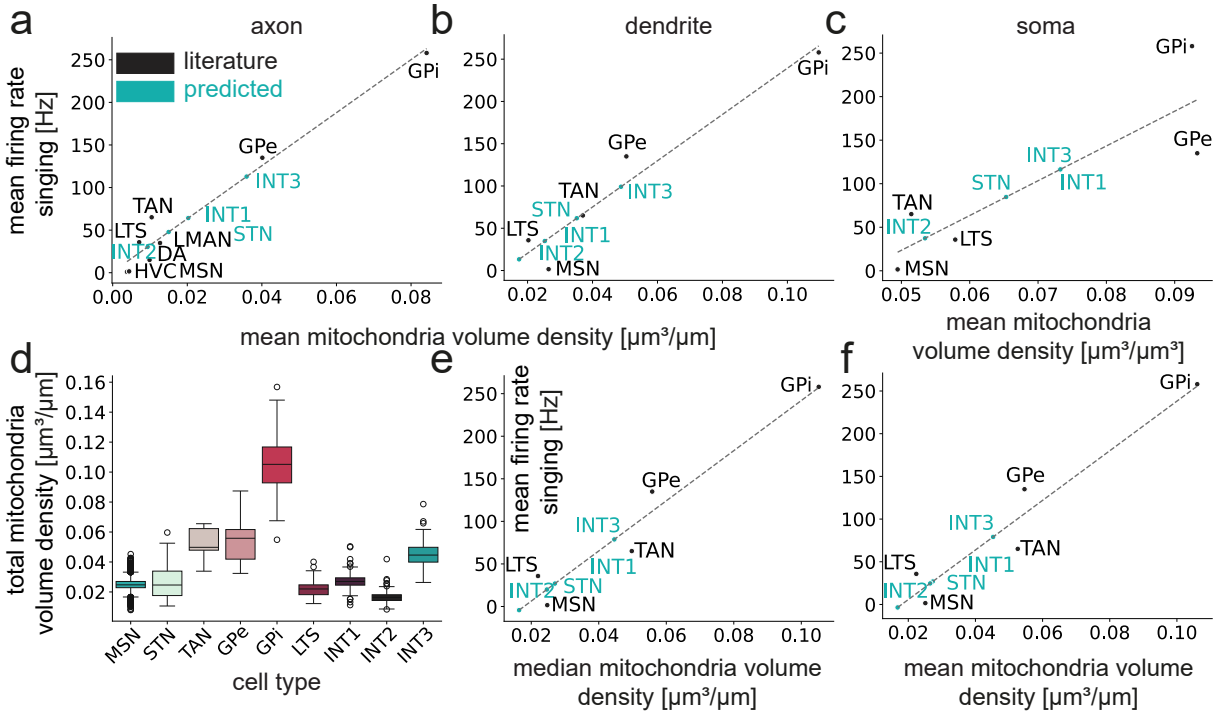

Figure A16: Mitochondrial volume density in different cell types in relation to firing rates. Black values represent mean firing rates during singing from the literature. Turquoise values are predicted by linear regression. a-c Mean firing rates predicted based on mean mitochondrial volume density in the axon, dendrite, and soma. d Total mitochondrial volume density in different cell types. c, d Mean firing rates predicted based on mean and median mitochondrial volume density.

cell type	**total**			**axon**			**dendrite**			**soma**		
	mean	std	median	mean	std	median	mean	std	median	mean	std	median
DA				0.010	0.003	0.010						
GPe	0.055	0.014	0.056	0.040	0.012	0.040	0.050	0.012	0.050	0.093	0.014	0.090
GPi	0.106	0.023	0.105	0.084	0.019	0.084	0.110	0.024	0.113	0.093	0.042	0.103
HVC				0.004	0.002	0.004						
INT1	0.027	0.006	0.027	0.020	0.005	0.022	0.025	0.006	0.025	0.073	0.022	0.072
INT2	0.017	0.004	0.016	0.009	0.003	0.010	0.017	0.004	0.017	0.053	0.015	0.054
INT3	0.045	0.010	0.045	0.036	0.008	0.037	0.049	0.009	0.049	0.073	0.011	0.073
LMAN				0.013	0.008	0.011						
LTS	0.022	0.007	0.022	0.007	0.003	0.007	0.020	0.004	0.020	0.058	0.013	0.056
MSN	0.025	0.004	0.025	0.004	0.001	0.004	0.026	0.003	0.026	0.049	0.010	0.049
STN	0.027	0.011	0.025	0.015	0.008	0.014	0.035	0.015	0.031	0.065	0.023	0.061
TAN	0.053	0.011	0.050	0.010	0.001	0.011	0.037	0.003	0.037	0.051	0.010	0.053

Table A20: The mean, median, and standard deviation were computed for axon and total mitochondrial volume densities. For projection axon cell types (DA, HVC, and LMAN), only the axon volume density was computed.

statistical test	statistic	p-value
total mitochondria volume density	676.26	9.226e-141
axon mitochondria volume density	22175.61	0.0
dendrite mitochondria volume density	755.77	6.98e-158
soma mitochondria volume density	495.67	5.96e-102

Table A21: Kruskal-Wallis test results for total mitochondrial volume density, as well as for axon, dendrite, and soma volume densities. For the projecting axon cell types (DA, HVC, and LMAN), only the axon mitochondrial volume density was computed. A post hoc Wilcoxon rank sum test showed p-values $<$ 0.005 for all pairs except: total: GPe vs TAN (0.84), INT1 vs STN (0.01), INT3 vs TAN (0.04), LTS vs STN (0.06), MSN vs STN (0.65); axon: DA vs INT2 (0.27), DA vs TAN (0.20), GPe vs INT3 (0.18), INT2 vs TAN (0.19), LMAN vs STN (0.005), LMAN vs TAN (0.70), STN vs TAN (0.28); dendrite: GPe vs INT3 (0.67), STN vs TAN (0.26); soma: GPe vs GPi (0.19), GPi vs TAN (0.008), INT1 vs INT3 (0.81), INT1 vs STN (0.01), INT2 vs LTS (0.20), INT2 vs TAN (0.53), LTS vs STN (0.06), LTS vs TAN (0.26), MSN vs TAN (0.55), STN vs TAN (0.06)

	coefficient	intercept	r-squared	adj. r-squared	f-statistic	p-value	spearman correlation coefficient	spearman p-value
total mean	2905.10	-52.40	0.928	0.904	38.59	6.41e-03	0.90	0.04
total median	2945.25	-52.59	0.945	0.926	51.20	5.62e-03	0.90	0.04
axon mean	3113.43	1.10	0.965	0.959	166.50	1.33e-05	0.88	3.85e-03
axon median	3096.82	2.50	0.966	0.961	172.90	1.19e-05	0.88	3.85e-03
dendrite mean	2736.40	-34.34	0.937	0.916	44.58	6.85e-03	0.90	0.04
dendrite median	2613.05	30.09	0.933	0.911	42.05	7.44e-03	0.90	0.04
soma mean	3993.13	-176.13	0.758	0.677	9.38	0.0549	0.80	0.10
soma median	3885.54	-174.03	0.900	0.866	26.89	0.0139	0.90	0.04

Table A22: The statistics of the different linear regressions are based on the mitochondria volume density, as calculated with StatsModels. Additionally, the Spearman correlation was calculated for the mean and median of the corresponding parameters.

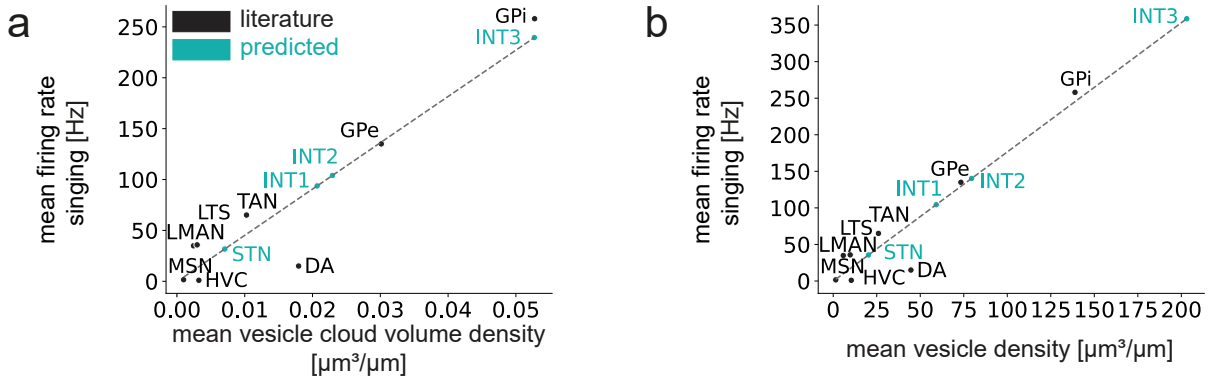

Figure A17: Vesicle cloud volume density and vesicle density of the axon in different cell types in relation to their firing rates. The black values are mean firing rates during singing obtained from the literature. The turquoise values are those predicted by linear regression. a Mean firing rates predicted based on mean axon vesicle cloud volume density. b Mean firing rates predicted based on mean axon vesicle density.

cell type	mean vesicle cloud volume density	std vesicle cloud volume density	median vesicle cloud volume density	mean vesicle density	std vesicle density	median vesicle density
DA	0.018	0.010	0.015	44.64	24.66	38.43
GPe	0.030	0.009	0.030	73.36	20.68	70.35
GPi	0.053	0.016	0.055	138.91	37.53	139.90
HVC	0.003	0.006	0.001	10.38	23.28	2.60
INT1	0.021	0.009	0.023	59.19	26.13	65.38
INT2	0.023	0.011	0.027	79.54	39.43	94.03
INT3	0.053	0.011	0.053	203.11	47.34	202.92
LMAN	0.002	0.004	0.002	5.79	7.10	3.82
LTS	0.003	0.003	0.002	9.74	7.09	8.88
MSN	0.001	0.001	0.001	1.47	2.51	1.05
STN	0.007	0.004	0.007	20.29	12.99	18.74
TAN	0.010	0.004	0.009	26.00	12.40	23.42

Table A23: The mean, median, and standard deviation of the vesicle cloud volume density and the vesicle density of the axon.

statistical test	vesicle cloud volume density	vesicle density
Kruskal-Wallis statistic	11980.87	12728.95
Kruskal-Wallis p-value	0.0	0.0

Table A24: Results of the Kruskal-Wallis test for the vesicle cloud volume density and the vesicle density of the axon. The post hoc Wilcoxon rank sum test showed p-values < 0.005 for all pairs except: vc volume density: DA vs TAN (0.01), GPe vs INT2 (0.01), GPi vs INT3 (0.99), LMAN vs LTS (0.03), STN vs TAN (0.10), vesicle density: DA vs TAN (0.01), GPe vs INT1 (0.09), GPe vs INT2 (0.02).

	coefficient	intercept	r-squared	adj. r-squared	f-statistic	p-value	spearman correlation coefficient	spearman p-value
mean vesicle cloud volume density	4548.55	-0.34	0.883	0.864	45.30	5.24e-04	0.67	0.07
median vesicle cloud volume density	4393.16	5.82	0.910	0.895	60.80	2.35e-04	0.83	0.01
mean vesicle density	1.77	-0.24	0.892	0.874	49.45	4.13e-04	0.67	0.07
median vesicle density	1.75	5.16	0.915	0.901	64.54	1.99e-04	0.83	0.01

Table A25: The statistics of the different linear regressions are based on vesicle cloud volume density and individual vesicle density, as calculated with StatsModels. Additionally, the Spearman correlation was calculated for the mean and median of the corresponding parameters.

cell type	mean soma GA volume density	std soma GA volume density	median soma GA volume density	mean total GA volume density	std total GA volume density	median total GA volume density	mean soma GA area density	std soma GA area density	median soma GA area density
GPe	0.019	0.004	0.019	0.0025	0.0009	0.0024	0.64	0.12	0.65
GPi	0.018	0.017	0.017	0.0040	0.0018	0.0041	0.65	0.81	0.62
INT1	0.019	0.007	0.019	0.0015	0.0009	0.0013	0.53	0.18	0.54
INT2	0.017	0.004	0.017	0.0014	0.0008	0.0012	0.50	0.13	0.52
INT3	0.017	0.003	0.017	0.0018	0.0011	0.0014	0.68	0.13	0.68
LTS	0.017	0.006	0.016	0.0028	0.0014	0.0027	0.44	0.15	0.45
MSN	0.013	0.010	0.012	0.0017	0.0014	0.0015	0.32	0.26	0.28
STN	0.018	0.007	0.017	0.0017	0.0010	0.0014	0.47	0.15	0.48
TAN	0.014	0.003	0.014	0.0083	0.0026	0.0075	0.60	0.05	0.60

Table A26: The mean, median, and standard deviation for soma GA volume density, total GA volume density, and soma GA area density.

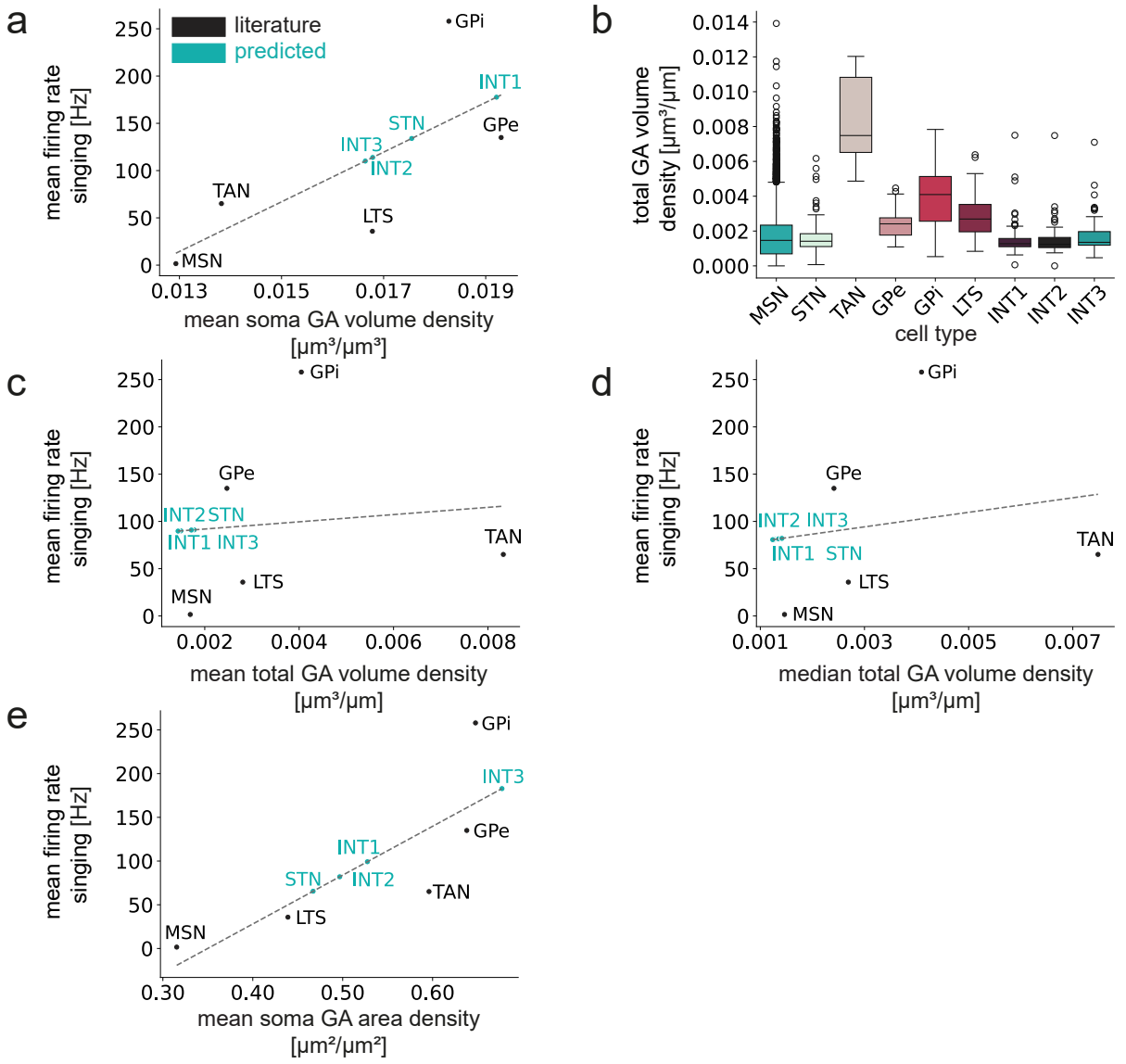

Figure A18: GA volume and area density in different cell types in relation to their firing rates. The black values are mean firing rates during singing from the literature and the turquoise values are those predicted by linear regression. a Mean firing rates are predicted based on soma GA volume density in relation to the estimated soma volume. b Total GA volume density is shown in relation to the cell's total skeleton path length in different cell types. c, d Mean firing rates predicted based on mean and median GA volume density in relation to pathlength. e Mean firing rates predicted based on mean GA area density, calculated as the surface area of the GA in relation to the soma surface area.

statistical test	soma GA volume density	total GA volume density	soma GA area density
Kruskal-Wallis statistic	212.06	147.53	452.96
Kruskal-Wallis p-value	1.83e-41	6.40e-28	8.57e-93

Table A27: Kruskal-Wallis test results for GA volume and area density. The post hoc Wilcoxon rank sum test showed p-values < 0.005 for all pairs except: soma GA volume density: GPe vs GPi (0.21), GPe vs INT1 (0.95), GPe vs INT2 (0.006), GPe vs LTS (0.02), GPe vs STN (0.18), GPi vs INT1 (0.14), GPi vs INT2 (0.97), GPi vs INT3 (0.98), GPi vs LTS (0.92), GPi vs MSN (0.07), GPi vs STN (0.54), GPi vs TAN (0.34), INT1 vs LTS (0.029, INT1 vs STN (0.11), INT1 vs TAN (0.007), INT2 vs INT3 (0.72), INT2 vs LTS (0.58), INT2 vs STN (0.20), INT3 vs LTS (0.91), INT3 vs STN (0.17), INT3 vs TAN (0.02), LTS vs STN (0.27), LTS vs TAN (0.09), MSN vs TAN (0.35), STN vs TAN (0.02); total GA volume density: GPe vs LTS (0.32), INT1 vs INT2 (0.66), INT1 vs INT3 (0.02) , INT1 vs MSN (0.38), INT2 vs STN (0.02), INT2 vs TAN (0.009), INT1 vs STN (0.06), INT2 vs INT3 (0.009), INT2 vs MSN (0.25), INT3 vs MSN (0.22), INT3 vs STN (0.65), MSN vs STN (0.28), soma GA area density: GPe vs GPi (0.58), GPe vs INT3 (0.35), GPe vs TAN (0.08), GPi vs INT1 (0.21), GPi vs INT2 (0.048), GPi vs INT3 (0.21), GPi vs LTS (0.049), GPi vs STN (0.03), GPi vs TAN (0.74), INT1 vs INT2 (0.28), INT1 vs TAN (0.12), INT2 vs STN (0.03), INT2 vs TAN (0.01), INT3 vs TAN (0.04), LTS vs STN (0.21).

	coefficient	intercept	r-squared	adj. r-squared	f-statistic	p-value	spearman correlation coefficient	spearman p-value
mean soma GA volume density	26277.04	-327.19	0.513	0.351	3.160	0.174	0.80	0.10
median soma GA volume density	25658.96	-300.14	0.483	0.311	2.806	0.192	0.80	0.10
mean total GA volume density	3822.26	84.31	0.010	-0.320	0.02977	0.874	0.50	0.39
median total GA volume density	7685.76	71.20	0.032	-0.291	0.09824	0.774	0.50	0.39
mean soma GA area density	558.63	-195.44	0.637	0.517	5.276	0.105	1.00	1.40e-24
median soma GA area density	471.76	-146.31	0.525	0.367	3.317	0.166	0.90	0.037

Table A28: The statistics of the different linear regressions are based on GA volume and area density, as calculated with StatsModels. Additionally, the Spearman correlation was calculated for the mean and median of the corresponding parameters.

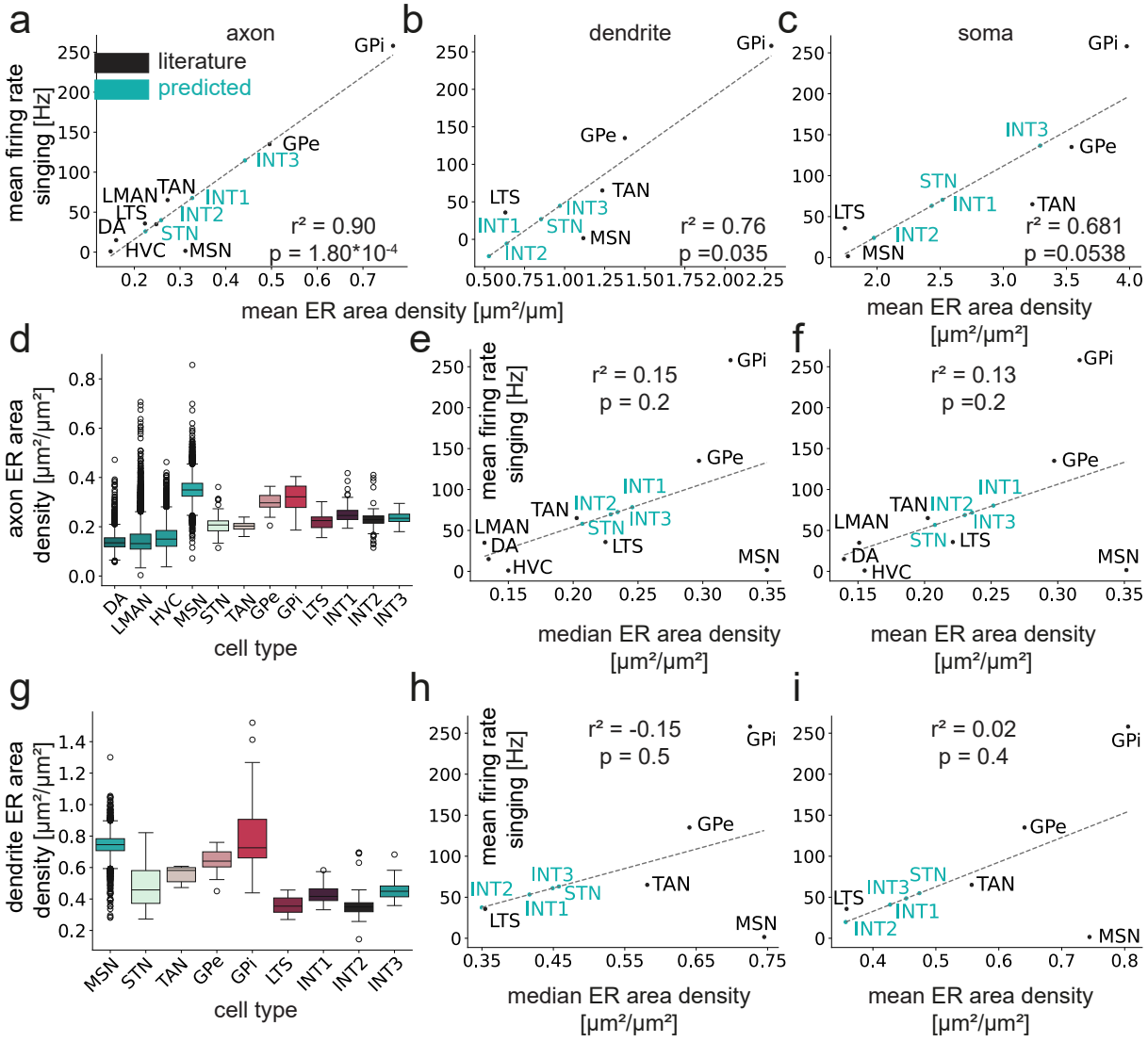

Figure A19: ER area density in different cell types in relation to their firing rates. The black values are the mean firing rates during singing obtained from the literature. The turquoise values are the predicted values based on linear regression. a-c Mean firing rates predicted based on the mean ER surface area in relation to the skeleton pathlength (axon or dendrite) or surface area (soma). d ER surface area in the axon in relation to the axonal surface area. e, f Median and mean values from (d) in relation to the mean firing rate from the literature. g ER ER surface area in the dendrite in relation to dendritic surface area. h, i Median and mean values from (g) in relation to mean firing rates from the literature. e, f, h, i INT1, INT2, INT3 and STN values were predicted with linear regression

statistical test	Kruskal-Wallis statistic	Kruskal-Wallis p-value
axon ER area per skeleton pathlength	17324.70	0.0
dendrite ER area per skeleton pathlength	908.54	8.13e-191
axon ER area density per surface area	20212.04	0.0
dendrite ER area per surface area	1162.50	1.21e-245
soma ER area per surface area	721.61	1.59e-150

Table A29: Kruskal-Wallis test results for the ER surface area in relation to the axon and dendritic pathlength, as well as in relation to the surface area of the different compartments. The results of the Spearman correlation coefficient are also shown. For projecting axon cell types (DA, HVC, and LMAN), the total and axonal mitochondrial densities were the same. A post hoc Wilcoxon rank sum test showed p-values < 0.005 for all pairs except: axon ER density per pathlength: GPe vs INT3 (0.04), INT1 vs TAN (0.01), INT2 vs TAN (0.40), LMAN vs TAN (0.02), LTS vs STN (0.82), LTS vs TAN (0.02), MSN vs TAN (0.06), STN vs TAN (0.03); axon ER density per surface area: DA vs LMAN (0.05), GPe vs GPi (0.08), INT1 vs INT3 (0.02), INT2 vs INT3 (0.06), INT2 vs LTS (0.20), INT2 vs TAN (0.02), INT3 vs LTS (0.02), LTS vs STN (0.02), LTS vs TAN (0.17), STN vs TAN (0.75); dendrite ER density per pathlength: GPe vs TAN (0.06), INT1 vs LTS (0.51), INT2 vs LTS (0.006), MSN vs TAN (0.03); dendrite ER density per surface area: GPi vs MSN (0.82), INT1 vs STN (0.02), INT2 vs LTS (0.34), INT3 vs STN (0.68), STN vs TAN (0.03)

	coefficient	intercept	r-squared	adj. r-squared	f-statistic	p-value	Spearman corr. coeff.	Spearman p-value
axon ER area per pathlength mean	407.38	-65.38	0.918	0.904	66.95	1.8×10^{-4}	0.74	0.037
axon ER area per pathlength median	379.80	-51.28	0.909	0.894	60.03	2.4×10^{-4}	0.76	0.028
dendrite ER area per pathlength mean	151.60	-102.42	0.818	0.758	13.52	0.0348	0.90	0.037
dendrite ER area per pathlength median	176.24	128.30	0.778	0.705	10.54	0.0476	0.90	0.037
axon ER area per surface area mean	538.25	-55.11	0.254	0.129	2.04	0.203	0.36	0.39
axon ER area per surface area median	525.85	50.80	0.269	0.147	2.21	0.188	0.33	0.42
dendrite ER area per surface area mean	300.06	-87.27	0.268	0.024	1.10	0.371	0.40	0.50
dendrite ER area per surface area median	237.21	-45.47	0.135	-0.154	0.47	0.543	0	1
soma ER area density mean	85.58	-145.01	0.761	0.681	9.543	0.0538	0.90	0.037
soma ER area density median	80.84	-139.04	0.842	0.789	15.95	0.0281	0.90	0.037

Table A30: The statistics of the different linear regressions based on ER area density in different compartments were calculated using StatsModels. Additionally, the Spearman correlation was calculated for the mean and median of the corresponding parameters.

	INT1 [Hz]	INT2 [Hz]	INT3 [Hz]	STN [Hz]
total mi volume density	26.93	<0	78.79	19.93
axon mi volume density	69.52	32.23	116.69	47.01
dendrite mi volume density	34.72	14.46	96.95	51.85
soma mi volume density	106.04	36.72	110.08	61.99
vc volume density	107.52	123.57	238.64	35.39
vesicle density	119.64	169.81	360.47	37.97
axon ER area density (pathlength)	73.29	46.33	115.39	31.54
dendrite ER area density (pathlength)	<0	<0	<0	11.14
soma ER area density	61.97	28.17	132.42	47.41

Table A31: Predicted mean firing rates [Hz] during singing, based on linear regression of median organelle volume and area density parameters. The cell types used for the prediction are: MSN, GPe, GPi, LTS, and TAN. Mean firing rates during singing were based on literature for parameters in the dendrite, soma, and all GA parameters. The DA, HVC and LMAN were also used for parameters calculated in the axon. For total mitochondrial volume density, estimates from DA, LMAN, and HVC were used. Predictions smaller than 0 are not physiologically possible and were only indicated as such. mi = mitochondria, vc = vesicle cloud

	accuracy without parameter	
parameters	all cell types	without MSN
soma diameter	0.992	0.880
spine density	0.991	0.884
axon length	0.992	0.874
dendrite length	0.992	0.867
axon median radius	0.991	0.859
dendrite median radius	0.991	0.871
soma surface area	0.991	0.859
axon surface area	0.992	0.861
dendrite surface area	0.992	0.861
axon myelin fraction	0.991	0.874
cell volume	0.992	0.865
axon mi volume density	0.991	0.865
dendrite mi volume density	0.992	0.865
soma mi volume density	0.992	0.861
vesicle density	0.991	0.845
axon synaptic area density per surface area	0.991	0.863
dendrite synaptic area density per surface area	0.992	0.857
soma synaptic area density per surface area	0.992	0.859
soma GA area density	0.992	0.863
axon ER area density	0.992	0.869
dendrite ER area density	0.991	0.880
soma ER area density	0.991	0.861

Table A32: Parameters given to the RFC for training and were then potentially selected by the RFECV. One round was done with MSNs and one without. Without MSNs, all parameters were selected; with MSNs, all parameters except soma GA area density were selected. An RFC was trained without each of these parameters, and the resulting accuracy score was calculated.

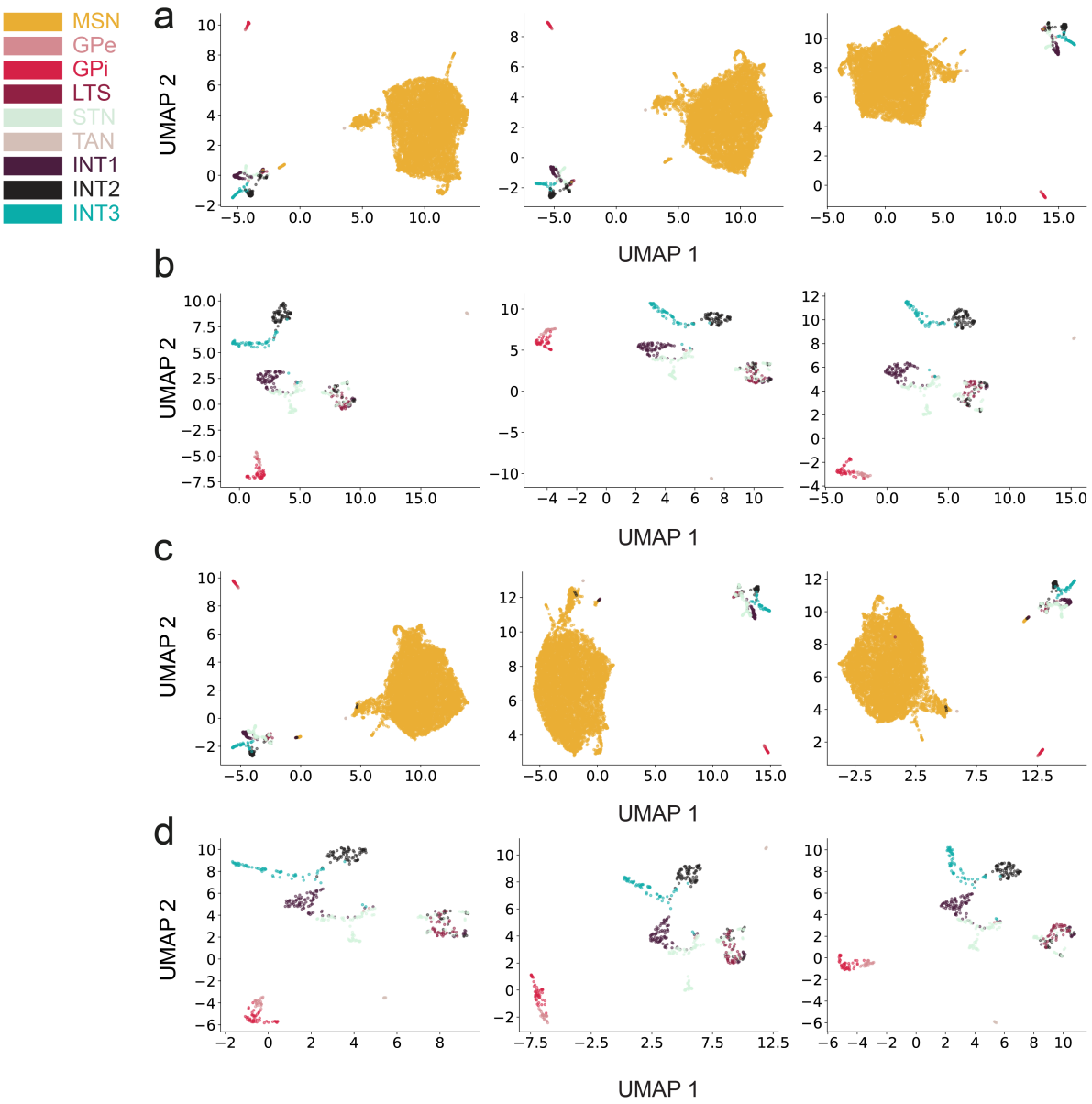

Figure A20: UMAP clustering based on morphological parameters and organelle densities. a UMAP clustering is based on a 22-dimensional feature vector with parameters from appendix table A32, variations from figure 3.21 a. b Same as (a), but without MSN cells and with different runs, as in figure 3.21 b. c Same as (a), but with vesicle cloud volume density instead of vesicle density. d Same as c Same as (c), but with clustering done without MSN.

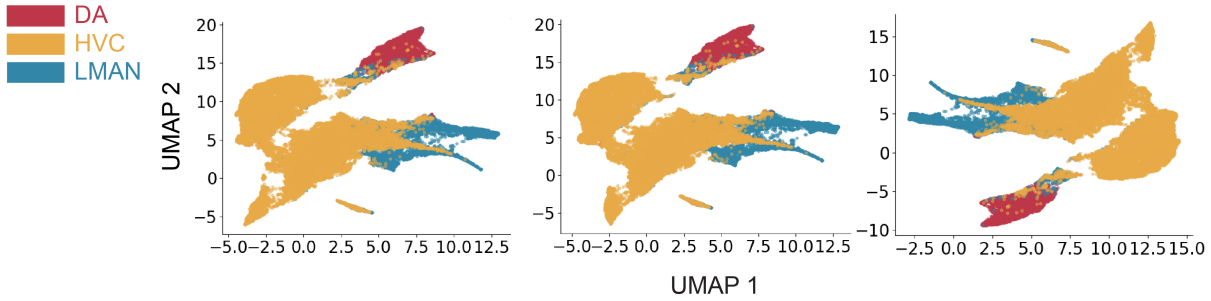

Figure A21: UMAP clustering based on parameters in the axon, as shown in A32. Projecting axon cell types were clustered based on an eight-dimensional array of parameters (axon length, myelin fraction, surface area, median radius, mitochondrial volume density, vesicle density, synaptic area density, and ER area density).

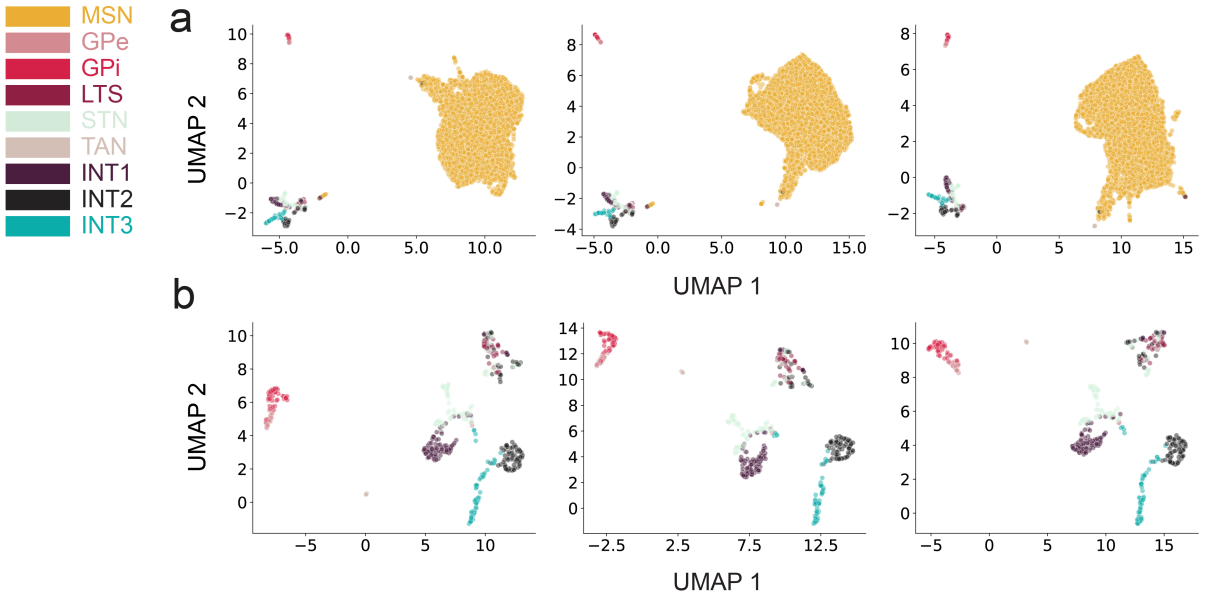

Figure A22: UMAP clustering based on morphological parameters and organelle densities. a UMAP clustering is based on a 21-dimensional feature vector with parameters from A32,with variations shown in figure 3.21 d. b Same as (a), but clustered without MSN, with variations shown in figure 3.21 e.

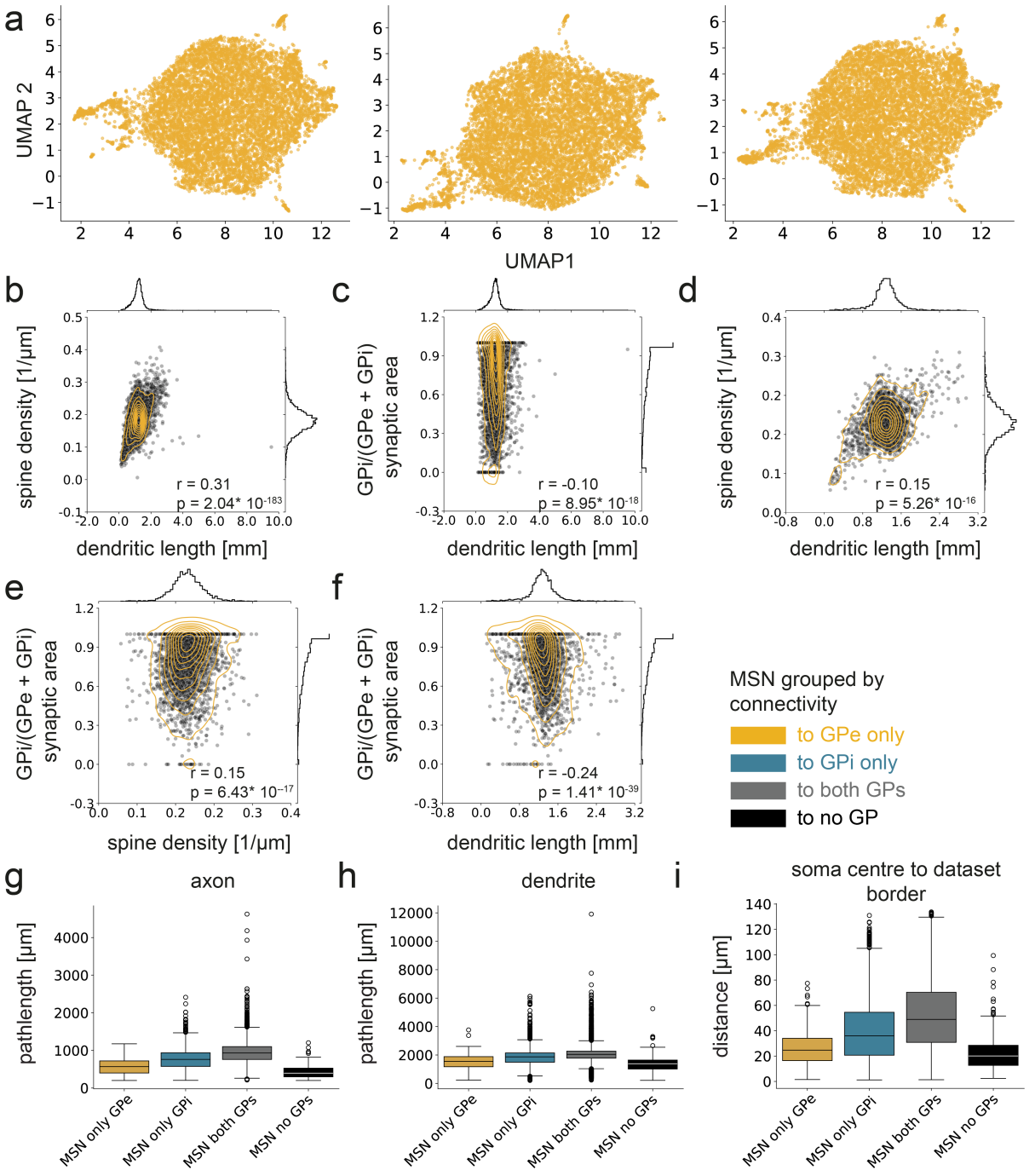

Figure A23: Morphology and connectivity of MSN cells. a UMAP based on a 22-dimensional feature vector for MSN morphology only; parameters from A32. b A broad spectrum of MSN morphologies exists, where spine density is slightly correlated with dendritic length. c Ratio of GPe and GPi in relation to dendritic length in all MSNs. d Spine density and dendritic length in MSNs with complete dendrites only (n = 3,052). e, f Ratio of GPe and GPi in relation to spine density and dendritic length in MSNs with no cutoff dendrites. MSN both = 80.3% (2451 cells), MSN only GPe = 0.78% (24 cells), MSN only GPi = 18.2 % (556 cells), MSN no GP = 0.69 % (21 cells). g Axon skeleton length in MSNs grouped by connectivity to GPe and GPi. h Dendrite skeleton pathlength. i Distance of the soma center to the closest dataset border. g-i have significant differences between all groups (Wilcoxon rank-sum test; all $p < 0.005$), except for dendritic length in MSNs with no GPe vs. MSNs with only ($p = 0.027$; see appendix table A33)

	n	p-value
MSN groups axon length	3052 MSN cells	all $< 10^{-14}$
MSN groups dendrite length	3052 MSN cells	all $< 10^{-17}$ only GPe vs none $= 1.34 \times 10^{-3}$
MSN groups soma centre to dataset border	3052 MSN cells	all $< 10^{-18}$ only GPe vs none $= 0.027$
MSN synapse sizes to GPe, to GPi	MSN - GPe = 28297 MSN - GPi = 76329	5.3×10^{-142}
MSN number of multi synapses to GPe, GPi	MSN - GPe = 343 MSN - GPi = 3516	1.75×10^{-121}
MSN summed size per GP cells, to GPe, to GPi	MSN - GPe = 343 MSN - GPi = 3516	2.51×10^{-251}

Table A33: Results of two-sided Wilcoxon rank-sum test related to different analyses shown in figure 3.23 or appendix figure A23.

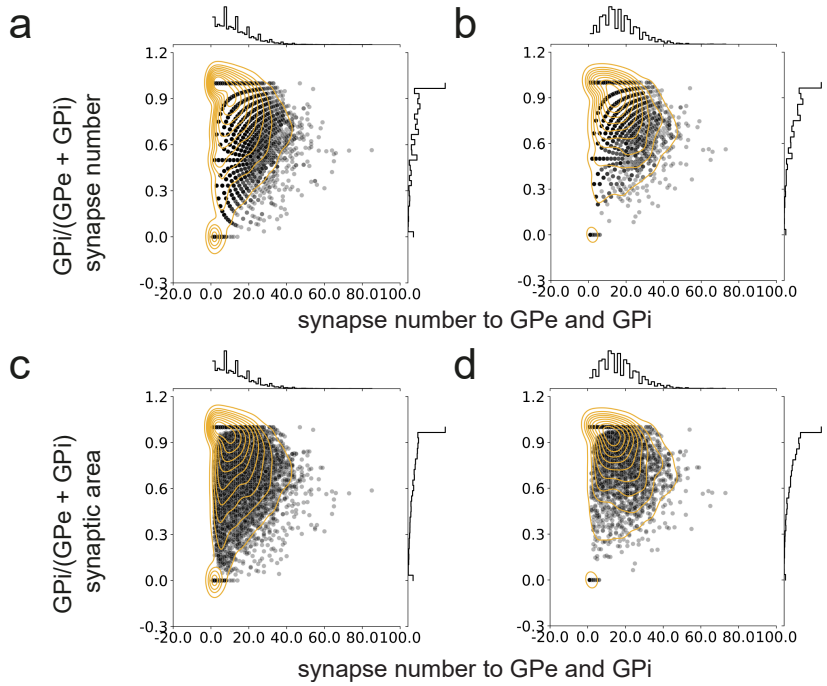

Figure A24: MSN synapse numbers to GP. a GP ratio of synapse numbers in relation to the cell's total synapse numbers to GPe and GPi for all MSNs. b (a) for only those with full dendrites. c GP ratio of synaptic area in relation to total synapse numbers to GPe and GPi for all MSNs. d (c) for only those with full dendrites.

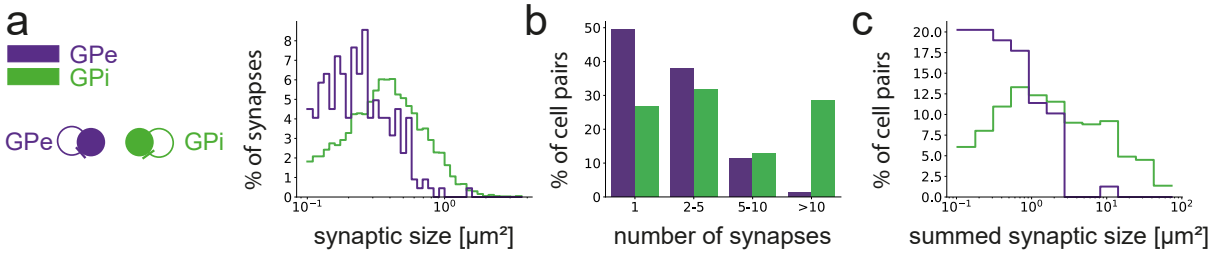

Figure A25: Synaptic connectivity within GPe and GPi cells. a Comparison of the size of individual synapses. b Number of synapses in multi-synaptic connections. c Summed synaptic area of multi-synaptic connections.

	n	p-value
GPe - GPi synapse sizes	GPe–GPi = 766, GPi–GPe = 124	0.13
GPe - GPi number of multi-synapses	GPe–GPi = 179, GPi–GPe = 63	8.47×10^{-4}
GPe - GPi summed size per partner cell	GPe–GPi = 179, GPi–GPe = 63	0.02
GPe–GPe vs GPi–GPi synapse sizes	GPe = 222, GPi = 6438	7.69×10^{-25}
GPe–GPe vs GPi–GPi number of multi-synapses	GPe = 79, GPi = 511	2.15×10^{-7}
GPe–GPe vs GPi–GPi summed synapse sizes per partner cell	GPe = 79, GPi = 511	3.39×10^{-14}
GPe–GPe vs GPi–GPe synapse sizes	GPe–GPe = 222, GPi–GPe = 124	9.25×10^{-6}
GPe–GPe vs GPi–GPe number of multi-synapses	GPe–GPe = 79, GPi–GPe = 63	0.13
GPe–GPe vs GPi–GPe summed synapse sizes per partner cell	GPe–GPe = 79, GPi–GPe = 63	0.43
GPi–GPi vs GPe–GPi synapse sizes	GPi–GPi = 6428, GPe–GPi = 766	0.08
GPi–GPi vs GPe–GPi number of multi-synapses	GPi–GPi = 511, GPe–GPi = 179	4.72×10^{-7}
GPi–GPi vs GPe–GPi summed synapse sizes per partner cell	GPi–GPi = 511, GPe–GPi = 179	6.37×10^{-10}

Table A34: Results of the two-sided Wilcoxon rank-sum test related to the different analyses shown in figure 3.24 or appendix figure A25.

STN connectivity	number of STN cells	percent of STN cells
GPe and GPi	58	56.86
no GP	18	17.65
STN only GPe	18	17.65
STN only GPi	8	7.84

Table A35: The number of STN cells that project to both the GPe and the GPi, to neither, or to only one of the two.

	n	p-value
STN - GPe vs STN- GPi synapse sizes	GPe = 2148, GPi = 7923	1.32*10-76
STN - GPe vs STN- GPi number multi-synapses	GPe = 450, GPi = 1066	7.62*10-17
STN - GPe vs STN- GPi summed syn size per partner cell	GPe = 450, GPi = 1066	1.39*10-22
GPe- STN vs GPi - STN synapse size	GPe = 1969, GPi = 14586	2.15*10-86
GPe- STN vs GPi - STN number multi-synapses	GPe = 348, GPi = 1309	5.65*10-3
GPe- STN vs GPi - STN summed syn size per partner cell	GPe = 348, GPi = 1309	2.51*10-251

Table A36: Results of the two-sided Wilcoxon rank-sum test are related to the different analyses shown in figure 3.25 pathway or appendix figure 3.25.

connection	cell number input and output	fraction cells binary specific	median number of partner cells incoming	median number of partner cells outgoing	median fraction synapse sum size overlap incoming	median fraction synapse sum size overlap outgoing
STN - GPi	64, 47	0.141, 0.191	13, 28	21, 23	0.90, 0.75	0.62, 0.75
STN - GPe	70, 27	0.186, 0.185	5, 13	4, 16	0.76, 0.73	0.60, 0.48
MSN - TAN	29, 8	0.276, 0	1, 236.5	1, 18.5	0.30, 0.0029	0.27, 0.063

Table A37: Cell-specific recurrency for connections between different cell types.The number of cells that project to and receive input from another cell type is referred to as cell number input and output. Note that all full cells from GPe, GPi, and TAN do this for the given projections, while only a small fraction of MSNs ($< 0.5\%$) projects to TAN cells and receives input from them. Binary specificity relates to the number of cells where the strongest input is also the strongest output. The fraction of synaptic summed size overlap is calculated by dividing the summed area of synapses from cells that are both inputs and outputs by either the sum of the summed area of all inputs from this cell type (including cells in the analysis) or the sum of all outputs

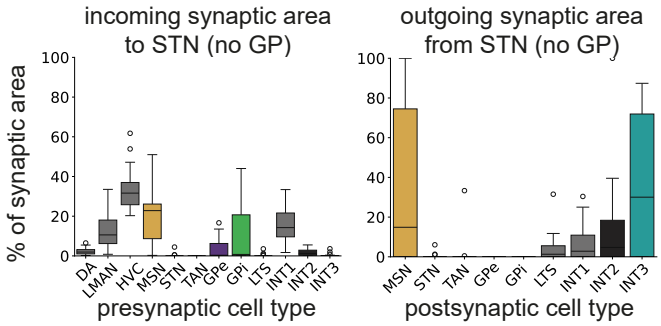

Figure A26: Connectivity of STN cells that do not project to GPe or GPi cells (18 percent of STN cells, see table A35).

cell type	r-squared (0.5 µm)	p-value (0.5 µm)	r-squared (1 µm)	p-value (1 µm)	r-squared (2 µm)	p-value (2 µm)
total	0.05	0.0	0.03	1.50E-233	-0.01	8.20E-44
DA	0.18	1.85E-174	0.17	3.984E-160	0.15	1.18E-122
GPe	0.47	0.0	0.42	0.0	0.30	0.0
GPi	0.38	0.0	0.35	0.0	0.18	1.87E-252
HVC	0.43	0.0	0.42	0.0	0.40	0.0
INT1	0.59	0.0	0.45	0.0	0.32	0.0
INT2	0.30	0.0	0.20	0.0	0.12	8.71E-277
INT3	0.26	0.0	0.21	0.0	0.12	0.0
LMAN	0.40	0.0	0.39	0.0	0.31	0.0
LTS	0.27	8.475E-48	0.25	4.06E-40	0.22	5.27E-31
MSN	0.28	0.0	0.29	0.0	0.26	0.0
STN	0.32	0.0	0.30	0.9	0.24	0.0
TAN	0.17	0.017	0.23	8.98E-4	0.29	3.43E-05

Table A38: Spearman correlation results for vesicle number and synapse size in different cell types and at different distance thresholds from the synapse.

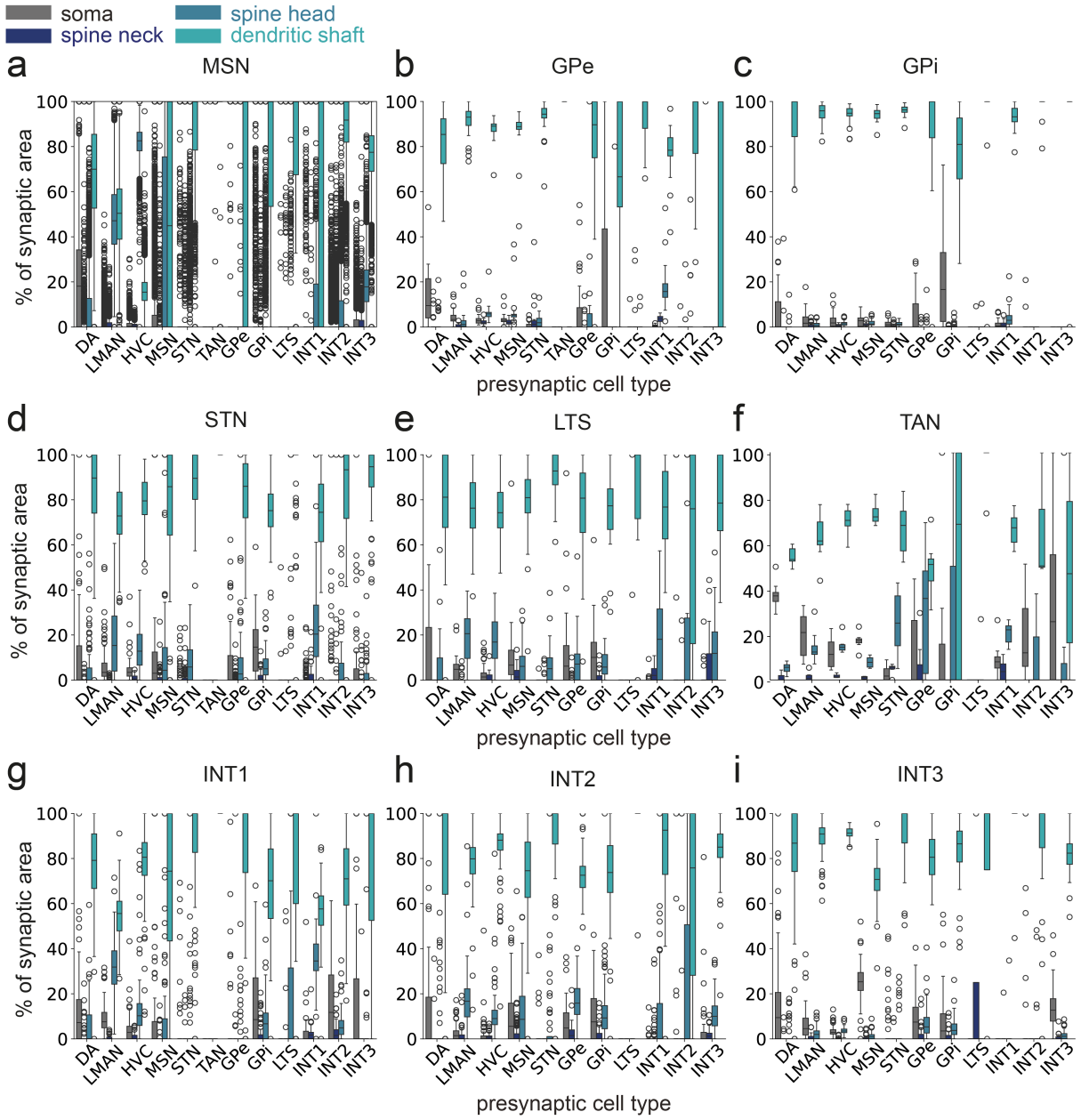

Figure A27: Compartment-specific connectivity for all neuronal cell types residing in Area X. the percentage of synaptic area per presynaptic cell type. The percentages for each presynaptic cell type add up to 100 percent. Each data point represents one postsynaptic cell. a-i Compartment-specific connectivity for different postsynaptic cell types. In c, e, f, h, i, TAN is missing because no TAN synapses were detected ($n_{TAN} = 8$).

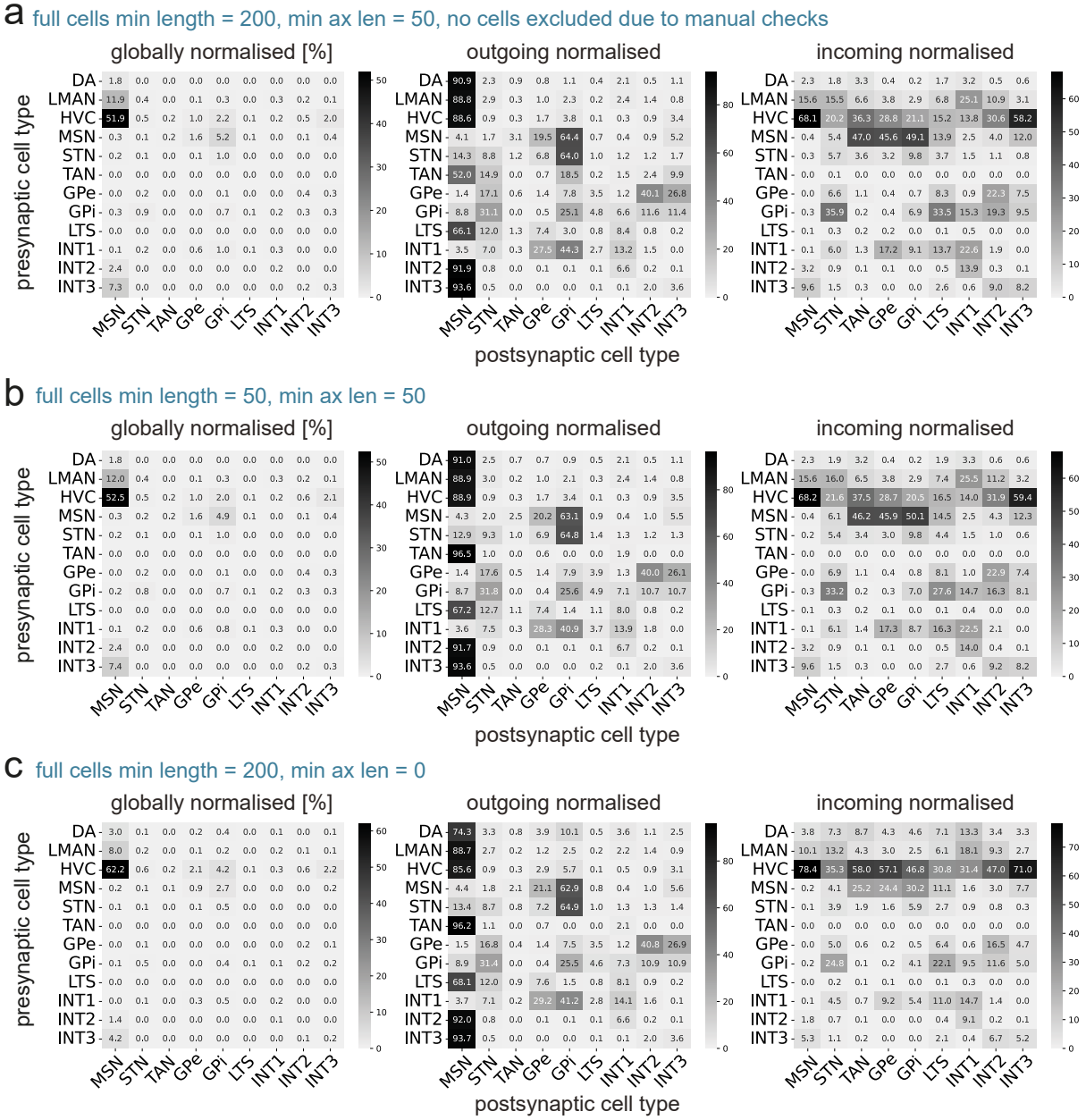

Figure A28: The connectivity matrices show the percentage of synaptic areas with different normalizations and filtering criteria. a Matrices similar to those in 3.31, but for the STN, GPe, GPi, TAN, and LTS cell types no cells were excluded due to mergers or incomplete cells (see appendix table A14). b Matrices with full cells filtered to a minimum skeleton length of 200 µm for each, the axon and dendrite. Projecting axon cell types (DA, HVC, LMAN) filtered with a minimum skeleton length of 50 µm. c Matrices with full cells filtered to a minimum skeleton length of 200 µm for the axon and dendrite, projecting axon cell types with a length of 0 µm, representing fragments consisting of only one skeleton node.

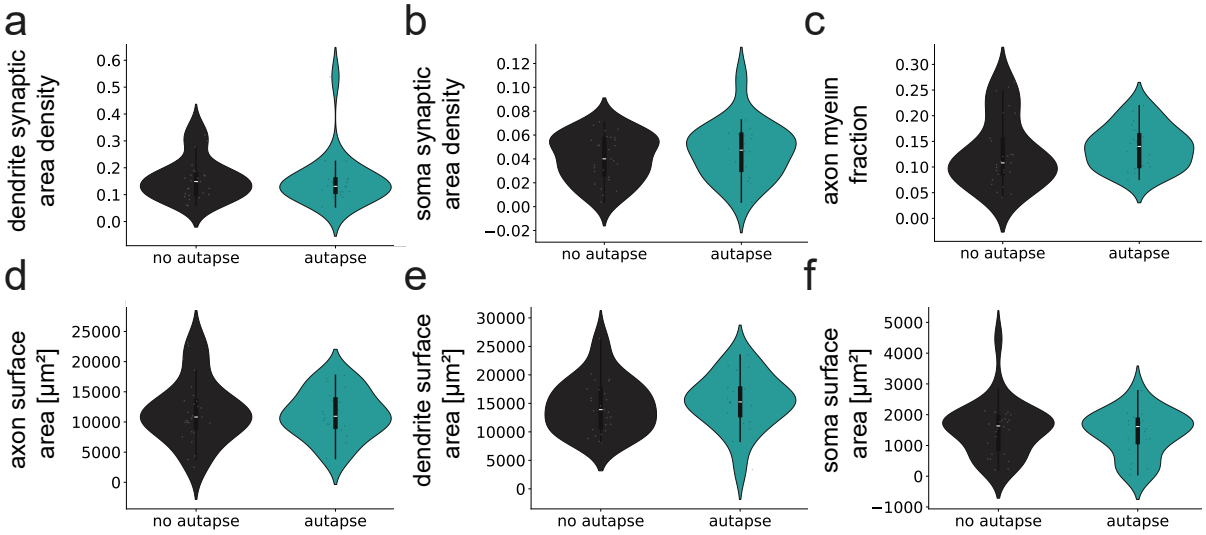

Figure A29: Comparison between GPi cells with and without autapses (n = 20, 27). a, b, Dendrite and soma synaptic area in relation to the compartment surface area. c Myelin fraction of the axon. d-f Surface area of different compartments. Wilcoxon rank sum test: all $p > 0.05$.

cell type	r-squared (0.5 µm)	p-value (0.5 µm)	r-squared (1 µm)	p-value (1 µm)	r-squared (2 µm)	p-value (2 µm)
total	0.003	1.28E-3	0.003	1.54E-3	-0.03	0.0
DA	0.054	5.01E-17	0.088	1.618E-43	0.08	1.21E-39
GPe	0.101	5.52E-45	0.266	1.03E-309	0.21	3.30E-192
GPi	0.030	5.06E-09	0.157	1.02E-200	0.08	2.14E-57
HVC	0.312	0.0	0.354	0.0	0.34	0.0
INT1	0.223	0.0	0.278	0.0	0.20	0.0
INT2	0.097	4.50E-187	0.107	7.786E-228	0.06	2.39E-78
INT3	0.059	3.74E-201	0.089	0.0	0.04	9.74E-113
LMAN	0.249	0.0	0.297	0.0	0.25	0.0
LTS	0.153	6.63E-16	0.157	1.03E-16	0.13	3.86E-12
MSN	0.172	0.0	0.196	0.0	0.18	0.0
STN	0.177	0.0	0.224	0.0	0.18	0.0
TAN	-0.015	0.83	0.033	0.64	0.09	2.08E-01

Table A39: Spearman correlation results for the number of membrane-close vesicles and synapse size in different cell types and at different distances from the synapse.

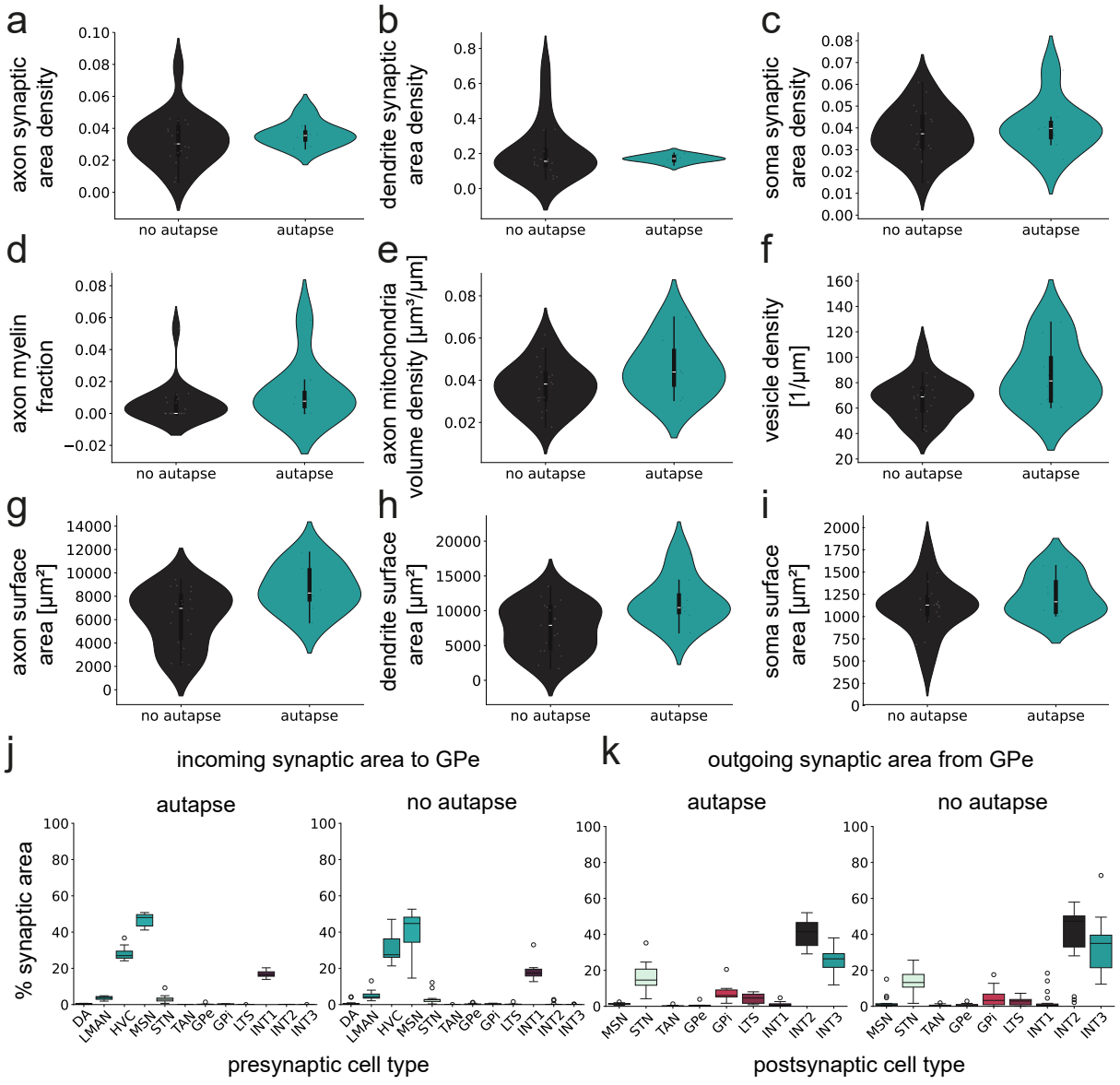

Figure A30: Comparison between GPe cells with and without autapses (n = 8, 19). a-c Synaptic area in relation to the surface area of different compartments. d Myelin fraction of the axon. e Axon mitochondrial volume in relation to axonal pathlength. fNumber of vesicles in the axon in relation to axonal pathlength. g-i Surface area of different compartments. The Wilcoxon rank sum test revealed that all p values > 0.05, except for the axon and dendritic surface areas ($p = 0.033$ and 0.049, respectively). j, k show the incoming and outgoing connectivity in the GPe with and without autapses.

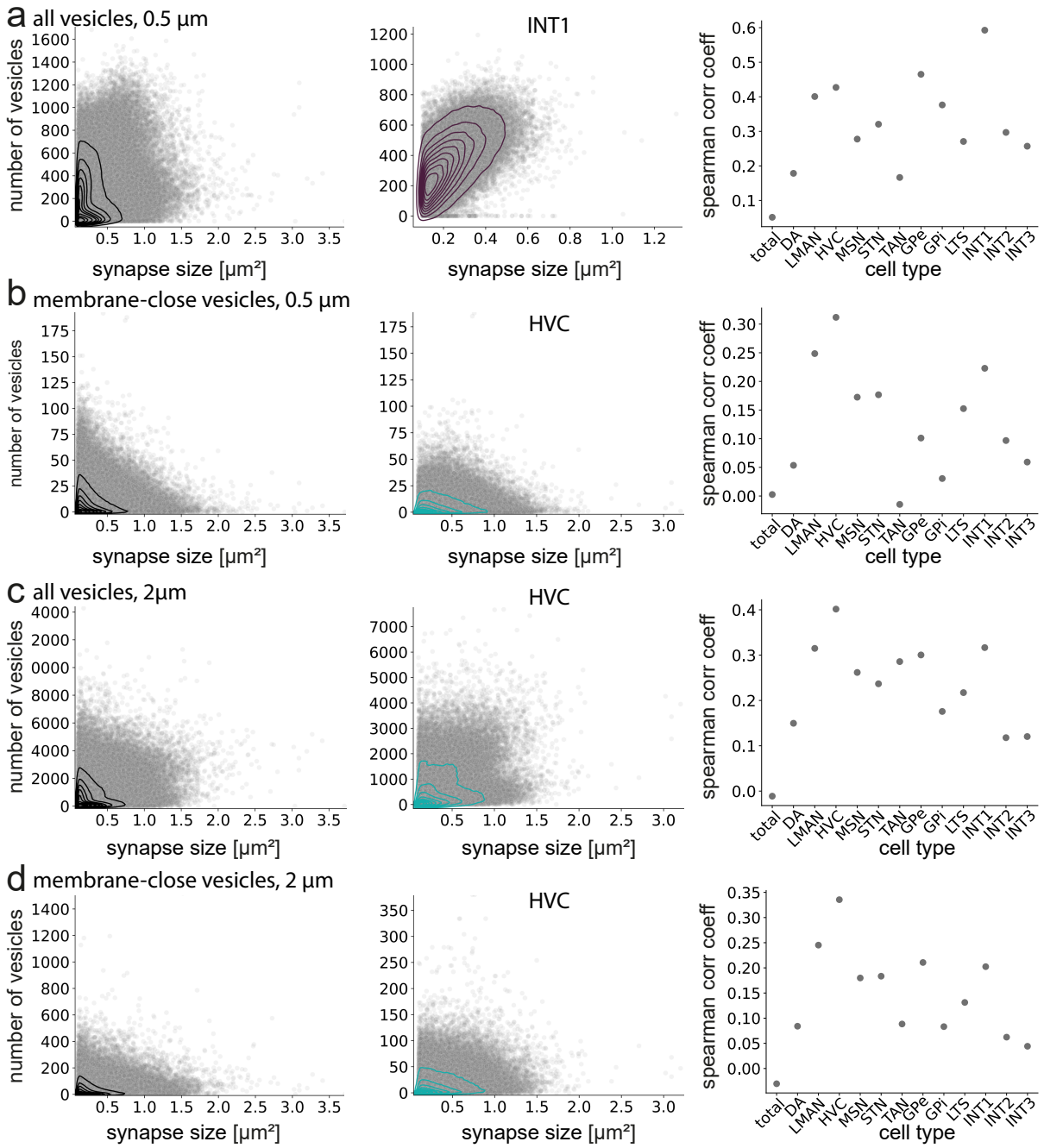

Figure A31: Synaptic areas and the number of vesicles at different distances. a Number of all vesicles and membrane-close vesicles in relation to their synaptic areas within 0.5 µm of the synapse, for all synapses, and only INT1 synapses and vesicles (highest spearman correlation coefficent within 0.5 µm of the synapse). Spearman coefficients for all cell types within 0.5 µm of the synapse are also shown. b Same as (d), but only for membrane-close vesicles. c, d Similar to (a, b), but within 2 µm of the synapse.

cell type	median	mean	std
DA	80.87	110.43	90.50
GPe	7.47	7.81	1.88
GPi	8.46	8.54	2.71
HVC	18.81	61.74	90.85
INT1	9.89	20.90	45.48
INT2	3.81	11.74	21.93
INT3	2.75	2.86	0.56
LMAN	13.43	58.27	120.98
LTS	43.13	67.42	75.61

Table A40: The median, mean, and standard deviation of the distance between synapses on the axons of different cell types are shown in micrometers.

	1 µm	2 µm	3 µm	4 µm
fraction non-synaptic membrane close vesicles stats	12610.04	12219.76	11618.32	11196.66
fraction non-synaptic membrane close vesicles p-value	0.00	0.00	0.00	0.00
density non-synaptic membrane close vesicles stats	14506.21	14783.14	14511.68	14193.64
density non-synaptic membrane close vesicles p-value	0.00	0.00	0.00	0.00
density synaptic membrane close vesicles stats	4300.92			
density synaptic membrane close vesicles p-value	0.00			

Table A41: Kruskal-Wallis test results for density of synaptic and non-synaptic membrane-close vesicles with different distance thresholds for what is counted as non-synaptic. A post hoc Wilcoxon rank sum test showed p-values < 0.005 for all pairs except: density synaptic membrane close vesicles: DA vs TAN (0.12), GPe vs GPi (0.14), GPe vs INT1 (0.52), GPi vs INT1 (0.005), HVC vs LTS (0.36), HVC vs TAN (0.08), LMAN vs LTS (0.68), LMAN vs TAN (0.01), LTS vs TAN (0.006), MSN vs TAN (0.68); fraction non-synaptic membrane-close vesicles: 1 µm: DA vs TAN (0.06), GPe vs HVC (0.47), GPe vs INT2 (0.58), GPe vs INT3 (0.16), GPi vs LMAN (0.18), HVC vs INT2 (0.09), HVC vs INT3 (0.68), INT2 vs INT3 (0.31), LMAN vs STN (0.07), LTS vs MSN (0.15); 2 µm: DA vs TAN (0.10), GPe vs HVC (0.02), GPe vs INT2 (0.20), GPe vs INT3 (0.92), GPi vs HVC (0.23), GPi vs INT1 (0.44), GPi vs INT2 (0.09), HVC vs INT2 (0.72), LMAN vs LTS (0.35); 3µm: DA vs TAN (0.09), GPe vs HVC (0.01), GPe vs INT2 (0.20), GPi vs HVC (0.47), GPi vs INT1 (0.35), GPi vs LMAN (0.03), HVC vs INT1 (0.06), LMAN vs STN (0.10); 4 µm: DA vs TAN (0.10), GPi vs HVC (0.69), GPi vs INT1 (0.13), GPi vs LMAN (0.05), GPi vs STN (0.005), HVC vs INT1 (0.90), LMAN vs STN (0.11); density non-synaptic membrane close vesicles: 1 µm: DA vs TAN (0.11), GPe vs INT1 (0.78), GPe vs INT2 (0.005), GPe vs TAN (0.31), INT1 vs TAN (0.17), INT2 vs TAN (0.74); 2 µm: DA vs GPi (0.15), DA vs TAN (0.07), GPe vs STN (0.18), GPi vs INT3 (0.20), GPi vs TAN (0.28), INT1 vs INT2 (0.06), INT3 vs TAN (0.49); 3 µm: DA vs TAN (0.08), GPe vs INT2 (0.38), GPe vs LTS (0.009), GPe vs STN (0.71), GPi vs TAN (0.81), INT1 vs INT3 (0.03), INT2 vs STN (0.11), LTS vs STN (0.01); 4 µm: DA vs TAN (0.09), GPe vs INT2 (0.01), GPe vs INT3 (0.77), GPe vs LTS (0.33), GPe vs STN (0.45), GPi vs TAN (0.38) , INT2 vs LTS (0.21), INT3 vs LTS (0.15), INT3 vs STN (0.66), LTS vs STN (0.09).

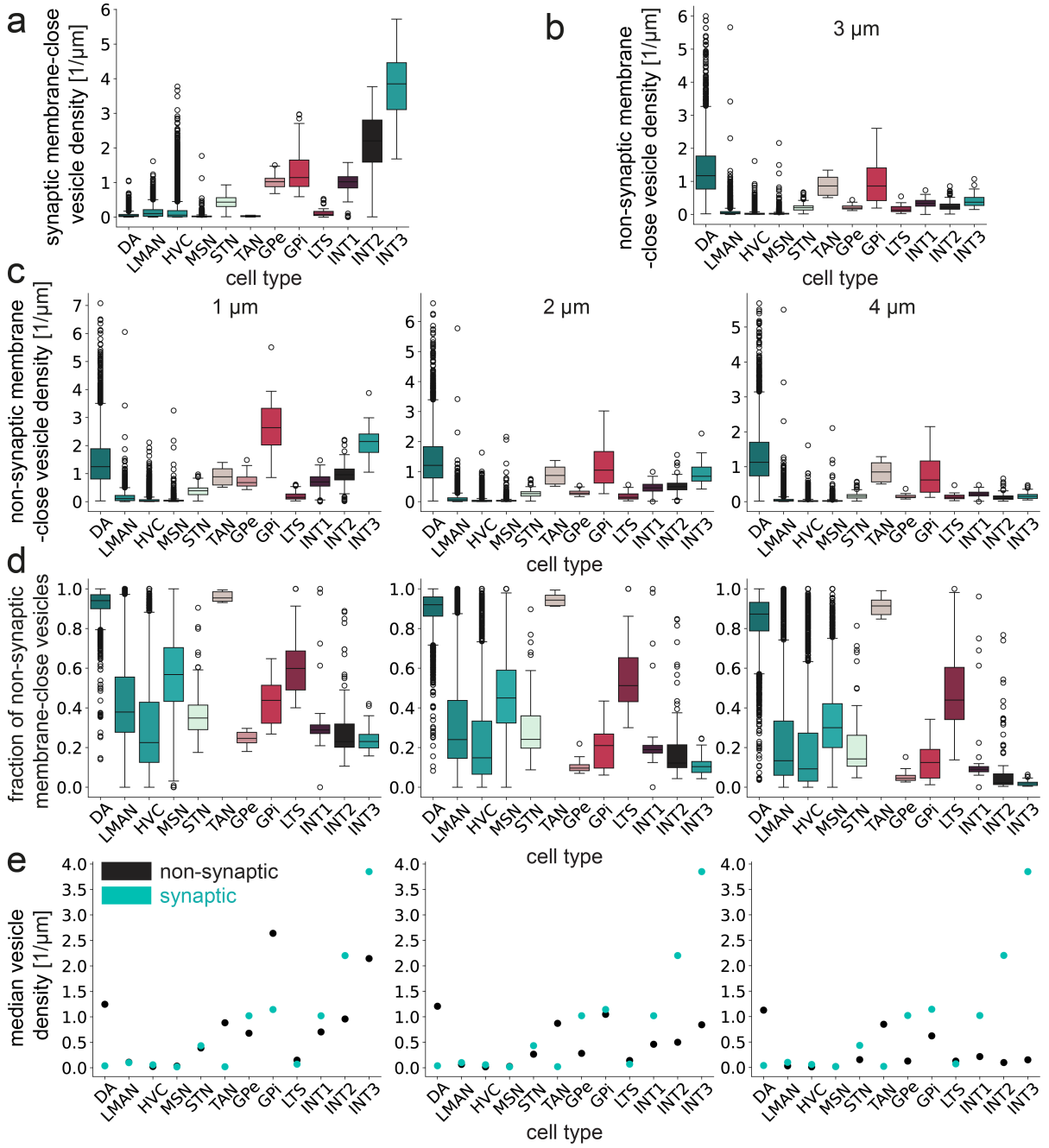

Figure A32: Density of synaptic and non-synaptic membrane-close vesicles. Vesicles are considered membrane-close when the calculated distance to the cell membrane is less than 10 nm. a Density of synaptic membrane-close vesicles. Vesicles within 500 nm are counted as synaptic. b Non-synaptic membrane-close vesicle density. Vesicles are counted as non-synaptic if they are more than 3 µm away from the next synapse. c Non-synaptic membrane-close vesicle density with different distance thresholds to the synapse. d Fraction of non-synaptic membrane-close vesicles with different distance thresholds. e Median vesicle densities for synaptic and non-synaptic vesicles with different distance thresholds for non-synaptic vesicles.

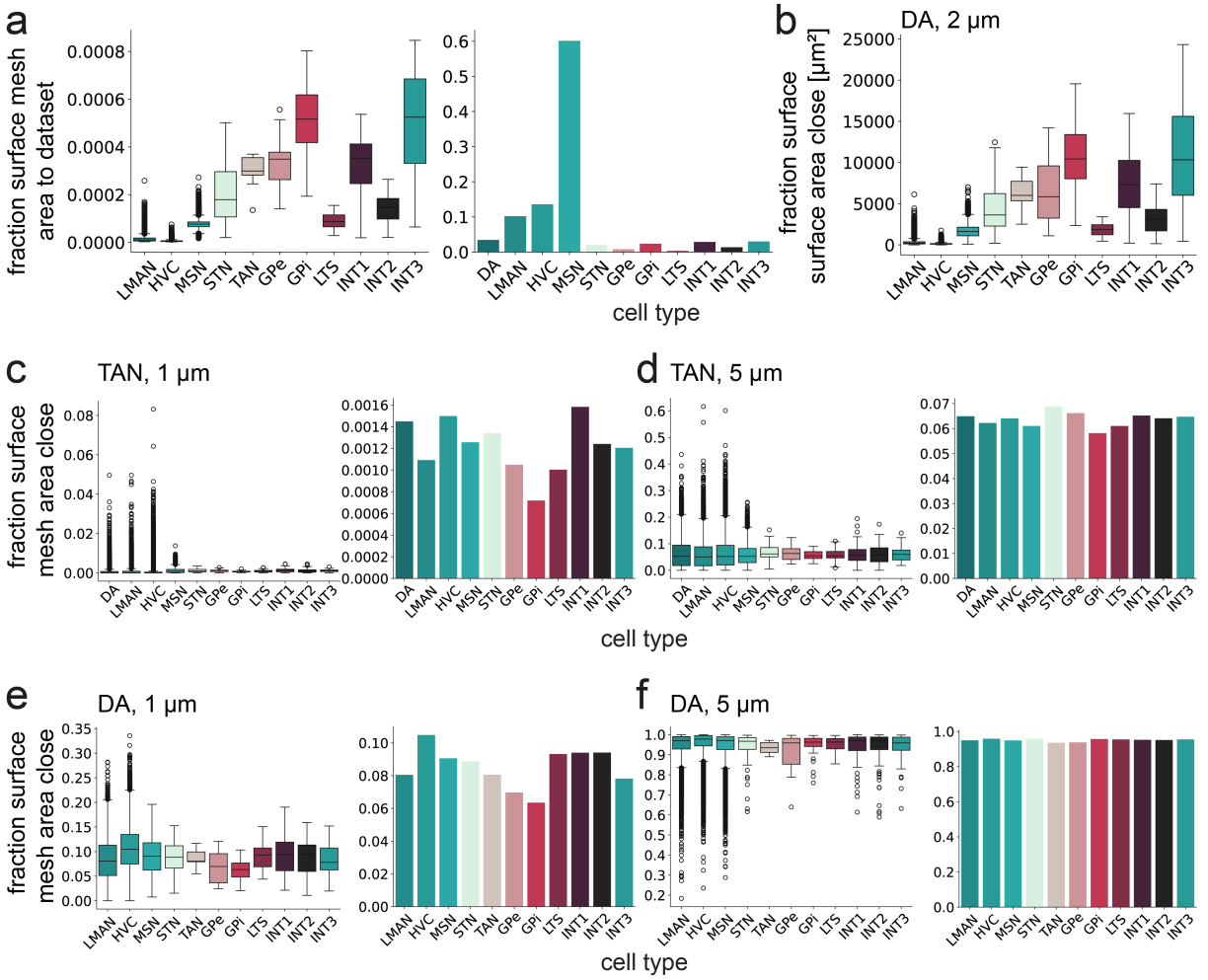

Figure A33: TAN and DA non-synaptic close-membrane vesicles in proximity to cells of different types at different distances from the vesicles. a The fraction of the surface area of a given cell type in relation to the total surface area of the mesh for all considered cells is shown on the left (per cell) and on the right (summed per cell type). b Summed surface area within 2 µm of DA non-synaptic, membrane-close vesicles. c-f Fraction of the surface area of the mesh close to the membrane related to the total surface area of cells (left) or cell types (right) for TAN and DA at different distances.

cell type	1 µm (absolute)	1 µm (%)	2 µm (absolute)	2 µm (%)	5 µm (absolute)	5 µm (%)
DA	78653	7.99	369673	37.57	919321	93.44
TAN	1061	0.11	6889	0.70	57056	5.80

Table A42: Number of synapses within a certain distance of non-synaptic, membrane-close TAN or DA vesicles. The total number of synapses that fulfill these criteria is 983,887

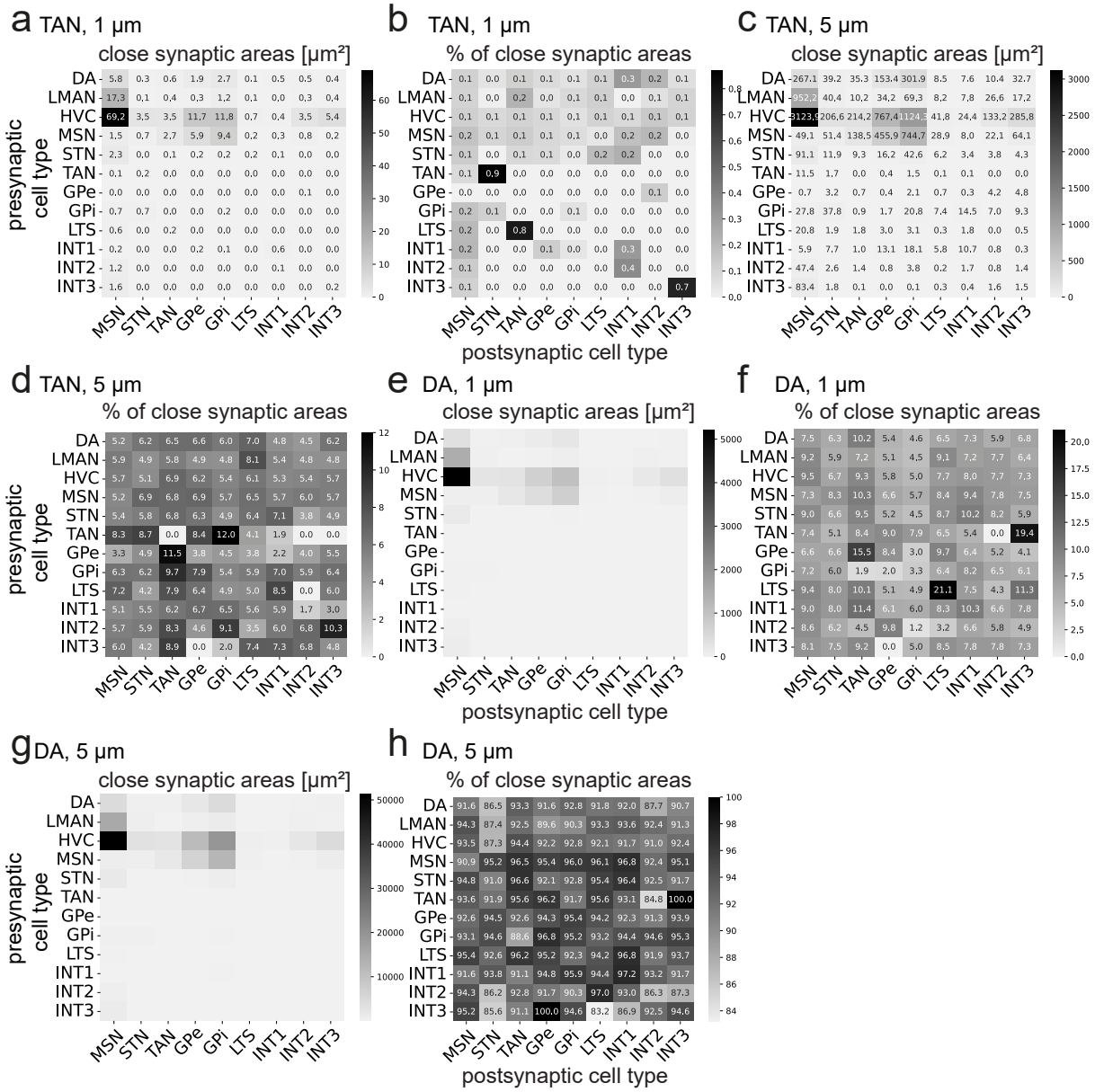

Figure A34: TAN and DA non-synaptic close-membrane vesicles in proximity to synapses in the dataset with different distances to the vesicles. a, c, e, g Summed synaptic area in proximity to the vesicles. b, d, f, h Percent of synaptic areas related to the overall synaptic areas in the dataset (see figure 3.31 c for synaptic areas normalized to the whole dataset).

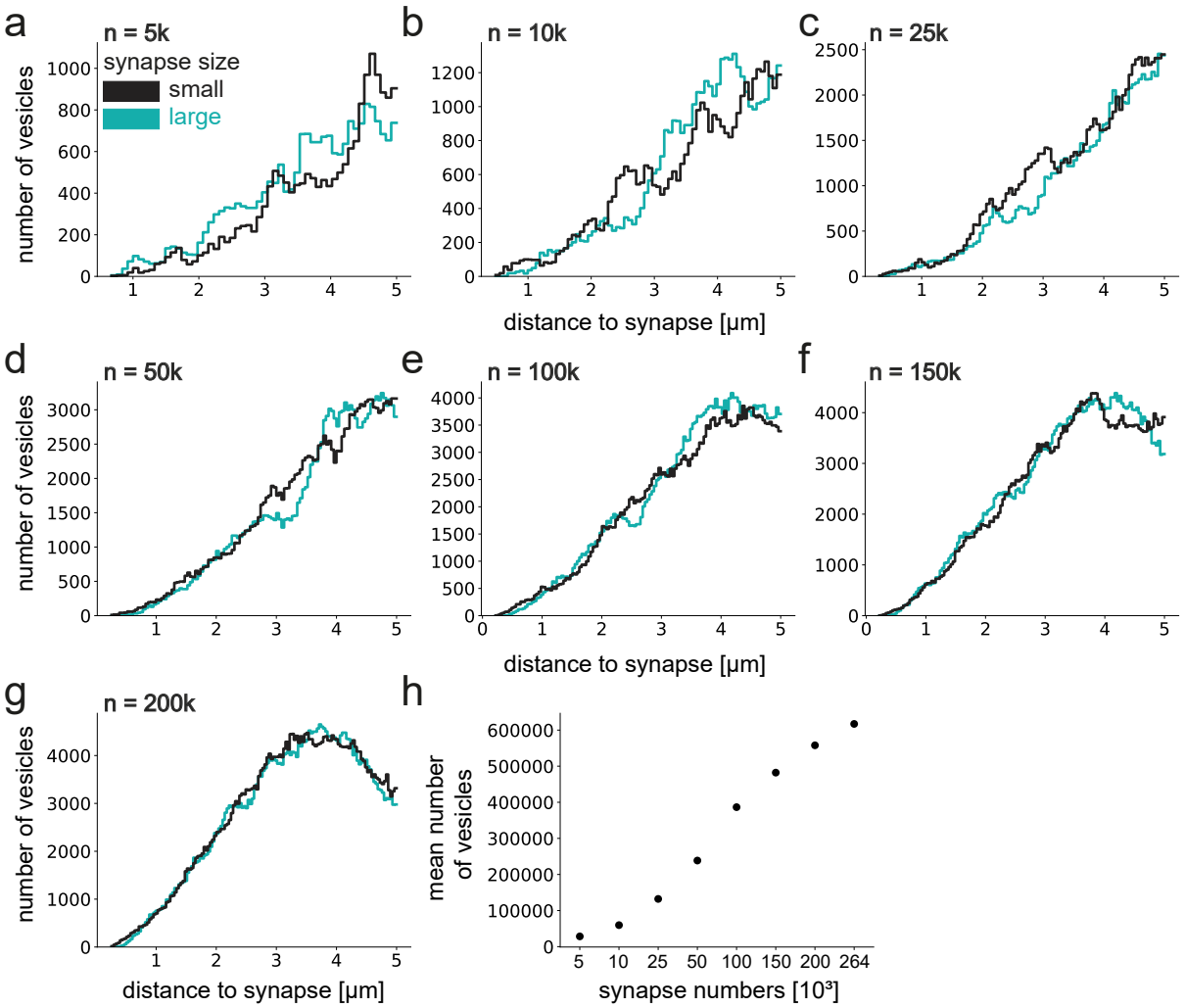

Figure A35: TAN non-synaptic vesicles in proximity to small and large synapses of HVC-MSN, as well as to different random subsets of synapses. Vesicles were counted as non-synaptic if they were at least 3 µm away from a synapse. Synapses were randomly selected without replacement from the entire distribution. Then, the smallest and largest quantiles of this subset ("small" and "large," respectively) were selected to calculate the distance to the vesicles. With n = 10k, 2,500 synapses are shown in each distribution. a-g Distance to subsets of different numbers of synapses. h Mean number of vesicles around small and large synapses in relation to the numbers of synapses in different subsets and in the real distribution (264,000 synapses). The number of synapses, vesicles, and p-values for the graphs are in appendix table A43.

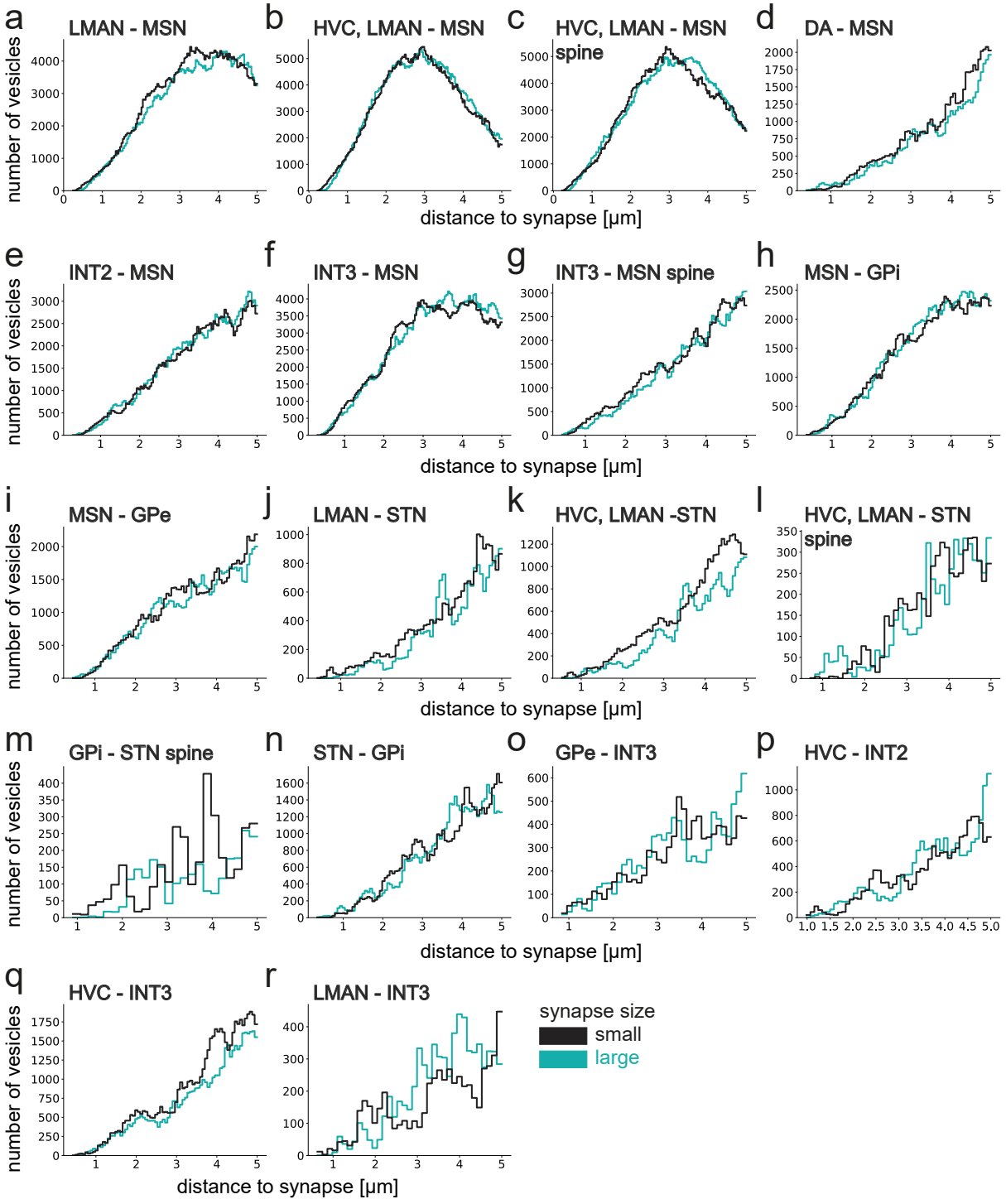

Figure A36: TAN non-synaptic vesicles in proximity to small and large synapses of different cell types. Vesicles were classified as non-synaptic if they were at least 3 µm away from a synapse. The distance of these vesicles from the smallest and largest quantile ("small" and "large," respectively) synaptic connections between different cell types was analyzed. c, g, l Only synapses mapped to the "spine head" of the postsynaptic cell were counted. The number of synapses, vesicles, and p-values for the graphs shown are found in the appendix tables: A44, A45.

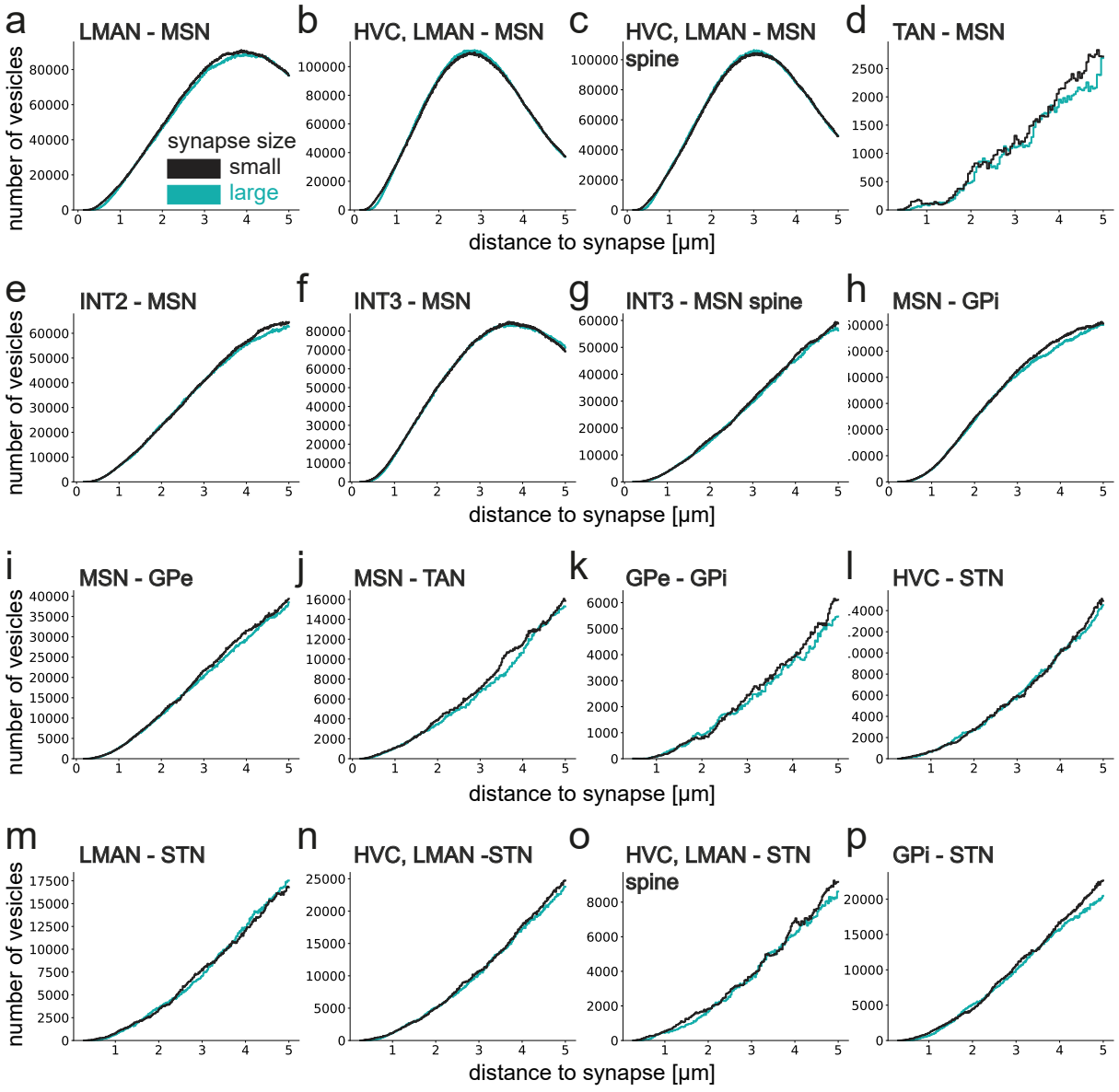

Figure A37: DA non-synaptic vesicles in proximity to small and large synapses of different cell types. Vesicles were classified as non-synaptic if they were at least 3 µm away from a synapse. The distance of these vesicles from the smallest and largest quantile ("small" and "large," respectively) synaptic connections between different cell types was analyzed. c, g, o Only synapses mapped to the "spine head" of the postsynaptic cell were counted. The number of synapses, vesicles, and p-values for the graphs shown are found in the appendix tables: A44, A46, A47.

n syns total	n vesicles small	n vesicles large	max syn size small [µm²]	min syn size large [µm²]	ranksums p-value	KS statistic	KS p-value
5000	18139	20558	0.14	0.31	1.07E-104	0.11	1.29E-95
10000	39218	40829	0.14	0.31	1.19E-19	0.08	1.46E-120
25000	91382	81664	0.14	0.3	1.47E-59	0.05	1.08E-102
50000	160861	155424	0.14	0.3	1.70E-41	0.04	2.42E-119
100000	254519	263933	0.14	0.3	1.16E-27	0.03	1.02E-74
150000	319072	326151	0.14	0.3	2.67E-05	0.01	2.50E-21
200000	373564	368582	0.14	0.3	0.49	0.01	2.84E-09
263715*	409741*	414768*	0.14*	0.3*	2.70E-4	0.01	8.25E-14

Table A43: TAN non-synaptic vesicles within 5 µm of HVC–MSN synapses. Synapses were randomly selected to evaluate the dependence of vesicle number on synapse count. Results using all synapses are shown in rows marked with an asterisk (*, see appendix table A44).

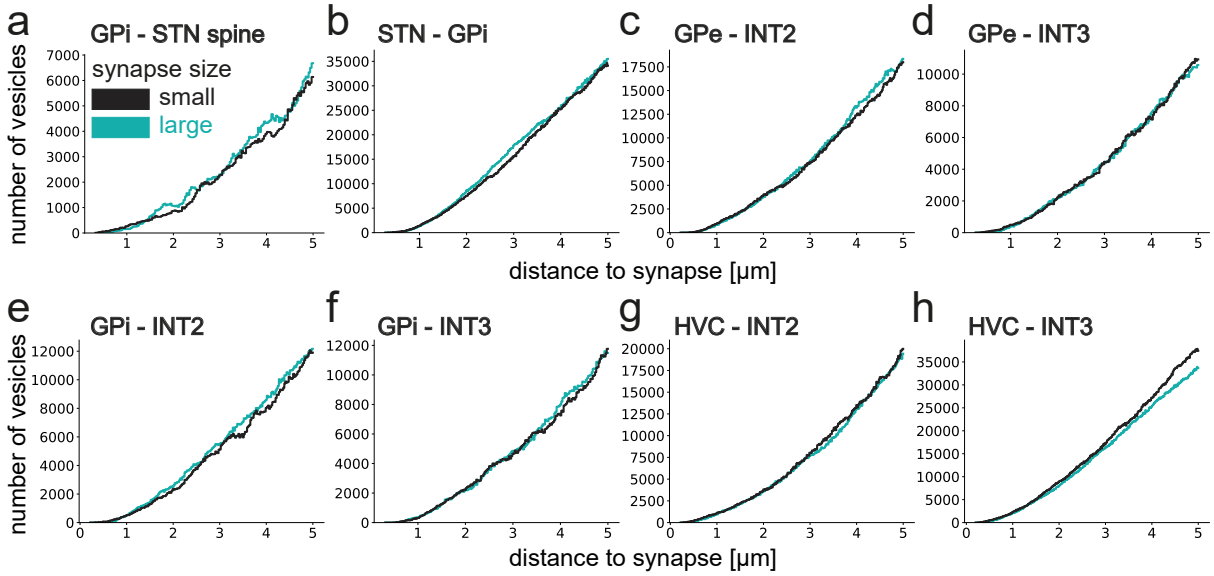

Figure A38: DA non-synaptic vesicles in proximity to small and large synapses of different cell types. Vesicles were classified as non-synaptic if they were at least 3 µm away from a synapse. The distance of these vesicles from the smallest and largest quantile ("small" and "large," respectively) synaptic connections between different cell types was analyzed. c, g, o Only synapses mapped to the "spine head" of the postsynaptic cell were counted. The number of synapses, vesicles, and p-values for the graphs shown are found in the appendix tables: A44, A46, A47.

modulatory cell type	pre cell type	post cell type	spiness?	vesicle number small	vesicle number large	synapses total (n)	max synapse size smallμm^2>μm^2	min synapse size largeμm^2>μm^2	ranksums p-value	KS statistic	KS p-value
TAN	HVC	MSN	None	409741	414768	263715	0.14	0.3	0.00026989	0.01	8.25E-14
TAN	LMAN	MSN	None	350239	332297	180854	0.13	0.27	3.28E-89	0.03	7.00E-101
TAN	HVC, LMAN	MSN	None	473525	479815	444569	0.14	0.29	5.71E-49	0.02	1.06E-64
TAN	HVC, LMAN	MSN	spine only	446188	448426	329776	0.14	0.27	4.21E-73	0.03	1.29E-161
TAN	INT3	MSN	None	316915	320548	190814	0.12	0.19	3.02E-110	0.03	6.33E-126
TAN	INT2	MSN	None	150489	153561	65929	0.12	0.19	0.0164	0.01	2.20E-09
TAN	INT3	MSN	spine only	123636	116166	37071	0.12	0.19	8.94E-46	0.03	1.46E-59
TAN	MSN	Gpe	None	74897	71475	28006	0.17	0.3	0.000235	0.02	2.93E-09
TAN	MSN	Gpi	None	127420	130231	76568	0.17	0.34	2.99E-06	0.02	1.49E-17
TAN	GPe	GPi	None	3371	2580	759	0.23	0.53	0.0003158	0.16	4.37E-33
TAN	GPe	INT2	None	15115	15589	5626	0.19	0.37	1.25E-82	0.11	4.80E-82
TAN	GPi	INT2	None	7141	5283	2655	0.26	0.57	6.25E-13	0.19	1.36E-95
TAN	GPi	INT3	None	9158	9433	2427	0.25	0.53	0.1	0.05	1.96E-11
TAN	GPi	INT3	None	4535	7846	2160	0.32	0.71	4.11E-15	0.14	2.57E-46
TAN	HVC	INT2	None	15639	16213	5093	0.12	0.17	4.31E-07	0.06	8.25E-24
TAN	HVC	INT3	None	59489	49472	17169	0.14	0.22	0.6438	0.02	6.18E-14
TAN	LMAN	INT2	None	12714	13324	3753	0.13	0.21	2.57E-46	0.12	2.54E-80
TAN	LMAN	INT3	None	5703	7083	1794	0.14	0.23	0.0002579	0.11	4.00E-35
TAN	HVC	STN	None	16553	12222	3155	0.13	0.23	1.81E-12	0.08	2.05E-44
TAN	LMAN	STN	None	20968	18115	4621	0.17	0.39	1.07E-12	0.06	3.98E-33
TAN	HVC, LMAN	STN	None	35148	27201	7776	0.15	0.32	9.14E-06	0.04	1.40E-25
TAN	HVC, LMAN	STN	spine only	5722	5449	1576	0.16	0.37	0.0077	0.06	1.76E-08
TAN	GPi	STN	None	26505	21653	8111	0.24	0.57	5.16E-29	0.05	1.54E-29
TAN	GPi	STN	spine only	3367	2444	745	0.18	0.35	0.237	0.12	7.80E-17
TAN	STN	GPi	None	50769	50006	15084	0.18	0.34	0.9873	0.03	1.41E-22
TAN	DA	MSN	None	54151	47466	16928	0.11	0.15	4.40E-05	0.02	9.87E-13
DA	HVC	MSN	None	41120740	41306591	263715	0.14	0.3	4.48E-121	0	1.58E-250
DA	LMAN	MSN	None	34194234	33351317	180854	0.13	0.27	0	0.01	0
DA	HVC, LMAN	MSN	None	47167065	47488354	444569	0.14	0.29	3.94E-09	0.01	3.94E-09
DA	HVC, LMAN	MSN	spine only	44199264	44395951	329776	0.14	0.27	6.48E-100	0	2.02E-286
DA	INT3	MSN	None	31337641	31184741	190814	0.12	0.19	4.98E-245	0	2.26E-170
DA	INT2	MSN	None	15816283	15536490	65929	0.12	0.19	0	0.01	0
DA	INT3	MSN	spine only	11910049	11653354	37071	0.12	0.19	0.154	0	2.08E-17
DA	MSN	GPe	None	6409969	6176899	28006	0.17	0.3	0.0656	0	3.33E-54
DA	MSN	GPi	None	15301668	14839202	76568	0.17	0.34	7.50E-18	0	9.15E-135
DA	GPe	GPi	None	316480	297519	759	0.23	0.53	1.70E-46	0.02	1.97E-48
DA	GPe	INT2	None	1711560	1774642	5626	0.19	0.37	9.60E-67	0.01	2.12E-91
DA	GPi	INT2	None	921757	987548	2655	0.26	0.57	4.83E-66	0.01	1.98E-50
DA	GPe	INT3	None	807255	803004	2427	0.25	0.53	0.0309	0	5.55E-09
DA	GPi	INT3	None	824300	843809	2160	0.32	0.71	4.08E-26	0.01	3.29E-72
DA	HVC	INT2	None	1874988	1817477	5093	0.12	0.17	1.78E-29	0.01	6.11E-61
DA	HVC	INT3	None	5378060	4945970	17169	0.14	0.22	1.44E-136	0.01	1.44E-136
DA	LMAN	INT2	None	1373543	1261291	3753	0.13	0.21	2.06E-121	0.01	7.02E-88
DA	LMAN	INT3	None	659978	596036	1794	0.14	0.23	1.73E-280	0.03	8.27E-237
DA	HVC	STN	None	1217533	1205492	3155	0.13	0.23	6.06E-66	0.01	3.90E-80
DA	LMAN	STN	None	1686153	1697965	4621	0.17	0.39	6.38E-124	0.02	5.30E-171
DA	HVC, LMAN	STN	None	2811125	2728165	7776	0.15	0.32	1.75E-23	0.01	5.91E-31
DA	HVC, LMAN	STN	spine only	637435	602216	1576	0.16	0.37	2.49E-06	0.01	1.89E-58
DA	GPi	STN	None	2576454	2441581	8111	0.24	0.57	1.21E-147	0.01	2.30E-159
DA	GPi	STN	spine only	314972	339134	745	0.18	0.35	9.72E-19	0.02	1.16E-32
DA	STN	GPi	None	4920004	5165882	15084	0.18	0.34	0	0.02	0
DA	MSN	TAN	None	1479091	1387320	5150	0.15	0.26	1.80E-95	0.02	8.20E-196
DA	TAN	MSN	None	109765	98375	276	0.11	0.14	2.49E-05	0.02	5.81E-14

Table A44: Non-synaptic vesicles of TAN and DA in proximity to synapses from different connections. Vesicles were classified as non-synaptic if they were at least 3 µm away from the synapse. There were 546,364 non-synaptic TAN vesicles and 5,449,9825 non-synaptic DA vesicles. Small and large synapses represented the lowest and highest quantiles of synapse sizes in that connection, respectively. The resulting absolute values are shown in the table. The ranksums p-value shows the p-value of the Wilcoxon rank sum test. The Kolmogorov-Smirnov (KS) test was used to compare the distribution of distances to small and large vesicles; the statistic represents the effect size.

			bootstrapping			
pre cell type	post cell type	spiness?	n	median ranksums p-value	ks test p-value	percentage p-values y 0.05
HVC	MSN	None	1000	0.4855	0.5238	5.7
LMAN	MSN	None	1000	0.236863851	2.63E-62	19.1
HVC, LMAN	MSN	None	1000	0.417348345	1.56E-10	10.5
HVC, LMAN	MSN	spine only	1000	0.345091888	4.00E-26	14.6
INT3	MSN	None	1000	0.21334246	1.54E-84	24.6
INT2	MSN	None	1000	0.505	0.8205	4.3
INT3	MSN	spine only	1000	0.20167	2.85E-87	24.7
MSN	GPe	None	1000	0.46	0.0082	6.5
MSN	GPi	None	1000	0.47	0.011	7.1
GPe	GPi	None	1000	0.033959898	0	56.6
GPe	INT2	None	1000	1.04E-06	0	99.9
GPi	INT2	None	1000	0.00366	0	84.2
GPe	INT3	None	1000	0.481	0.0119	7.7
GPi	INT3	None	1000	0.001088	0	93
HVC	INT2	None	1000	0.208	7.20E-85	22.4
HVC	INT3	None	1000	0.48977	0.3928	5.8
LMAN	INT2	None	1000	6.32E-05	0	98.4
LMAN	INT3	None	1000	0.159	4.42E-122	27.7
HVC	STN	None	1000	0.0559	1.47E-274	48
LMAN	STN	None	1000	0.108	2.54E-173	35.6
HVC, LMAN	STN	None	1000	0.363997	4.63E-18	11.9
HVC, LMAN	STN	spine only	1000	0.2457	2.44E-63	17.3
GPi	STN	None	1000	1.94E-02	0	64.9
GPi	STN	spine only	1000	0.439	0.000548	6.2
STN	GPi	None	1000	0.508	0.91	4.8
DA	MSN	None	1000	0.414	1.32E-07	8.9
LMAN	MSN	None	2000	0.1308	2.84E-158	35
HVC, LMAN	MSN	None	2000	0.31	2.07E-32	13.6
HVC, LMAN	MSN	spine only	2000	0.2156	3.72E-75	24.9
INT3	MSN	None	2000	0.066958	1.08E-243	45.4
INT3	MSN	spine only	2000	0.0684	2.59E-282	43.3
MSN	GPi	None	2000	0.4289993	4.90E-05	7.7
DA	MSN	None	2000	0.392556	1.07E-20	11.5

Table A45: Non-synaptic TAN vesicles in proximity to synapses from different connections. Vesicles were classified as non-synaptic if they were at least 3 µm away from the synapse. The total number of non-synaptic TAN vesicles was 546,364. Small and large synapses represented the lowest and highest quantiles of synapse sizes in that connection. More information on vesicle and synapse numbers can be found in appendix table A44. Bootstrapping was performed with 1000 iterations, each with 1000 or 2000 samples. Two thousand samples per iteration were only used for connections with a high number of potential vesicles. The median p-value is the median of the p-values calculated after bootstrapping with the Wilcoxon rank sum test. A Kolmogorov-Smirnov (KS) one-sample test was performed on the p-value distribution of the Wilcoxon rank-sum test after 1,000 iterations of bootstrapping to test whether the distribution is uniform.

pre cell type	post cell type	spiness?	n	median ranksums p-value	ks test p-value	percentage p-values 0.05
HVC	MSN	None	1000	0.5097	0.68358	5.4
LMAN	MSN	None	1000	0.4686	0.10689	5.8
HVC, LMAN	MSN	None	1000	0.4877669	0.3528	4.4
HVC, LMAN	MSN	spine only	1000	0.4828878	0.2646	4.6
INT3	MSN	None	1000	0.4972	0.955	5.5
INT2	MSN	None	1000	0.463	0.026	5.4
INT3	MSN	spine only	1000	0.48279	0.4864	6
MSN	GPe	None	1000	0.5056	0.746789	5.2
MSN	GPi	None	1000	0.4825	0.13695	5.1
GPe	GPi	None	1000	0.3428	3.42E-23	13.2
GPe	INT2	None	1000	0.473	0.0327	6.7
GPi	INT2	None	1000	0.4245	2.80E-08	8.8
GPe	INT3	None	1000	0.515	0.367	4.4
GPi	INT3	None	1000	0.465076	0.014	7.2
HVC	INT2	None	1000	0.477493	0.2037	6.3
HVC	INT3	None	1000	0.4499	0.001877	7.4
LMAN	INT2	None	1000	0.41	4.13E-10	10.4
LMAN	INT3	None	1000	0.157287	1.54E-129	28.7
HVC	STN	None	1000	0.48019775	0.033	7.4
LMAN	STN	None	1000	0.42	5.40E-07	9.7
HVC, LMAN	STN	None	1000	0.495657	0.49368776	5.9
HVC, LMAN	STN	spine only	1000	0.5192	0.475	4.6
GPi	STN	None	1000	0.4465	0.000219	6.9
GPi	STN	spine only	1000	0.44318	4.04E-05	8.1
STN	GPi	None	1000	0.41516	1.98E-07	10
MSN	TAN	None	1000	0.4304	1.65E-07	8.1
TAN	MSN	None	1000	0.466	0.0195	4.9
HVC	MSN	None	2000	0.506	0.95	5.2
LMAN	MSN	None	2000	0.427	3.62E-06	7.2
HVC, LMAN	MSN	None	2000	0.49959	0.953	4.5
HVC, LMAN	MSN	spine only	2000	0.4936	0.377	5.9
INT3	MSN	None	2000	0.4786	0.16655	6.6
INT2	MSN	None	2000	0.45869	9.37E-05	7
GPe	GPi	None	2000	0.25398	5.88E-57	19.1
GPe	INT2	None	2000	0.4206	9.88E-08	9.6
GPi	INT2	None	2000	0.37	1.87E-17	13
GPi	INT3	None	2000	0.444	0.00077	7.6
HVC	INT3	None	2000	0.4895	0.304	6
LMAN	INT2	None	2000	0.3571	2.97E-21	15.8
LMAN	INT3	None	2000	0.04253	0.00E+00	51.9
HVC	STN	None	2000	0.41	3.57E-10	10.2
LMAN	STN	None	2000	0.35767795	1.31E-21	12.5
GPi	STN	None	2000	0.387	4.75E-16	12.4
GPi	STN	spine only	2000	0.405	1.53E-09	10.5
STN	GPi	None	2000	0.32	6.75E-30	16.6
MSN	TAN	None	2000	0.388	3.79E-17	11.4
TAN	MSN	None	2000	0.421	3.46E-07	8

Table A46: The bootstrapping results are shown for non-synaptic vesicles with n = 1,000 and n = 2,000 for DA. See the caption of appendix table A45 for a full explanation.

pre cell type	post cell type	spiness?	n	median ranksums p-value	ks test p-value	percentage p-values 0.05
HVC	MSN	None	5000	0.48058	0.3586	6.4
LMAN	MSN	None	5000	0.393	1.17E-13	10.2
HVC, LMAN	MSN	None	5000	0.51407	0.1	5.1
HVC, LMAN	MSN	spine only	5000	0.46689	0.038	5.3
INT3	MSN	None	5000	0.458	0.011	6.8
INT2	MSN	None	5000	0.4179	8.34E-08	9.1
GPe	INT2	None	5000	0.294	6.96E-40	15.6
GPi	INT2	None	5000	0.225	3.55E-70	22
GPi	INT3	None	5000	0.35577889	1.41E-19	11.9
LMAN	INT2	None	5000	0.166	1.58E-117	28.3
LMAN	INT3	None	5000	0.001378	0.00E+00	88.6
HVC	STN	None	5000	0.253	4.23E-56	20.3
LMAN	STN	None	5000	0.18	4.54E-98	25.5
GPi	STN	None	5000	0.244894	3.34E-64	21
GPi	STN	spine only	5000	0.303	8.49E-43	18.6
STN	GPi	None	5000	0.175	3.77E-105	26.6
MSN	TAN	None	5000	0.22	5.29E-76	21.7
HVC	INT3	None	5000	0.371	4.13E-17	12.1
HVC	MSN	None	10000	0.451	0.004375	7
LMAN	MSN	None	10000	0.263897	2.40E-52	19.4
HVC, LMAN	MSN	None	10000	0.515	0.458	5.2
HVC, LMAN	MSN	spine only	10000	0.472	0.053	6.3
INT3	MSN	None	10000	0.40666	3.08E-10	9.4
INT2	MSN	None	10000	0.297589	7.18E-40	15.6
GPe	INT2	None	10000	0.191	2.76E-88	26.5
LMAN	INT2	None	10000	0.0366957	0.00E+00	55.5
HVC	STN	None	10000	0.1128	3.47E-165	34.6
LMAN	STN	None	10000	0.06	1.24E-246	46.1
GPi	STN	None	10000	0.1097	7.26E-187	36.7
STN	GPi	None	10000	0.052	1.78E-289	49.5
MSN	TAN	None	10000	0.082	7.79E-220	39.7
GPi	INT2	None	10000	0.085	2.74E-209	39.7
HVC	INT3	None	10000	0.2549	8.40E-54	19.4

Table A47: The bootstrapping results are shown for non-synaptic vesicles with n = 5,000 and n = 10,000 for DA. See the caption of appendix table A45 for a full explanation.

	statistic	p-value
mitochondria	1141.31	2.40e-243
GA	245.96	2.99e-50
ER	772.43	1.39e-163

Table A48: Kruskal-Wallis test results for the different organelle volume densities in the glial cell types, migratory neurons, MSN, and GPi as shown in 3.42 b-d. The post hoc Wilcoxon rank sum test showed p values less than < 0.005 for all comparisons except: mitochondria: ASTRO vs GPi (0.02), MICRO vs OLIGO (0.44), MICRO vs OPC (0.10), OLIGO vs OPC (0.13); GA: ASTRO vs MICRO (0.008), GPi vs MSN (0.06), MICRO vs MIGR (0.04), MICRO vs OPC (0.87), MIGR vs OPC (0.02); ER: MICRO vs OLIGO (0.47), OLIGO vs OPC (0.32)

cell type	sum surface mesh area [µm^2]
ASTRO	1464086.21
OLIGO	11747.32
OPC	324445.74
MICRO	120388.87
MSN	33420555.22
STN	1120082.43
TAN	211414.04
GPe	436766.72
GPi	1343106.41
LTS	174336.75
INT1	1589200.63
INT2	732312.75
INT3	1683024.02
MIGR	46767.79

Table A49: Sum of surface areas for all suitable cells from different glial and neuronal cell types. The values were calculated by Delta Schick.

Acknowledgments

Working on this project for several years until the completion of a PhD Thesis would not have been possible without the support I received.

First, I would like to thank my supervisors, Jörgen Kornfeld and Winfried Denk, for their guidance and feedback over the years. I am particularly grateful to Jörgen for introducing me to the dataset he acquired, which sparked my newfound fascination with the basal ganglia. I would also like to thank my TAC members, Benedikt Grothe, Emilie Mace, and Michael Fee, for their feedback and support throughout my thesis. Additionally, I thank Michael Fee for our discussions that helped me to put my connectivity findings into a functional context.

I thank the Max Planck Society and the IMPRS-LS graduate school for the funding that made this research possible.

I would also like to thank the Denk and Kornfeld departments for their feedback and helpful discussions. Specifically, I would like to thank Jonas Hemesath for the many experiments we performed together, the related discussions, and the helpful feedback on all aspects of the PhD, both research-related and otherwise. I thank Maria Kormacheva for her guidance on embedding and cutting, as well as for her mentorship and emotional support throughout my PhD. I thank Philipp Schubert for introducing me to SyConn and for his support when I was taking my first steps with connectomic data analysis, which evolved into thousands of lines of code over the years. I thank Rangoli Saxena for her help with focusing and electron microscopy, as well as her emotional support. I thank Franz Rieger for his feedback and discussions on machine learning, as well as his support with the computing cluster. I would also like to thank Sebastian Willenberg, Nelson Medina, Caitlin Gillespie, and Csilla Pataki for their helpful discussions. Finally, I thank everyone who joined for movie nights and made the PhD more enjoyable with great—and not-so-great—movies.

I am also grateful for Hashir Ahmad's work when we processed the data together. Debugging the bugs we encountered was truly an adventure. I would also like to thank Martin Bucella for setting up and training a model to predict new organelles and extract individual vesicles.

I would also like to thank the students I have supervised over the years. I thank Delta Schick for his work on bachelor's and master's theses, synapse annotations, and reviewing synapse and organelle annotations. I am grateful that your interest in glial cells sparked my interest as well, and that we were able to present our work together at two conferences. I thank Riccardo Morbio for his work on a bachelor's thesis, especially the manual annotations and evaluations. These include manual annotations of synapses and organelles and several evaluations of synapses, organelles and cell meshes; all while being able to point me to curious shapes and phenomena in the data. I thank Laura Werner, Katyayni Ganesan, Deniz Üreneyer, Merve Çetiner, Gizem Karabiyik, Ata Kan, Dominik Melzer, Yona Perstat, Akshaya Rajan, and Maria Nikitina for their work on synapse, mitochondria, ER, GA, and vesicle annotations.

Additionally, I thank Laura Werner for her manual synapse evaluations and Julian Hendricks for his synapse annotations and reviews.

I would also like to thank Julia Kuhl for her feedback on the figures, Barbara Strasser for her help with organizational tasks, as well as the workshop team for trimming the embedded samples.

I would also like to thank Ben Scott, Naomi Shvedov and Simon Castonguay for identifying the migratory neurons and for their collaboration, which taught me a great deal about these neurons. I would also like to thank JoAnn Buchanan for her help in identifying the OPCs.

I would also like to thank Michał Januszewski and the team at Google Research for the cell, synapse, mitochondria, and vesicle cloud annotations. I would also like to thank Lorenz Hüdepohl and Christian Guggenberger for their support at the MPCDF in Garching.

I would also like to thank all my friends who supported me via Zoom or in person. They reminded me how much fun life can be, despite all the failures I experienced while working on this thesis. I would like to thank Julia; the Wood Lane Ladies: Inês, Paula, Tina, and María; and my university friends: Lilly, Melanie, Corinna, and Tina. I would also like to thank the members of my gymnastics and volleyball teams, especially Adina, Resi, Lisa, Vera, and Alina, who danced my PhD thesis. I am still amazed that this COVID project turned into a synchronized video in a time when we couldn't meet in person.

Lastly, I thank my family and the Trattnig family for their support over the years. I am especially grateful to have two sisters that understand me so well and help me recharge with zumba or spinning classes, musical visits or holidays. I also thank my partner, Stephan, for ensuring that my devices are always charged, being my personal IT support, helping me through several (near-) panic attacks, and just generally providing me with so much joy and support.

Affidavit

Herewith I certify under oath that I wrote the accompanying dissertation myself.

Title: *Connectomic Analyses of Songbird Area X*

In the thesis no other sources and aids have been used than those indicated. The passages of the thesis that are taken in wording or meaning from other sources have been marked with an indication of the sources (including the World Wide Web and other electronic text and data collections). Furthermore, all parts of the thesis that were de novo generated with the help of artificial intelligence tools were identified by footnotes/annotations at the appropriate places and the artificial intelligence tools used were listed. The prompts used were listed in the appendix. This statement applies to all text, graphics, drawings, sketch maps, and pictorial representations contained in the Work.

Munich, 19.09.2025, _____

Alexandra Elke Rother

Declaration

Hereby, I declare

☒ that this work, complete or in parts, has not yet been submitted to another examination institution

☒ that I did not undergo another doctoral examination without success

Munich, 19.09.2025, _____

Alexandra Elke Rother